Measurement of Dissolved Oxygen in Highly Restricted (Picoliter) Volumes Utilizing Thin Film Luminescent Sensors

Noel Sean Fitzgerald

A dissertation submitted in partial fulfillment of the requirements for the degree of

Doctor of Philosophy

University of Washington

2013

Reading Committee:

Lloyd W. Burgess, Chair

Robert E. Synovec

Richard H. Gammon

Program Authorized to Offer Degree:

Department of Chemistry

University of Washington

Abstract

Measurement of Dissolved Oxygen in Highly Restricted (Picoliter) Volumes Utilizing Thin Film Luminescent Sensors

Noel Sean Fitzgerald

Chair of the Supervisory Committee:
Research Professor Lloyd W. Burgess
Department of Chemistry

Researchers at the Microscale Life Sciences Center undertook an ambitious project to examine the metabolic and genomic processes in single mammalian cells related to esophageal adenocarcinomas in Barrett's Esophagus patients. Examination of one cell at a time was necessitated by the need to resolve questions related to cellular heterogeneity and thus required that experiments be conducted in highly restricted (picoliter) volumes. Measurement of dissolved oxygen is a key parameter in understanding cellular metabolism. This need to examine oxygen consumption rates of single mammalian cells motivated the development of new sensors and new methods for the measurement of dissolved oxygen in picoliter volumes. Commercially available luminescent sensors as well as in-house customized luminescent sensors were characterized. Key parameters that were characterized included sensor deposition into microwells, sensor lifetime measurement for dry and wet sensors, sensor adhesion assessment, photodegradation studies, and measurement of singlet oxygen emission signals. This characterization work led to the development of a new lifetime measurement method for luminescent sensors, dubbed Long-Pulsed Luminescence (LPL). Application of this new method determined that a modified platinum porphyrin sensor was the best performer in terms of analytic usefulness, but the best application-driven sensor was a commercially available microsphere product, which also utilized a platinum porphyrin reporter chemistry.

TABLE OF CONTENTS

LIST OF FIGURES

Figure Page

LIST OF TABLES

Table Page

ACKNOWLEDGEMENTS

I would like to acknowledge Lloyd Burgess for the extended tutelage in this study, as well as the patience of the committee members. Robert Synovec, Richard Gammon, and Michael Yost all provided valuable feedback. This study could not have been completed without the assistance of Sei-Hum Jang and Jeff Yang of the Jen Group and the variety of sensors that they produced. I would like to thank the staff at the MLSC for assistance, including Martin Suchorolski, Tim Strovas, Tim Molter, Judy Anderson, and Sarah McQuaide. Michael Konopka provided assistance with diffusion modeling as well as a multitude of other tasks. I am grateful to the review of biological information by Tom Paulson. I would also like to thank Wendy Santoso for the invaluable assistance with creation of graphic arts.

Chapter One: Introduction

1.1 Overview

Researchers at the Microscale Life Sciences Center (MLSC) investigated single-cell oxygen consumption rates for several years, in order to better understand adenocarcinomas related to Barrett's Esophagus (BE). Previous work, especially that of Joseph Dragavon,[1,2] successfully developed a platform in which to study the oxygen consumption rates of isolated single mammalian cells, within an aqueous based media solution. In order to study single cells, the volume around each cell was typically highly restricted and diffusionally isolated, on the order of ~300 pL. While Dragavon's work also employed luminescent sensors as the reporter chemistry, practical use of the methods by other researchers at the MLSC did not yield repeatable results. It was the intent of this study to improve the repeatability of the measurement of dissolved oxygen, in highly restricted volumes. Improving sensor deposition methods, employing new data collection methods, creating new algorithms for data processing, improving calibration methodology, and investigating new sensor materials achieved that goal. The best optical performance results were obtained with a customized platinum porphyrin type sensor, utilizing a high-resolution ratiometric imaging method, while a commercially available sensor was found to be best suited to the demands of the given application.

1.2 The Microscale Life Sciences Center (MLSC)

The MLSC was funded by the National Institutes of Health over a 10-year period (2001–2011) and was an interdisciplinary effort amongst scientists and engineers from

Arizona State University, the University of Washington, the Fred Hutchinson Cancer Research Center, and Brandeis University. The stated goals[3,4] of the MLSC were to develop microscale instruments for measuring parameters in single living cells, so that scientists could study biological problems that require the analysis of heterogeneous cell populations. By developing such technologies, the desire was to study functional genomics, one cell at a time. A desirable initial target for these technologies was the study of adenocarcinomas related to Barrett's Esophagus.

1.3 Barrett's Esophagus and Esophageal Adenocarcinoma

Barrett's Esophagus (BE) is a condition in which the normal squamous epithelium in the distal end of the esophagus is replaced with a metaplastic columnar epithelium.[5] The condition was first recognized in 1906[6] and definitively characterized in 1957 by Barrett.[7] Initially, the condition of BE was classified as the presence of columnar epithelium more than 3 cm (from the stomach/esophagus transition), but now can be any length. Additionally, BE more than 3 cm in length is identified as long-segment BE and less than that, short-segment BE.[6] Another simple, yet highly effective description is: "…that congenital abnormality which from the outside looks like oesophagus and from the inside looks like stomach."[18] (However, note that modern definitions would no longer classify the condition as congenital). BE in effect makes the lining of the lower esophagus more resistant to the damage that can occur from gastroesophageal refluxate containing acid and bile.

Gastroesophageal reflux disease (GERD) is a strong indicator for the potential presence of BE.[19] Obesity is an important risk factor for GERD[20] and as such, might be

expected to be an important risk factor for BE. However, the evidence suggests that the pattern of obesity is far more important as a risk factor for BE than the presence of obesity alone.[21] Central adiposity or excess weight around the abdominal area has been found to be most significant, with the likelihood of BE roughly 2-4 times greater[21] for patients with abdominal obesity. Smoking is another risk factor for BE. The risk due to smoking has been reported to be moderate without evidence of a dose-response relationship.[21,22]

Obesity is also a major risk factor for esophageal adenocarcinoma (EA), as are alcohol consumption and smoking.[20-23] It may appear logical to assume an association between BE and EA; BE is associated with a 40-fold increase in risk of developing EA.[5] The majority of adenocarcinomas diagnosed in the population are very aggressive and

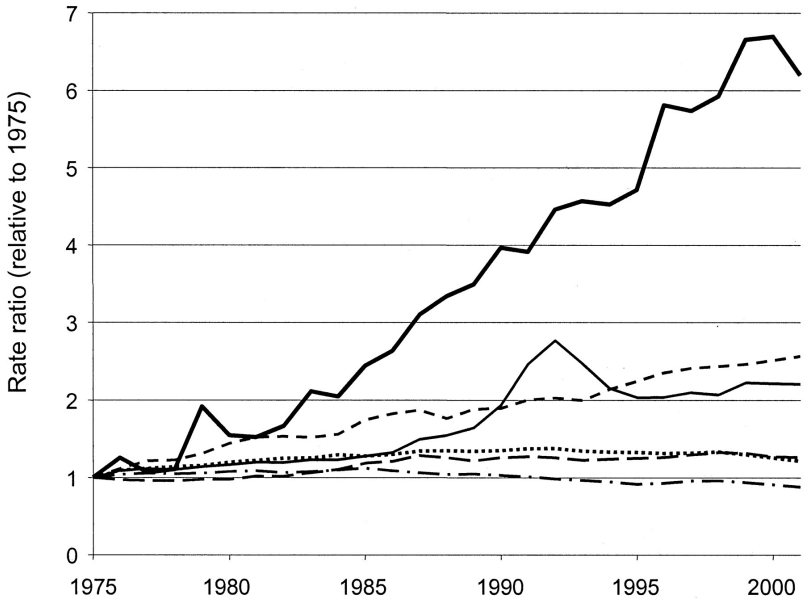

Figure 1: Relative change in incidence of esophageal adenocarcinoma and other malignancies (1975-2001)[8]. Data from the National Cancer Institute's Surveillance, Epidemiology, and End Results program with age-adjustment using the 2000 U.S. standard population. Baseline was the average incidence between 1973 and 1975. **Solid black line** = esophageal adenocarcinoma; **short dashed line** = melanoma; **line** = prostate cancer; **dashed line** = breast cancer; **dotted line** = lung cancer; **dashes and dotted line** = colorectal cancer. Reprinted with permission, Oxford University Press.

esophageal cancers in general have a poor prognosis, with only a 10-13% 5-year survival rate in the United States.[5] Pohl and Welch also show that EA were increasing in incidence faster than any other cancer[8] in their study (see Figure 1). However, squamous cell carcinoma in the esophagus is not increasing in incidence at all,[23] which is puzzling, given the rapid increase in EA incidence. The rapid increase in incidence of EA and the substantial increased risk associated with BE, has made research in this area of keen interest to the National Institutes of Health. However, recent research efforts are suggesting the potential need for a paradigm shift. Reid *et al*[24] suggest that the incidence of EA in BE patients is actually quite small, while paradoxically, patients with advanced EA almost always present with BE. The result is that patients in medical surveillance for BE are classified as premalignant, yet rarely die from EA, while patients with EA most often present for the first time with advanced disease, and subsequently discover that they also had BE.[24]

Once a diagnosis of BE is made, lifestyle changes such as weight control, smoking cessation, and reduced alcohol intake are indicated.[6] While there is preliminary evidence that selenium, aspirin regime, and consumption of ellagic acid found in some foods, such as freeze-dried strawberries, reduce the risk of progression to esophageal adenocarcinoma,[5] the standard of care for patients with Barrett's esophagus is periodic endoscopic surveillance with biopsy for the early detection of cancer.[25] With the detection of dysplasia, additional treatments may include reflux control with proton pump inhibitor therapy, photodynamic therapy, mucosal ablation therapy, and in the case of high grade dysplasia, possible surgical resection (esophagectomy).[25] Endoscopic

surveillance may successfully detect carcinomas, however, any biomarkers that aid in early detection of neoplastic progression would be of great benefit to BE patients.

1.4 Cellular Heterogeneity and the Need for Dissolved Oxygen Measurement

Researchers at the MLSC have consistently recognized the need to study cellular heterogeneity.[4] As Figure 2 shows, this is a very straightforward concept. In the cartoon, the graph represents the response (phenotypic expression) of a bulk cell population to some stimulus. The graph shows that an examination of bulk response may be misinterpreted as a graded response by the bulk population to the stimulus. In fact, the response may actually represent the phenotypic variability within subpopulations of cells. In the cartoon, this is expressed by the propensity for various subpopulations to "turn on" under different levels of stimulus, with some subpopulations never being activated. Unless individual cells are examined, there is no way to to detect if apparent phenotypic variation of a bulk population is really a graded response of the population as a whole, or the summation of heterogeneous phenotypic expression of individual subpopulations. An early goal of researchers at the

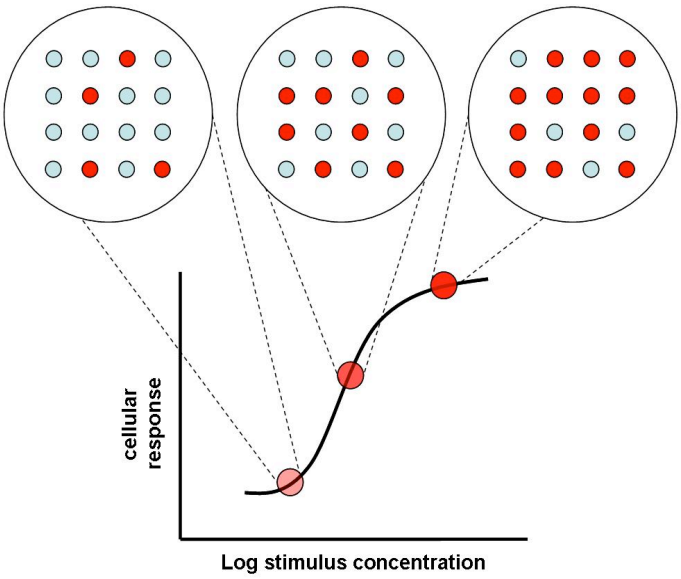

Figure 2: Cartoon of cellular heterogeneity
Reprinted with permission, J.M. Dragavon

MLSC was to examine indvidual cells in high throughput, culminating in the work of Dragavon, with his Living Cell Array.[1] The Living Cell Array allowed the examination of individual cells, by holding them in highly restricted microwells, with a volume typically on the order of ~300 pL.

Spechler *et al,*[6] reviewed the works of researchers that suggest phenotypic and genomic heterogeneity keeps increasing as BE progresses from phenotypic changes only, to low-grade dysplasia, to high-grade dysplasia, then finally to metastasizing adenocarcinoma. More specifically, Maley *et al*[10] report that genetic lesions, such as ploidy abnormalities and loss of heterozygosity, are measurable indicators of increasing clonal diversity, and that the accumulation of clonal diversity may be fundamental to understanding neoplastic progression in BE. Other researchers at the MLSC have also made some progress in trying to characterize the genomics[9] for BE cell lines. High throughput single cell analysis would appear to be a desirable goal for research into BE cell lines, when relevant genomics analysis is included.

Warburg first reported that cancer cells seem to survive via glycolysis in aerobic environments, rather than the oxidative phosphorylation process typical of cells in aerobic environments.[11] He boldly suggested that the state of carcinogensis may be gleaned by measuring the metabolic state of sample cells.

More recently, researchers report the importance of oxygen monitoring in tumor microenvironments as gradients may exist from normoxic to anoxic, and a wide variety of hypoxia levels.[12,13] Others opine that the disorganized microenvironment will lead to increased diffusion distances for oxygen and other species, leading to regional hypoxia and the metabolic changes that Warburg reported.[14] Bristow and Hill[15] also discuss at

length, how hypoxia can lead to resistance to radiotherapies and chemotherapies in malignant cells. Whether specific mechanisms are understood or not, it appears that it remains important to monitor oxygen levels in the cellular environment, in conjuction with relevant genomics analysis.

In summary, we see that adenocarcinomas related to BE are rapidly increasing in incidence in the US and other industrialized nations and the ability for early detection of progress to EA is highly desirable; cellular heterogeneity is critical to understanding the growth and treatment for cancers, so it is best to study single cells, necessitating analysis in highly restricted volumes. A study of the relevant genomics would reveal the most interesting biological information, while oxygen measurement is just one important parameter to analyze in concert with biological studies. However, the focus of this work shall be on the development of dissolved oxygen sensors and methods, to be utilized in conjuction with biological experiments. These factors motivated the research carried out in this study.

Perhaps Marusyk *et al*[26] say it best: "Multi-parameter high-throughput analysis at the single-cell level is the most desirable approach; however, despite successful application of single cell-based analysis in several recent studies, the widespread applicability of this approach will require additional technical improvements."

1.5 Repeatability Challenges

Stochastic processes, genomic diversity, structural diversity, and instabilities in gene regulatory networks all contribute to heterogeneity[26] in cell populations that may be undergoing neoplastic progression. These same factors would contribute to variability in

making biological measurements, especially for genomics analysis. To confound the situation even more, Edelman and Gally[16] also point out that there is degeneracy in biological systems. By this, they mean that identical functions can be carried out by structurally different elements and that this phenomena can be observed at all levels of biological systems, from protein folding mechanisms to highly complex individual biological entities. How does one then separate normal experimental variation from biological heterogeneity?

The solution would be to control as many variables as possible, ideally only changing one variable in each experiment, and make replicate measurements. Assuming that there is little experimental variation in replicate measurements, then differences in observables can potentially be attributed to cellular heterogeneity. In Dragavon's work, this was the goal of the Living Cell Array (LCA).[1,2] The LCA (see Figure 3) was simply an array of microwells etched into a glass slide, with the volume of each microwell on the

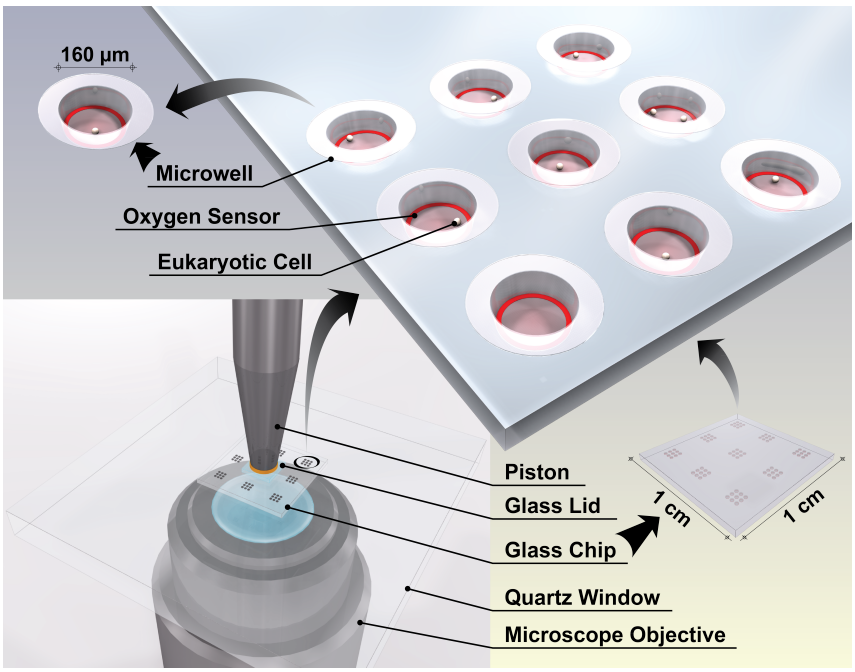

Figure 3: The Living Cell Array

order of a few hundred picoliters. Each microwell contained an optical sensor to report the concentration of dissolved oxygen. A set of subarrays could be diffusionally isolated with a glass lid with applied pressure, in order to make oxygen drawdown measurements (a measure of dissolved oxygen over time, with the lid sealed). The LCA would be placed into a controlled environment where temperature was held at 37 °C. Each microwell would typically contain a single mammalian cell in appropriate media solution, but one microwell would typically be left empty as a control. Microwells were randomly seeded with cells, so there could also be the case that a single microwell contained 2-3 mammalian cells.

Dragavon often reported[1] an RSD of 20-25% for some type of characterizing measurements of the LCA and an overall RSD of ~3% in actual oxygen concentration measurements, (no cells present). By RSD, the author means relative standard deviation, which is defined in the usual manner (RSD = standard deviation/mean*100%). Dragavon was a careful experimentalist and when he reported RSDs on the order of 30% for actual cell measurements,[2] this did not seem out of place, given the characterization work he performed on the LCA. However, RSDs degraded to a mean of 31-74% for later trials.[17] Researchers at the MLSC could no longer determine the difference between cellular heterogeneity and experimential variation. Improving the repeatability of replicate measuremnents therefore became the driving motivation for the work carried out in this study. Several steps were carried out in order to accomplish this goal.

1.6 A New Sensor Characterization Test Station

In order to better characterize potential oxygen sensor materials, a new test station was built. This section will be an overview of the test station; specific details will be discussed in chapter three. Much like the Living Cell Array of Dragavon, sensor material was held in microwells of highly restricted volume (~300 pL). Figure 4 is a photo of a "plunger" and "chip." The chips were 10 mm x 10 mm glass slides of fused silica. Not visible in this photo, are the arrays of microwells etched into the glass. An array is a 3x3 arrangement of microwells, and there was also an arrangement of 3x3 for the arrays on each chip, so that each chip contained 81 total microwells. The plunger was a steel piston with a small glass slide of microscope coverslip material mounted with epoxy that also provided a cushion layer. The plunger was utilized to provide the diffusional seal for an array. The glass slide was 3x3 mm and would cover one array of nine microwells at a time.

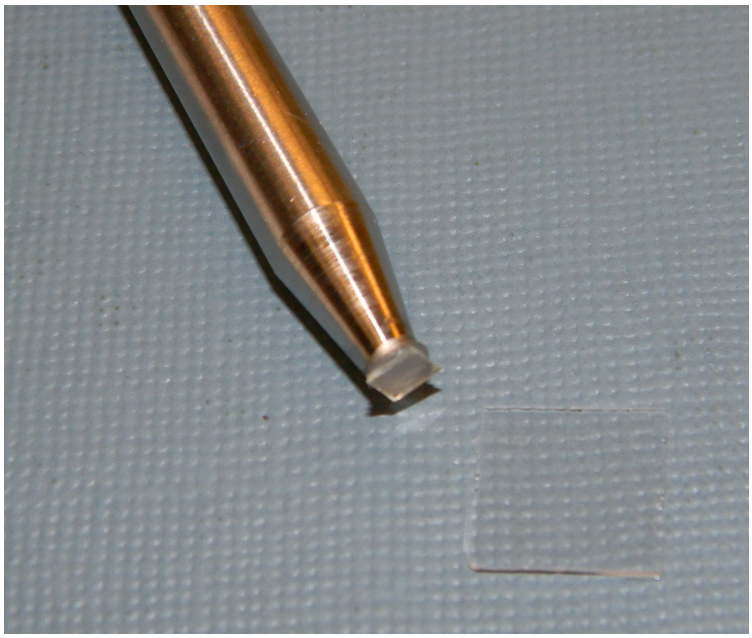

Figure 4: Photo of chip and plunger

The chip was held in a controlled environment. The chip would be immersed in clean deionized water, 5-6 mL in volume. Biological experiments were carried out in aqueous media solution, but for sensor characterization, water was substituted. The

temperature of the water bath would be held to 37 °C for most experiments and the ambient pressure was monitored with an absolute pressure sensor. Figure 5 depicts the chip holder assembly. The chip would sit inside the metal box that was tightly sealed with an acrylic top. The bottom of the chip holder is not visible, but was a large quartz window, which enabled viewing of the microwells by a microscope. In the photo, purple wires are attached to dual cartridge heaters which precisely controlled the temperature, via a feedback signal from a thermocouple (brown wires). The pale white tubes in the photo allowed premixed gasses to be injected into the chamber. The large tube allowed purging of gasses, while the small tube allowed sparging of gasses. The dark gray vertical cylinder in the photo is a Clark microelectrode, which enabled the real-time monitoring of dissolved oxygen levels. The Clark microelectrode served as a the reference standard for all calibration measurements; the microelectrode itself was typically calibrated against ambient oxygen levels (20.95%) and anoxia (0%). The thick metal bars in the forefront of the picture are merely safety guards. Finally, the entire chip

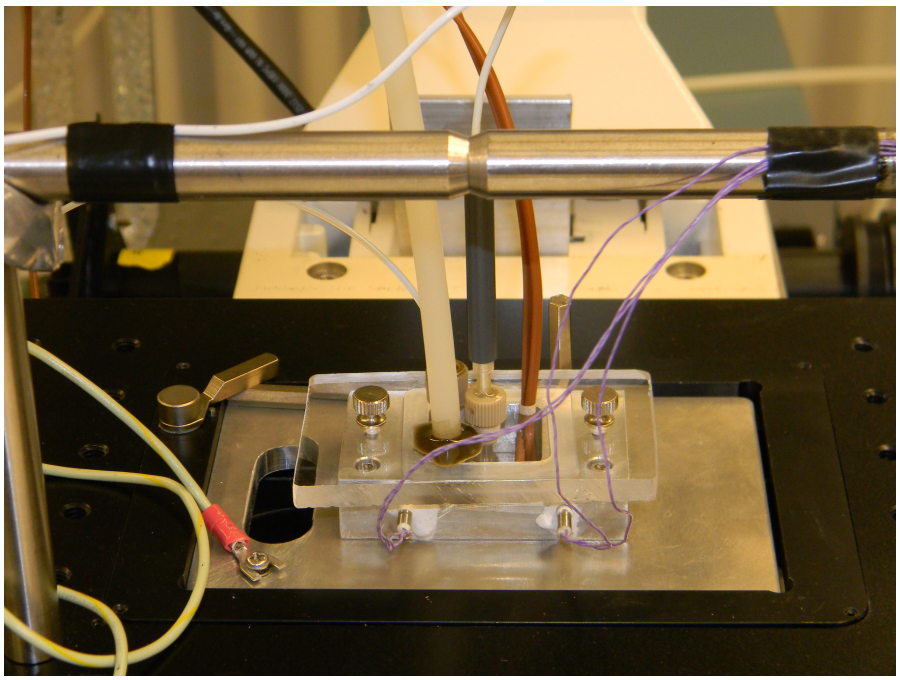

Figure 5: Photo of chip holder

holder chamber was tightly sealed, except for the thermocouple wire entry point. That was a loose fit that allowed the exhaust of purge gasses, in order to maintain pressure at ambient levels.

Figure 6 shows an overview of the test station. The chip holder was mounted to

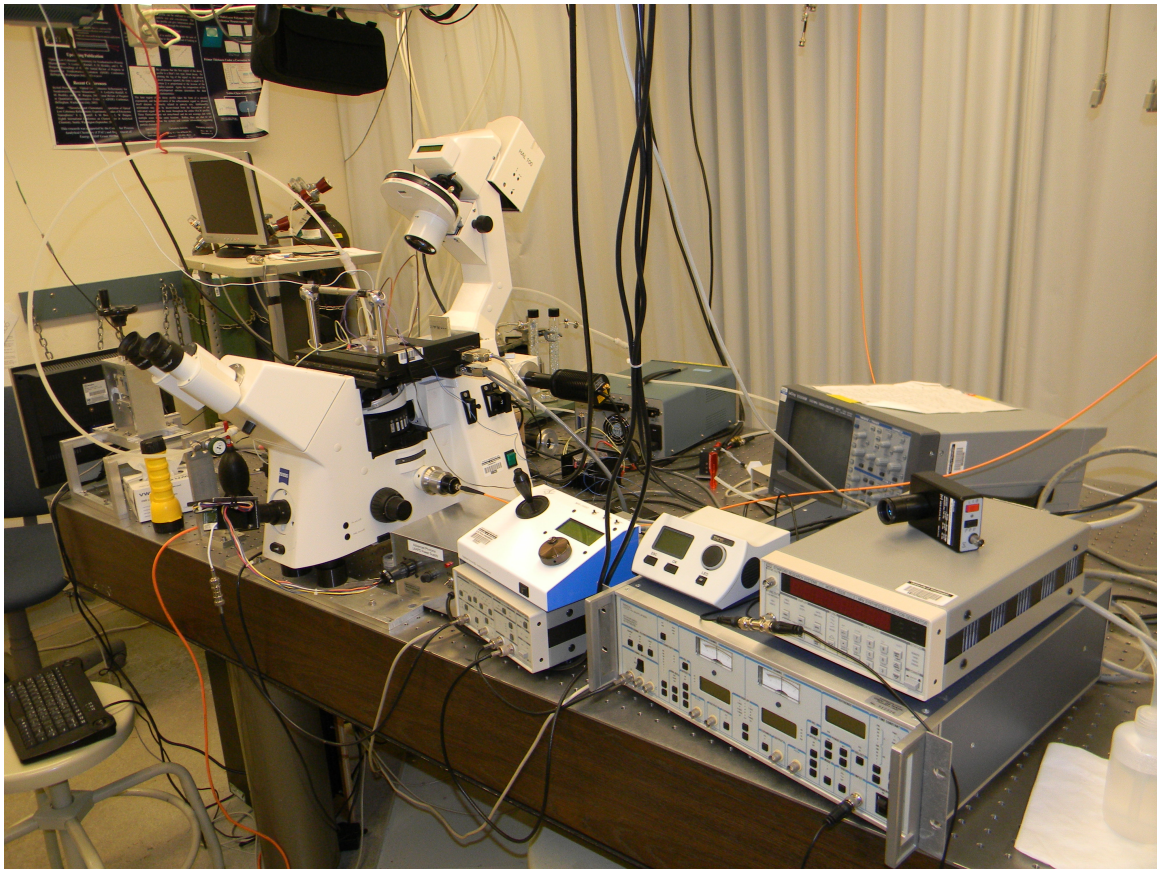

Figure 6: Overview of the test station

an inverted epifluorescence style microscope. The microscope held several filter cubes for various combinations of excitation and emission filters. Multiple ports allowed the attachment of a fiber-coupled spectrometer, an avalanche photodiode detector, intensified CCD camera, and while not utilized very much, a photomultiplier tube could also be mounted to the microscope. Mounted excitation sources included a halogen bulb source and two high-power LEDs; one that was pulsed and one that could be modulated. To the right of the microscope are various instruments; a signal preamplifier, joystick control for

the microscope platen, a digital oscilloscope for data analysis and capture, LED modulation controls, and a lock-in amplifier for small signal detection. With these instruments, the decay rates for luminescent sensors could be measured directly, or measured via phase-modulation methods. A femtowatt receiver was also available for detection of near-infrared signals.

Figure 7 below shows the left side of the test station, where more instruments were located, as well as mass flow controllers to control the gas mixtures for testing. Three mass flow controllers are visible as all mixtures were one or more combinations of

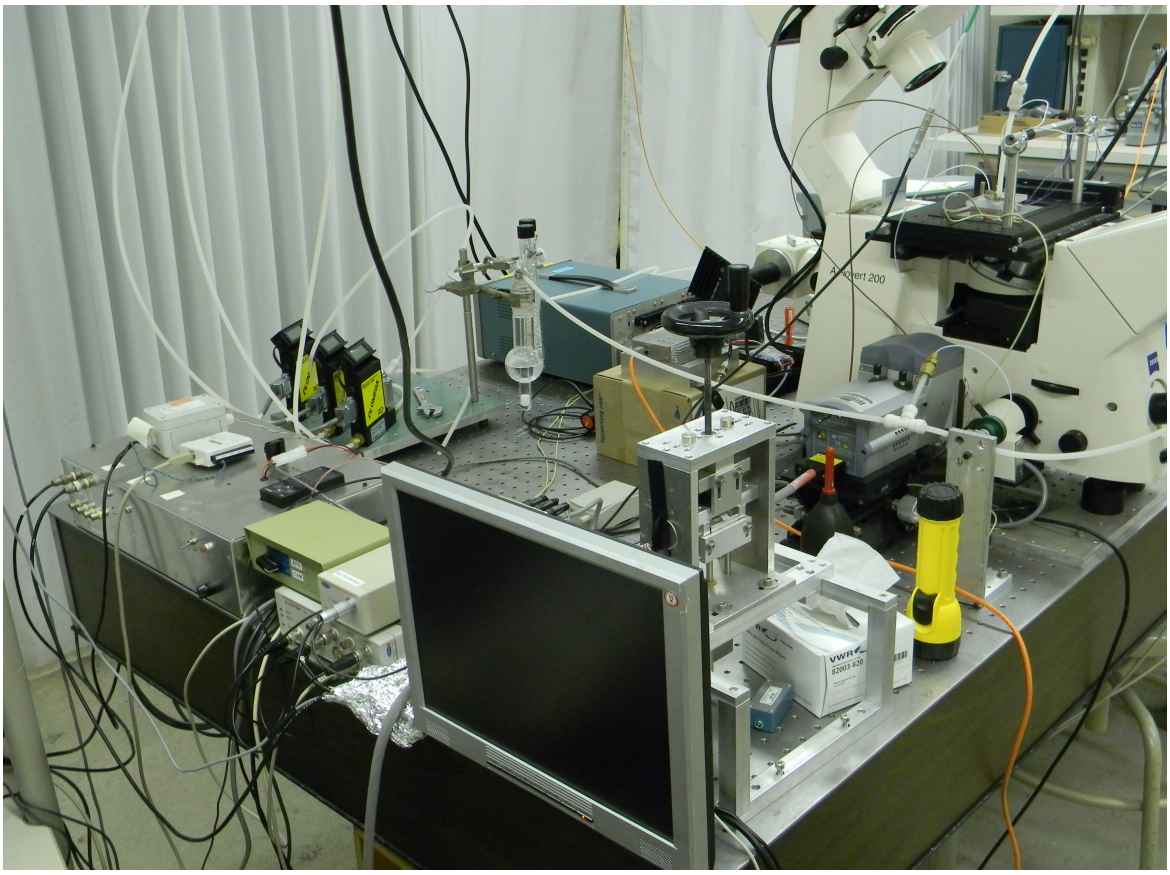

Figure 7: Gas control side of the test station

nitrogen, oxygen, and carbon dioxide. The gasses were turbulently mixed in glass beads, then humidified by bubbling through water. Additional instruments recorded data

electronically from the Clark microelectrode, a thermocouple, and an absolute static pressure sensor. The large metal frame with black wheel on top was utilized to hold the plunger and apply force to it. A strain gauge sensor allowed the level of force to be monitored. Visible on the side of the microscope is the intensified CCD camera. Nearby instruments include power supplies and controllers for the pulsed LED excitation source.

With these instruments, the temperature and gas composition inside the chip holder was precisely known and controlled. The ambient absolute pressure was also monitored. The remaining suite of instruments allowed the sensor to be excited in various ways and its emission signal recorded as a direct decay, phase measurement, or a series of images. Characterization and calibration experiments were then conducted for various types of sensors.

Chapter Two: Background

2.1 Phosphorescence Theory

Most of the luminescent sensors in this study rely upon phosphorescence as the emission mechanism and all sensors are porphyrin based. An important observation about porphyrins is that they are surprisingly planar and have a ring of π electrons that

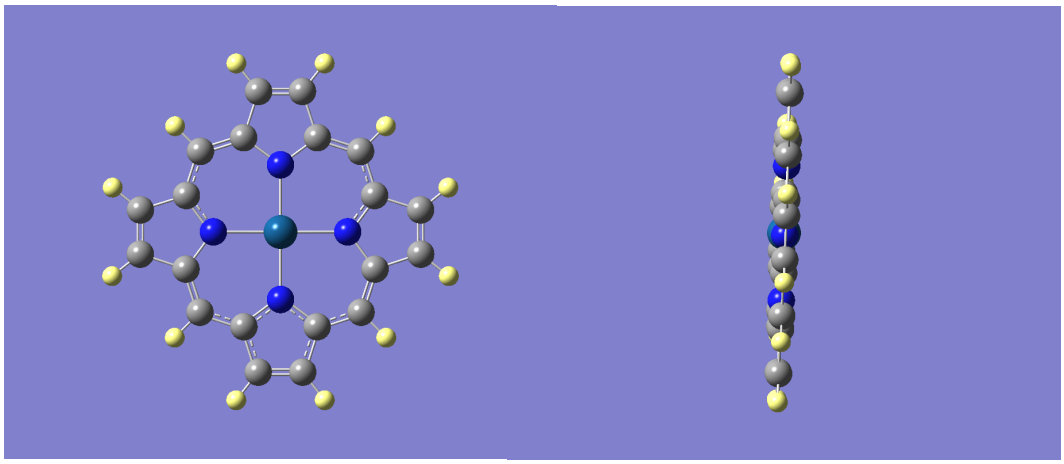

Figure 8: Platinum (II) porphyrin computational model. Yellow = H atom; gray = C atom; blue = N atom; aqua = platinum atom. Top and side views.

are all conjugated. Therefore, they are aromatic molecules (see Figure 8). In Figure 8, we see a simple computational model performed on a desktop computer, utilizing the *GAUSSIAN03* software package. The computation was performed with density functional theory utilizing the LanL2MB basis set. This model does not depict bond order very well, but there are 22 π electrons, with the shortest cyclic route of conjugation containing 18 π electrons. The model does depict geometry to a good first approximation and the side-view of the molecule on the right side of Figure 8 depicts the surprising planarity nicely. Sensor molecules are more complicated with substituents attached at

exterior hydrogen positions. This discussion does not imply that the overall molecule for sensors utilized will remain planar, but that retention of planarity at the porphyrin center will retain aromaticity and thus retain important spectral features.

The phosphorescence process begins with absorption of energy, in order to bring the molecule to an excited state. This is governed by equation 2-1, where ψ_2^* represents

$$M = \int \psi_2^* \mu \psi_1 d\tau \tag{2-1}$$

the complex conjugate of the wavefunction of the excited state and ψ_1 represents the wavefunction of the ground state. The appropriate volume element for integration is represented by $d\tau$, while μ is the transition moment operator, and M is the transition moment. For absorption of light, the transition moment operator is the dipole moment operator, which is the sum of all vector products between the charge of an electron and the displacement vectors for the electronic coordinate system. Furthermore, the wavefunction is typically separated into an electronic component, vibrational component, and spin component for ease of calculation (the Born-Oppenheimer approximation), with appropriate coordinate spaces chosen for each component. The absorption process occurs instantaneously (10^{-15} sec),[27] relative to the phosphoresence process.

Metalloporphyrins in general have two regions of absorption; the Q bands and the Soret bands.[28] Both arise from ($\pi \rightarrow \pi^*$) transitions from the aromatic system. The Q bands are quasi-allowed since there is a large change in net angular momentum, while the Soret bands are strongly allowed, with no net change in angular momentum. The Q bands appear in the 500-600 nm region and often appear as two bands; a (0,0) vibronic transition and a (1,0) vibronic transition. The Q bands represent a transition to the first excited singlet state, while the Soret bands represent a transition to the second excited

singlet state. The strongly allowed Soret band appears as a broad and exceedingly intense absorption in the 380-420 nm region. The Soret band also may contain a (0,0) and (1,0) vibronic transition, though distinction between the two is often not apparent in room temperature spectra.

Once the molecule is excited, it must emit energy and there are several ways for this to occur. Electrons populating higher vibrational modes will transition to the lowest vibrational mode in stepwise fashion, in order to obey the harmonic oscillator selection rule ($\Delta v = 1$). This vibrational relaxation process occurs on the order of 10^{-13} sec.[27] and energy is collisionally dissipated (i.e. thermally). Once in the lowest vibrational mode, electrons may then populate higher vibrational modes in lower energy vibronic levels. This may be due to good overlap between the lowest vibrational mode of the excited vibronic level and higher vibrational modes from the lower enegy vibronic level, or by quantum mechanical "tunneling," in the case of poor overlap. The process occurs on the order of 10^{-12} sec.[27] and is called "internal conversion." The same vibrational relaxation process will occur to return electrons to the lowest vibrational mode in the next lower energy vibronic level.

The processes described above do not account for the case when vibrational mode overlap is impossible and quantum mechanical tunneling is improbable, which is another way of describing the state when vibronic energy levels are simply too widely separated for efficient internal conversion (i.e. small Franck-Condon factors). This situation typically occurs at the lowest energy excited states, where the energy gap to ground state is large. While internal conversion always has some probability of occuring, when it is exceedingly improbable, the molecule may have a higher energy level populated

sufficiently long in order for radiative decay to occur, by emission of a photon. This process is called luminescence and when the process results in transition to a lower vibronic energy level without change of spin multiplicty (i.e. $\Delta S = 0$), the process is more precisely defined as fluorescence. All luminescence emissions are orders of magnitude slower than internal conversion and for metallporphyrins, fluorescent lifetimes are known to be on the order of ~60 ns.[28]

A typical lifetime for the lowest energy singlet excited state of an aromatic moleclue is on the order of 10^{-8} sec.[27] This is sufficient time for other processes to compete with internal conversion and fluorescence. Photochemical reactions may also compete, but in this study, sensors were encased in rigid polymer matrices, so environmental photochemical reactions are not important, with one critical exception, enabling these materials to operate as a sensor. This important exception is a quenching mechanism by molecular oxygen, which will be discussed later.

Another possiblity is for spin-orbit coupling to occur and allow a transition from the lowest energy excited singlet state, to an excited triplet state, lower in energy than the singlet state. The process occurs on the order of 10^{-7} to 10^{-12} sec.[28] and is known as "intersystem crossing." Once in the lower energy triplet state, intersystem crossing may again occur, but radiative emision may also occur. Radiative emission is especially probable, since the lowest energy triplet state typically has a lifetime ranging from 10^{-5} sec. to several seconds.[27] When a luminescence process occurs as the result of energy transition to a lower energy state, with $\Delta S \neq 0$, the process is more precisely called phosphorescence. Finally, the process of intersystem crossing may also reverse with the input of energy (such as thermal energy, or triplet-triplet collisions in solution) and then

radiatively emit from the lowest energy singlet excited state. Such a process is called delayed fluorescence, but was not important in any of the sensors utilized in this study. Figure 9 and Table 1 summarize the relationships discussed thus far; Figure 9 also introduces the concept of oxygen quenching graphically.

Table 1: Summary of Photophysical Processes

Photophysical Process	Approximate Timescale (s)	Energy Dissipation
Absorption of photons	10^{-15}	N/A
Vibrational relaxation	10^{-13}	Thermal
Internal Conversion	10^{-12}	Thermal
Fluorescence	10^{-8}	Emission of radiation
Intersystem crossing	10^{-12} to 10^{-7}	Thermal
Phosphorescence	10^{-5} to 10^{0}	Emission of radiation

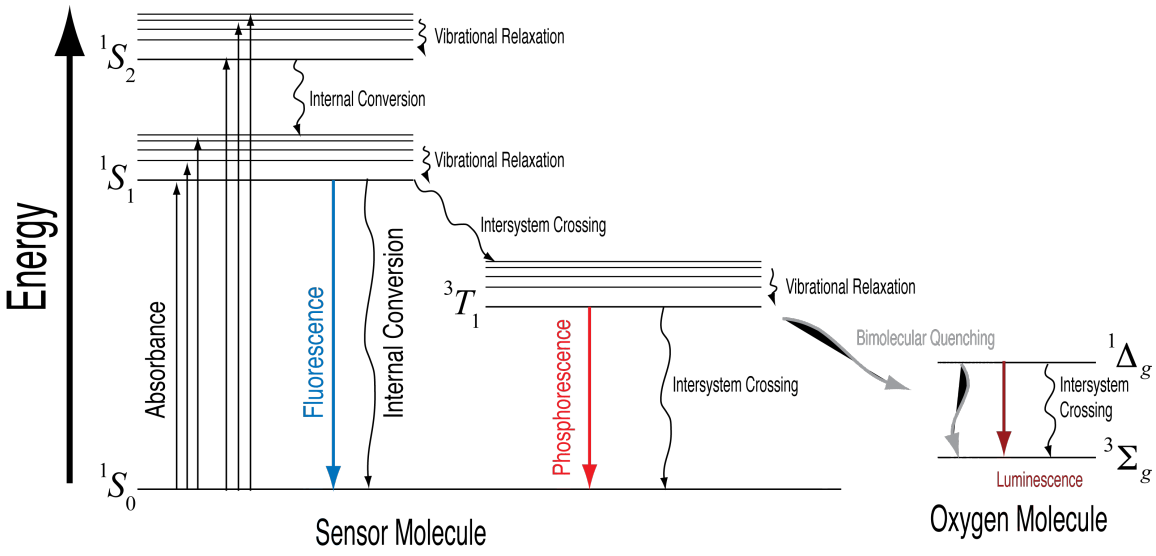

Figure 9: Simplified energy level schematic.

The lowest energy excited singlet state and the lowest energy excited triplet state are both long-lived enough to interact with the environment. A species that reacts with the luminophore will quench the emission, whether that interaction occurs at the lowest energy excited singlet state (fluorescence) or the lowest energy excited triplet state (phosphorescence). In static quenching, complex formation occurs between the ground state of the luminophore and the potential quencher; this was not known to be important in this study. The more common process is dynamic quenching, also referred to as diffusional quenching, whereby the potential quencher reacts with the luminophore in its excited state. From Figure 9, one can readily observe that if a quencher competes with radiative processes, the radiative yield will decrease as quencher concentration increases, which is observed by a drop in emission intensity from the luminophore. Additionally, a competitve process will increase the rate at which the lowest energy excited state is depopulated, and this will be observed as a decrease in the lifetime of the emission signal from the luminophore, as quencher concentration increases.

For the metallopoprhyrins utilized in this study, oxygen is a known quencher.[27-28] Molecular oxygen is unusual in that its ground state is a triplet state ($^3\Sigma_g^-$) and as such, can readily interact with the lowest energy excited triplet state of the metalloporphryins ($^3T_1$) utilized in this study. This interaction was also demonstrated computationally by Sy and Kasai.[29] As discussed above, molecular oxygen will thus decrease signal intensity and decrease the lifetime of the emission signal, as its concentration increases.

It is also worth mentioning that there is a practical side to this theoretical discussion. The reader may contemplate that even when quenching occurs, collisional deactivation would be very rapid in the open environment, destroying any hopes of

successful sensor development. The reader would be correct. The reporter chemistry for the sensors will be metalloporphyrins that are selectively quenched by oxygen, but in order to operate as a sensor, the diffusion of oxygen must be slowed, by affixing the luminophores to a solid matrix, such as a polymer film. Within this form, an oxygen sensor is then achievable, but this also opens up opportunities for further interference with sensor operation. The development of luminophores into a polymer matrix as a useful sensor was initially developed by the Gouterman group at the University of Washington, as they developed pressure sensitive paints initially targeted at the airfoil design and testing industry.[30-42]

It was mentioned that environmental photochemical reactions are not important in this study, but photochemical reactions within the sensor system could potentially be quite important. The excited state metalloporphyrin (*M**) will be quenched by oxygen in a bimolecular process, where Δ has its usual meaning as thermal energy:

$$M^* + {}^3O_2 \rightarrow M + {}^1O_2 + \Delta \qquad (2\text{-}2)$$

Ideally, the singlet oxygen that is produced by the sensor simply relaxes back to its ground state:

$${}^1O_2 \rightarrow {}^3O_2 + \Delta \qquad (2\text{-}3)$$

$${}^1O_2 \rightarrow {}^3O_2 + h\nu \qquad (2\text{-}4)$$

Equations 2-3 and 2-4 depict that singlet oxygen is known to relax thermally (intersystem crossing) or radiatively, via emission in the near IR (1270 nm).[47] While not depicted as an equation, bimolecular collision of singlet oxygen with other oxygen molecule is another possibility. Undesirable reactions may also occur, as shown in equations 2-5 through 2-7.

$$M^* \rightarrow X \pm \Delta \quad (2\text{-}5)$$

$$M + {}^1O_2 \rightarrow {}^3O_2 + \mathrm{Y} \quad (2\text{-}6)$$

$$M + {}^1O_2 \rightarrow Z \quad (2\text{-}7)$$

In equation 2-5, we see unimolecular decomposition of the excited state luminophore, while in equations 2-6 and 2-7 we see destruction of the luminophore by singlet oxygen, which may or may not regenerate ground state oxygen. It may also be possible for singlet oxygen to initiate a radical within the polymer matrix of the sensor, which could lead to propagating reactions. In any case, destruction of the luminophore, destruction of the polymer matrix, and/or consumption of oxygen are all undesirable potential interferences with sensor operation.

Finally, enhancement of the luminescent signal shall be examined briefly. Teyssedre *et al*[43] demonstrate how an electric field may be utilized to enhance phosphorescent emissions (i.e. electroluminescence). This method would necessitate application of the sensor layer onto a conductive layer. Pan and Rothberg[44] as well as Previte *et al*[45] discuss the enhancement of phosphorescence via plasmon resonance. This method would also require close physical contact with an appropriate plasmon resonance material, such as silver nanoparticles. Minaev[46] performs computation chemistry on metalloporphyrins to demonstrate great enhancements at low temperature, in noble gas matrices. These methods were not investigated further for two reasons. First, the room temperature quantum efficiences of many metalloporphyrins is known to be ~90%.[28] With such excellent quantum efficiency, the only worthwhile enhancement was the reduction of concentration quenching, which is included in this study. Secondly, the application must be kept in mind. These sensors will be utilized in a microwell with a

living mammalian cell. Exposure to toxic metal nanoparticles, application of high electric fields, or working at cryogenic temperatures are all undesirable features for such experiments.

2.2 Stern-Volmer Theory

The response of a quenched luminophore in a homogenous environment is analyzed with a Stern-Volmer equation.[27] One may arrive at the correct equation by careful analysis of quantum efficiency ratios, but perhaps a more direct way to see the relationship is via a kinetics analysis. It will be beneficial to refer back to Figure 9 when contemplating the first-order relationship:

$$-\frac{d[M^*]}{dt} = k_p + k_{ic} + k_q[O_2] \tag{2-8}$$

For equation 2-8, k_p is the rate constant for phosphorescence, k_{ic} is the rate constant for intersystem crossing from the porphyrin excited triplet state to its ground singlet state, and k_q is the bimolecular rate constant for quenching by oxygen. For this relationship, we neglect any static quenching and we presume there is no delayed fluorescence. Both of these assumptions were previously discussed as reasonable assumptions employed by other researchers. Next, we presume that $[O_2] \gg [M^*]$, so that the oxygen concentration may treated as a constant for integration. Integration yields:

$$[M^*] = [M^*]_0 e^{-(k_p + k_{ic} + k_q[O_2])t} \tag{2-9}$$

From equation 2-9 it is straightforward to obtain the lifetime (τ) for the quenched phosphorescence:

$$\tau = \frac{1}{k_p + k_{ic} + k_q[O_2]} \tag{2-10}$$

And then it is also straightforward to form a ratio with the natural lifetime (τ_0), which is the lifetime in the absence of any quencher:

$$\frac{\tau_0}{\tau} = \frac{k_p + k_{ic} + k_q[O_2]}{k_p + k_{ic}} = 1 + k_q\tau_0[O_2] = 1 + K_{SV}[O_2] \quad (2\text{-}11)$$

K_{SV} is the Stern-Volmer constant and is simply the product of the bimolecular rate constant and the natural lifetime of the phosphor. In this study, all oxygen concentrations will be expressed as a percentage, which for an ideal gas is another statement of the mole fraction. The mole fraction is directly proportional to the oxygen partial pressure and ultimately, the partial pressure of oxygen is the true stimulus for the reporter chemistry. This is fortuitous, as the calibration tool (Clark microelectrode) was calibrated to the partial pressure of oxygen.

Next, from the final form of equation 2-11, we see that a plot of $\frac{\tau_0}{\tau}$ versus oxygen concentration should be linear, with a slope K_{SV} and an intercept of 1. However in practice, there is a departure from linearity, especially at low oxygen concentration.[34] Previous researchers from the University of Washington found that a close approximation to linearity can be achieved with utilization of an average lifetime,[34,36] for the types of metalloporphyrins used in this study. The near linear behavior is achieved by utilizing a biexponential fit to lifetime data, then calculating a coefficient weighted average as a mean lifetime:

$$\langle\tau\rangle = \frac{\sum_i \alpha_i\tau_i}{\sum_i \alpha_i} \quad (2\text{-}12)$$

In equation 2-12, the alpha's are the preexponential factors for each lifetime fitted to a set of decay data and in practice, all fits were biexponential in this study.

The Stern-Volmer equation assumes a homogenous environment for the sensor. The need for a biexponential fit clearly shows that the environment is heterogeneous. An alternative method is to ratio emission intensities to obtain an identical form of the Stern-Volmer equation. However, for this study, such an idea was not utilized. Determination of the decay lifetime is more challenging than simple measurement of emission intensity, however, it is immune to issues that can affect the emission intensity. These issues include variation in the output of the excitation source, luminophore heterogeneity due to aggregation, changes in the index of refraction of the medium, optical geometry variations, self-illumination sources, and photodegradation of the luminophore. It was observed that slight changes in microscope focal length and optical geometry variations did in fact result in enormous changes in detected signal and would have dealt a fatal blow to any studies utilizing emission intensities.

A key point should be clarified at this time. Lifetime measurements are immune to heterogeneity in the luminophore, but this issue is completely different than sensor heterogeneity. Luminophore heterogeneity simply refers to subtle variations in the concentration of the luminophore in localized areas. Recall that to make a successful sensor, the luminophore must be affixed to a rigid environment, such as a polymer matrix. Sensor heterogeneity refers to the unlimited variety of void spaces that are possible when the luminophore is dispersed into a polymer matrix. This is most certainly the source of a nonlinear Stern-Volmer response and the nature of this effect has been debated in the literature for years.[48-51] The view that is often accepted,[48-49] is that heterogeneity arises from different types of sites within the matrix, most likely surface sites and embedded sites. However, one must proceed with caution; the use of a

biexponential fit to decay data, as utilized in this study, does not imply a two-site system. The chemical environment is likely a distribution of sites and a biexponential fit to data *only* indicates that two exponentials fit a decay curve better than a single exponential, a less than surprising result. In fact other suggestions are that complex decays result from nonlinear solubility of oxygen within the polymer matrix,[50] or other interesting work that may indicate the source of heterogeneity is more closely tied to improper treatment of background intensity signals.[51] All the analyses in the literature have the common theme that multiexponential fits to complex decay data are more robust than a single exponential. Due to the complexity of the chemical environment, the debate is likely to continue for some time.

2.3 Photodegradation and Induction Effects

Photodegradation, also known as photobleaching will be mentioned briefly here, and the induction effect will be introduced. Photodegradation is a result of the undesirable reactions outlined in equations 2-5 through 2-7. Loss of the sensor due to these reactions will result in a drop in emission intensity. While this will not directly affect lifetime measurements, if the effect is too severe, signal-to-noise ratios may drop below the limit of reliable signal detection. Photodegradation reactions may also be destructive to the polymer matrix, increasing matrix heterogeneity or even causing loss of sensor material, as it can lose adherent properties keeping it in the sampling area. We shall see later that photodegradation was evident in most sensors, both in a quantitative sense and via direct observation of decreasing sensor brightness with increasing exposure to excitation sources. The quantitative assessment will simply be to monitor the signal

intensity with continuous exposure, followed by a rest period, then another continuous exposure. Finally, many sensors in this study were perfluorinated. The highly electronegative fluorine moiety was thought to limit the reactivity of the luminophore with highly reactive singlet oxygen[33] and thereby limiting photodegradation reactions.

The "induction effect" essentially refers to the consumption of molecular oxygen by the sensor material. An ideal sensor will not consume the analyte. The calibration tool utilized in this study (Clark microelectrode) functions by analyte consumption, and was the primary reason it was not utilized for these measurements in highly restricted volumes. A major advantage of optical sensors was always thought to be the lack of analyte consumption. However, the existence of the induction effect indicates that the analyte, molecular oxygen, is in fact consumed to some extent. The background of the effect and the coining of the term, "induction effect" is revealed by Gouterman.[31] In his research with pressure sensitive paints for airplane design, it was noted that early materials would have an increase in signal intensity upon initial exposure. This was explained as loss of molecular oxygen that happened faster than diffusion of oxygen from the ambient atmosphere could replace it. The solution was to hold the excitation source on, until a photostable steady-state was achieved. Later materials proved to be faster responding to oxygen diffusion, and the induction effect was no longer observed.

In this study, the induction effect was always observed. In the highly restriced volumes utilized, the methods were sensitive to any loss of molecular oxygen, as the reservoir for diffusive replacement is very limited. Researchers at the MLSC initially dubbed this the "mystery effect" or the "ghost effect," but the term was changed to induction effect when the historical precedent was located in the literature. While some

luminophores may exhibit a decreased induction effect, there is no known optical sensor that is completely devoid of the problem. Fortunately, the effect was also observed to be very stable and highly repeatable. As long as the effect was not too large, it could be accounted for by always keeping at least one microwell empty during an experimental trial as a blank (e.g. see Figure 3). During data analysis the oxygen consumption rates exhibited by mammalian cells could be adjusted by subtracting the small contribution from the induction effect.

2.4 Simple Diffusion Model

At this point, it should be clear that diffusion plays a critical role in sensor operation. In fact, Mills[52] demonstrates how to fine tune luminophore lifetime values with the diffusive behavior of oxygen in a polymer matrix to customize a sensor to desired specifications. However, that was not the point of this study. The diffusion of oxygen in water or cell media is of concern. One must ensure that sensor response time is fast enough to sense changes in oxygen concentration.

There are two areas of concern; the microwell and the sample chamber (see Figure 5). The sample chamber is much larger in volume (~6 mL) compared to the microwell (~300 pL). However, measurements in the sample chamber were for the purpose of sensor characterization and thus continually monitored by Clark microelectrode. It is a simple matter to observe the Clark electrode signal for achievement of a steady-state signal, prior to making optical measurments, rendering any complex diffusion calculations unnecessary. In the microwell, any biological measurements would occur on the order of once every 5-10 minutes.[53] The sensor

materials in this study were known to have a response time on the order of seconds.[31,33,53] As long as diffusion is a fast process in the microwell, there will be no temporal issues of concern. Within such a highly restricted volume, one may simply employ a two dimensional random walk model:[54]

$$\langle x^2 \rangle = 4Dt \tag{2-13}$$

In this simple diffusion model, we take the mean square displacement $\langle x^2 \rangle$ as 16 μm (typical microwell depth) and the diffusion coefficient for oxygen in water, D, as 3 x 10^{-5} cm^2/s, to obtain a typical transport time of ~20 ms. Thus we see there is no cause for concern at the typical rate of collecting experimental data points (every 5-10 minutes).

2.5 Oxygen Solubility

As was previosly discussed, all data sets in this study will work with oxygen concentration in percentage by volume, as a surrogate for the partial pressure of oxygen. The primary purpose for this is for ease of experiments, as gasses for sensor characterization are mixed on a volume basis via mass flow controllers. However, oxygen consumption rates of microorganisms are typically reported in fmol/min.[53] Therefore, to get oxygen readings from a percentage to femtomoles, one must know the solubility of oxygen in the media being studied. Originally, this was going to be a substantial effort in this study, but the idea was abandoned, due to time constraints.

Henry's Law provides a simple way to convert from partial pressure to concentration and is the basis for such conversions in the literature:

$$c = K_H P \tag{2-14}$$

In equation 2-14, c is concentration and P is the partial pressure of the gas of interest (oxygen in our case). K_H is Henry's Law constant and units are chosen such that desired concentration units are achieved (often molality in the literature). Benson and Krause performed rigorous work in this regard for both freshwater[55] and seawater.[56] Their work was refined by Rettich *et al*[57] and this work is touted in the literature as the most accurate source of data. Tromans[58] has prepared thermodynamic arguments which allow direct calculation of desired parameters, however the author has not always obtained accurate results in this manner.

The conversion to solubility for the deionized water solvent used throughout this characterization study would have been straightforward. However, the application of interest occurs in cellular media solutions, which are often highly concentrated in electrolytes. As such, they are subject to the phenomena of "salting out," which has been known for some time.[59] In the discussion above, the given form of Henry's Law was fine; now we must refine it. The more rigorous form would replace concentration with activity and partial pressure with partial fugacity. In deionized water, both the activity coefficient and the fugacity coefficient will always be near unity, at the temperatures and pressures encountered in this study. However, the presence of high concentrations of electrolytes will alter the activity coefficient to such an extent, that the solubility of the nonelectrolytic gas could "salt out." At the temperatures and pressures of interest in this study, the drop in actual concentration of oxygen can be on the order of 20%. It is important to note that the fugacity coefficient will remain near unity, so that the solubility of oxygen will drop appreciably *without* a change in partial pressure. One might expect

that optical sensor response may change little in various fluids, even though the solubility has changed, because of this phenomenon.

The salting out problem has been addressed to some extent in the literature, but was not examined further in this study. Tromans[60] again presents a theoretical approach. Rasmussen and Rasmussen[61] take an interesting approach to the problem. They suggest that the concentration can be calculated for water, then adjusted via experimental calibration with the media solution of interest. Their approach was not examined in great detail, but the method is designed for any arbitrary media solution, so would be of great interest.

2.6 Measurement of Dissolved Oxygen with the Clark Microelectrode

The Clark microelectrode is an electrolytic cell that is highly selective for oxygen measurement. This is achieved by placing the anode/cathode system in an electrolytic solution (1 *M* KCl in these studies) and separating the system from the environment by a gas permeable membrane. In these studies, a teflon membrane was initially utilized, but was found to be too fragile. Later experimental trials used a polypropylene member which decreased the dynamic range, but was still within acceptable limits and the membrane was much less prone to physical wear and tear, relative to teflon. The Clark microelectrodes used in this study were supplied by Microelectrodes, Inc. (Bedford, NH model #MI-730). These microelectrodes consisted of a thin platinum wire encased in glass that served as the cathode, with the glass sheathed by silver to serve as the anode. The membrane holder screwed around the electrodes to provide a very small contact area between anode, electrolyte, and membrane. In fact, the diffusion volume around the

microelectrode was only ~50 μL.[62] Such a small volume was very adequate for sampling the chip holder volume (~6 mL) but certainly much too large to ever utilize in the microwells.

The redox chemistry for a Clark microelectrode can occur in basic or acidic solution.[59] The acidic chemistry shall be the focus here, as all trials were pH stabilized via inclusion of carbon dioxide in all gas mixtures. Operation is known to occur via a two step process:[59]

$$O_2 + 2H^+ + 2e^- \rightarrow H_2O_2 \quad (2\text{-}15a)$$
$$H_2O_2 + 2H^+ + 2e^- \rightarrow 2H_2O \quad (2\text{-}15b)$$
$$O_2 + 4H^+ + 4e^- \rightarrow 2H_2O \quad (2\text{-}15)$$

Thus we see that the sensor is consumptive. A potential of -750 mV is applied to the cathode for operation as an electrolytic cell, producing a current as the analyte signal. The current is read with a sensitive current reading instrument, typically in a range from 1 pA to 2 nA. It should be noted from equation 2-15, that a complex series of side reactions may occur.[59] Hydrogen peroxide may revert to oxygen and water at the anode, but may also participate in a wide variety of electron and proton transfers. Additionally, some oxygen may oxidize the electrode surfaces, eventually leading to fouling of the sensor. The point of the discussion is that these side reactions will always produce some baseline current. In the devices utilized for this study, this current was exceedingly low. The microelectrode was observed to have an open circuit current of ~1.1 pA and the lowest observed current under anoxic conditions was 2.2 pA. Anoxia was observed by noting when the current remain relatively flat upon exposure to pure nitrogen and in the case of aqueous measurements, pure nitrogen plus an oxygen scavenger in solution.

The analyte signal from a Clark microelectrode is known to be sensitive to temperature and pressure fluctuations.[59] Observation of the analyte signal demonstrated that the device was in fact very sensitive to temperature fluctuations, with variations quite consistent with thermocouples utilized to monitor the temperature in the sampling area. However, all aqueous trials were conducted isothermally (37 ± 0.1 °C), so this variation was not important for this study. Ambient pressure was monitored, but variations due to changing pressures were very slight, except in the case of sudden weather changes, in which case experimental trials could be delayed or repeated.

2.7 Methods for Lifetime Measurement

We have already discussed the preference for a lifetime measurement versus an intensity measurement, so now we shall examine the different ways in which to obtain a lifetime reading. The most direct way is to simply measure the decay signal from the luminophore, then fit the curve in a least-squares sense with an exponential model. Parts of this study do that and as mentioned previously, a biexponential model was actually found to be appropriate as an apparent lifetime for the luminophore. The lifetime can also be determined by a phase modulation method, also utilized in this study. For this method, a single exponential phase was utilized as the apparent lifetime. However, to accommodate the LCA, it was desirable to find a lifetime imaging method that would produce an apparent lifetime. Ratiometric methods were found to work very well. Finally, time-correlated single photon counting methods are available, but the available instruments were not amenable to this method and it will not be discussed further.

Researchers at the MLSC employed a phase modulation method prior to this study,[63] which was based upon the methods of Shonat and Kight.[64] That method was found to be cumbersome, slow, and produced poor data and was abandoned. A nice review of phase techniques is presented by Gratton *et al*.[65] Later in the literature, we see a heuristic method[66] to improve Stern-Volmer behavior of a luminophore method by a phase technique, as well as further refinements on multifrequency methods[67] and an approach to accommodate high background signals.[68]

When the phase modulation method is available, it offers rapid determinations of lifetime and is very simple to use. One only needs to know the phase difference (ϕ) between the excitation light source (typically sinusoidally excited) and the detected signal. Then the lifetime is merely

$$\tau = \frac{\tan \phi}{2\pi f} \tag{2-16}$$

where f is the modulation frequency. An alternative method to calculate the lifetime from the phase is based upon the depth of modulation. However, the phase modulation instruments used in this study were ac coupled only, excluding that method of measurement.

Ratiometric methods proved invaluable to this study. Researchers at the MLSC switched to these methods[53,69-70] and experienced improved results. These methods are highly amenable to microscopic imaging, the main focus of this study. The methods reflect excellent work from the University of Virginia and James Madison University. An optimized ratiometric lifetime determination (ORLD) method[71-72] was initially implemented in this study and worked quite well for bright sensors. The same research group also published an alternative method[73] that is very similar to the new method

discussed in the next section and they also discuss similar ideas for biexponential systems.[74]

Ratiometric methods involve a straightforward examination of exponential decays. Figure 10 depicts a schematic of the ratiometric methods. Original methods

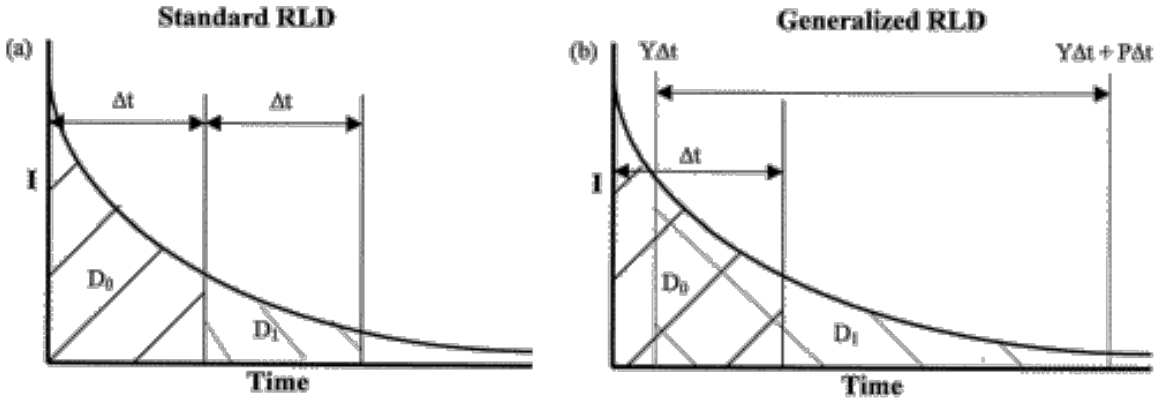

Figure 10: Schematic of Ratiometric Methods. The standard method utilizes equal bins, while the generalized or optimized method uses unequal and overlapping bins.

Reprinted from S.P, Chan, Z.J. Fuller, J.N. Demas, B.A. DeGraff, Optimized Gating Scheme for Rapid Lifetime Determinations of Single-Exponential Luminescence Lifetimes, *Anal. Chem*., **55**, 1245-50. Copyright 2001 American Chemical Society.

utilized equal, adjacent bins, while later methods were generalized to include overlapping and unequal bins, which optimized results. The "bins" discussed above refer to integration areas under the exponential decay curve. Since this study is interested in lifetime imaging data, these methods are a natural fit as CCD cameras function by integrating photons and the camera utilized in this study included a fast-acting gater.

The extraction of an apparent lifetime from integrated data may not be immediately obvious; the most simple case to examine is the standard RLD method. We can obtain the areas D_0 and D_1 by simple integration:

$$D_0 = \int_0^{\Delta t} Ae^{-t/\tau} = -A\tau\left|e^{-t/\tau}\right|_0^{\Delta t} = -A\tau\left(e^{-\Delta t/\tau} - 1\right) \tag{2-17}$$

$$D_1 = \int_{\Delta t}^{2\Delta t} Ae^{-t/\tau} = -A\tau\left|e^{-t/\tau}\right|_{\Delta t}^{2\Delta t} = -A\tau e^{-\Delta t/\tau}\left(e^{-\Delta t/\tau} - 1\right) \tag{2-18}$$

In equations 2-17 and 2-18, τ is of course the desired lifetime and *A* is the preexponential factor, which will shortly become irrelevant. Now we simply ratio the two bins, which gives rise to the term "ratiometric" for this method:

$$\frac{D_1}{D_0} = e^{-\Delta t/\tau} \Rightarrow \tau = \frac{-\Delta t}{\ln(D_1/D_0)} \tag{2-19}$$

From equation 2-19, one may directly calculate the lifetime. The standard RLD method does not produce the best results. The ORLD method is able to combat the rapidly decreasing signal-to-noise ratio in the decay signal and give more precise and more accurate results. For work with the MLSC, the most common settings were to find a desirable *Δt* setting heuristically, then set *Y = 0.25* and *P = 4* to obtain reliable results. The identical solving method outlined above is used with the ORLD method to obtain an open-form solution:

$$\frac{D_1}{D_0} = \frac{e^{(-R(P+Y))} - e^{-YR}}{e^{-R} - 1}, \quad \text{where } R = \Delta t/\tau \tag{2-20}$$

In order to utilize equation 2-20, an iterative solving method is utilized to converge to a solution for *R*. Then the lifetime is readily determined as *Δt* is an experimentally set parameter. Alternatively, one may also say that the ratio (D_1/D_0) is the analyte signal and varies monotonically with oxygen concentration and there is not necessarily a need to compute the lifetime.

2.8 Convolution of Source and Detector Signals

The ORLD method presumes that the excitation source is an impulse response and the detector response is devoid of any convolution effects. Instruments were chosen that were fast-acting to minimize the problem of convolution effects. However, when

attempting a variety of experiments, two observations really stood out. The shape of the excitation pulse was substantially altered in the presence of a luminophore and other researchers at the MLSC reported an advantage to long excitation pulses. The latter observation was especially disturbing. As Table 1 reveals, the time for the absorptive process is just a few femtoseconds. The ORLD method was originally designed for researchers at the MLSC around an excitation pulse of 2-5 μs. When Molter *et al*[53] reported using an excitation pulse of 150 μs, this was clearly cause for concern. The reasoning was that sensor brightness increased and improved signal-to-noise ratios (SNR). The cause for this phenomena was simply a convolution effect.

The observation that the excitation pulse was substantially altered in the presence of a luminophore was noted while trying to solve a persistent problem with some type signal contamination. This problem and its solution will be further discussed in section 3.8. For now, we see an example of the issue in Figure 11, on the following page. The sample of excitation light is a nice rectangular wave, plus a capacitive spike at the leading edge when the high-power LED is turned on. However, when that same light is passed through a contaminating luminophore, the pulse shape changes dramatically. Note that the two plots are on different time scales, but it is only the shape that concerns us here. It is fairly easy to demonstrate that this shape is simply the convolution of the rectangular excitation pulse with the exponential decay of the luminophore. When that realization was combined with the observation that long pulses substantially improve sensor brightness, it was contemplated that the lifetime information must also be encoded in the convoluted waveform, and pursuing this would be of great advantage for SNR improvement.

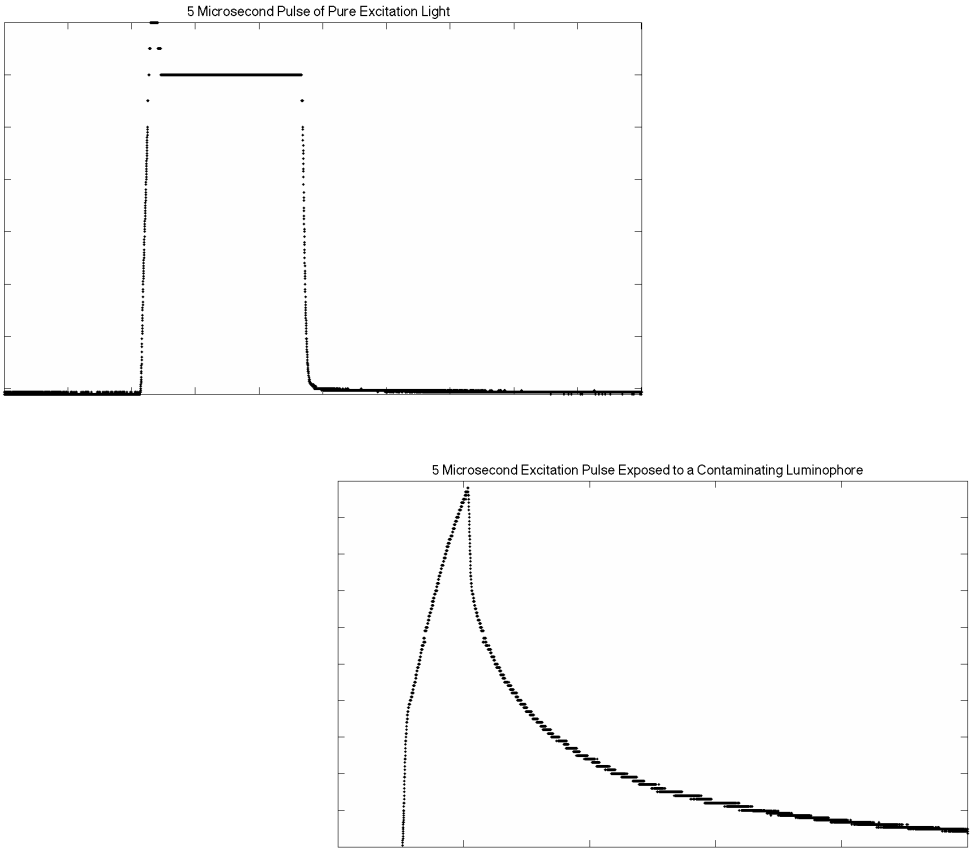

Figure 11: Excitation Pulse Distorted. The presence of a contaminating luminophore, substantially distorts the excitation pulse (Intensity vs. Time).

An investigation into this idea was undertaken. First, a model rectangular pulse was convolved with an exponential decay, via Matlab (R2011a). Both waveforms had unity amplitude and the width was set to 30 time units, simply because that was found to be nice visually. The result of this process is depicted in Figure 12, on the next page. This shape was a match to observations of real data, with the exception that the capacitive on spike of real rectangular pulses would slightly change the leading edge. So, not only did observations support the idea of convolution but one would expect the detector signal to be a convolution of all the potential responses in the system. The primary convolution

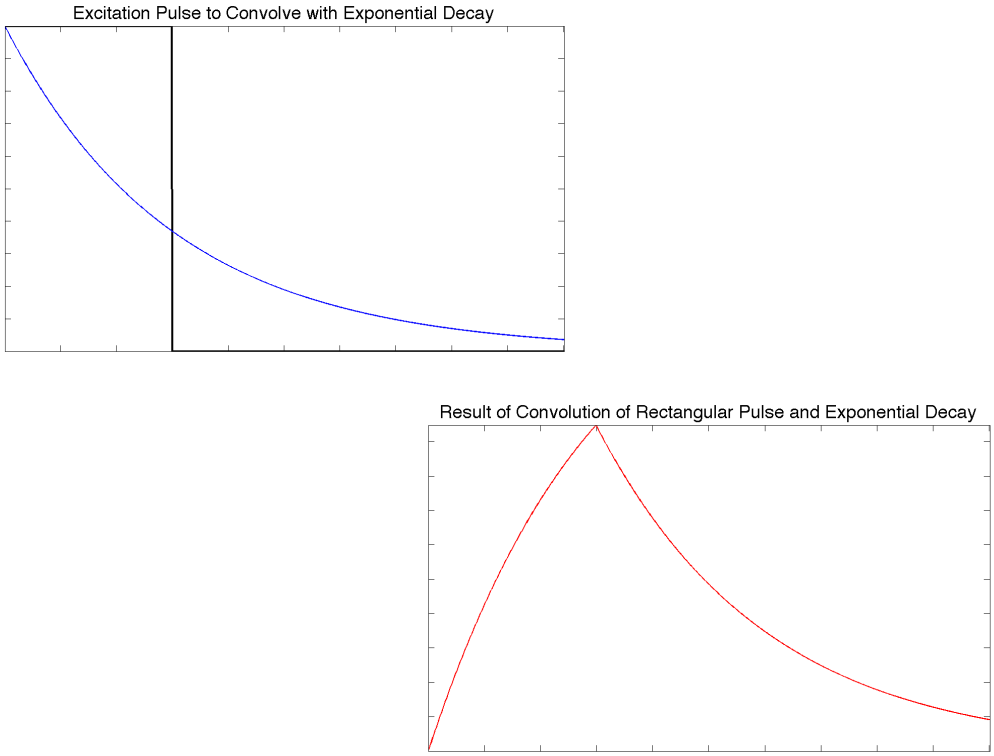

Figure 12: Convolution Result. A model rectangular pulse was convolved with an exponential decay to produce the "distorted" shape observed in real data (Intensity vs. Time).

between a rectangular pulse and an exponential decay is therefore quite important to analysis of the data.

Next, a model was developed. While many may be tempted to move to the Laplacian domain for such convolutions, the mathematical analysis of this system is really quite easy. Define a rectangular pulse as follows:

$$f(t) = \begin{cases} 0, & t < 0 \\ A, & 0 \le t \le T \\ 0, & t > T \end{cases} \tag{2-21}$$

Where A is a constant real number (i.e. amplitude of the pulse) and T is some pulse period (i.e. width of the pulse). Now define the exponential decay with preexponential factor C and $k = 1/\tau$, where τ is the lifetime:

$$h(t) = Ce^{-kt} \tag{2-22}$$

Note that the reciprocal lifetime was utilized only because integrals will be easier to follow that way; we shall swap back to lifetime in the end. Now compute the convolution:

$$y(t) = f(t) * h(t) = \int_{-\infty}^{\infty} f(\lambda)h(t-\lambda)d\lambda \tag{2-23}$$

To do this, it is best to work in two distinct cases (note that the integral will vanish for $-\infty < t < 0$):

$$Case\ i\text{:}\ 0 \le t \le T,\quad y(t) = \int_0^t ACe^{-k(t-\lambda)}d\lambda = \frac{AC}{k}e^{-kt}(e^{kt}-1) \tag{2-24}$$

$$Case\ ii\text{:}\ t > T,\quad y(t) = \int_0^T ACe^{-k(t-\lambda)}d\lambda = \frac{AC}{k}e^{-kt}(e^{kT}-1) \tag{2-25}$$

Now we can rewrite these expressions in terms of lifetime:

$$Case\ i\text{:}\ 0 \le t \le T,\quad y(t) = AC\tau\left(1-e^{-t/\tau}\right) \tag{2-26}$$

$$Case\ ii\text{:}\ t > T,\quad y(t) = AC\tau\left(e^{\frac{T-t}{\tau}}-e^{-t/\tau}\right) \tag{2-27}$$

So expressions have been produced that are remarkably simple. Note that equation 2-27 indicates that the assumption of a single exponential decay for the ORLD method is not valid and that systematic errors become increasingly worse as the pulse width (*T*) increases. The results of integration also demonstrate that the case of multiexponentials is a simple extension of the model for the convoluted signal:

$$y(t) = A\sum_i C_i\tau_i\left(1-e^{-t/\tau_i}\right) \tag{2-28}$$

Equation 2-28 was not utilized for ratiometric methods in this study, but was utilized for direct decay curve fitting purposes. In this sense, decay curve is a misnomer, since the curve would be rising, as depicted in the convolution result of Figure 12.

The next step would be to extend these ideas to the ratiometric method. The identical methodology utilized in equations 2-17 through 2-20 was applied. The integrals were a bit messier, but just as straightforward to yield:

$$\frac{D_1}{D_0} = \frac{\Delta t + \tau\left(e^{-2\Delta t/\tau} - e^{-\Delta t/\tau}\right)}{\Delta t + \tau\left(e^{-\Delta t/\tau} - 1\right)} \tag{2-29}$$

In equation 2-29, bins do not overlap and are of equal width. The ORLD method optimized a different binning scheme in the interest of salvaging SNR. In this method, SNR is at the maximum achievable value, so no benefit was forseen from more complex binning methods. As in the standard RLD and ORLD methods, the pulse amplitude and preexponential factors vanish, which is especially satisfying here, as this new method could potentially be prone to variation, since data is collected during the on-cycle of the excitation pulse. One note with equation 2-29; the introduction of *R*, as in equation 2-20, was found to continually cause failure in nonlinear solving tools and is not recommended.

With the qualitative evaluation and modeling results looking so satisfying, a simulation was conducted next. A Monte Carlo experiment was performed with a synthetic excitation pulse and a single exponential decay with a lifetime of 250 time units. Again, the value of the time unit was merely to make plots that were easily observed and this value can be arbitrary. The width of the excitation pulse was then varied from 0.5 to 10 times the lifetime, with 1,000 trials conducted for each setting. The excitation pulse and exponential decay waveforms both had Gaussian white noise added that was approximately proportional to levels encountered with real data. These simulations were performed in LabVIEW 2010.

Figure 13 shows a screen shot of the simulator running, so that the reader gets a better view of the type of challenging signals in this study.

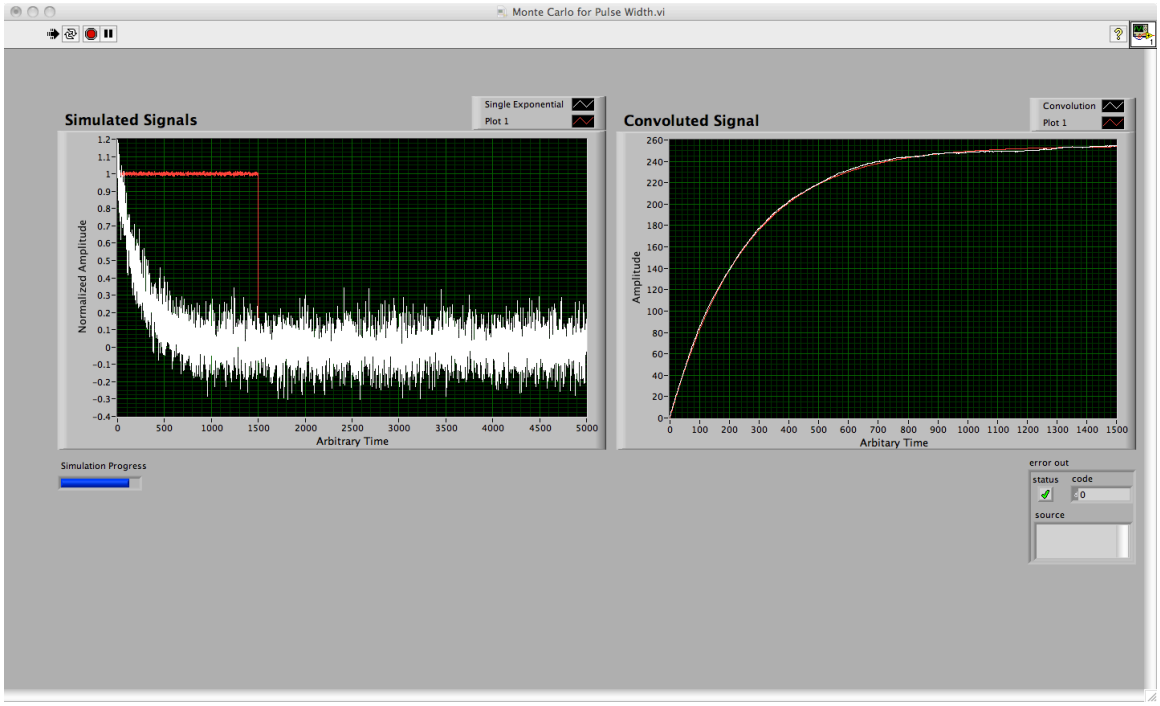

Figure 13: Monte Carlo Simulation. Screen shot of the running simulator. Synthetic signals with Gaussian white noise are on the left. On the right, the white line is the convoluted signal and the red line is a nonlinear fit to the signal, using the model of equation 2-26.

The excitation pulse and exponential decay were convolved together and the result is the white plot on the right side of Figure 13. The red line in Figure 13 represents a nonlinear fit to the convolved data, using equation 2-26 as the model. Finally, an apparent lifetime was extracted by employing a nonlinear solver with the method of Levenberg-Marquardt, uisng equation 2-29 as the model. The lifetime and the relative standard deviation were calculated for each pulse width and the result is presented in Figure 14, on the following page. From Figure 14, we can see that accuracy and precision are fairly flat with a pulse width setting between 3 and 10 times the lifetime of the luminophore.

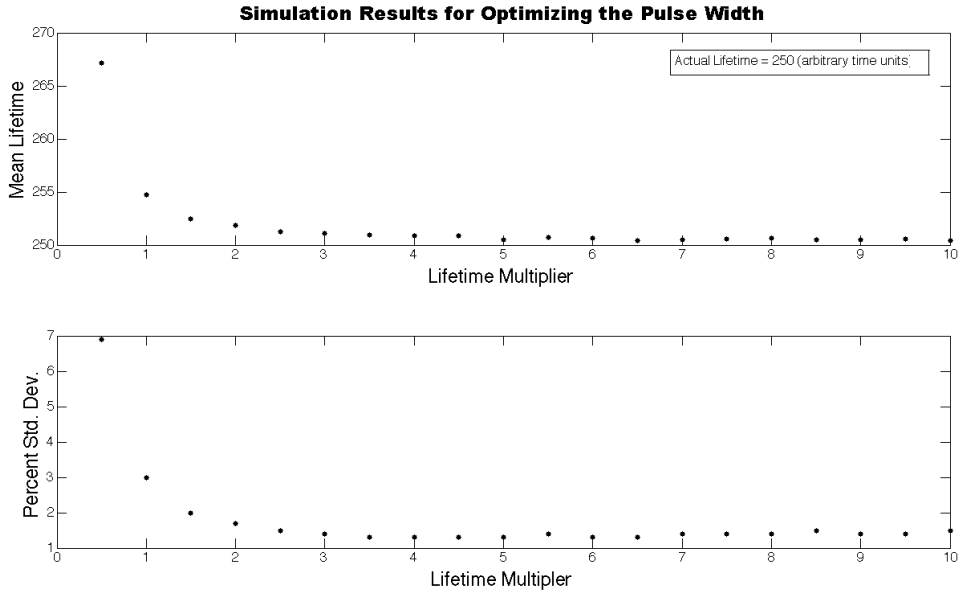

Figure 14: Results of Monte Carlo Simulation. Precision and accuracy appear acceptable for pulse widths of 3-10 times the luminophore lifetime.

Finally, we have seen that convolution explains observations satisfactorily, a mathematical model was fairly simple to derive, and simulations look promising and provide guidance for experimental parameters. The effect was observed on a detector that responds to overall signal, but this convolution effect should also occur on the imaging system. The effect would not be observable by the imaging system under normal operating conditions, but it was still desirable to ensure that the same effect holds true if the camera is gated appropriately in small steps at the correct time, to verify detection of the phenomenon. This prediction was verified, with the correct qualitative shape, as presented in Figure 15 on the subsequent page.

This method for lifetime determination has not been published to the author's knowledge and will hereby be named long-pulsed luminescence (LPL).

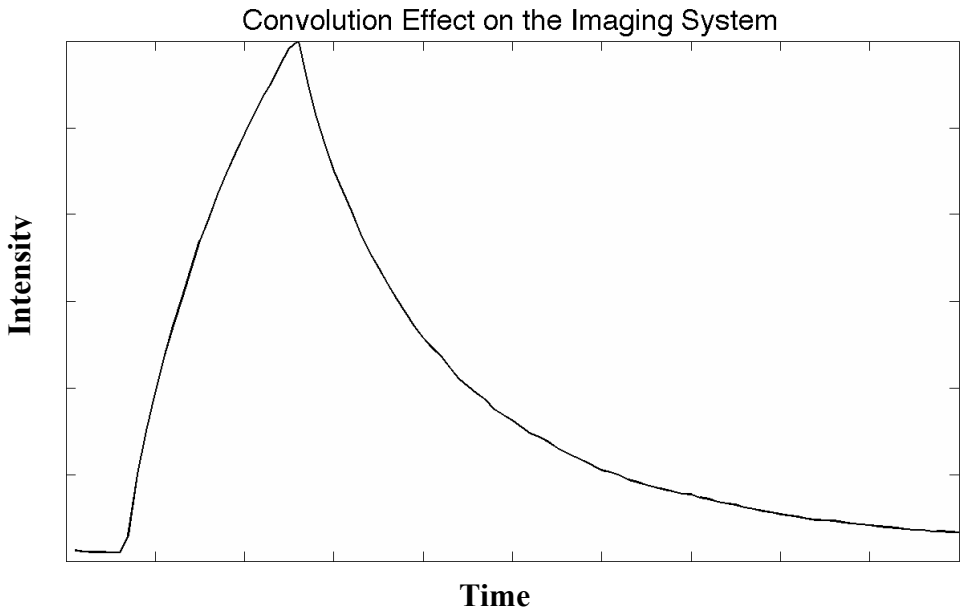

Figure 15: Convolution Effect on the Camera. A gate-stepping procedure was employed to show that the convolution effect occurs as predicted on the camera.

Chapter Three: Development of the Sensor Characterization Station

3.1 Sensor Deposition by Picoinjection

In the highly restricted volume of the microwell (perhaps they should have been called picowells!), getting sensor material into the right location was a challenge. Prior to this study, sensor material was simply squeegeed over the glass chip,[53] leaving much residue behind. The residue was perhaps a strong contribution to lack of repeatability, so the first goal was to improve sensor deposition. A trip to the MLSC partner, Arizona State University, was undertaken to explore a newly developed piezodispenser[75] for injection of sensor material. This mission failed for the sensor materials in use at the time; the instrument simply could not inject sensor material in small enough volume to be useful.

The next tool to try was a picoinjector. This is an instrument that utilizes pressure pulses from a compressed gas source, to move fluids out of capillary tips in very small and very repeatable volumes. The model chosen was a PLI-100, from Harvard Apparatus (Holliston, MA). This was attached to a bottle of compressed nitrogen, set to 90 p.s.i.g. for the instrument connection. The picoinjector is most often used with glass capillary tips, for injection in media solutions into cells. For this study, the normal glass capillary tips were too fragile for reliable use. Instead, the set-up was modified to use polyimide coated glass capillary tubing, to provide flexibility at the tip, for reliable dispensing.

The glass chip to receive sensor material was placed upon a micromanipulator stage (Model 6000, The Micromanipulator Co., Inc., Carson City, NV), which included a

camera for observation of the magnified glass chip on a nearby computer screen. The set-up is depicted in Figure 16:

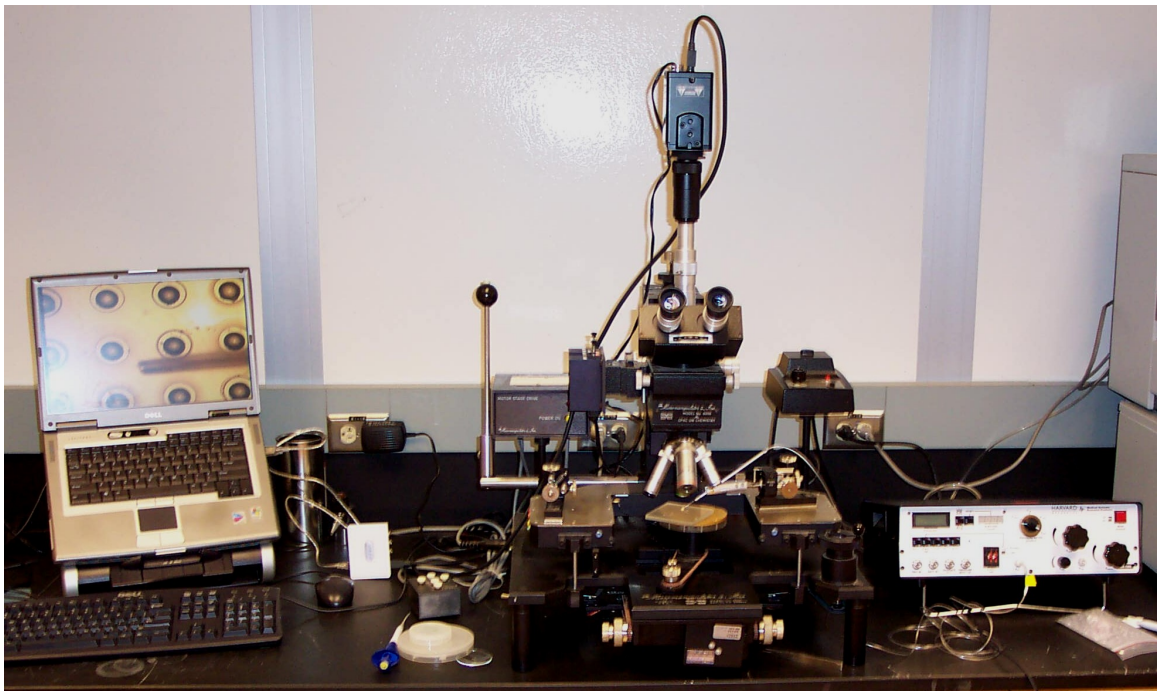

Figure 16: The Picoinjector Station.

For the picoinjector station picture, the computer display on the left shows a magnified image of the glass chip (note: old design was 4x4 versus the new 3x3 arrangement) from the camera on the micromanipulator stage, which is the large device towards the center of the picture. To the right of the micromanipulator is the picoinjector itself. The picoinjector will dispense a precisely calibrated volume when utilized with approved capillary tips. In this study, custom tips were made in-house, so the volume was not known precisely. However, the injection process could clearly be observed on the computer screen and volumes appeared extremely consistent. Settings were manipulated to fill the microwell, so the dispensed volume was ~300 pL.

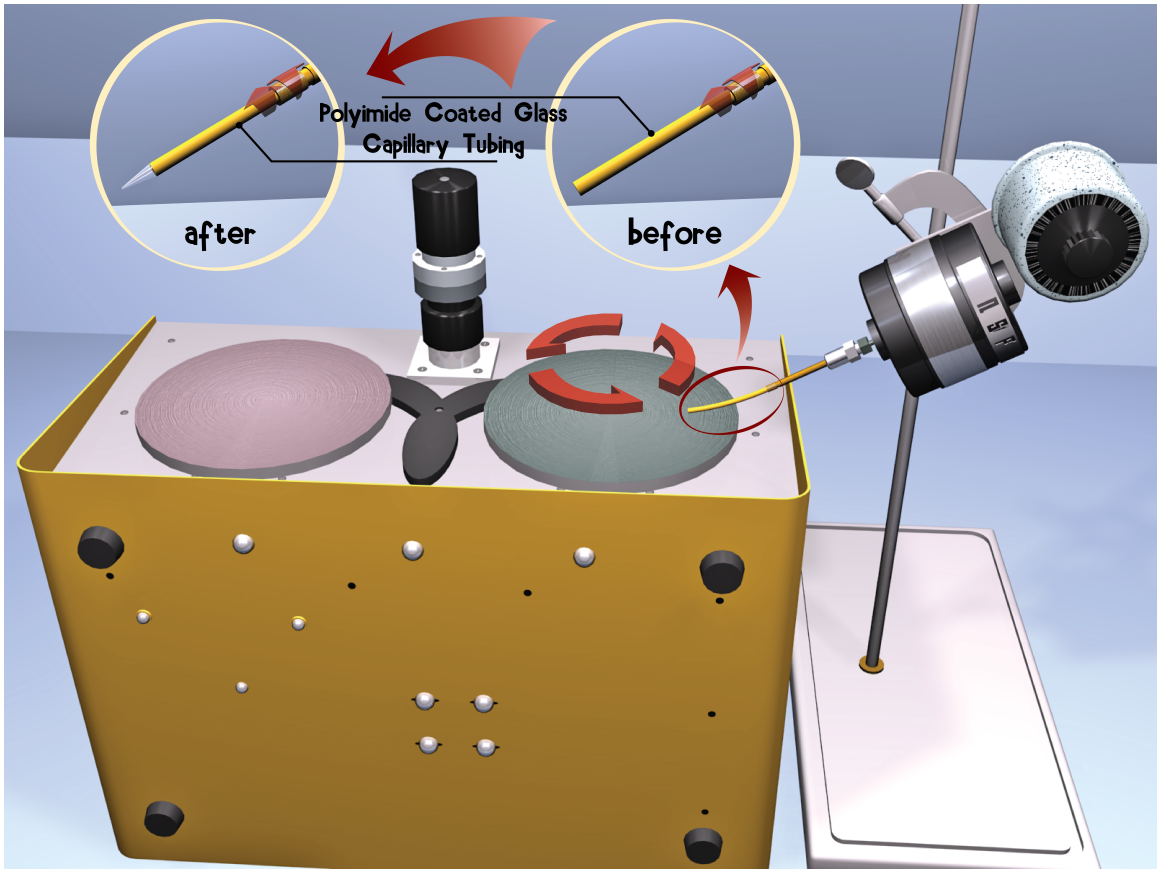

Figure 17: The Tip Polishing Station

The custom tips were made from capillary tubing, Part #2000009 (Polymicro Technologies, LLC, Phoenix, AZ). They were 365 μm O.D. and 20 μm I.D. Other sizes were attempted, but that was the only size in which success was achieved. To gain access to the microwell, the tubing was polished to a tip (see Figure 17) and joined to the outlet tubing of the picoinjector via an inner-lok glass capillary union (CM Scientific, part #6600991, Silsden, UK). The tip polishing station involved rotating the tip via a motor and then placing against the rotating pad on a fiber optic polisher. Note that appropriate adapters were utilized to connect the picoinjector outlet tubing to large-bore capillary tubing, which was sized appropriately for the inner-lok glass capillary union. Procedures for tip creation and for picoinjection are included in Appendix A. A nice example of the

improved deposition is included in Figure 18. In Figure 18, the photo on the left is on

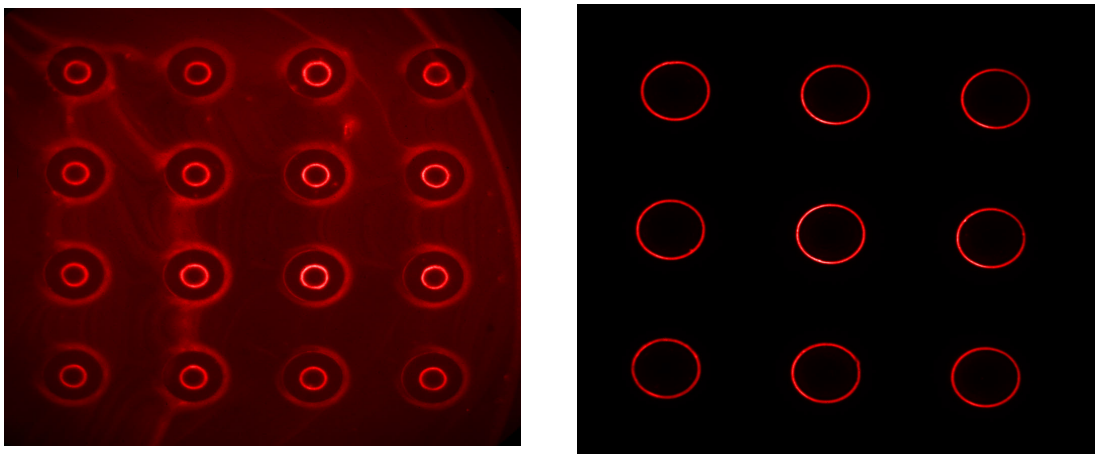

Figure 18: Photos of Deposited Sensor

old style (4x4) glass chip that had sensor material deposited by the squeegee method, whereas the photo on the right is a new style (3x3) glass chip with sensor picoinjected. Staff researchers were encouraged to move away from the 4x4 design as picoinjection was difficult and there was great concern with the close proximity of the microwells to each other in terms of crosstalk. Crosstalk was the potential mixing of emission signal from one microwell to another. The other researchers at the MLSC concurred and switched to the 3x3 design (fused silica) and only those types of chips were included in this study. The photos speak for themselves in expressing the value in the substantial improvement in sensor deposition. It is worth mentioning that the "coffee ring" effect was desired in order to keep sensor material as far away as possible from the cell under study. The effect is very reproducible when materials are within appropriate density, concentration, and particle size limits.[76]

The thickness of the sensor layer could also be of concern. Without knowing an accurate dispensing volume from the picoinjector, this could be a tough problem to

analyze. We shall examine the problem with several assumptions and see that these estimates are likely to be close to the actual thickness. First, there is an empirical observation that other MLSC researchers have looked at the glass chips with sensor via SEM micrographs and the sensor material is not visible or barely visible. This would suggest a monolayer. We must clarify what we mean by monolayer here. The only SEM data available was for the commercial sensor; they are polystyrene latex microspheres. By monolayer, we mean a single layer of microspheres that has collected in the bottom corners of the microwell via the coffee ring effect. For other sensor materials, we shall say that a monolayer is the lowest estimate and an upper bound will be less than two orders of magnitude thicker. The reason for that is that two orders of magnitude will represent a thickness that would be easily discernible during picoinjection, since the sidewalls of the glass chips were only ~16 μm tall.

From the vendor's datasheet, we know that the concentration of particles is 1.1×10^{14} per mL, and that this solution was used in a 1:1 dilution with deionized water. If we assume an injection volume of 300 pL, this means each microwell received 16.5 million particles. The rings visible in Figure 18 typically had an outer diameter of 70 pixels and an inner diameter of 55 pixels. We also know from the well size (via profilometry) that there is approximately 1 μm per pixel, at the resolution used throughout this study. Therefore, we can calculate the volume of the ring, where the thickness is an unknown parameter. This must match the dispensed volume. However, we also know from the vendor's datasheet, that the batch of microspheres utilized had a mean diameter of 43 nm (dry). We simply use the volume of a sphere ($\frac{4}{3}\pi r^3$) and multiply by the number of microspheres to find the total volume occupied by sensor

material; the result is 6.87×10^{-16} m^3. Divide this value by π and the difference in squared radii of the ring to find the height as ~117 nm. The microspheres go through a curing process after injection, to improve adhesion. They are exposed to 160 °C for 30 minutes in a tube furnace. This exceeds the glass transition temperature for polystyrene, so the sensor material is presumed to melt. Recall that the maximum packing efficiency for spheres[77] is $\frac{\pi}{3\sqrt{2}} \cong 74\%$, so now the estimate is well within a lower bound of 30 nm.

3.2 Instruments

Several instruments were utilized throughout this study and will be described in this section. All the luminophores utilized in this study were platinum porphyrins (and one free-base porphyrin) and as such, were expected to have a strong Soret band around 390 nm and an emission around 650 nm.[28] These regions were verified spectroscopically. First, a strong absorption was verified around 390 nm by placing a sample in a quartz cuvette in the appropriate solvent. This step was completed on model 8453 diode array spectrophotometer (Agilent Technologies, Santa Clara, CA). Next, excitation and emission spectra were obtained via a model LS-50B luminescence spectrophotometer (Perkin Elmer, Waltham, MA). A quartz cuvette (fluorescence style) was utilized with sample in a 1:1 dilution with appropriate solvent. When an increase in SNR was indicated, aliquots of 100 μL were added until reasonable spectra were obtained. Excitation and emission slits were set to either 5 or 10 nm (whichever gave reasonable looking spectra). Results are included in chapter four, but there really were no surprises.

Emission spectra from the sensor material within the microwells, was also obtained with the glass chips placed on the microscope used in this study. Spectra were obtained for a dry sample and a sample submerged in deionized water. These spectra were obtained via an Ocean Optics (Dunedin, FL) model SD2000 spectrophotometer coupled to a fiber optic (400 μm, 0.22 NA HOH type, Romack, Inc., Williamsburg, VA). Light from the microscope was coupled to this fiber optic via a fiber collimating lens assembly. This procedure was done to avoid unexpected optical contamination. As will be discussed in section 3.8, there were some optical surprises during the course of this study and this part of the sensor characterization was carried out simply to verify light sampled from the sensors was as expected.

The microscope was clearly a central part of the instrumentation for this study. It was an inverted epifluorescence microscope, model Axiovert 200 from Zeiss (Göttingen, Germany). It was equipped with a model MS2000 translation stage from Applied Scientific Instrumentation, Inc. (Eugene, OR). A halogen light source was available for general illumination, but not generally used throughout this study, other than for capturing brightfield images of glass chips. A swinging mirror allowed attachment of two light sources for epifluroescence imaging and that light path was equipped with an adjustable aperture and adjustable field stop. The objectives utilized in this study were a Zeiss Plan-Neofluar which was 10x in magnification with 0.30 NA (numerical aperture) and an LD Achroplan, also from Zeiss, which was 40x in magnification with 0.60 NA. Several positions were available in the form of filter cubes, in order to add various combinations of excitation filters, dichroic mirrors, and emission filters. For capturing light, four ports were available, as well as the eyepiece. The left port was equipped with

the intensified CCD camera (see section 3.4), the right port with the fiber-coupled spectrometer, and the front port with other detectors. The bottom port was used for mounting of side-view photomultiplier tubes, which were an invaluable aid to understanding optical performance of the system, but were not used to collect any data for this study.

Two other detectors that were attached to the front port as needed, were a model 2153 femtowatt receiver (New Focus, Inc., Santa Clara, CA) for detection of slowly modulated near infrared signals, or an avalanche photodiode (APD). Light was collected onto the femtowatt receiver via a 30 mm focal length near infrared plano-convex lens. The APD was a model SD 197-70-72-661 (Advanced Photonix, Inc., Camarillo, CA) large area red-enhanced silicon module. Light was collected via a 25.4 mm focal length biconvex lens. Both of these detectors were amplified by a model SR560 (Stanford Research Systems, Sunnyvale, CA) low-noise preamp. This preamp could also provide signal filtering if desired. The preamp was observed to significantly distort the temporal characteristics of a signal, but only under gain overload conditions. In the case of very weak signals, it was the standard practice to find the gain that caused an overload indication, then to reduce the gain by at least two levels. When within normal operating parameters, the preamp had a maximum bandwidth of 1 MHz, sufficient for any of the temporal responses encountered in this study.

Light sources utilized for luminophore excitation consisted of high power LEDs. A 405 nm LumiBright LED (Innovations in Optics, Inc., Woburn, MA) was utilized for the image acquisition data and direct decay data. A few experiments were also conducted with a 530 nm LED (model LXHL-LM5C Lumileds Lighting, LLC, San Jose, CA). Both

of these sources were collimated with an appropriate plano-convex lens before light entered the microscope port. The 405 nm LED was filtered by a bandpass filter (FF01-405/10-25, Semrock, Rochester, NY), while the 530 LED was equipped with an FF01-543/22-25 bandpass filter. For sinusoidal modulation, a 365 nm LED was utilized (LEDD3-365, Thor Labs, Inc., Newton, NJ). This source was also equipped with an appropriate collimating lens and bandpass filter (FF01-377/50-25). Bandpass filters were located directly on the light sources as opposed to the microscope's filter cube so that the same dichroic mirror and emission filter could be utilized for different light sources.

The 405 nm LED and the 530 nm LED were driven by a PP520F controller (Gardasoft Vision, Ltd., Cambridge, UK). This controller allowed operation in continuous mode or pulsed mode up to a frequency of 1500 Hz and a pulse width from 1 μs to continuous. LED current could be set on a linear scale in terms of %Brightness. Up to two LEDs could be driven simultaneously and independently, though that feature was not needed in this study. The 365 nm LED was driven by its LEDD3 controller, also from Thor Labs, Inc. This controller allowed continuous operation or modulated mode and the LED current was also adjustable. The modulation mode could be internal for very high frequency (> 1 MHz); an external source was used for the lower frequencies needed for this study (< 35 kHz). The external modulation source was a model DS335 function generator (Stanford Research Systems, Sunnyvale, CA) and was set for sinusoid modulation, 9.00 V peak-to-peak, with a 5.50 VDC offset. An optimal frequency was determined from direct decay measurements and automatically set via software control.

The filter cubes within the microscope were equipped with several choices, within five turret positions. The five positions are listed on the following page:

Table 2: Microscope Turret Positions

Turret Position	*Excitation Filter*	*Dichroic Mirror*	*Emission Filter*
#1	None	None	None
#2	None	FF555-Di02-25x36	FF02-655/40-25
#3	None	FF705-Di01-25x36	NB-1292-080
#4	None	FF510-Di01-25x36	FF01-655/40-25
#5	D425/40X	50/50 Beamsplitter	None

The dichroic mirrors were from Semrock, while the 50/50 beamsplitter was from Chroma Technology Corp. (Rockingham, VT). The D425/40X bandpass filter was also from Chroma. The FF series bandpass filters used for emission were from Semrock. The near infrared bandpass filter (turret #3) was from Spectrogon, Inc. (Mountain Lakes, NJ). Turret position #1 was utilized for general viewing and capturing of brightfield images. Position #2 was utilized for luminescence, when using the 530 nm LED. Position #3 was appropriate for near infrared signals, using the femtowatt receiver for detection. Position #4 was the most used position and was also for capture of luminescence data or images, while using the near UV LEDs. Finally, position #5 was used as a phase modulation reference signal.

The power output of the LEDs could be monitored with a model PM100 light meter, with model S130A germanium detector (400 - 1100 nm), both of which were provided by Thor Labs, Inc. The detector was dual range for either 5 mW or 500 mW. The LED power output was not routinely monitored as oscilloscope traces showed the pulsed output to be extremely stable. Obtaining the output at the microscope objective with an LED in continuous mode was useful, however pulsed measurements were not possible as the meter has a maximum response rate of 6 Hz.

Additional instruments were used for signal capture. These included a digital oscilloscope and a lock-in amplifier. The digital oscilloscope was a 500 MHz model 9350AM from LeCroy (Chestnut Ridge, NY). This scope was utilized for general signal

checking and for capturing direct decay measurements. Data was saved over a GPIB interface to personal computer. The lock-in amplifier was model SR530 from Stanford Research Systems. This was utilized for phase measurements for the phase modulation experiments. Data was also saved to a personal computer via GPIB interface. The output signal of the lock-in amplifier was monitored by an auxiliary oscilloscope, model TDS 2012 from Tektronix (Beaverton, OR). While the auxiliary scope played no role in data capture, it proved invaluable for data quality control.

3.3 Control and Monitoring of the Environment

This section will focus on the control and monitoring of conditions within the chip holder (see Figure 5). This was an area 5 cm x 5 cm and ~2 cm deep. It contained the glass chip, which was held in place by a stainless steel positioner. Within this volume, the temperature and gas composition were controlled, and then the temperature, absolute pressure, and oxygen concentration were monitored. While some experiments were conducted with the chip holder area dry, most were in deionized water. The volume of water added was ~6 mL. This brings out an important point for this type of research. Such a volume is quite small from the perspective of a human observer. The volume of the microwells at ~300 pL also appears very small from the human perspective. However, the difference between these two volumes is actually a factor of 20 million! Therefore, one must be very careful when characterizing sensors to ensure that the chip holder environment is consistent with what may exist in the microwell during biological experiments.

Oxygen concentration was monitored via Clark microelectrode as previously discussed. This microelectrode was most often read by a picostat instrument (model EA-162, eDAQ, Inc., Colorado Springs, CO), which was in turn controlled and read by an electronic chart recorder (eCorder model 401, eDAQ). The eCorder also recorded temperature and pressure data at a rate of 1 Hz, with a 10 Hz low-pass filter in place. The Clark electrode was only used in static reading mode; a dynamic reading mode is possible[59] but was not germane to this study. The Clark microelectrode has been firmly established as having a linear response,[59] so only a two-point calibration was needed. The ambient atmosphere (20.95% O_2) provided one very convenient point, while anoxia provided the other. A small diaphragm pump pumped air into the chip holder area, operated at 3.4 VDC, with the inlet attached to a HEPA filter (0.1 μm). The steady linear response of the Clark microelectrode does depend upon constant temperature and atmospheric pressure. All wet experiments in this study were controlled to 37 ± 0.1 °C and the absolute pressure was monitored, with runs repeated if a significant change in atmospheric pressure was encountered (i.e. weather changes). However, one must be cautious that anoxia is truly achieved. Initially, this was extremely difficult in the chip holder. After trial and error, it was determined that there were two problems; oxygen was permeating through supply tubes and the chip holder itself was a substantial oxygen sink. The original housing piece for the chip holder was made of Delrin, which was found to absorb a substantial amount of oxygen, so was replaced with an aluminum piece, with much improved results. The gas supply tubing was a collection of a variety of materials that were available in the lab. However, it was learned that some of these materials were quite permeable to oxygen, so were replaced with thick-walled PVDF (polyvinylidene

fluoride) tubing, which specifications showed were similar to stainless steel in oxygen permeation performance. With these changes, anoxia was achieved and defined as a steady current less than 50 pA. As was mentioned previously, the best anoxic current observed was 2.2 pA, but recall from the previous chapter that side reactions will continually contaminate the measurement to a very small extent. Relative to an ambient current that was usually several hundred to one thousand pA, an anoxic current off by a few picoamps would have no bearing on the oxygen concentration measured to a precision of ~10^{-4} oxygen concentration. One additional procedure is worth mentioning. The ability to reach anoxia via purging and sparging in deionized water was a lengthy process and typically much of the water would evaporate before a stable point was reached. To assist in this, when anoxia was desired, a 100 μL aliquot of 2% (w/w) sodium sulfite freshly made (within 48 hours) would be added to the solution to ensure anoxia. A second or third aliquot was often added to convince the author that the signal really was steady at the lowest achievable level.

Once the Clark microelectrode was calibrated, the concentration of oxygen was set by mass flow controllers. For anoxia, pure nitrogen was utilized, but all other mixtures were combinations of nitrogen, oxygen, and carbon dioxide, with the carbon dioxide always maintained at 5% (v/v). The carbon dioxide level was implemented at the urging of biologists in order to avoid the introduction of potential variation, since they always conduct experiments in a 5% CO_2 atmosphere. All gasses were obtained from Praxair (Seattle, WA) and regulated before attachment to the mass flow controllers. The mass flow controllers were all obtained from Omega Engineering, Inc. (Stamford, CT). Model FMA5510 was utilized for oxygen with a maximum flow rate of 200 sccm; model

FMA5508 was used for carbon dioxide with a maximum flow rate of 100 sccm; model FMA5512 was utilized for nitrogen with a maximum flow rate of 500 sccm. The three outputs were joined and connected to a U-tube filled with glass beads to ensure adequate mixing. This output was bubbled through a glass frit into deionized water to ensure a water-saturated mixture prior to entering the tube connected to the chip holder. A water-saturated mixture was desired to reduce any potential temperature variation due to evaporative cooling. The chip holder contained a larger tube for purging and a smaller tube connection for sparging. A manual diversion valve was typically adjusted until sparging just began to occur. All control of the mass flow controllers was via software running in LabVIEW. While mass flow controller settings were typically fairly close to measured oxygen concentrations, the readings from the Clark microelectrode were always utilized as the true value.

The temperature in the chip holder environment was always monitored and all wet experiments were controlled to 37 ± 0.1 °C via thermocouple feedback control. The thermocouples were T-type form Omega Engineering, Inc. (part no. HSTC-TT-T-24S-36-SMPW-CC). Note that these thermocouples are electrically insulated, which was found to be critically important when being used in the area of a Clark microelectrode. The temperature monitor thermocouple was read by a model EP306 thermocouple pod from eDAQ, which in turn was recorded by the eCorder. The temperature control thermocouple was utilized by a model CN712 process controller (Omega Engineering, Inc.) in autotuned PID mode, for the most precise temperature control (typically ± 0.1 °C variation). This process controller pulsed electric cartridge heaters installed into the

aluminum housing around the chip holder area. Two cartridge heaters were utilized and they were model CS-01110/120, from Omega Engineering, Inc.

The absolute pressure in the chip holder was also monitored. For this study, that was simply to ensure no substantial changes occurred, but future studies could look at pressure effects more closely. Omega Engineering, Inc. supplied the static pressure sensor model PXM209-1.60AI. As an absolute pressure sensor, it was of course calibrated to zero at its point of manufacture (NY), which meant use in Seattle would be slightly off. This was studied by extensive comparisons with publicly available data from sensors at the University of Washington atmospheric sciences building, to find that a small correction was needed. This sensor was also monitored by the eCorder. Data was collected for several hours on a day when weather fronts were moving in, for a nice comparison. The result is included as Figure 19. In Figure 19, the blue trace represents

Figure 19: Pressure Sensor Performance

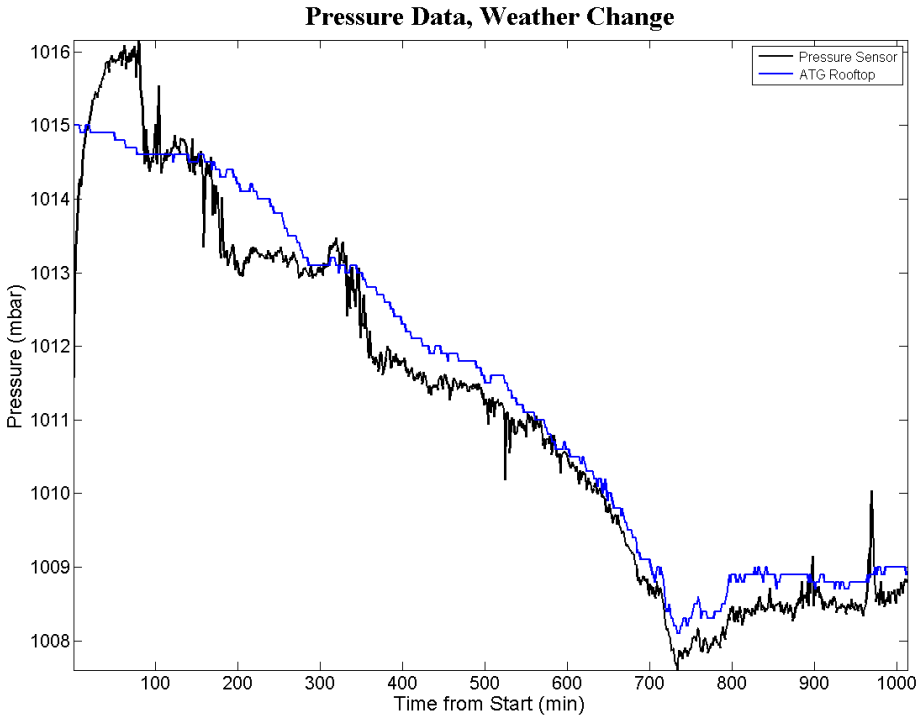

data from the nearby building, while the black trace represents data from the static pressure sensor. Considering that the pressure sensor was located indoors and subject to slight variations from HVAC systems, the performance was deemed to be quite acceptable for this study.

3.4 Optimizing Camera Operations

The camera utilized in this study was an intensified, gated CCD type, model DH734-18F-73 from Andor Technology (Belfast, UK). It was controlled by Solis software, which was provided by the vendor. This software allowed manual operation, or the creation of scripts similar to the BASIC language for automated control. The camera was also equipped with its own thermoelectric controller and internal delay generator. However, the operation mode chose for this study also necessitated an external delay generator; a model DG535 was chosen (Stanford Research Systems). Operational features of the camera had been optimized previously by Dragavon,[1] which included pixel readout time and gain settings. The findings of Dragavon (RSD studies) were supported in this study for pixel readout (1 μs) and his optimized gain setting of 150 was generally used as a starting point. The gain setting was simply an arbitrary scale (0 - 255) created by the vendor, but did increase exponentially with increasing gain setting.

The setting for the thermoelectric cooler was looked at in more detail. Dragavon reported[1] that the cooler setting did not affect results. However, it was observed that images would have a “hot” corner when the cooler was not utilized. Looking just at RSD was not deemed to be sufficient, but the background signal had to be examined. This was completed at full resolution and the optimal temperature for operation was determined to

be -10 °C. A nice way to show the "hot" corner was by looking at a blank background image at room temperature, then creating a mesh plot to capture the shape; this was done for Figure 20.

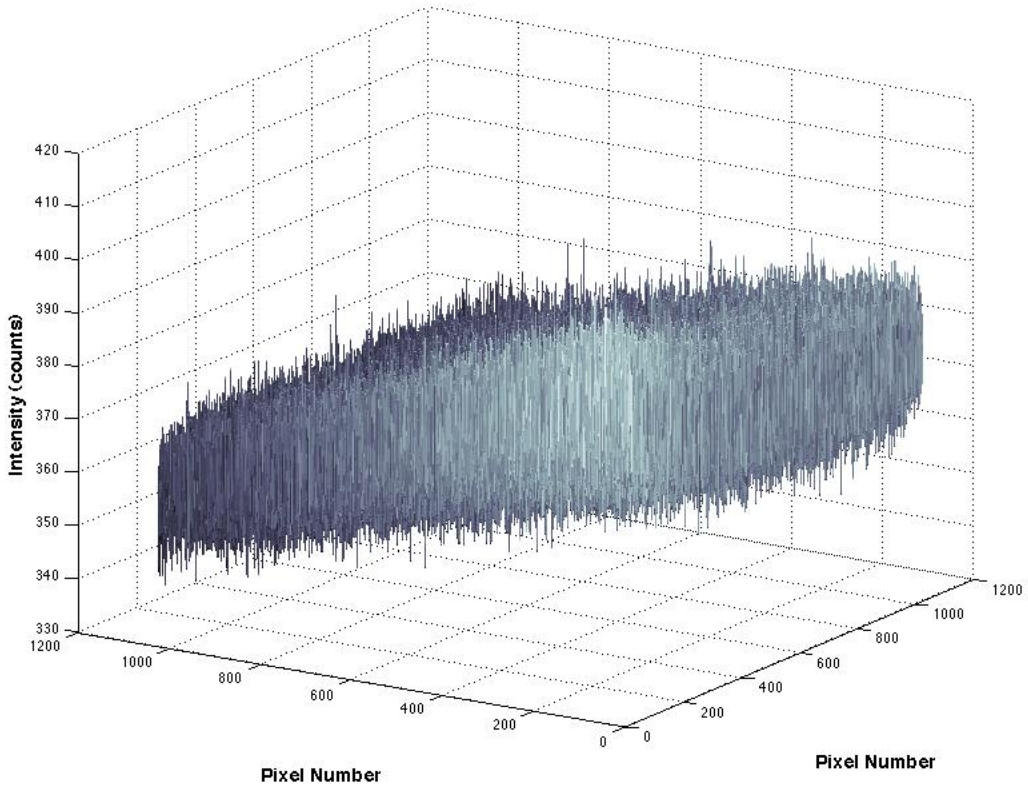

Figure 20: The Background Signal with Hot Corner. The image is tilted without a thermoelectric cooler and will flatten when it is turned on.

The vendor readily admits that the CCD array will suffer this problem when the thermoelectric cooler is not utilized, due to its close proximity to heat emitting circuitry. All data in this study was collected with the camera set for -10 °C.

Additional issues with the data collected previous to this study, were low spatial resolution and poor SNR. The SNR was quickly improved by switching camera operation to a mode called "integrate-on-chip" (IOC). Previously, data was recorded by averaging several frames together, which is a slow process and includes the readout noise

from every read operation from the CCD array. With IOC mode, photons are collected for multiple frames, and then read only once, which greatly reduces the readout noise from the CCD array. To use this mode, the camera's internal delay generator was incapable of producing the pulses needed to drive the LED, but this problem was solved by the addition of the external delay generator. In this manner, the camera's internal delay generator orchestrated the data acquisition process, but merely triggered the external delay generator, which then pulsed the LED excitation source appropriately and completely in sync with the data acquisition process. The spatial resolution problem was corrected by merely changing the camera settings. Previously, the camera was operated in "super pixel" mode, in which a sub-array of pixels (10 x 10 binning) was treated during CCD readout as a single super pixel. This was done because examination of past data clearly showed the camera resolution was not sufficient to capture the sensor image accurately, which was only exacerbated with the implementation of picoinjection. As discussed prior, picoinjection allowed for sensor rings to be just a few micrometers in width, so the camera resolution was changed to its maximum (1 x 1 binning), which produced images 1024 x 1024 in pixels in size. This way the spatial resolution would be ~1 μm, consistent with the capabilities of the picoinjection method for sensor deposition.

An additional point is worth mentioning. To implement the ratiometric methods for lifetime determination, two images are needed. Ideally, one would split the captured image with a 50/50 beamsplitter and direct each image onto independently gated and parallel intensifiers, and then have the CCD array in the camera set to capture each image on one-half of its surface area. Such technology was not available for this study. The next best choice would be to capture two images in rapid succession and this was the

method utilized throughout this study. Each image was also independently corrected for background variations. The Solis software was rather slow to save images, but an improvement made in the experimental procedure was to save in native Andor format, rather than the ASCII format that had been used previously. By switching to native Andor format (.sif), the images could be saved in ~5 seconds on the personal computer attached to the camera, rather than ~15 seconds prior to the format change. It is very likely this could be reduced even further to a few hundred milliseconds by optimizing the memory management in the control software, but as chapter four will reveal, data was already so dramatically improved, there was little motivation to pursue this.

3.5 Data Processing Algorithm for the Lifetime Imaging Method

With the optimization of the camera settings, came new problems. Refer back to Figure 18 (right-side image). A method to automatically detect the sensor rings in software was needed. Previously, this was done by what was essentially a pixel-by-pixel spatial convolution of a binary mask for each microwell, with the sensor rings, and keeping the spatial position that resulted in the strongest signal.[63] The binary mask was simply a ring of appropriate dimension to capture the sensor signal. Such a method is pure brute force, which is slow and computationally intensive. The method worked with old binning settings (10 x 10), but with the new binning settings (1 x 1), the existing software would typically crash before completing its task. The reader may contemplate that one could simply identify the center of the sensor ring and provide those coordinates to an algorithm, which would substantially decrease the search area for spatial convolutions. This was in fact done for the very weakest sensors that did not respond

well to the new algorithm described below. However, this was a slow and tedious process and definitely not desirable for the high throughput needs of biological experiments.

The new algorithm was very successful. Previously, the sensor ring finding step would usually crash, or need at least 45 minutes to complete. After upgrading the algorithm, a computer crash was never experienced and the run-time was ~5 seconds. The algorithm was written in Matlab (R2010b) and relied heavily upon image processing tools. The goal was to rapidly locate an approximate center of the sensor ring, then utilize spatial convolution over a much reduced area, in order to fine-tune the sensor ring location. Another advantage to this new method was the ability to easily change the size of the binary mask for spatial convolution, so that the ring size could be optimized for each individual glass chip. The first step was to locate the edges of the sensor rings. This was accomplished by utilizing the built-in edge finding function in Matlab. Most of the glass chips utilized the Prewitt method of edge detection, but some responded better to the Sobel method of edge detection. Next, the resulting binary image from edge detection was closed. Closure is an image processing method in which pixels are eroded, and then dilated, in order to remove spikes in brightness.[78] The effect results in smoother edges that appear more "closed." Once the binary image was closed, the tools in Matlab made it a simple matter to fill the closed area and locate its centroid (center of mass). Given that it was a binary image, all located pixels were of equal weight, so a centroid would correspond to the center of the circle-like region.

One complication that occurred was that the default edge detection threshold was too sensitive and would return a plethora of circular regions. However, the edge

detection function would also return the detection threshold (Matlab's best guess for a threshold was the default). Therefore, the process described above was iterated with an increasing threshold level, until the found region was approximately the same size as the circle that would fill the ring binary mask. Upon completion of the iteration, then the normal spatial convolution method was completed. The user had the option to invoke a diagnostic image. This was a valuable tool for a new glass chip, but typically was not needed once a particular array of microwells was shown to respond well to the algorithm. An example of the diagnostic image is included as Figure 21, on the following page. Color was added to the binary image to make it more understandable. The white region represents the filled circle-like region, with a red boundary. The green dot shows the location of the centroid. Figure 21 shows a nice example and some challenging examples. Note that most sensor arrays worked fine and it was a small minority that had to be handled manually.

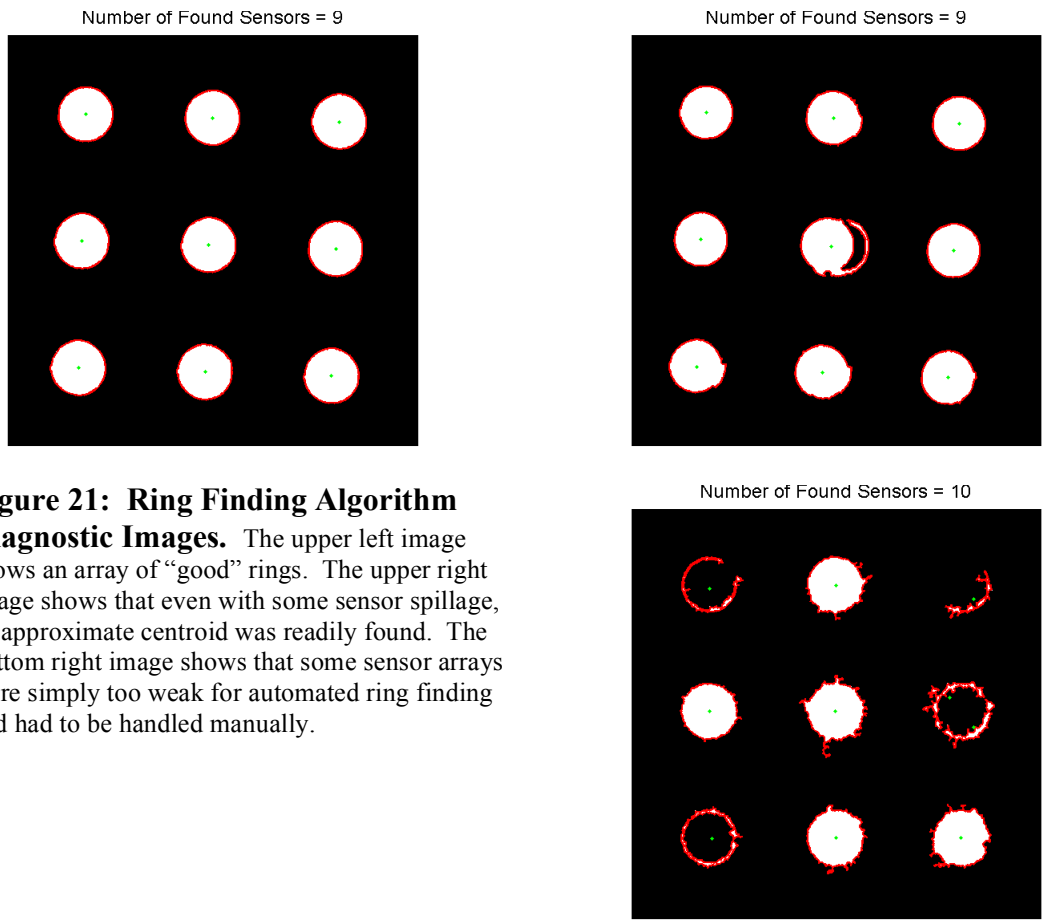

Figure 21: Ring Finding Algorithm Diagnostic Images. The upper left image shows an array of "good" rings. The upper right image shows that even with some sensor spillage, an approximate centroid was readily found. The bottom right image shows that some sensor arrays were simply too weak for automated ring finding and had to be handled manually.

3.6 Lifetime by the Decay Method

The determination of sensor lifetime has been discussed in prior sections, so this section will focus on the procedural aspects of the process. Recall that in this study, apparent lifetimes will be used. Direct decay methods will sample output signals from the APD and fit the data to the model of equation 2-28, with $i = 2$. With these two lifetimes, the apparent lifetime will be calculated form equation 2-12. This value could then be compared to apparent lifetimes obtained by the phase modulation and by the LPL method from image data.

All data for the direct decay method was collected on the LeCroy oscilloscope. Pulse widths for the LED were set to a multiple of 1, 2, or 5, as that was the most

compatible with the oscilloscope. The actual pulse width sent to the LED was this value plus 2-5 μs extra to avoid end effects. End effects were simply responses outside of the ideal LPL model due to capacitive on and off spikes from the LED. Once reasonable settings were obtained for pulse width, preamp gain, and oscilloscope gain (5-10 mV/division in all cases), then all control was handled via LabVIEW software written in-house. One hundred pulses were collected for each data point, which were automatically averaged by the LeCroy oscilloscope. This data was then analyzed in the custom LabVIEW software.

Within the custom software, the operator would view the raw data and verify that the data and settings were retrieved correctly. The oscilloscope data was oversampled, so then a boxcar average could be set (typically 20-50 points). A cursor screen would allow definition of the start point, to avoid end effects in the start of the data. The data was then fit with a nonlinear model, using the Levenberg-Marquardt method. The apparent lifetime was automatically calculated in the software and all data saved. The apparent lifetime was then used to suggest an optimal lifetime for phase modulation methods, which were incorporated into the software as a subVI.

Quality control for this method was simply observing the oscilloscope as it collected the waveforms. Note that occasionally a timing glitch would miss a pulse, but the software would detect this and only save valid waveforms.

3.7 Lifetime by the Phase Modulation Method

The phase modulation method relied upon a single frequency for determination of the apparent lifetime. As mentioned above, the optimum frequency was suggested by the

direct decay measurement and phase modulation measurements were carried out immediately after direct decay measurements of the lifetime. The lock-in amplifier was utilized for this task. The lock-in is capable of reading phase directly, but this is based upon a reference signal, which in this case would be the signal from the function generator modulating the LED. Normally, one would be inclined to optically sample the excitation source and utilize that as the reference signal for the lock-in amplifier, but such an arrangement was not possible from the available materials in the laboratory, so an alternative procedure was developed. The custom software would first collect phase signal from the excitation beam by analyzing signal from turret position #5. Then phase signal would be immediately collected from the sensors themselves (turret position #4) and the custom software would average 200 points to find the phase difference for the true phase measurement. Application of equation 2-16 would then yield the apparent lifetime measurement.

Quality control for this procedure was a two-step process. The auxiliary oscilloscope would monitor the lock-in signal in real time. Direct observation of this would indicate missing signal or overloaded signals and the data point could be repeated, after adjusting settings appropriately. Such events were always a case of operator error. When phase signal was collected, it was displayed in the custom software. With 200 points, one would expect to see a random distribution about a mean due to noise. When this did not happen, the data point was repeated. Occasional spikes were noted that appeared to coincide with building HVAC systems turning on or off, or passing cell phones that were transmitting. Another more common feature was a delayed amplifier response, which took the form of a slowly rising curve. No explanation was determined

for that other than perhaps the age of the lock-in amplifier. Repeating the data point corrected the situation

One additional point is noteworthy with the lock-in amplifier. The user manual stated that the use of the built-in bandpass filter will reduce the phase up to 5° and that this error should be accounted for or the bandpass filter turned off. With so many nearby instruments, it was observed that the bandpass filter was highly desired by direct observation of the lock-in signal on the auxiliary oscilloscope. Thus the bandpass filter was utilized for all data in this study. There seemed to be no clear pattern on when the phase error occurred. The practice was to adjust the apparent lifetime only if this made it more consistent with reading from the other instruments. That is evident in reported data when lifetimes determined by phase modulation are reported as adjusted lifetimes. The difference was relatively small. At the frequencies utilized throughout this study, the lifetime difference was 2-4 μs for any given data point.

3.8 Optical Challenges for Lifetime Measurements

Up to this point, it may appear as if the study progressed quickly and nicely. That much is true; picoinjection and algorithm improvements did occur quite early in the study and worked extremely well. However, a substantial challenge was then faced with direct decay and phase modulation measurements. Initially, direct decay measurements truly did involve a sampling of the decay waveform, rather than a sampling of the convoluted waveform modeled by equation 2-28. The ratiometric imaging method relied upon the ORLD method, which functioned well, except in the case of very weak sensors. In order to compare characteristics of different sensor formulations, it was desired that the ORLD

method should be verified as having reasonably accurate lifetime determinations. Verifying the ORLD determinations against a direct decay measurement and a phase modulation measurement was determined to be a reasonable level of verification for this study.

Upon implementing that task with the instruments described previously, it was found that the sensors did not operate at all; changes in oxygen concentration resulted in little or no change in sensor response. This seemed unbelievable and certainly counter to the data obtained via the ORLD method. A long and tedious study was undertaken to reveal the root cause of the problem. It became quite evident that a contaminating luminophore was present in the testing station. The lifetime appeared to be similar to the sensor materials under study and when utilizing a 40x objective, was similar or greater in magnitude than the sensor response. It appeared as if measurements were an elusive goal when interfering "noise" is very similar to the analytical signal and of similar magnitude!

At that point, it was thought that sensor material must have spilled into the inner optical train of the microscope. However, careful examination of the optical train inside the microscope revealed no trace of spillage. Fortunately during that exercise, an unexpected green glow was observed from the dichroic mirror in turret position #4. Autofluorescence of the mirror coating was presumed and the vendor was contacted. The vendor admitted that autofluorescence was possible or even very likely with the dielectric coatings utilized to make their optics, but that the effect was typically much smaller than the analytical signal. An alternative dichroic mirror was tried, but little change was noted.

At that point, all the optics in the optical train became suspect and were examined, one-by-one. This was accomplished by their removal from the microscope. The optic under test was then mounted inside an optical tube and exposed to excitation light. The APD was utilized for detection, which often necessitated the use of a pinhole aperture and/or neutral density filters, in order to not saturate the APD. At that point, it also became evident that convolution was a substantial factor in these experiments *and* that it also served as a very sensitive test for the presence of autofluorescence. The LED sources, apertures, neutral density filters, and the APD were verified to have no detectable convolution effect relevant to this testing. Then the other optics were tested. At that point, a shocking discovery was made; the emission filters utilized in turret positions #2 and #4 were emitting a very strong autofluorescence signal. Figure 11 is a demonstration of pure excitation light versus excitation light with a "contaminating luminophore." That "contaminant" is in fact, nothing but the 655/40 emission filter!

Determination of this problem is when the Ocean Optics spectrometer began to be utilized to verify that the problem was no longer present. Additionally, it is noteworthy that the problem is especially exacerbated by use of the 40x objective on the microscope and that up to that point in time, only the 40x objective provided a signal strong enough for detection by the APD. This explained why data could be collected via the imaging ratiometric method, as all those trials were conducted with the 10x objective. Correction of the problem turned out to be fairly straightforward. First, the autofluorescence was characterized spectroscopically. That was accomplished on a model FL3-21tau fluorescence spectrophotometer from Horiba Scientific (Edison, NJ). That instrument was necessary because it was the only one available that could examine solid disk

material, such as an optical filter. However, the instrument is not able to sample in the orthogonal direction, so a few angles were tried with the hope that spectral response would not be too anisotropic. The result is included as Figure 22.

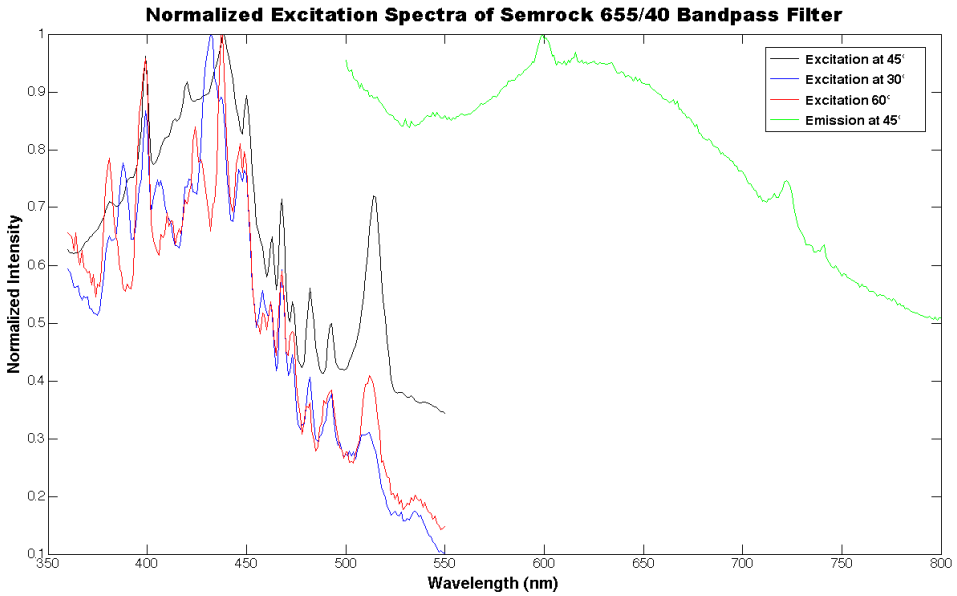

Figure 22: Spectra of the Emission Filter

From Figure 22, it is noteworthy that the excitation spectrum is very broad. Also note that an emission spectrum is included, which may not be very meaningful on a reflective instrument. However, rather than seeing noise with perhaps some second-order peaks, we do observe a broad and intense emission in the region of interest. It was further contemplated that adding bandpass filters to the excitation sources would in fact reduce the autofluorescence problem. That was found to be the case. This explains the choice of filters on the LED sources and the excitation filter in turret position #5. All of these choices were verified as producing negligible amounts of autofluorescence signal. The problem was not eliminated completely, but reduced to such a small amount, that

there should only be a minor effect in the data. An example is depicted in Figure 23.

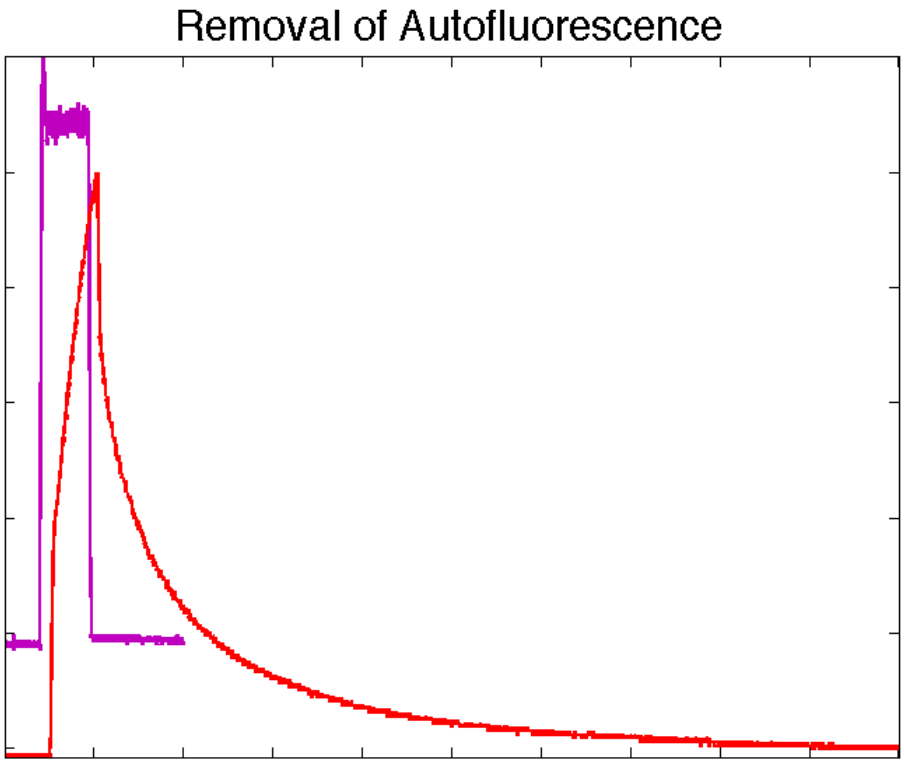

Figure 23: Reduction of Autofluorescence from the Emission Filter. The purple trace shows the normalized intensity of the excitation pulse, after installation of a clean-up filter (405/10) and after passing through the 655/40 emission filter (i.e. detection of leakage photons). Its shape is nearly rectangular, as desired. The red trace shows the normalized intensity of the excitation pulse leaking through the emission filter, without a clean-up filter in place. In that case, the presence of autofluorescence "contamination" is unmistakable. Traces are Intensity vs. Time.

In Figure 23, we see the excitation pulse (purple trace, shifted for clarity) exposed to the 655/40 emission filter after being "cleaned-up" by the 405/10 bandpass filter. The red trace shows the excitation pulse without the 405/10 bandpass filter. Autofluorescence was substantially reduced. However, the purple trace showing a slight upslope during the on period and a slightly elevated baseline after the pulse, are both indicative of trace amounts of autofluorescence remaining.

Especially in context of the LPL method, there may be some concern about the amount of scattered excitation light captured in images for the ratiometric procedure. This is a valid concern and turned out to be an important challenge. It was important to not change anything in the glass chip holder. Collected data would be dramatically different if any variable substantially altered the scattered light component. The most severe effect from this was the Clark microelectrode. It was initially mounted directly over the array being characterized, which was fine for the ORLD method. However, for the LPL method, so much light was reflected off the shiny polypropylene membrane of the electrode, that the sensor signal would be overwhelmed with excitation light leaking through the emission filter. In that case, it is probably more correct to call it specular reflected light, rather than scattered light. The solution was simple; to change the mounting position for the Clark microelectrode off to the side, out of view of the microscope objective. Upon completion of that task, data improved.

Chapter Four: Experimental Results

4.1 Improved Repeatability

The primary goal of this study was to improve repeatability. That was achieved fairly quickly by implementation of three key steps: development of the picoinjection method for sensor deposition; optimization of camera settings to reduce readout noise by 2-3 orders of magnitude; software algorithm improvements that allowed increased spatial resolution of sensor rings by 100x. Recall that Dragavon reported[1] RSDs between 3% and 30%, depending upon the context of the experiment. Only sensor characterization studies were carried out in this study. The improved methods described above were only sparingly implemented by other researches at the MLSC. Interest in single-cell measurements had shifted to the location at Arizona State University, where equipment in that laboratory did not permit similar ratiometric methods. Therefore, it is best to compare these results against Dragavon's laboratory results, which were typically on the order of 3% RSD.

Table 3 on the next page shows a typical run. Unless stated otherwise, all data in this study were an average of five data points (i.e. ten images to produce 5 ratio points). The results are outstanding and such results were highly consistent throughout the study. Whenever RSDs exceeded 1%, there was never a case of method instability that was observed. Investigation of such points always revealed real phenomena associated with the drift. Such phenomena include shifting of the glass chip due to vibrations, debris floating into the field of view, or the beginning of a sensor problem, such as delamination.

Table 3: Typical Ratiometric RSDs (%) for Wet Run of MOD Sensor

	Microwell #								
[O2]	*1*	*2*	*3*	*4*	*5*	*6*	*7*	*8*	*9*
24%	0.1758	0.2424	0.1556	0.3307	0.1574	0.1732	0.3981	0.2128	0.3130
Ambient	0.1156	0.2998	0.2734	0.1219	0.2842	0.1497	0.1719	0.2993	0.2408
18%	0.1298	0.2166	0.1860	0.2494	0.1950	0.2744	0.2940	0.1617	0.2700
15%	0.1519	0.2596	0.2500	0.2081	0.2466	0.1915	0.2352	0.2545	0.1643
12%	0.1836	0.1226	0.2322	0.0683	0.1433	0.1969	0.1672	0.1708	0.0612
9%	0.1702	0.1521	0.1802	0.1628	0.0953	0.1465	0.1115	0.0839	0.1750
6%	0.0910	0.0938	0.1578	0.1054	0.0795	0.0916	0.1883	0.1780	0.2102
3%	0.2772	0.0728	0.2163	0.1081	0.1020	0.1006	0.2128	0.0934	0.0752
< 1%	0.1077	0.1015	0.1954	0.0810	0.1102	0.1386	0.1428	0.1869	0.1716
Anoxia	0.1105	0.1314	0.1292	0.0659	0.0825	0.0682	0.1290	0.1735	0.1309

4.2 Characterization of the FB Sensor

Six sensors were characterized in this study. The naming convention was very brief as the glass chips utilized in the study were quite small. The FB sensor refers to a free-base porphyrin. The Alex Jen Group at the University of Washington provided the sensor material. It was prepared by dissolving ~1 mg of the luminophore and ~0.1 g of polystyrene in 10 mL of toluene. Free-base porphyrin is a generic term used to describe a porphyrin structure lacking a metal center. These materials often exhibit fluorescence, but not phosphorescence. The proper name of this material would be 5,10,15,20-Tetrakis(pentafluorophenyl)porphyrin. As a note to the reader, within this study, the abbreviation TFPP may be used to refer to tetrakis(pentafluorophenyl). One would think that TPFP would make more sense, but the literature is replete with the former, so tradition was followed in writing this dissertation. Figure 24 is a display of the structure. The luminophore was chosen as a negative control. Since the luminophore exhibits

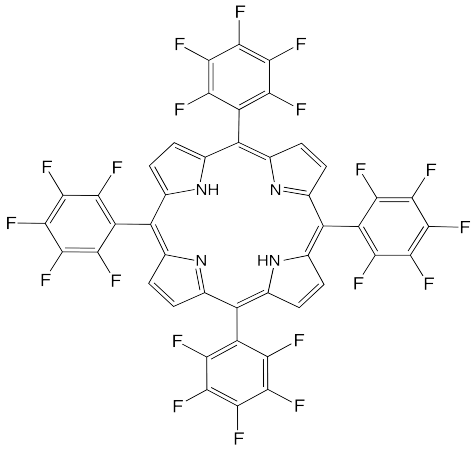

Figure 24: TFPP Structure

only fluorescence, it should not respond to the methods utilized in this study.

The luminophore was presumed to adsorb to the polystyrene. Polystyrene was chosen as the support matrix since biologists from the MLSC reported no cytotoxicity problems with other polystyrene sensors. The material was picoinjected with some difficulty; the pressure settings were 148 kPa inject pressure for 40 ms, with a balance pressure of 6 kPa, utilizing the TD method (see Appendix A). Spillage occurred easily and the tip clogged often, but success was eventually achieved for a sufficient number of microwells to complete an analysis. The spectra for the sensor are included as Figure 25.

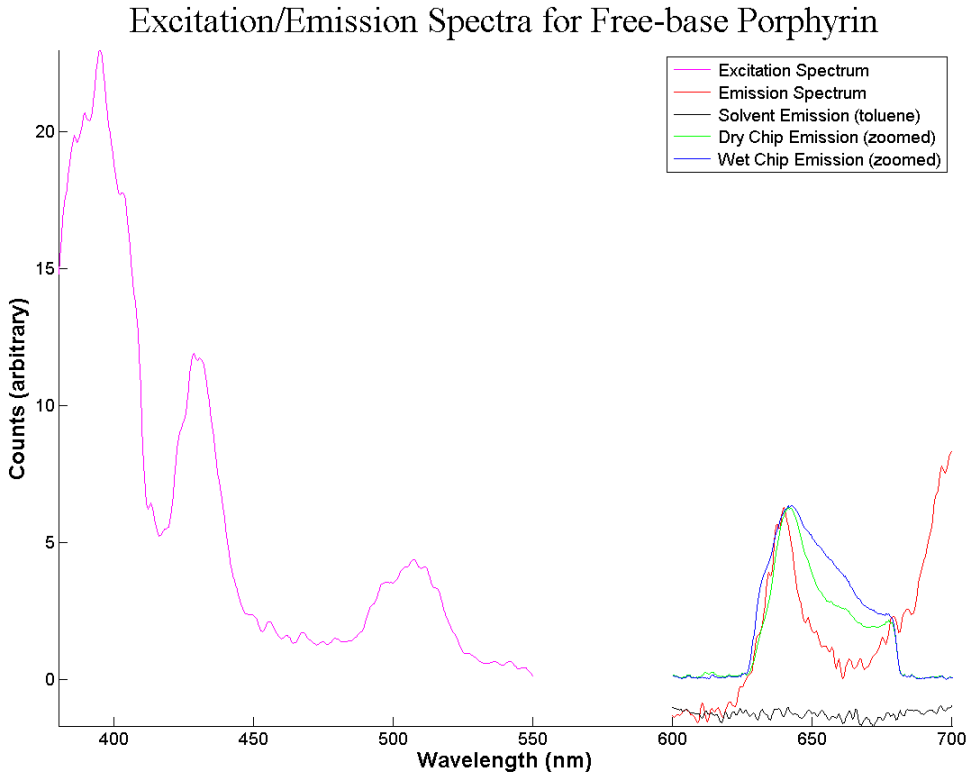

Figure 25: Excitation and Emission Spectra for the FB Sensor

The excitation spectrum reveals that this material shows the Soret band as two distinct regions and that the Q band is also present. The Soret band appearing as two distinct regions is unusual for this class of luminophores, but not unheard of.[28] The emission

spectrum indicates the expected red emission is present around 650 nm. The solvent emission spectrum is included to show that there are no solvent contributions to the emission spectrum. The emission spectra on the microscope are also included. The unusual shapes of these spectra arise from the bandpass filter, which cuts off sharply at its limits. The Ocean Optics spectrometer used on the microscope also has less resolution than the research grade fluorimeter used for the solvent based measurements, which can smooth out the spectra.

Next, we shall discuss the hydration effect. To simulate the environment of the cellular media used by biologists, almost all characterization tests were completed submerged in deionized water. A dry run was typically done at the beginning of characterization for comparison purposes, but all other tests were completed submerged. Early on in the study, it was unclear if there would be any delay in water soaking into the hydrophobic matrix of polystyrene, or other polymers utilized as the support matrix. If there was a delay before water was fully dispersed throughout the support matrix, or if water resulted in any polymer swelling, the diffusion of oxygen within the support matrix could be affected. Any phenomenon that disrupts the diffusion process would of course affect sensor lifetimes via the Stern-Volmer relationship and if lifetimes were effected, ratiometric data could also be affected.

The test was quite simple. After determining a reasonable set of camera settings for ambient exposure, an array was monitored for ratiometric changes over a long period. Those sensors that did appear to have an effect would typically change the most within the first hour. It is important to note that these experiments were conducted at 37 °C; earlier experiments at ambient temperatures indicated the time to a stable ratiometric

response was substantially increased. Given that changes would occur within the first hour, ratiometric monitoring was done often for the first hour, and then decreased for the subsequent time period. Figure 26 shows the lack of hydration effect for this sensor.

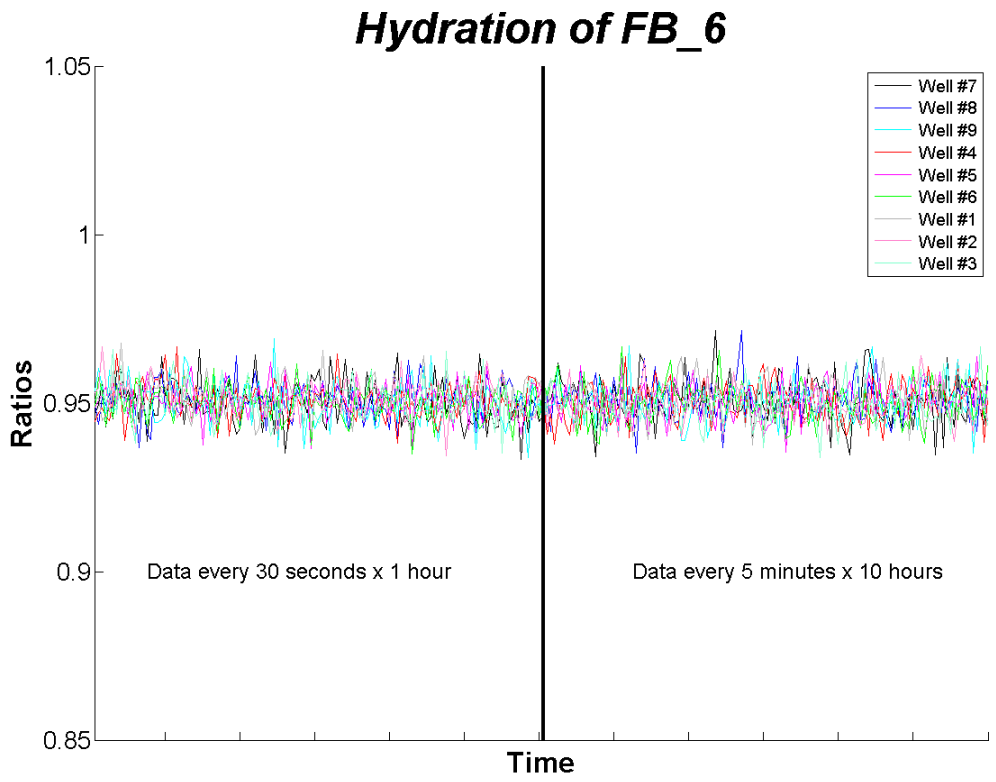

Figure 26: Hydration Effect for the FB Sensor

The traces for all microwells show a flat response for the first hour with data collected every 30 seconds, then a continued flat response for the next 10 hours, with data collected every 5 minutes.

The sensor ring size was optimized for image processing purposes to 57 x 70 pixels, which would indicate an approximate sensor ring width of 14 μm. An approximate lifetime under dry, ambient conditions was estimated in order to set experimental parameters. Then a wet run was conducted. In the terms of this study, a wet run shall indicate bringing the glass chip to a stable reading on the Clark

microelectrode under ambient oxygen conditions at 37 °C, and then changing the oxygen concentrations to approximately 24%, 18%, 15%, 12%, 9%, 6%, 3%, < 1%, and anoxia. These concentrations were approximate because the mass flow controllers were set to near the listed value; accurate concentrations were always obtained from Clark microelectrode data. The array under study had lifetimes measured via direct decay, phase modulation, and ratiometrically. In Figure 27, we see lifetime data for the FB sensor. Data from the direct decay and ratiometric methods appear rather consistent and surprisingly within the proper range. The expected lifetime would be on the order of 60 ns and given that these methods are not designed for such short periods, it was surprising that the results are about right. The phase modulation data is not very close to the other data. Lifetimes from phase modulation methods will be presented with the diagnostic plot, to show the measured phase differences. Given that the direct decay method suggest an optimized frequency directly via software control, the diagnostic plot should be close to 45° for phase readings. Looking back at equation 2-16, and realizing that the *tan* function is zero at zero phase and infinite at 90°, one can further analyze the propagation of errors to determine an optimal phase of 45° to minimize errors. It was upon this basis that the

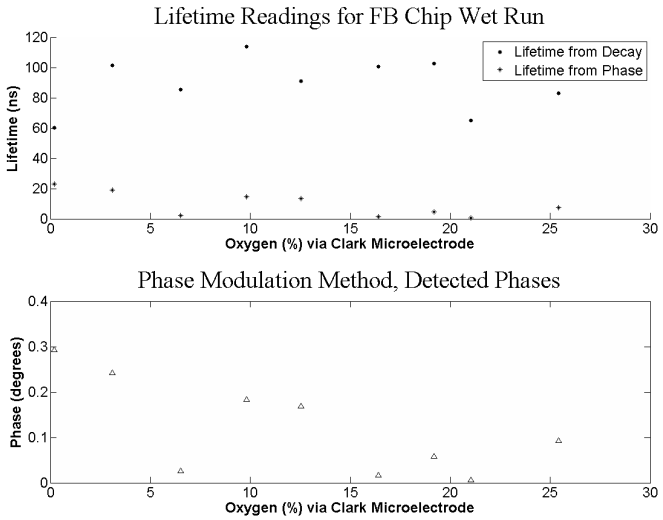

Figure 27: Lifetime Data for the FB Sensor

software optimizes the suggested frequency. Therefore, the diagnostic plot would suggest that all the lifetimes from phase modulation for this material should be rejected. This is not unexpected; recall that the instruments are not at all capable of modulating the signals fast enough for a proper phase reading within this temporal regime.

We may also suggest that the lifetime readings from the other methods are essentially unresponsive to changes in oxygen concentration. As the negative control, this was the desired behavior and the primary result was to show that the LPL method does produce a relatively flat response from a luminophore not quenched by oxygen.

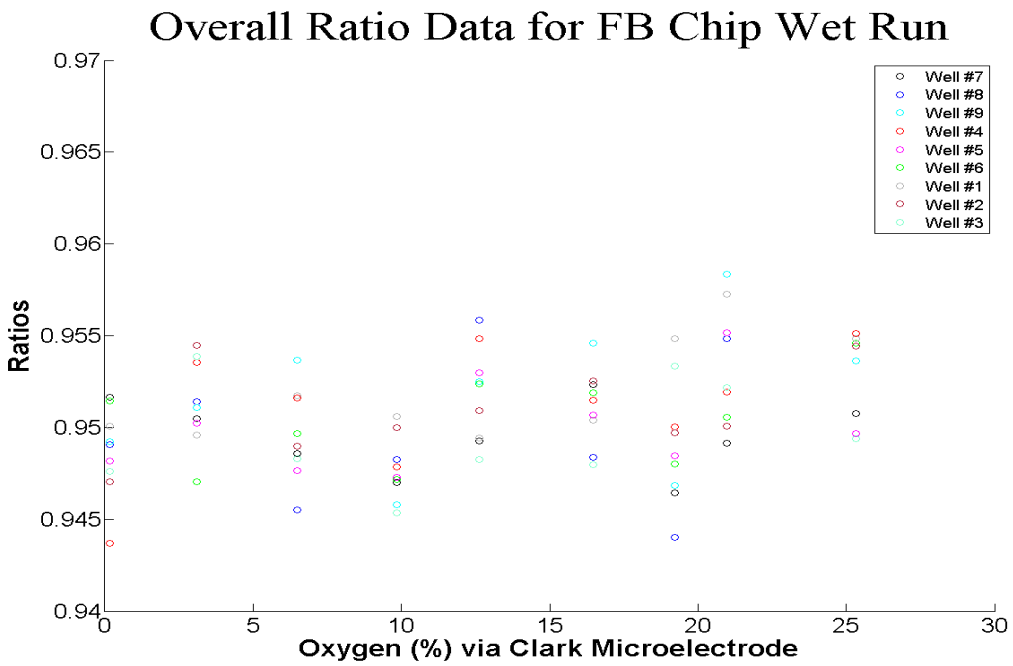

Figure 28: Ratio Data for the FB Sensor

In Figure 28 on the previous page, we see a summary of the ratiometric data itself for the wet run. This data has much more spread than is typical for the LPL method. Within such a short temporal regime, the LED pulse was set to a minimum width and thus consisted of substantial portions of the edge effects discussed previously. In the face of such an excursion from the model assumptions, it is again not surprising to see increased variability. The key point is that there was little, if any, change in ratiometric data as oxygen concentration decreased. Another diagnostic plot is displayed as Figure 29. This is a microwell specific summary of measurement variability from the LPL method. Throughout this study, errors were generally quite small, with only an occasional condition where the error bars can even be adequately discerned. However, this sensor was an exception for the reasons discussed above. Again, note that even

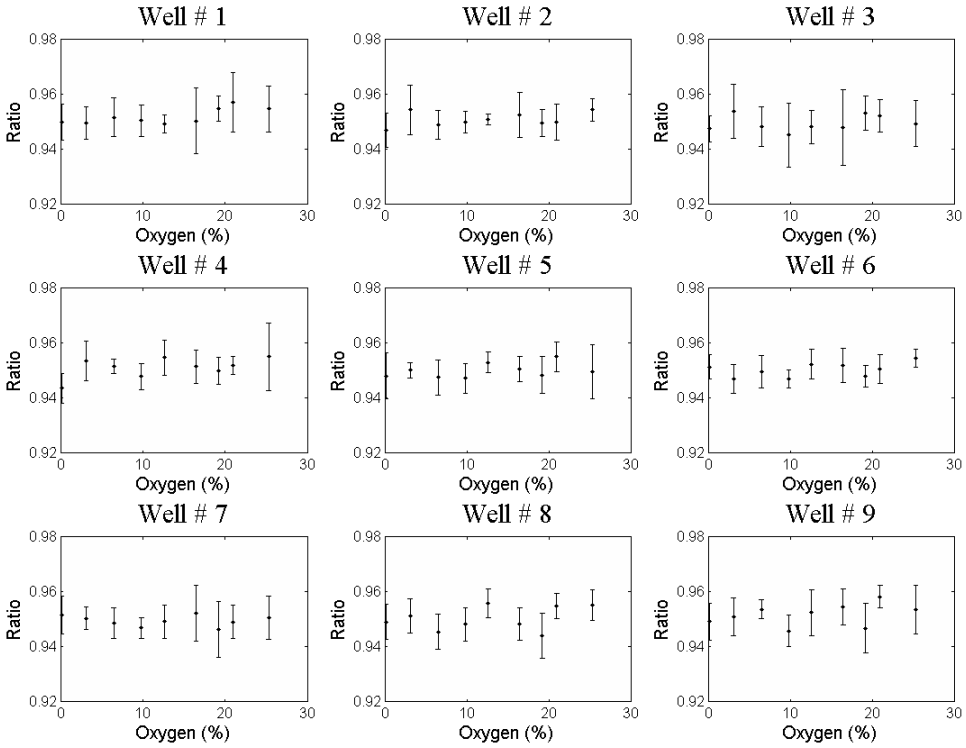

Figure 29: Error Data for the FB Sensor

looking at each microwell, there is no obvious trend within the data as the oxygen concentration was decreased.

4.3 Characterization of the IB Sensor

The term, IB sensor, refers to a commercial bead product from Invitrogen (Eugene, OR). Specifically, 40 nm carboxylate-modified polystyrene beads, part number F20886, impregnated with a luminophore were used extensively by researchers at the MLSC. The beads were provided in distilled water, 0.5% (w/w) solids with 2 mM sodium azide as a preservative. The vendor shared the manufacturing method as a solvent swelling process, whereby the luminophore was added to solvent, the beads were allowed to swell and absorb solvent, and then the beads were allowed to dry before dispersing into water. The solution appeared pink in color, indicative of leaching of luminophore into the water. The vendor would admit to the luminophore being a platinum porphyrin, but refused to identify the specific porphyrin. Spectral data might suggest platinum (II) octaethylporphyrin. For improved picoinjection results, it was found that dilution 1:1 in deionized water worked very well. Prior to any picoinjection, the beads were always vortexed at maximum speed for one minute, followed by two minutes of sonication. Those steps were thought to limit the aggregation of beads.

This sensor had the most successful picoinjection results. After some initial practice, very nice sensor rings could be produced on a consistent basis. The method used was the TTAW method (see Appendix A). The inject pressure was 175 kPa with the pressure pulse lasting 30 ms and zero balance pressure. Some spillage would be encountered occasionally. Tip clogs would only occur when moving too slowly, but

when they did, were often quite troublesome to clear. A "bulk" chip was also made by simple pipetting of 10 μL of the diluted material onto the flat, backside of a glass chip. Its use will be discussed later. Both types of chips were cured by heating to 160 °C in a tube furnace for 30 minutes. During subsequent use, the sensor ring size was optimized to 59 x 73 pixels, which corresponds to a sensor ring width of approximately 15 μm.

Figure 30 shows the spectral data collected for this sensor.

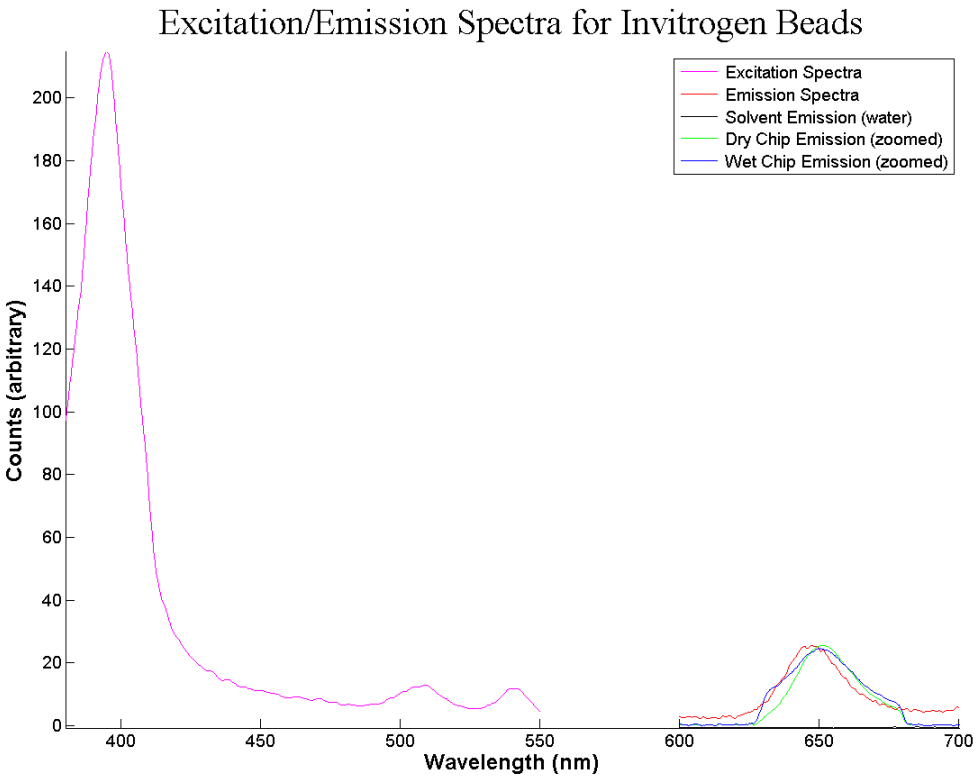

Figure 30: Excitation and Emission Spectra for the IB Sensor

The emission behavior of the luminophore for this sensor is similar, whether or not solvent (water) is present. Note that the emission spectrum for water is included above, but so weak that it is not really legible on the scale of Figure 30. The excitation spectrum had a nice clear Soret band with apparently two types of Q bands.

The IB sensor was next evaluated for its dry response. A complete dry run was conducted for each sensor in this study, except for the FB sensor. The purpose was to elicit if there was any change in behavior with the sensor between the dry state and the wet state. The presentation of data shall also follow a standard format. The lifetime data will be exhibited, and then the raw ratiometric and ratiometric error data will be presented, followed by a Stern-Volmer analysis of lifetime data. In Figure 31, we see the lifetime data for the dry IB sensor.

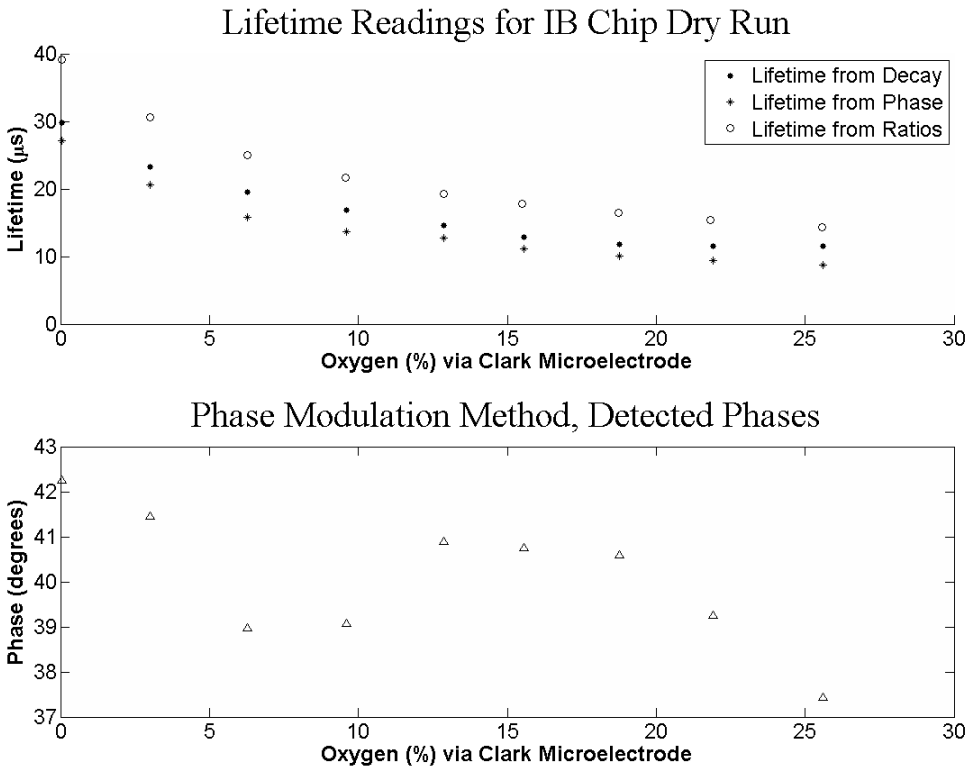

Figure 31: Lifetime Data for the Dry IB Sensor

The lifetimes via direct decay and phase modulation are fairly consistent, with an excellent phase diagnostic plot. The lifetimes via ratiometric means appear to be shifted upward. We shall see that this is the only lifetime plot with such a substantial deviation in lifetime data (and even then, the difference is not that great). Upon completion of analysis of the dry data, and the hydration effect for this sensor, the optical issue discussed at the end of section 3.8 was encountered. After changing the position of the Clark microelectrode, such a large deviation was not encountered again. It is also important to note the scale in Figure 31. Lifetimes are on the order of 10-40 μs, depending upon oxygen concentration. The vendor reports a natural lifetime for the sensor of 100 μs (the term natural lifetime is used throughout the literature to indicate the lifetime under anoxic conditions). Given that the material was utilized as a thin-film in this study, rather than in bulk, this seems reasonable. These results are consistent with literature values,[28,31,33-36] so all the methods employed in the study appear to have a reasonable degree of accuracy.

In Figure 32, the ratiometric data is presented for the dry IB sensor.

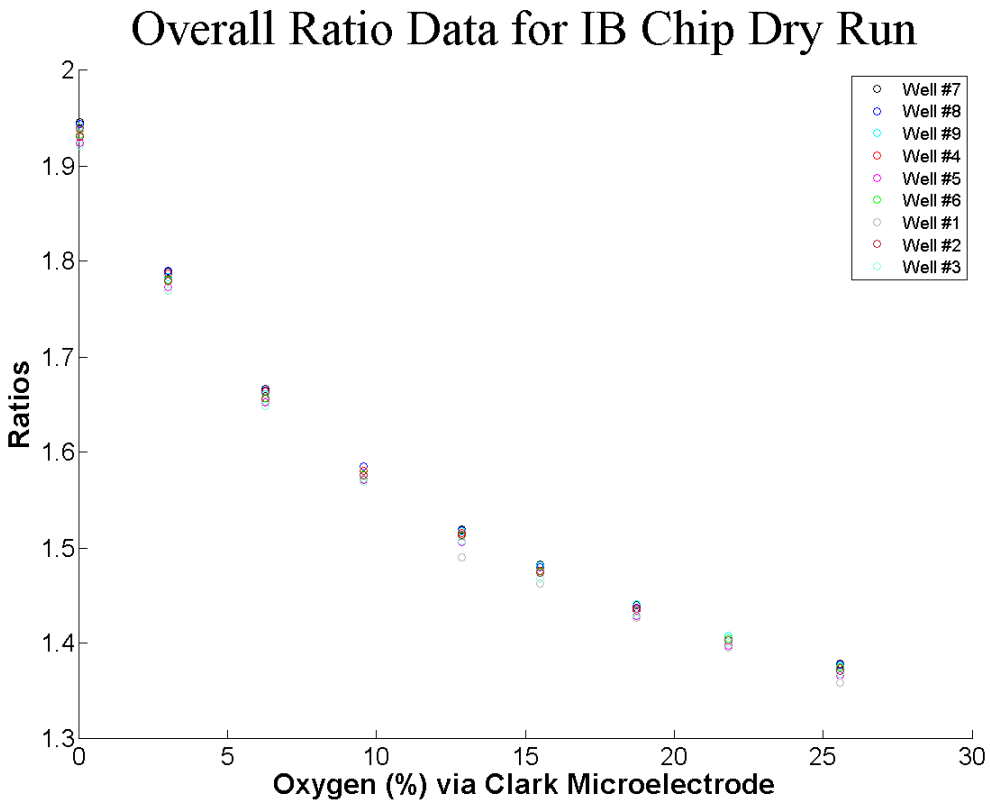

Figure 32: Ratio Data for the Dry IB Sensor

This data is much tighter than for the FB sensor, as should be expected since the methods are now within a regime in which they should function. Microwell #1 appears to have some anomalous behavior, but that microwell was observed to have some sensor clumping. That was not too unusual for microwell #1. That would be the first microwell injected in a given array and as such, the time delay from loading or array shifting was longer and less consistent then between other microwells. Such effects would support the case for calibration to occur for each individual microwell, rather than an average of an entire array. Calibration will be discussed in more detail in section 4.9.

Figure 33 presents the ratiometric error data for individual microwells.

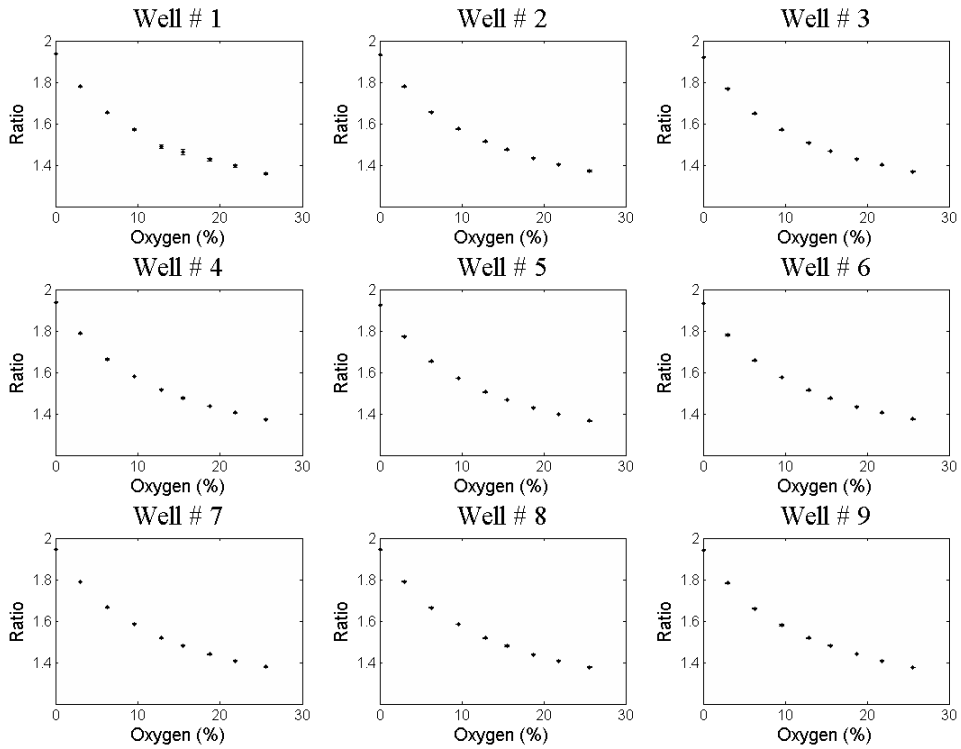

Figure 33: Error Data for the Dry IB Sensor

Errors are very small, with only a couple of cases even showing a discernible error bar. Figures 32 and 33 reveal that ratiometric data is clearly nonlinear with changes in oxygen

concentration. This is not necessarily a problem, as long as the data is always monotonic and repeatable. If the monotonicity and repeatability characteristics are present for a given sensor, then calibration to oxygen concentration is still an achievable goal.

The Stern-Volmer response was examined next for the dry IB Sensor. This data is presented in Figure 34.

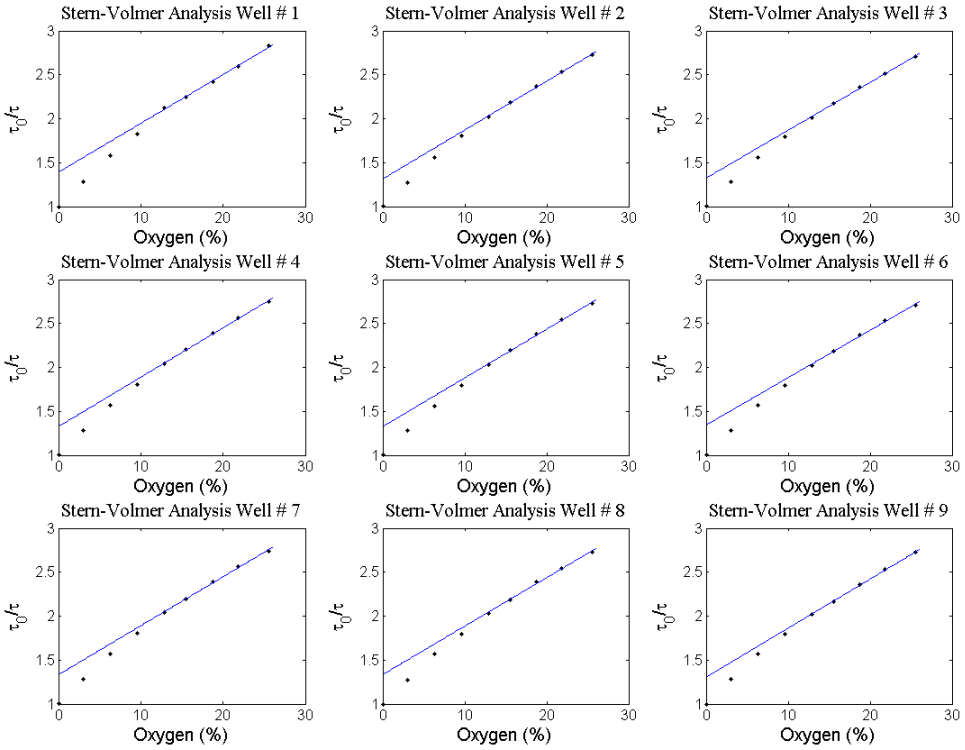

Figure 34: Stern-Volmer Response for the Dry IB Sensor

The downward curve is emphasized here by the choice of fitting scheme. As discussed previously, a Stern-Volmer plot for a homogeneous sensor will be linear with a slope giving the Stern-Volmer constant and an intercept of 1 (see equation 2-11). The reasons for deviation from linearity were discussed in section 2.2. In this study, biologists were primarily concerned with oxygen concentrations between 10% and 20%. Therefore, the Stern-Volmer data was fit to a linear response (in a least-squares sense), but only for the

five rightmost points (roughly 9% to 24% oxygen). That methodology was chosen merely as a way to observe a plot and immediately discern the extent of deviation away from a full linear response, but without suggesting any physical meaning from the reduced fit. As a reminder, for the Stern-Volmer plots, τ represents the measured lifetime at the given oxygen concentration, while τ_0 represents the lifetime under anoxic conditions. In every case within this study, an anoxic lifetime was measured for each trial and for each microwell. It may be tempting to get one accurate natural lifetime for the sensor material and not have to be bothered with the tedious measurement, but recent discussions in the literature[79] would suggest that this may not be a wise choice. There appears to be evidence that sensor heterogeneity may not be the only issue to consider. Microcrystalline features within the polymer support may contribute to heterogeneity amongst nonradiative decay processes. In other words, Stern-Volmer theory assumes that nonradiative decay processes are constant and the nice linear response results from competition between phosphorescence and quenching. Subtle heterogeneity at the molecular level (if it exists) would suggest that the natural lifetime could vary slightly between microwells and should thus be measured for every trial.

The next step in the characterization was to evaluate the hydration effect. The result is included as Figure 35, below.

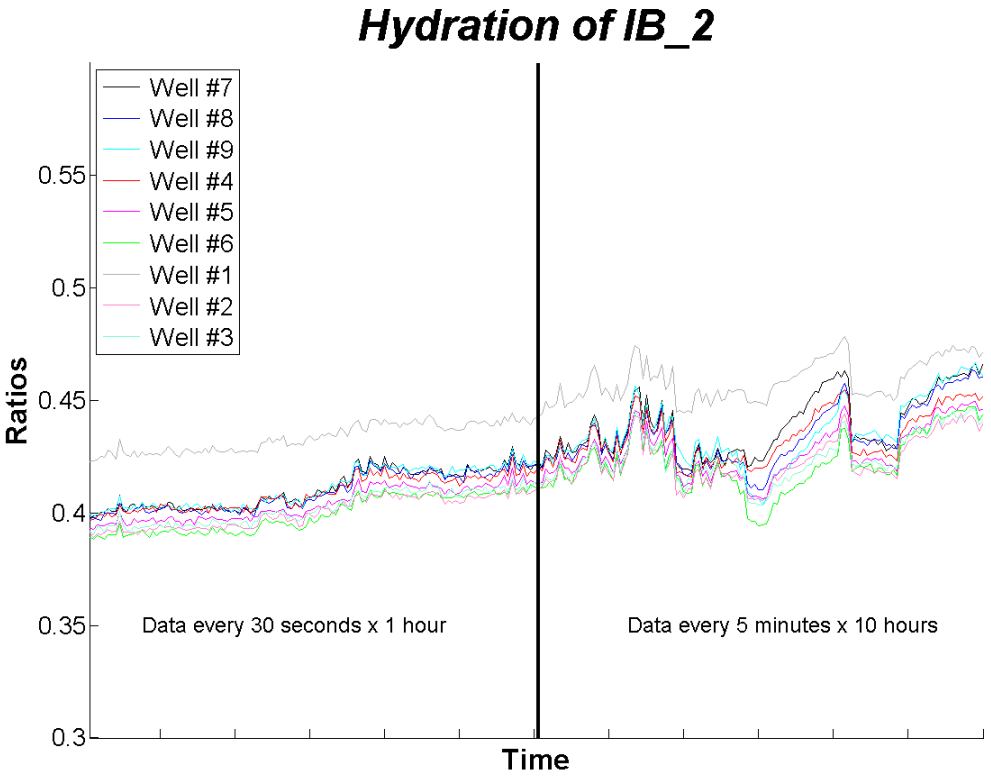

Figure 35: Hydration Effect for the IB Sensor

For this sensor material, we see that there initially appears to be anomalous behavior in the ratio data. Microwell #1 stands out, but this effect was just described previously. There is a trend over the first hour towards increasing ratios. The trend appears to continue for approximately another hour. Then the ratiometric behavior appears to become erratic. The erratic behavior simply indicates that insufficient water was placed into the chip holder and bubbling from the sparging tube was creating highly turbulent water motion over the glass chip area. With the addition of more water, the readings stabilized. Additional testing revealed that new sensors typically did require ~2 hours to stabilized, but that once hydrated, the sensor material retained stable behavior, even when

allowed to dry out for a few days (ambient conditions). This may sound like an undesirable feature, but the impacts are negligible. When beginning a wet experiment, the amount of time to achieve temperature stability, Clark microelectrode stability to air purging and sparging, set instrumental parameters, and adjust software scripts, was typically an hour or more. Simply waiting a bit longer for a newly created glass chip was not a burden. Additionally, during biological experiments, the glass chips were incubated in a submerged state for 16 hours, so any hydration effects would be well established by then.

It was contemplated that sensor thickness may play a role in its response. For each sensor, one of the arrays was prepared with multiple injections. One row (microwells 1-3) would be singly injected, one row (microwells 4-6) would be injected 2-5 times, and then one row (microwells 7-9) would be injected 4-10 times. Additionally there was still concern about possible crosstalk between microwells. It was further contemplated that any crosstalk problems would be easiest to detect in the thicker sensor material. Therefore, following the hydration test, a thickness test was completed. For the thickness test, the entire array was measured ratiometrically with the LPL method. Additionally, at each oxygen concentration point, an aperture was applied to select microwells. The microscope was equipped with an aperture that would limit the illumination area from the excitation source. Most fortuitously, the excitation area at minimum aperture size coincided with the microwell size, for the 3x3 glass chips in fused silica. By isolating a single microwell in this manner, any crosstalk issues should have been detectable. Typically, the aperture was applied to microwells 2, 5, and 8, so there was a sample from each degree of thickness in sensor material.

In Figure 36, the result of the thickness testing is provided.

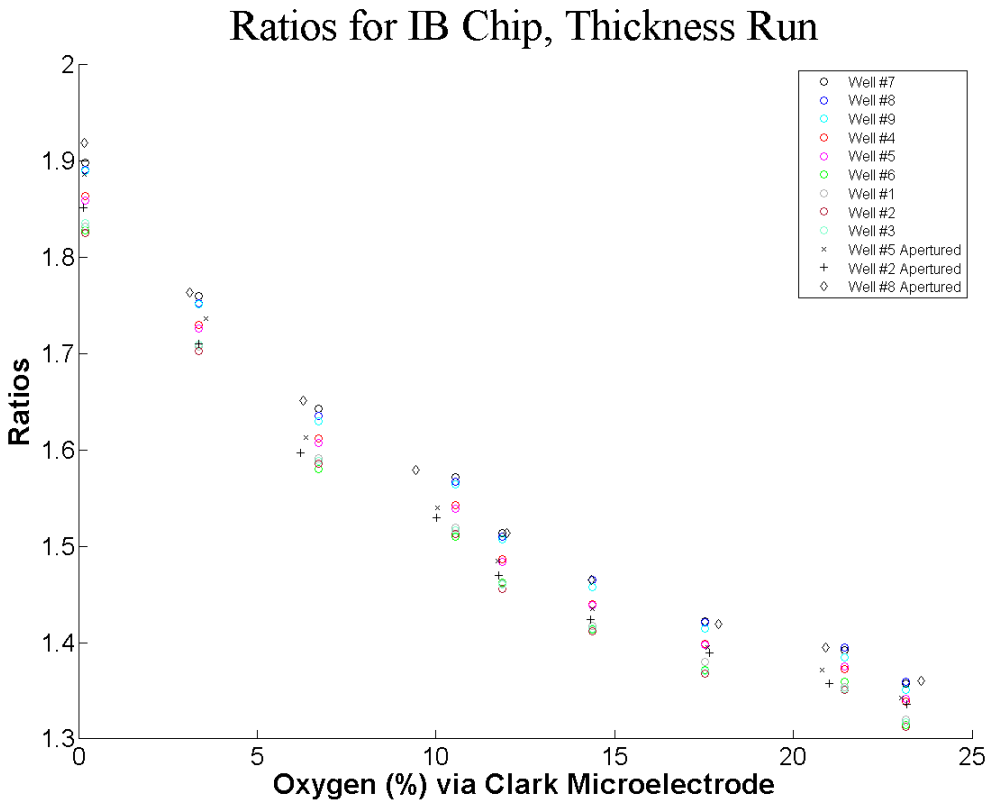

Figure 36: Thickness Data for the Wetted IB Sensor

All the ratiometric data points seem to cluster in groups. If we study the clusters, we see that microwells 1-3 are clustered, microwells 4-5 are clustered, and microwells 7-9 are clustered. The exception would appear to be microwell 6. However, that microwell had a defect that allowed spillage around the edge, which the ring finding algorithm responded to. Therefore, the sensor material that was actually measured consisted of a lot of spillage and was much thinner. It then would appear that thickness does affect the ratiometric response, though that effect is not very substantial. We also see that the aperture data is consistent with the thickness clusters, indicating the lack of any crosstalk.

Note that there were delays between some measurements, which is why there are some deviations on the x-axis (oxygen concentration).

Now lifetime results may be examined for the IB sensor under wet conditions.

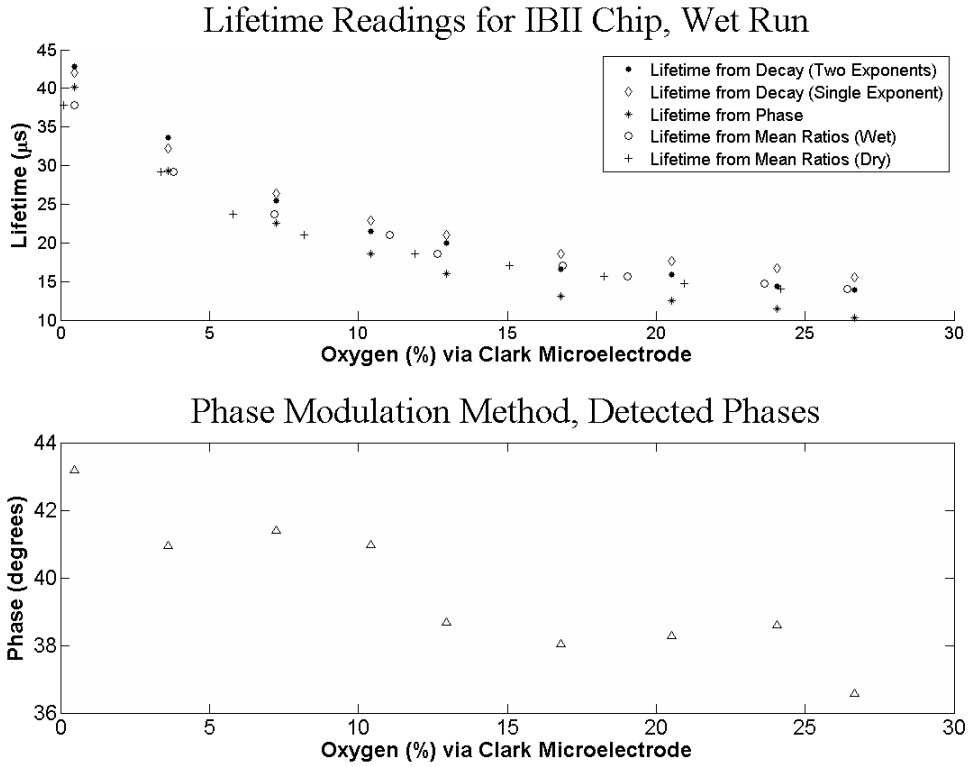

Figure 37: Lifetime Data for the Wetted IB Sensor

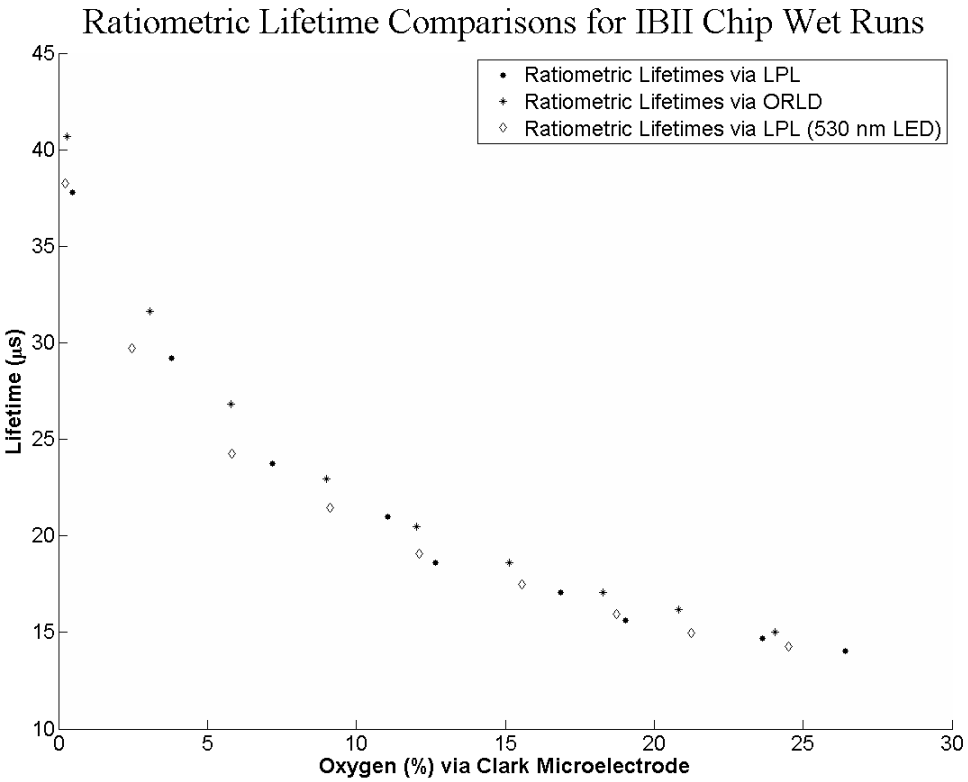

Figure 38: Additional Lifetime Data for the Wetted IB Sensor

Figures 37 and 38 display the data. More testing was completed for the IB sensor than with other sensors. The purpose of that was to verify that the LPL method was working as desired. In Figure 37, lifetime data is included for single exponential and biexponential fits to direct decay data, phase modulation data, and ratiometric data for both the dry and wetted sensors. The phase modulation diagnostic plot indicates excellent results for phase measurements. The single exponential fits and biexponential fits are similar, but the biexponential fits were more consistent with phase modulation and ratiometric lifetime data. There was also not much difference between ratiometric lifetimes obtained from the dry versus wetted sensor. Figure 38 provides additional information that was not included for other sensor materials in this study. The very

consistent data would support the idea that ratiometric lifetimes were all similar, whether from the LPL method, ORLD method, or the LPL method utilizing a different excitation source (530 nm). The reason for the latter test was to demonstrate that the autofluorescence issue had been satisfactorily resolved. Autofluorescence contamination from the optical train was only detected with the 405 nm sources.

Figure 39 then shows the raw ratiometric data, followed the by ratiometric error data in Figure 40.

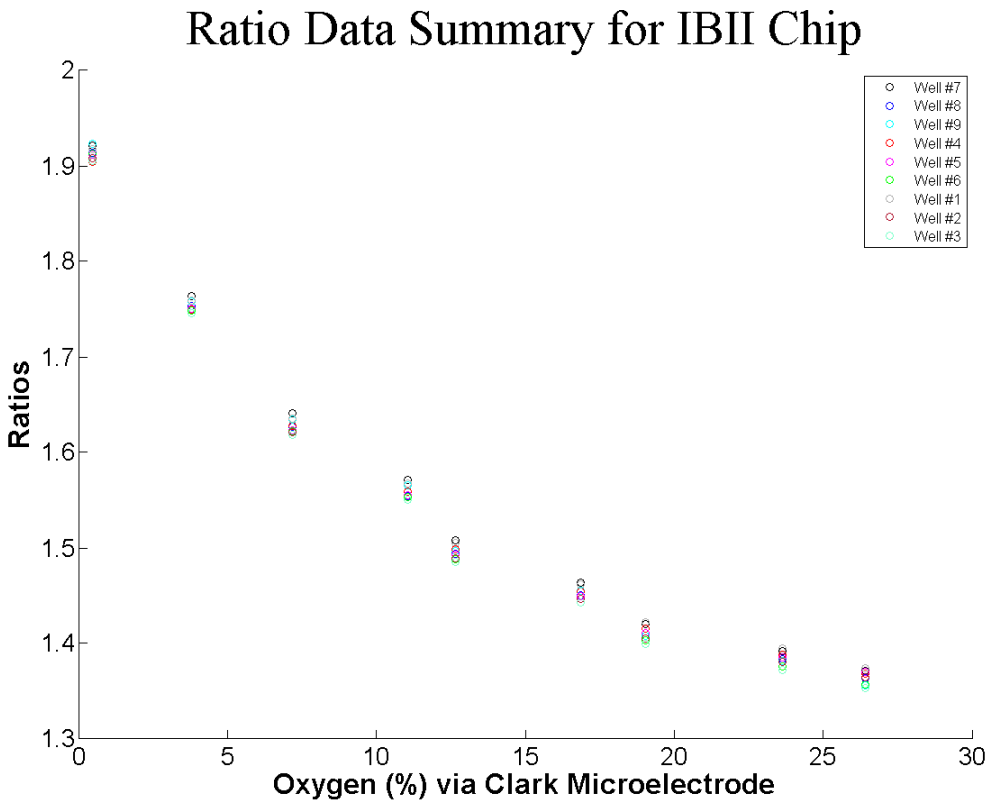

Figure 39: Ratio Data for the Wetted IB Sensor

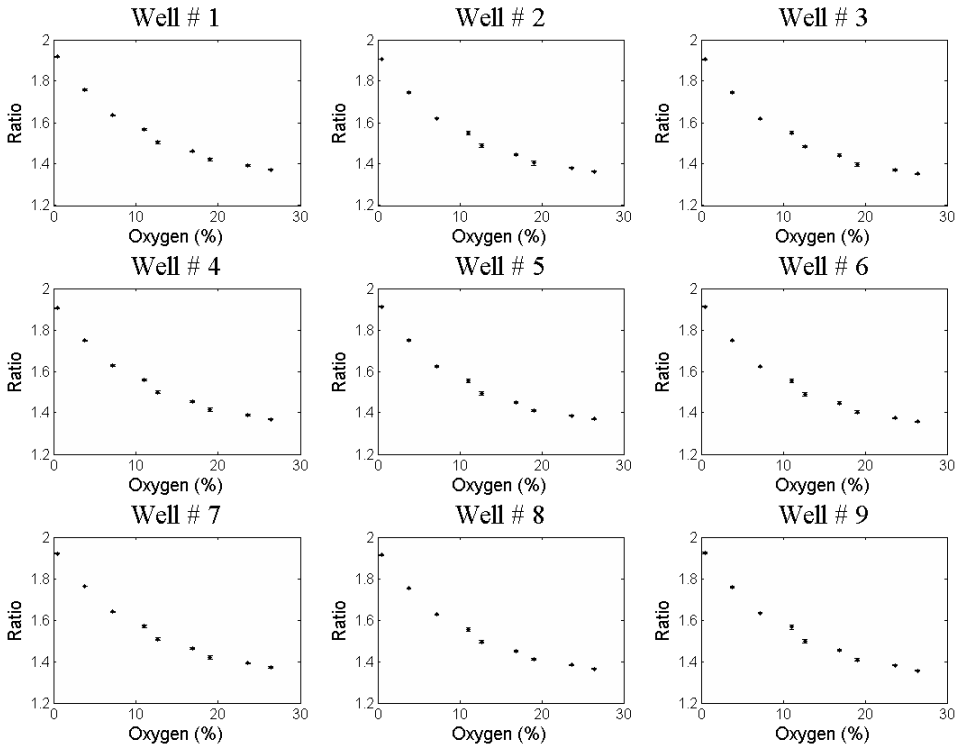

Figure 40: Error Data for the Wetted IB Sensor

Ratio data is fairly well clustered and the error bars are once again negligible. There is a suggestion of loss of monotonicity at some points, but the effect is minor. Investigation revealed that building vibrations had increased and were the likely explanation. Cushioning was added to the microscope stands and the vibration was eliminated, with improvement in the data repeatability.

Next, the Stern-Volmer response is depicted as Figure 41.

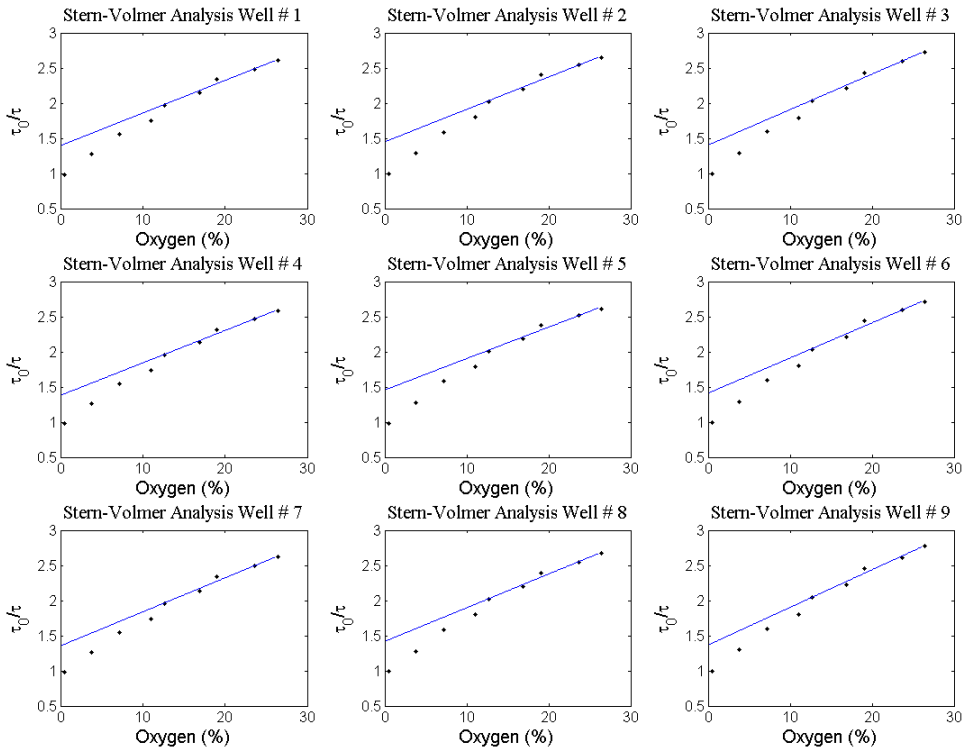

Figure 41: Stern-Volmer Response for the Wetted IB Sensor

The usual downward curvature was observed at low oxygen concentrations. The extent of deviation in a Stern-Volmer sense was also tracked as a characterization parameter. The value of the y-intercept (based upon the displayed fitted line) was determined for each microwell, and then averaged together. The deviation of this value from unity was recorded. For the IB sensor, this value was 0.41. There was no physical meaning attached to the parameter, but was simply a tool for comparison amongst the different sensor materials.

It was desirable to assess the calibration ability of the sensor materials and to examine the sensitivity of them. There are a couple of different approaches one could take for calibration. Other researchers at the MLSC had purchased bottles of premixed

gasses with various oxygen concentrations (typically 0%, 5%, 10%, 15%, and 20%) and exposed the sensor material in media solution to the premixed gas, in order to create a calibration curve. The challenge with that method is that there is no way to know precisely when the concentration is stable. Recall that the chip holder contains a volume 20 million times larger than the microwell, so it would not be unusual for workers to rush the calibration step. Another approach would be to simply monitor the concentration in the chip holder area with the Clark microelectrode. The ambient calibration point is always available, and then one would just need to obtain a stable zero reading for the second calibration point. One way around that would be to use a "virtual" zero for calibration. If the Clark microelectrode is inspected for damage regularly and intermittently calibrated to true zero, it was found that the calibration of the Clark microelectrode was a much quicker process. A typical sensitivity for the Clark microelectrode was on the order of 0.02 $\%O_2$/pA. Therefore, an error in the zero reading of 50 pA would be needed to skew the oxygen concentration readings by 1% O_2, which is why the concept of a virtual zero (i.e. the most recent reading) was used at times. From that point, a calibrated Clark microelectrode was utilized with the mass flow control system to set any desired calibration point for the sensor material. The advantage of this method, was that the signal from the Clark microelectrode need only be stable for the duration of the collection of ratiometric data (~50 s for 5 data points for each calibration point). It was much less challenging to obtain a quasi-stable signal than to have to wait for a completely stable signal.

The Clark microelectrode and mass flow control system was utilized for a static calibration, much like the method with the bottled gasses. Another approach was to

perform a dynamic calibration. For that method, a starting point (typically 22% O_2) was set with the mass flow control system. Then software control would automatically ramp down the oxygen percent at a slow rate and ratiometric data would be collected about every five minutes (3 data points at each interval). The slow ramp down would continue to any level, but was most often 8-9% O_2. The method was effective, but we shall see in section 4.9 that static calibration was even better. However, dynamic calibration was an effective tool in which to do a comparative analysis of sensor sensitivity. In Figure 42, we see the individual calibration plots for the IB sensor material.

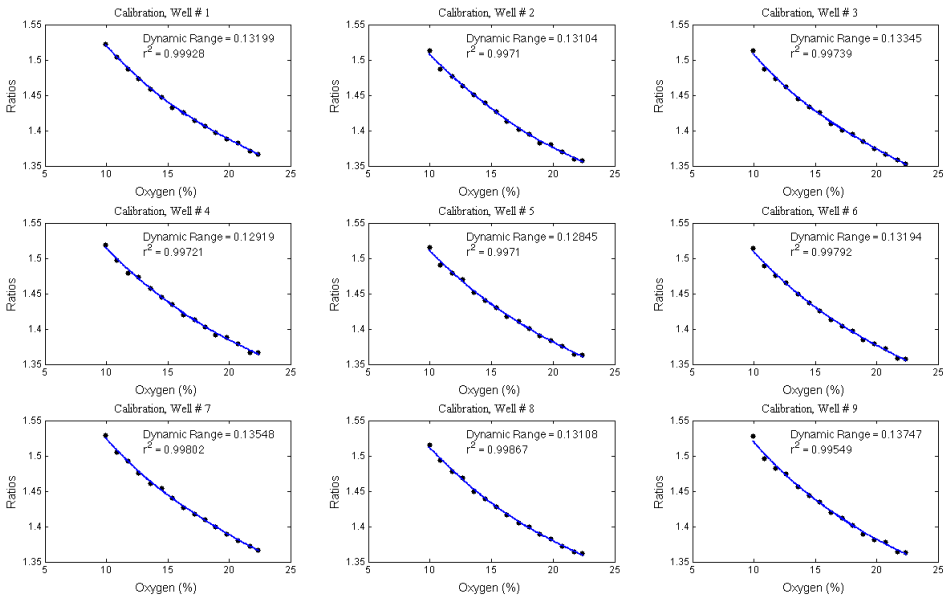

Figure 42: Dynamic Calibration for the Wetted IB Sensor

The response is clearly nonlinear and a special fitting method was chosen from the Matlab library for these curves. The plots also display the coefficient of determination (r^2) and the dynamic range for each microwell (10% to 20% O_2), with the dynamic range reported in terms of ratios. The ratiometric data is not linear, so should not be fitted with straight line. A polynomial fit could be done and will be done for later calibration

studies, but it was desired to bias the fit in favor of a given sensor material, without being held to a specific model. A smoothing piecewise polynomial fit was chosen from the Matlab library to fulfill these needs. With that fit, a piecewise polynomial is constructed from the data and smoothed according to a smoothing parameter that may be varied between 0 and 1. When the smoothing parameter is set to 0, the fit is completed in accord with a classic least-squares model for a linear fit. When the smoothing parameter is set to 1, the fit is completed as a cubic spline. A cubic spline fit will always provide a perfect fit to any given set of three points, since a third order polynomial is the lowest order polynomial that can accommodate curvature and inflection across three data points. A perfect fit means that every data point is connected and the coefficient of determination is exactly equal to one. The Matlab function would perform the cubic spline fit in piecewise fashion to every increment of three data points, including smoothing between sets of three data points. The data was analyzed by starting with the smoothing parameter set to 0. It was then increased in steps of 0.05 until the residuals plot appeared random. Four steps was the most utilized in any sensor for this study and for the IB sensor material, the smoothing parameter was set to 0.20 (four steps). See Figure 43 for the residuals plots for each microwell.

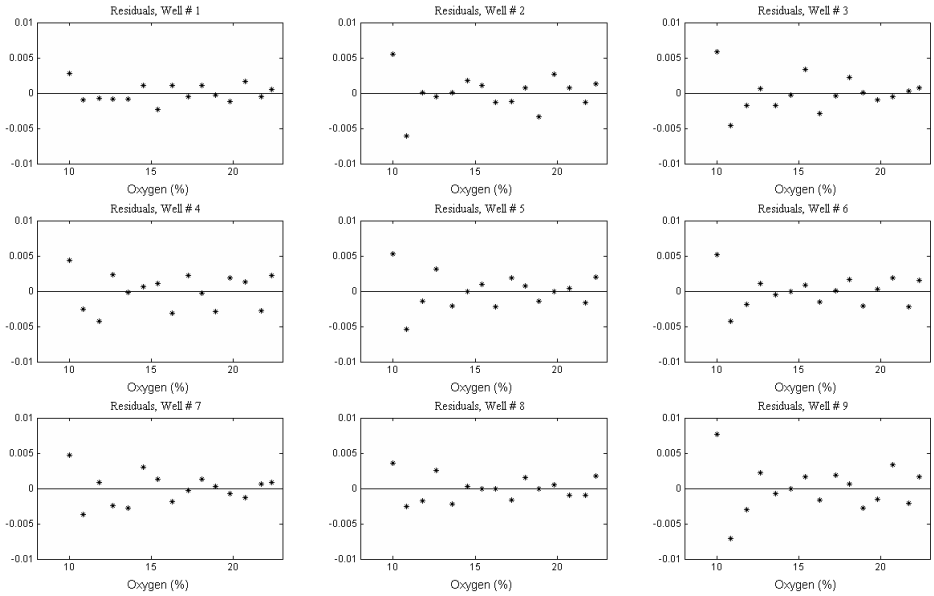

Figure 43: Residuals for the Wetted IB Sensor

No physical interpretation should be ascribed to this method. The method was chosen as a reasonable way to bias results in favor of any given sensor, but in such a way that sensor-to-sensor comparisons would be reasonable.

Additional statistics were gathered for the sensor material at this point. While Figure 42 displays the dynamic range in terms of ratios, expressing that in terms of lifetimes would have more meaning to the end user and be more relevant for any manuscripts submitted for publication. The focus on the biologically relevant range of 10% to 20% oxygen was retained. The fitted model was utilized to calculate a mean lifetime for these two oxygen concentrations, and then finding the difference. It was also of interest to report this dynamic range with an analysis of the propagation of errors accounted for. The generally accepted NIST rule[80] for error estimation by finding the root-mean squared sum of products of partial derivatives and standard deviations was

employed, to obtain the error (standard deviation) for each lifetime value. Then the two lifetime standard deviations were summed, also in a root-mean squared sense to obtain the total error. Therefore, a partial derivative of equation 2-29 was needed:

$$\frac{\partial}{\partial \tau} = \Delta t \frac{e^{-\Delta t/\tau}}{\tau^2} \tag{4-1}$$

One may also argue that the error in Δt must be accounted for. The partial derivative of equation 2-29 with respect to Δt will always be close to unity, so only the standard deviation in Δt would be important. That was not specifically tracked within the collected data. However, variation would arise from jitters within the LED pulse and jitters within the camera gating. Recall that the gating was shifted slightly in order to avoid end effects with the LED pulse, so only the gating jitters are important. The gating jitters would depend upon the internal delay generator within the camera, which was very, very good. According to the specifications, jitters would be less than the minimum gating resolution of 25 ps. That is six orders of magnitude less than the measured lifetimes, so would only contribute a small portion to error and could be safely ignored. For the IB sensor, we can therefore report the dynamic range over the region of interest as 4.6783 ± 0.0026 μs.

An additional comparative statistic was desired for this study. The dynamic range gives a strong sense of the sensitivity of a sensor material and the error propagation analysis gives an indication of measurement precision. With the models incorporated thus far, it might be challenging to compare sensor sensitivity, so a sensitivity parameter was created. There was a desire to account for dynamic range and variation over the range of interest. Therefore, a sensitivity parameter was created that was simply the ratio of dynamic range to the product of the range of interest (10% for this study) and the

standard deviation of the lifetimes from the wet run; the percent sign was ignored to keep the parameter dimensionless. For the IB sensor, we obtain a value of 1.75. The sensitivity parameter will thus be maximized for the largest dynamic range and smallest standard deviation, both desirable features of a given sensor material.

Another important issue to consider with each sensor was photodegradation. A sensor material that performs well would not be very useful if it is short-lived. A simple protocol was followed to quantify any photodegradation. Note that all sensors in this study were noted to degrade when exposed to the increased radiant flux density from light emitted from the 40x objective on the microscope. However, the protocol described in Appendix B provided a common method to quantitatively compare the sensors. The result for the IB sensor material is included as Figure 44.

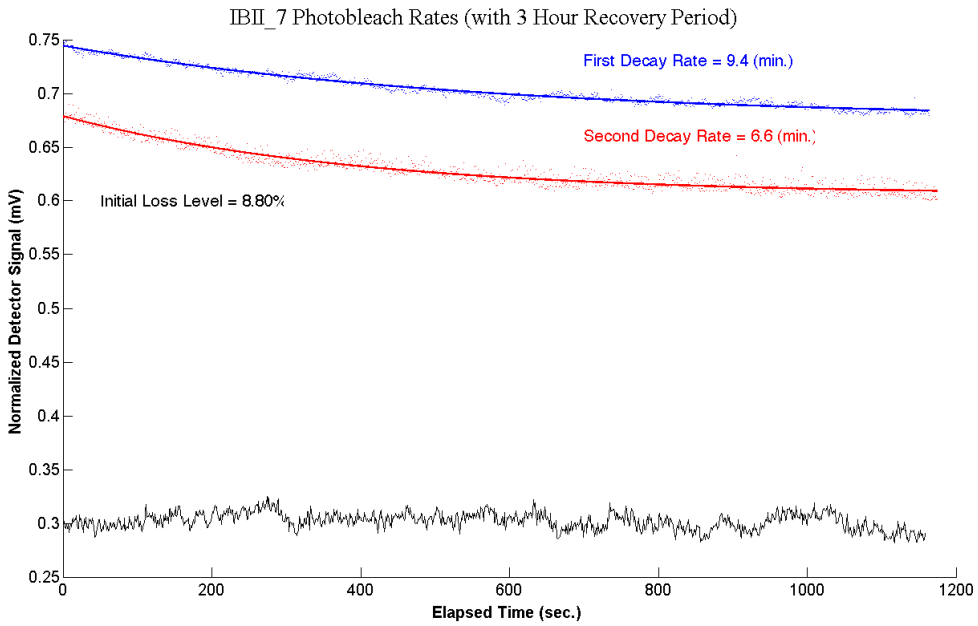

Figure 44: Photodegradation of the IB Sensor

The Figure also includes the black trace on the bottom and the other sensor materials in this study will not include that trace. That was a 20 minute exposure of a blank chip to

50% Brightness, under identical conditions as the photodegradation assessment. The purpose was to demonstrate that the measured decays were in fact due to sensor degradation, and not a thermal effect of the LED source. For the IB sensor material, we see that photodegradation appears to be permanent, and that the rate of degradation increased from the first trial to the second trial.

The radiant power from the LED may also be of interest in regards to photodegradation data. The previously described model PM100 light meter was utilized for this purpose. The LED was rated to produce a maximum radiant output of 1800 mW, at 100% brightness setting. The optical train within the microscope contained multiple optical components that would reduce this. The fact that a narrow bandpass filter was used on the LED to limit the autofluorescence problem, would also substantially reduce the radiant power. The PM100 probe was utilized by placing just above the 10x microscope objective. The objective was focused to fill the PM100 sensor area with light. Readings were obtained in increments of 10%, from 10% to 70% brightness setting, for continuous illumination. The PM100 meter was not capable of pulsed measurements, at the frequencies utilized in this study. A calibration curve was constructed from a classic least squares fit. The calibration formula was:

$$P = 0.06886(\%BS) - 0.01714 \tag{4-2}$$

P represents radiant power in mW and *%BS* is the brightness setting (%) for the LED. The residuals were not quite random, indicating a linear model may not be appropriate, but an r^2 value of 0.99926 and a linear appearance of the data supported this model as close enough for the purpose at hand. Since the PM100 sensor was filled and its area was

defined, we may also use equation 4-2 to report a radiant flux density for the photodegradation experiments as 3.43 mW/cm^2.

Delamination was also an issue. This refers to the propensity for some sensor materials to lose adhesion to the glass chip. Not only would loss of sensor material result in decreased signal, but the large departure from circularity in a delaminating sensor ring would wreak havoc with the ring finding algorithm. Therefore, it was important to attempt to quantify the time to delamination for this study. Delamination during actual experiments always followed repeated trials where the glass chip was pressed with the glass lid. A method to try and duplicate that process was attempted, but the glass lids were simply too fragile to stand up to the rigors of repeated trials. An alternative method

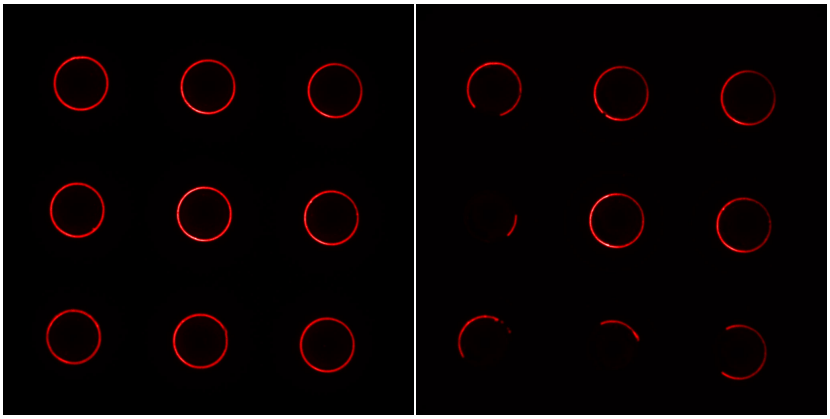

Figure 45: Delamination of the IB Sensor. The left picture shows an array prior to the delamination test. The right picture shows the same array after 62 total minutes of sonication time. Several microwells have begun to show delamination of sensor material.

was developed and is described in Appendix C. The rating for the IB sensor material was 62 minutes, with Figure 45 above depicting the delamination effect.

The final assessment for a sensor material was an attempt to quantify its production of singlet oxygen during operation. Much like the other characterizations throughout this study, a sensor-to-sensor comparison was desired, more than a rigorous

explanation of photophysical or photochemical phenomena. Based upon the work of Khalil *et al*,[47] it was thought that utilization of the femtowatt receiver (previously described) and turret position #3 (see Table 2) on the microscope should yield quantitative information. Several attempts were made to measure the singlet oxygen emission signal from the microwells.

The femtowatt receiver is a suitable instrument to utilize with a lock-in amplifier, as it works best with modulated signals. The sinusoidally modulated LED was utilized at a frequency of 650 Hz, with the function generator signal serving as reference for the lock-in amplifier. All measurements were autotuned for phase matching, in order to increase signal amplitude. Based upon the literature reports, it was thought that the emission bandpass filter should discriminate the singlet oxygen emission. Some type of signal was observed from the microwells. The signal was associated with sensor material. Moving the field of view to blank glass or to another position that had been deposited with 40 nm polystyrene beads with no luminophore added, resulted in a return to baseline of output signal. However, the signal from microwells containing sensor material remained strong even under anoxic conditions. Any changes in oxygen concentration resulted in no change in signal or very small and inconsistent changes in signal.

Such behavior would imply that the luminophore within the polymer matrix produced some type of emission that had not been characterized previously, or that substantial quantities of singlet oxygen were trapped within the polymer matrix. There was no equipment for spectral discrimination available for this study, precluding further study of this effect. However, one key piece of information was observed. The auxiliary

oscilloscope never gave an indication of a valid lock for the signal from the microwells. Placing a much larger volume of sensor material on the flat, backside of a glass chip produced much thicker regions that were also brighter. The brighter signal did produce the valid lock-in signal on the auxiliary oscilloscope. It was also noted that only when the auxiliary oscilloscope indicated a valid lock-in, did the emission signal produce a result consistent with expectations. The intense overall signal was always present, but small changes with oxygen concentration did produce changes consistent with the idea that an increased level of molecular oxygen should also increase the production of singlet oxygen. We should also note that a valid signal was only obtainable from the 40x objective.

The singlet oxygen emission for the IB sensor was assessed in accord with the procedure in Appendix D. The result is included as Figure 46.

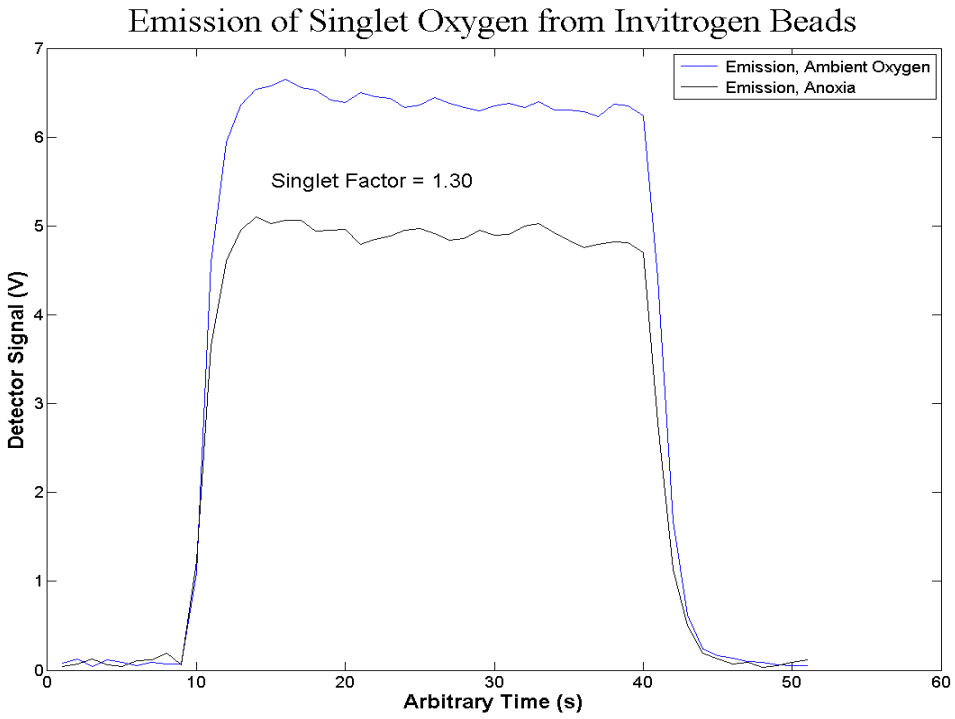

Figure 46: Singlet Factor for the IB Sensor

Note that there is a slight downslope to the data, indicative of photodegradation. It was observed that all sensors could exhibit increased photodegradation while exposed to excitation light from the 40x objective, as compared to exposure to excitation light from the 10x objective. Given that photodegradation was apparently enhanced for these measurements and that no satisfactory explanation was developed for the observed behavior of the majority of the signal intensity, the quantitative "singlet factor" should be viewed with skepticism. The singlet factor will be reported for all sensors in which an assessment was possible, but further studies would be needed to determine its validity.

4.4 Characterization of the ANH Sensor

This sensor material was prepared by the Alex Jen Group at the University of Washington. The sensor is a custom made bead type utilizing platinum (II) 5,10,15,20-tetrakis(pentafluorophenyl)porphyrin as the luminophore (Pt TFPP in our shorthand notation). The structure is shown in Figure 47. The bead size and concentration in water were reportedly similar to the specifications utilized for the commercial beads. These custom beads were prepared in a substantially different manner than for the commercial beads. The luminophore was dispersed in a polymer support of poly(methyl methacrylate), which was then overcoated with polystyrene. The intention was to hold the luminophore within a hydrophilic matrix, but protect it with an oxygen permeable polymer that was known to be

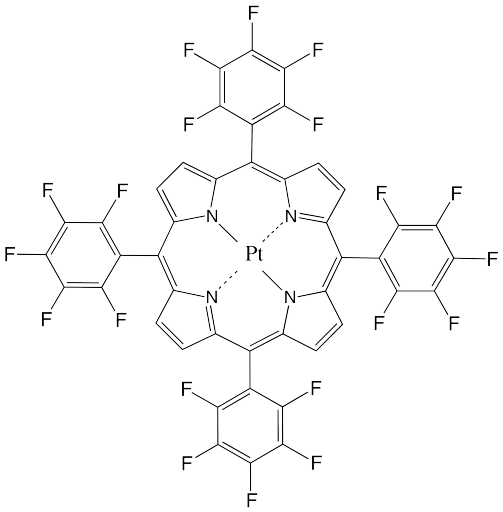

Figure 47: Pt TFPP Structure

acceptable to the biologists. The motivation for that was to prevent leaching of the luminophore. The sensor material appeared as a bluish-gray opaque dispersion, so it is likely that the non-leaching goal was achieved (recall the commercial beads appear as a pink dispersion). At the time, there was potential interest with intracellular oxygen measurements in addition to the extracellular oxygen measurements that had been completed. That motivation waned over time, especially when this sensor material was too weak to function with the ORLD method. Later development of the LPL method allowed for its characterization.

Figure 48 shows the spectral response for the sensor.

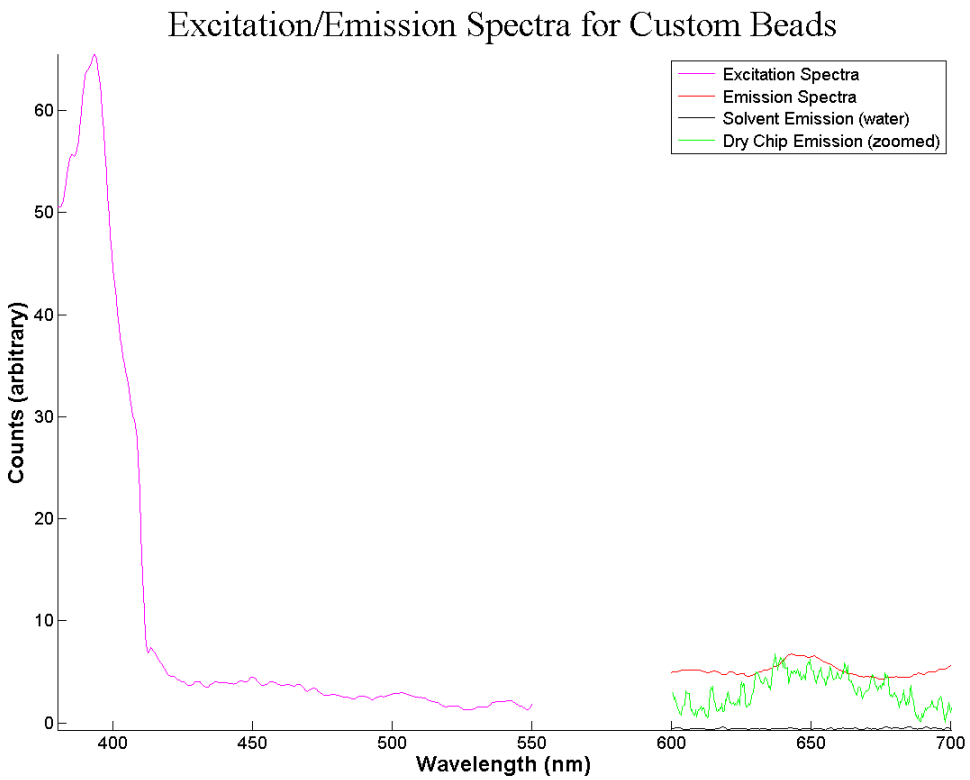

Figure 48: Excitation and Emission Spectra for the ANH Sensor

The spectra were difficult to obtain as the sensor material produced very weak emission signals. The excitation spectrum shows a strong Soret band, but one or two Q bands that

are very weak are also visible. The emission spectra do show the usual peak near 650 nm, but the measurements on the microscope were especially challenging. No wet emission spectrum was obtained on the microscope for reasons that will be explained shortly.

Much like the commercial beads, the ANH sensor material was best injected in a 1:1 dilution with deionized water. The picoinjection conditions were 155 kPa inject pressure for 30 ms, with no balance pressure, and utilizing the TTAW method. It was also necessary to inject each microwell two times, in order to fill it. The results were not as good as the commercial beads with spillage common, and maddening amounts of clogged tips. This sensor material was cured just like the commercial beads; 160 °C for 30 minutes in a tube furnace. Note that the sensor ring size was optimized to 62 x 71 pixels, which corresponds to a sensor ring width of approximately 10 μm. A chip for singlet emission checking was also prepared by pipetting 10 μL of sensor material onto the backside of a glass chip.

A dry run was completed for the ANH sensor, with the result depicted in Figure 49.

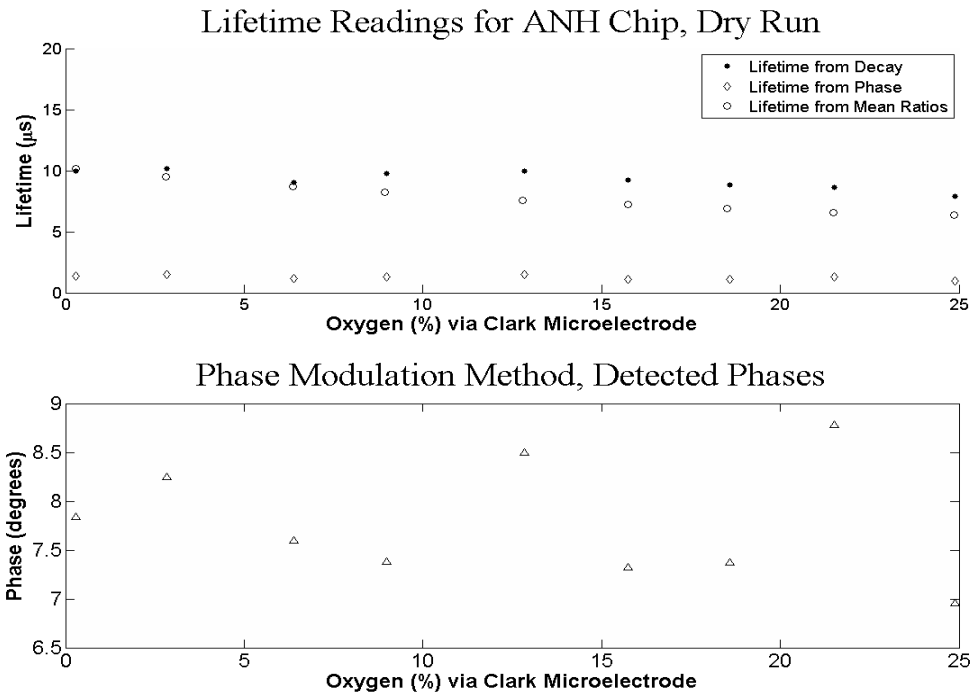

Figure 49: Lifetime Data for the Dry ANH Sensor

Here, the results were not very encouraging. The measured lifetimes were roughly 25% of the values for the commercial beads. The lifetimes from direct decay and ratiometric measurements appear very consistent, but the lifetimes from phase modulation are noticeably reduced. However, note that the phase diagnostic plot would indicate that the readings are not trustworthy. The most disconcerting feature is that there was little change in measured lifetimes as the oxygen concentration was changed.

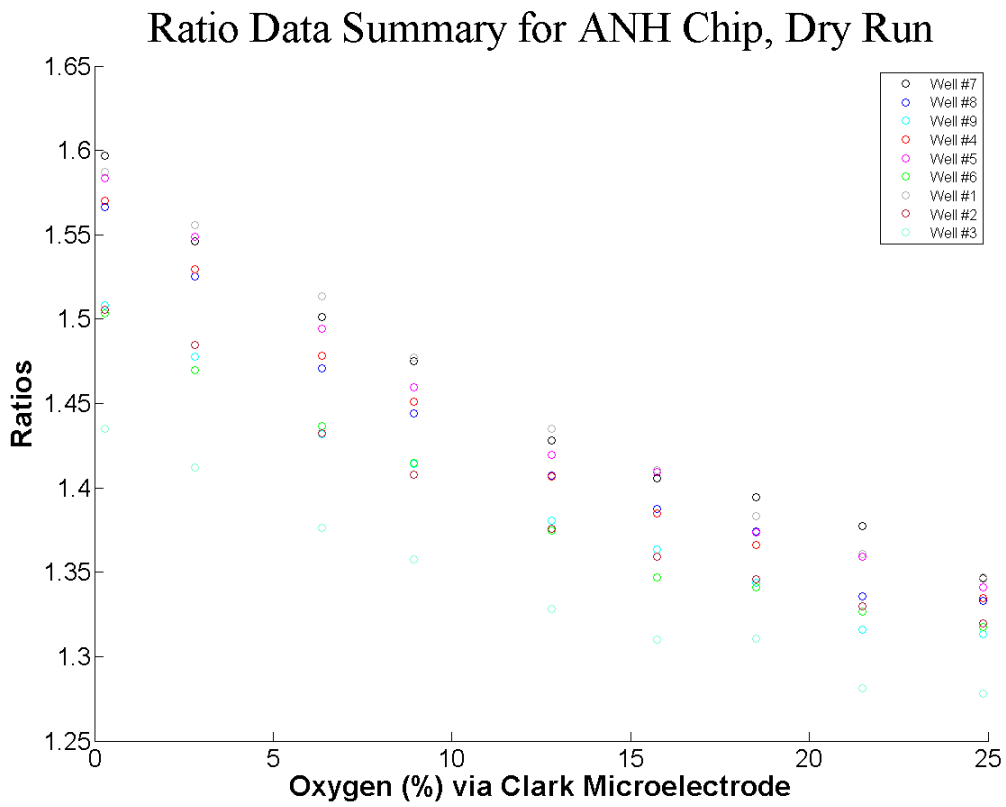

Figure 50: Ratio Data for the Dry ANH Sensor

Figure 50 might suggest that ratiometric data directly is more indicative of a change with oxygen concentration, but notice that the scale is zoomed in, so the dynamic range is really not very good with ratiometric data either. The ratio data is more spread out relative to other sensor materials, with potential clustering of some microwells that

did not appear to have an obvious explanation. It should also be noted that the sensor rings all had to be found by manual methods for this sensor material. Given the results thus far, it was not surprising to also see that error bars were much larger than normal (see Figure 51). The Stern-Volmer response was also less consistent than usual (see Figure 52).

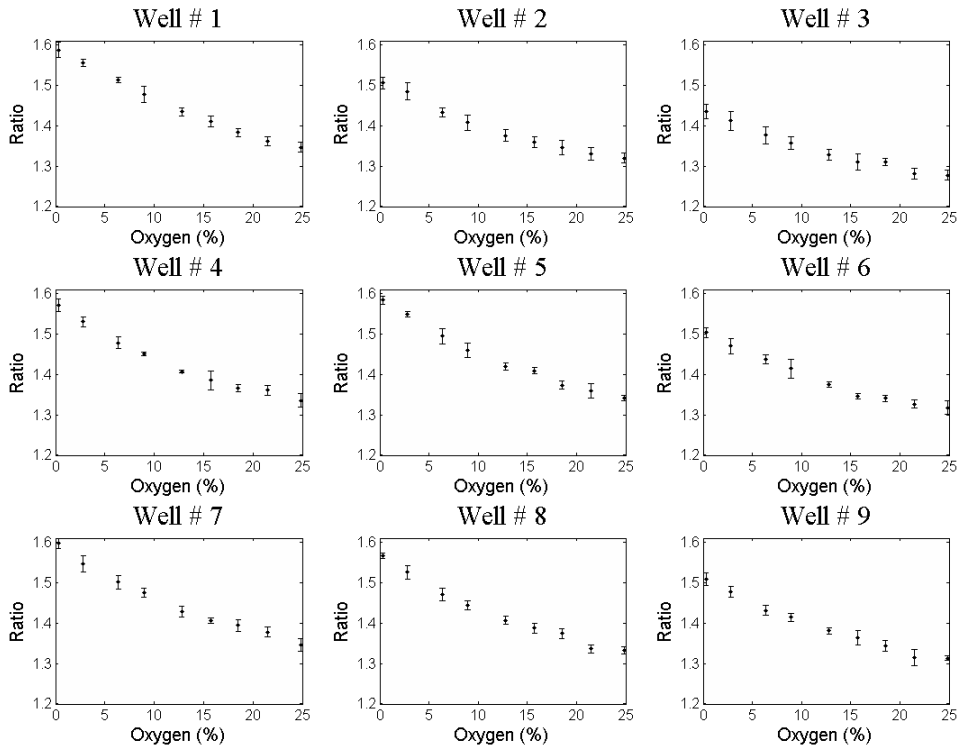

Figure 51: Error Data for the Dry ANH Sensor

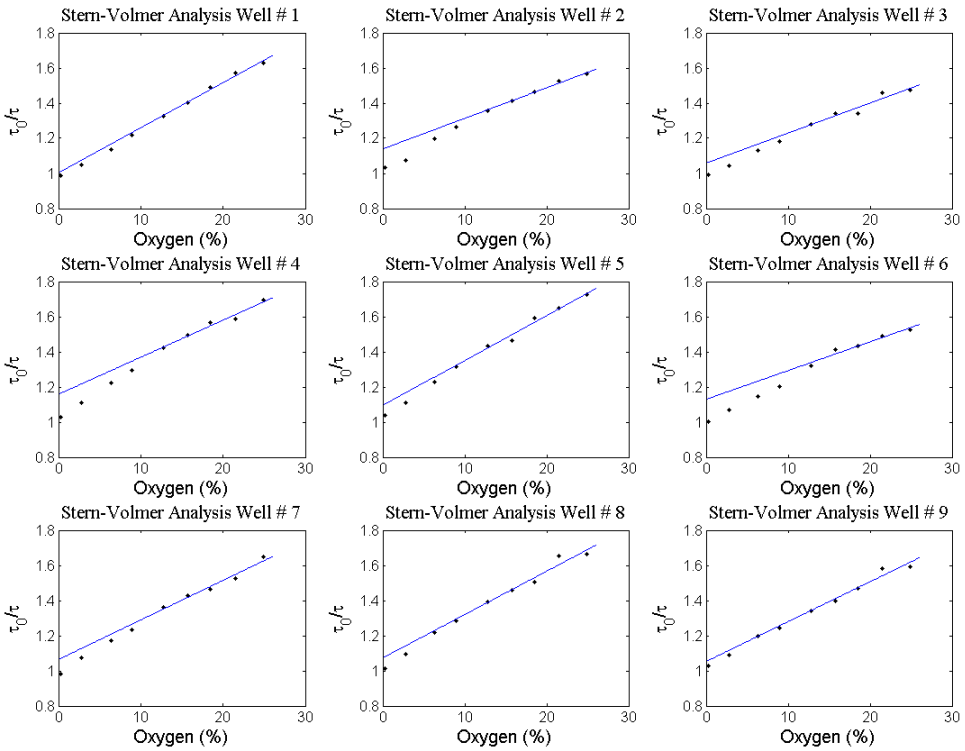

Figure 52: Stern-Volmer Response for the Dry ANH Sensor

The performance of the ANH sensor material was not very impressive, but it was contemplated that the wet response might be different. The first step was to evaluate the hydration effect. That was attempted, but failed completely. The ANH sensor material was found to disperse back into the water, before the hydration test was anywhere near complete. That was surprising, given that it was thermally cured the same way as the commercial bead sensor. However, one key difference between the two sensors was that the commercial beads were actually carboxylate modified at the surface, whereas the custom beads were not.

The result of the hydration test precluded any further testing, other than evaluation of the singlet oxygen emission signal. That test was conducted in accord with

the procedure in Appendix D. The result is included as Figure 53.

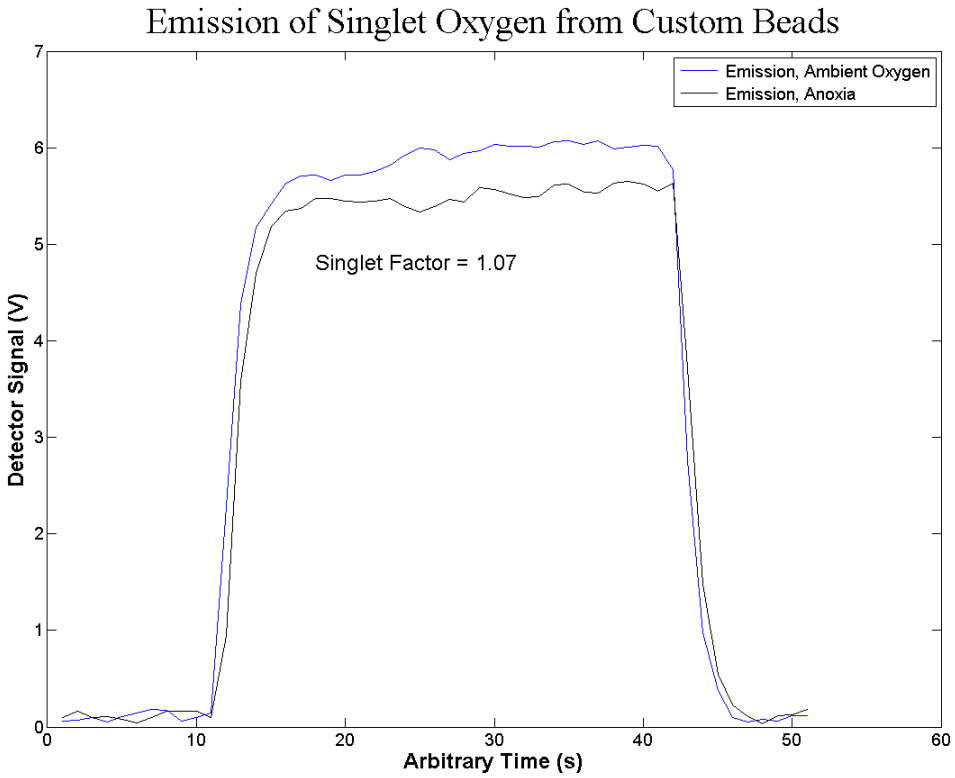

Figure 53: Singlet Factor for the ANH Sensor

Interestingly, the singlet factor was much smaller than for the commercial bead. However, the large signal under anoxic conditions was still present. It was also noted that the shape sloped upwards, which was different. Perhaps this sensor material had very limited photodegradation and was able to show a slow build-up of singlet oxygen during this experiment, was one thought that was contemplated.

4.5 Characterization of the PtF Sensor

The Alex Jen Group at the University of Washington also prepared this sensor material. It was prepared by dissolving ~1 mg of the luminophore and ~0.1 g of polystyrene in 10 mL of toluene. The luminophore was the same one used in the ANH

sensor (see Figure 47). The PtF sensor, the FB sensor, and the MOD sensor (see section 4.6) were made when interest in intracellular oxygen measurements had waned. The sensor did not necessarily have to be in bead form if only a thin film was needed in the microwells, so a luminophore was simply mixed with a polymer matrix that had been vetted by the biologists, and then mixed into a suitable solvent. The luminophore was presumed to adsorb onto the polymer matrix.

This sensor was challenging to picoinject. The method used was the TD method with inject pressure 148 kPa for 40 ms and 7 kPa balance pressure. Spillage was more frequent than for the IB sensor material. Tip clogs were also more frequent, but cleared very readily. A "bulk" chip was also made by simple pipetting of 10 μL of the diluted material onto the flat, backside of a glass chip. No curing process was employed with this sensor material as the researchers that produced it were concerned with thermal degradation. During subsequent use, the sensor ring size was optimized to 58 x 70 pixels, which corresponds to a sensor ring width of approximately 13 μm.

Figure 54 displays the spectra for the PtF sensor material.

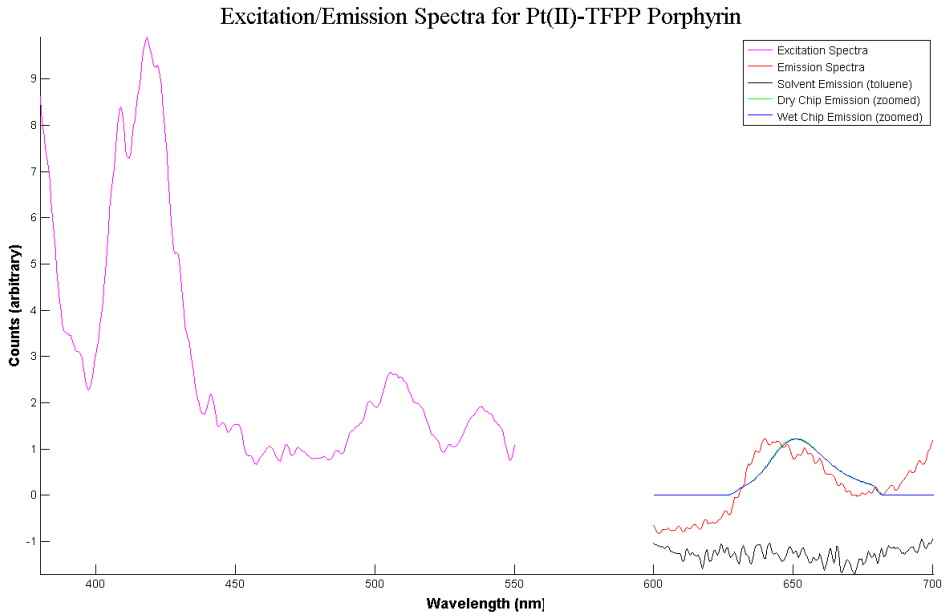

Figure 54: Excitation and Emission Spectra for the PtF Sensor

Within the excitation spectrum, the Soret band has some structure and the Q bands are clearly visible. The emission spectra in solvent appears to show more structure, but recall the resolution of the spectrometer for that spectrum was greater than the Ocean Optics spectrometer. Again, the bandpass filter is responsible for the unusual shoulder on the emission spectra from the microscope.

A dry run was then conducted for the PtF sensor material. The lifetimes from the three methods are displayed in Figure 55.

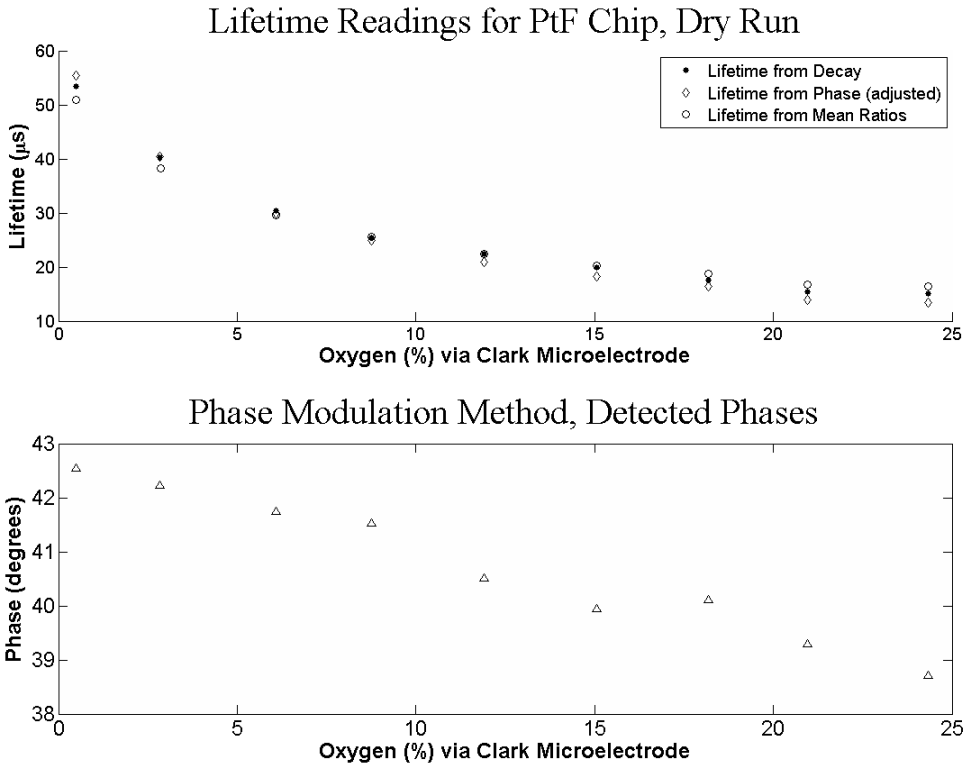

Figure 55: Lifetime Data for the Dry PtF Sensor

The data from all the methods are in a close agreement, with an overall dynamic range around 40 μs, which is improved over the IB sensor material. The phase diagnostic indicates valid phase readings. We also see very close agreement between microwells in

the ratio data, Figure 56.

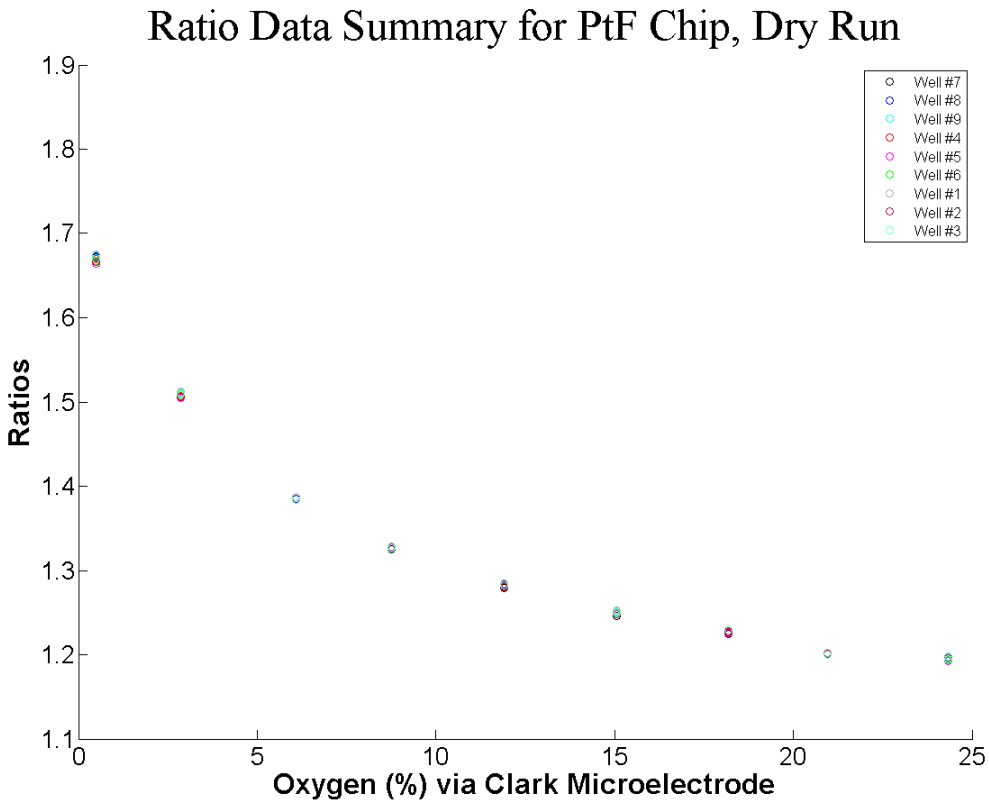

Figure 56: Ratio Data for the Dry PtF Sensor

The SNR for the PtF material was quite good and it would be difficult to improve upon the precision in the ratio data. Next, Figure 57

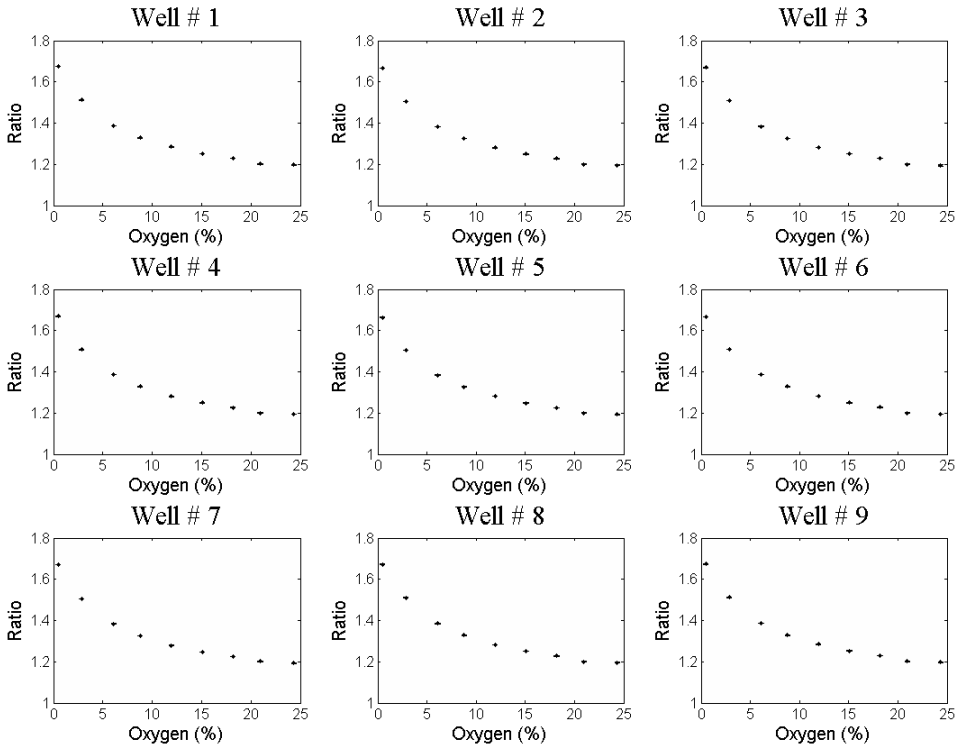

Figure 57: Error Data for the Dry PtF Sensor

shows the error bars for ratio data, which are so small as to be indistinguishable on the plot. Finally, Figure 58

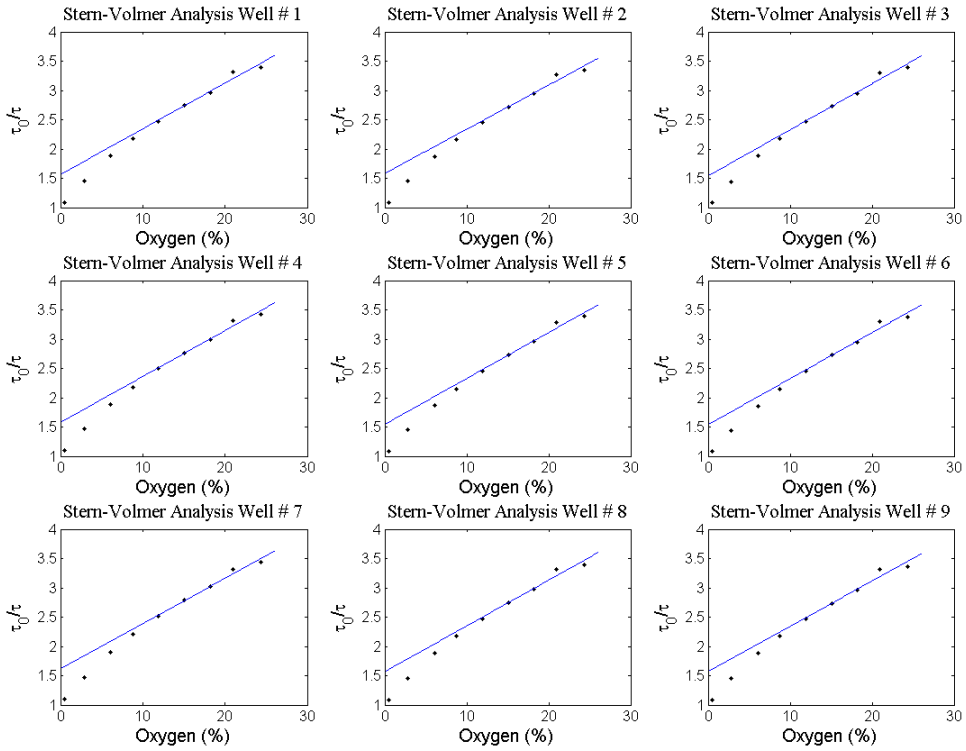

Figure 58: Stern-Volmer Response for the Dry PtF Sensor

shows the Stern-Volmer response for each microwell, which is fairly consistent. The departure from linearity is also quite clear, and in a downward direction.

The hydration effect was not very important for this sensor material. Figure 59 indicates that no more than one hour is ever needed to reach stability, for wet runs.

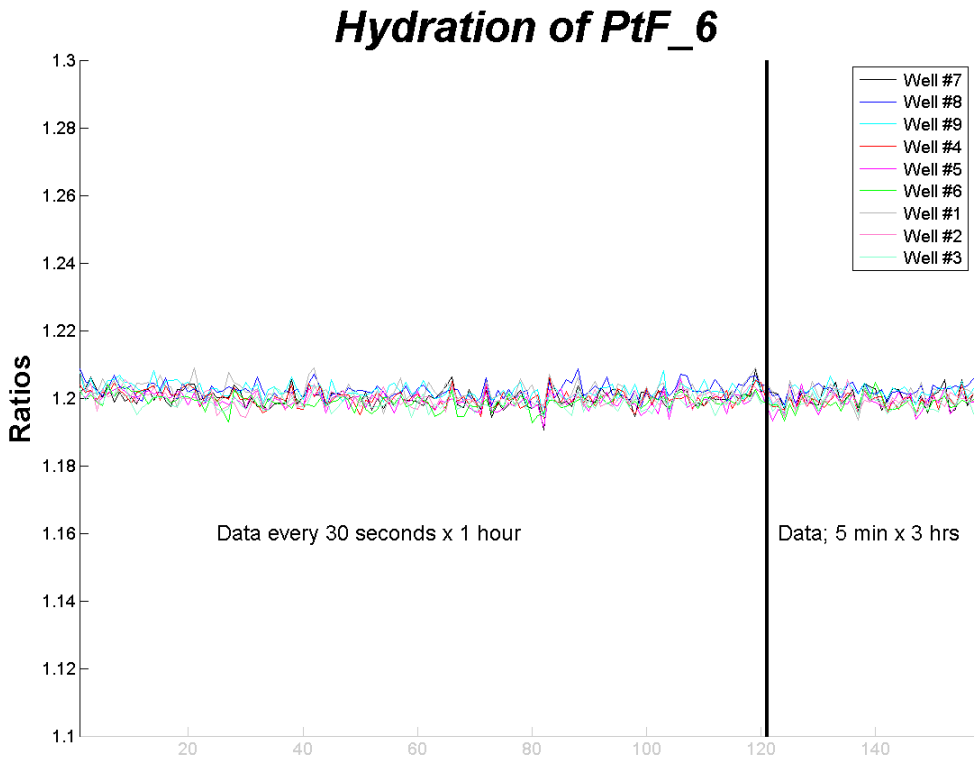

Figure 59: Hydration Effect for the PtF Sensor

There was a slight decrease in ratio data that clearly stabilized within an hour. At this point in the study, ratiometric data was checked intermittently, to avoid the loss of water issue that showed up in Figure 35. That also had the advantage of potentially stopping the experiment early, as for the PtF sensor material. Three hours into the longer part of the run, it was clear that the response was stable, so the experiment was halted.

The thickness run with aperturing is provided as Figure 60.

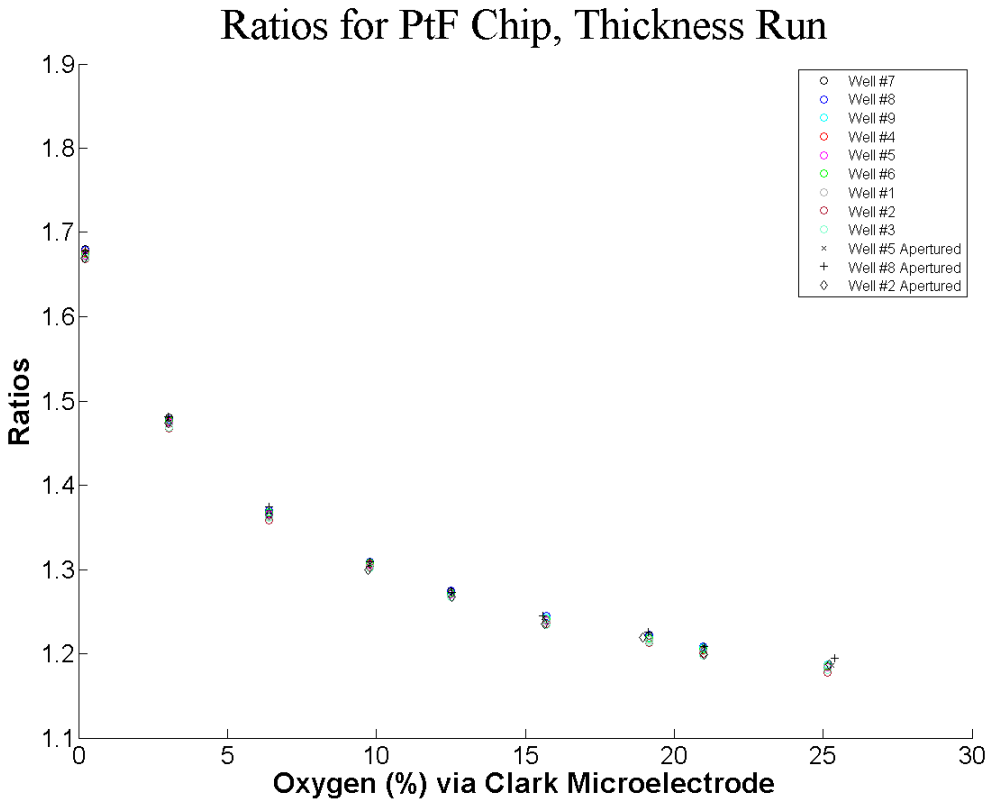

Figure 60: Thickness Data for the Wetted PtF Sensor

For this sensor material, it is very evident that sensor thickness and crosstalk were not an issue of concern, as all nine microwells are tightly clustered for all conditions. It should be noted that the picoinjection process for this sensor material was altered, as compared to the IB sensor material. The first row contained single injections, while the second row contained double injections, and the third row triple injections. The material

appeared to deposit in a thicker layer than the IB sensor material and picoinjection was much more challenging. It appeared that any further injections were simply going to create an amorphous blob of sensor material within the microwell, so were not pursued.

A wet run was then conducted for the PtF sensor material. The lifetimes from the three methods are displayed in Figure 61.

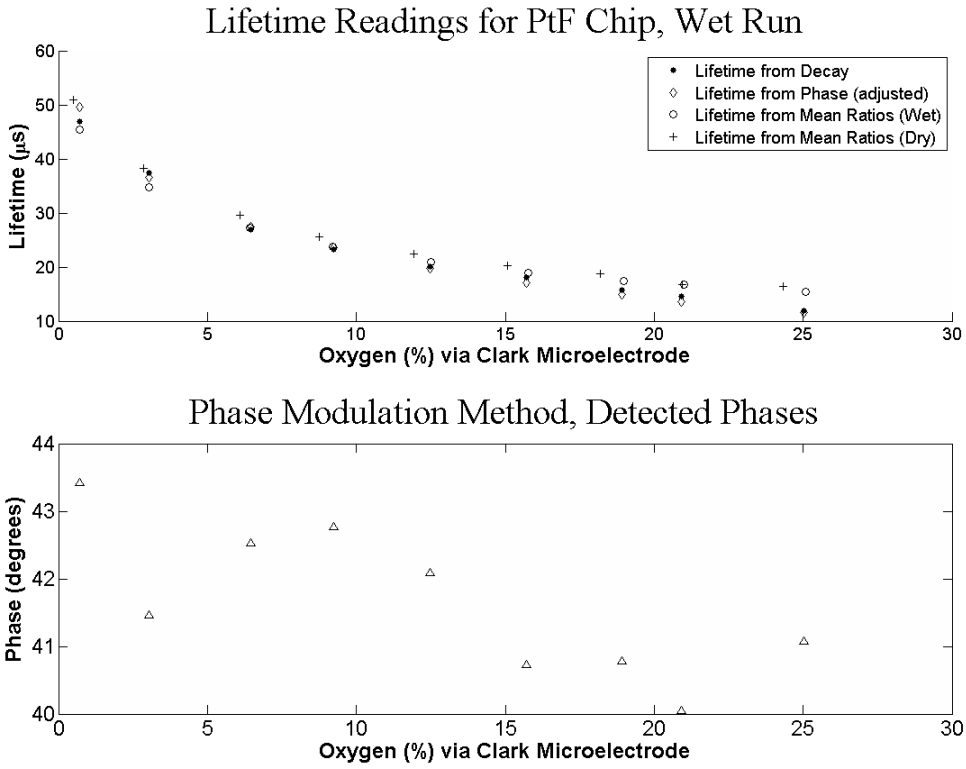

Figure 61: Lifetime Data for the Wetted PtF Sensor

The data from all the methods are in a close agreement, with an overall dynamic range around 40 μs. There was some spread in the data at higher oxygen concentrations. There was no real discernible difference between lifetimes from the dry run versus the wet run. The phase diagnostic indicates valid phase readings. We also see very close agreement

between microwells in the ratio data, Figure 62.

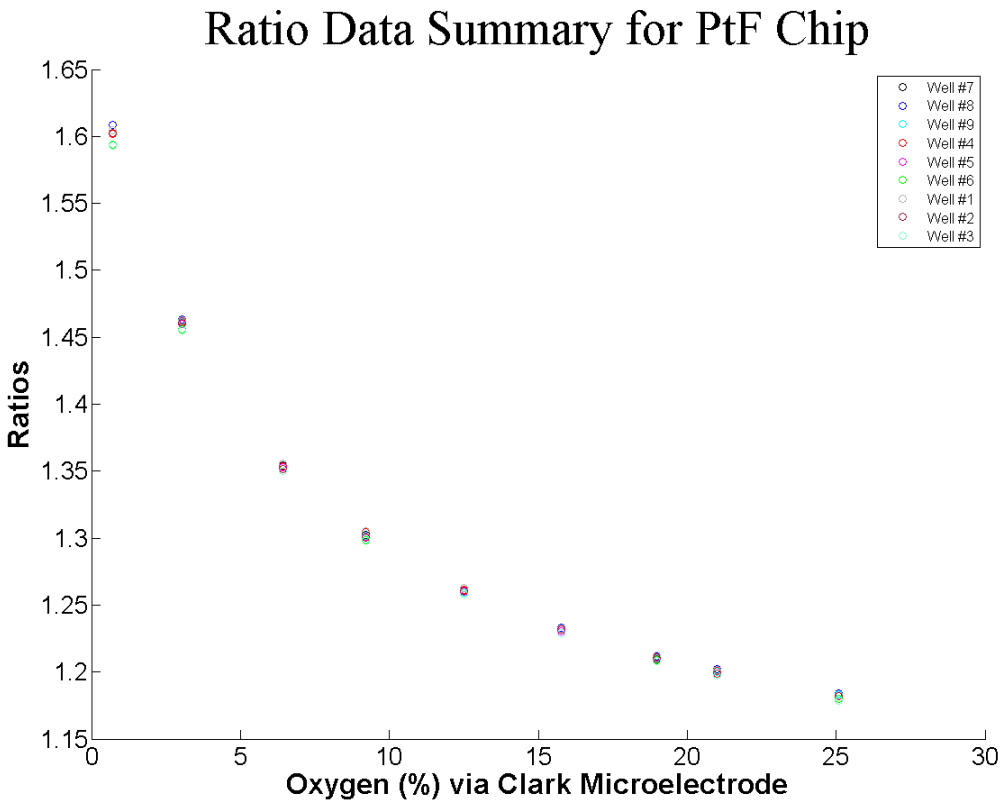

Figure 62: Ratio Data for the Wetted PtF Sensor

The precision in the data continues to be excellent, with a small amount of spread at the lowest oxygen concentration. Next, Figure 63

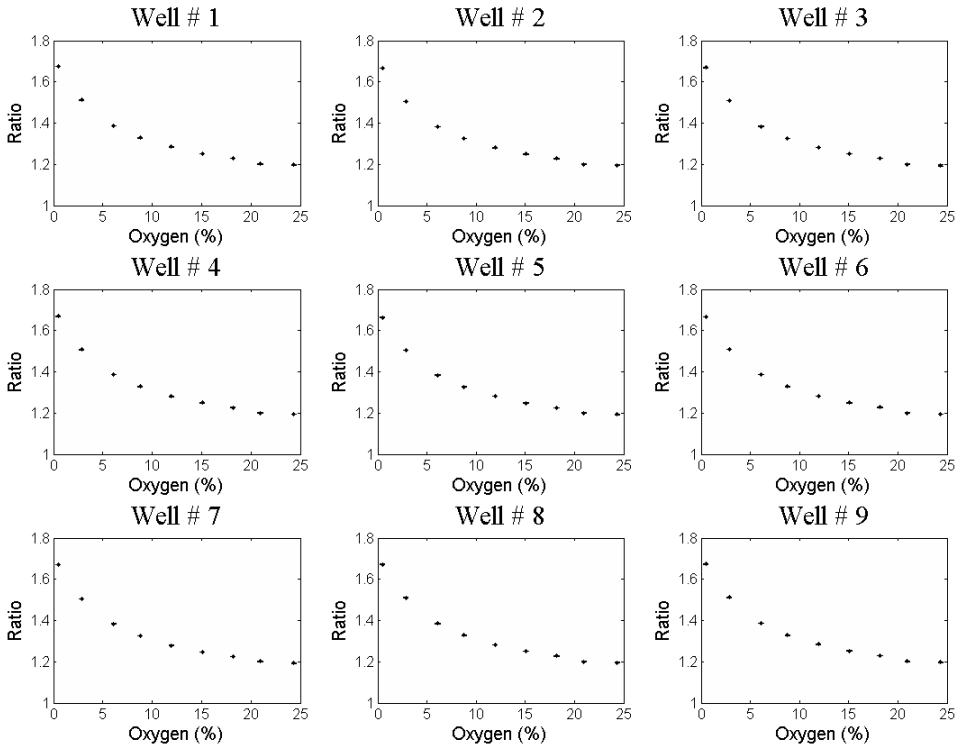

Figure 63: Error Data for the Wetted PtF Sensor

shows the error bars for ratio data, which are so small as to be indistinguishable on the plot. Finally, Figure 64

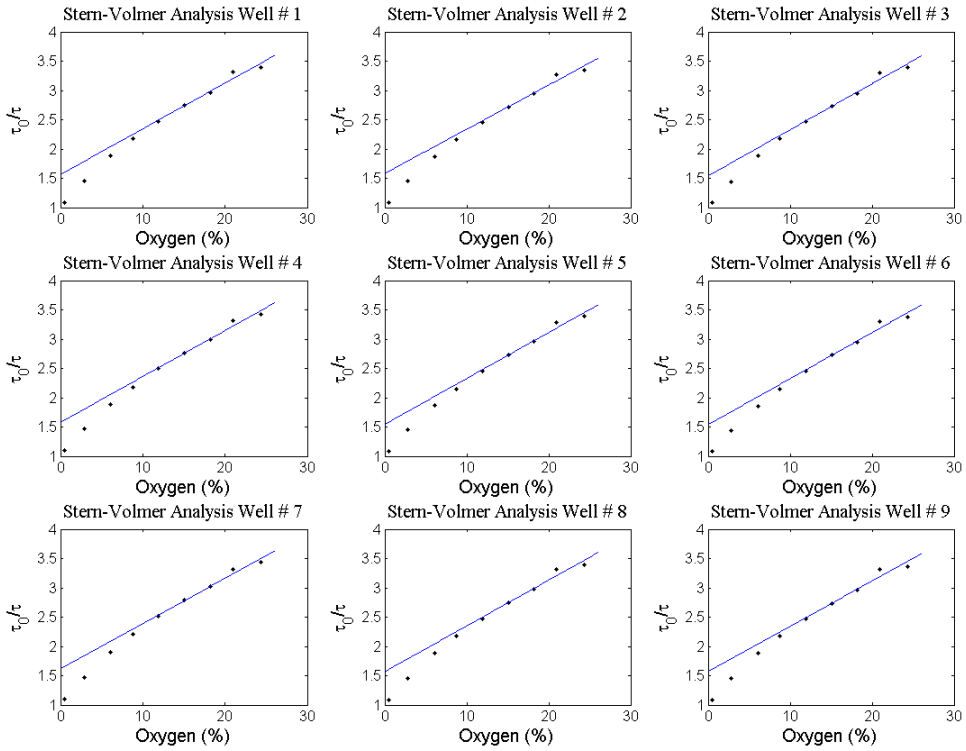

Figure 64: Stern-Volmer Response for the Wetted PtF Sensor

shows the Stern-Volmer response for each microwell, which is fairly consistent. The departure from linearity is also quite clear and in a downward direction. The overall departure from unity was 0.56, which is larger than for the IB sensor material.

Next, the dynamic calibration comparative analysis was completed. Figure 65

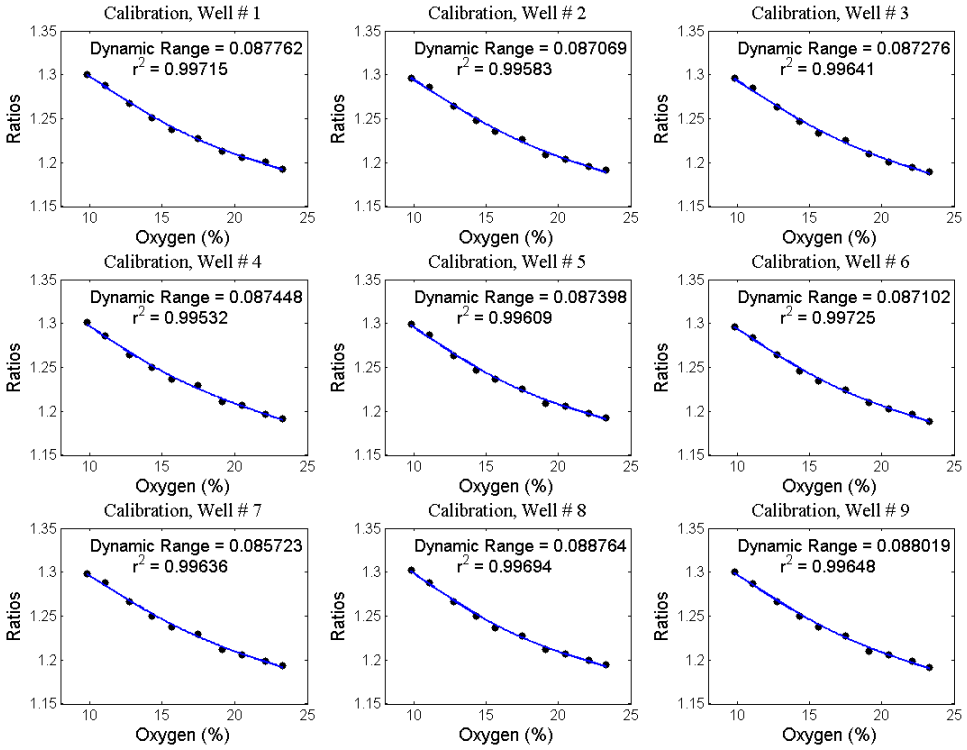

Figure 65: Dynamic Calibration of the Wetted PtF Sensor

indicated the typical nonlinear shape for each microwell. Figure 66 shows random residuals; the smoothing parameter was only 0.05 for this material.

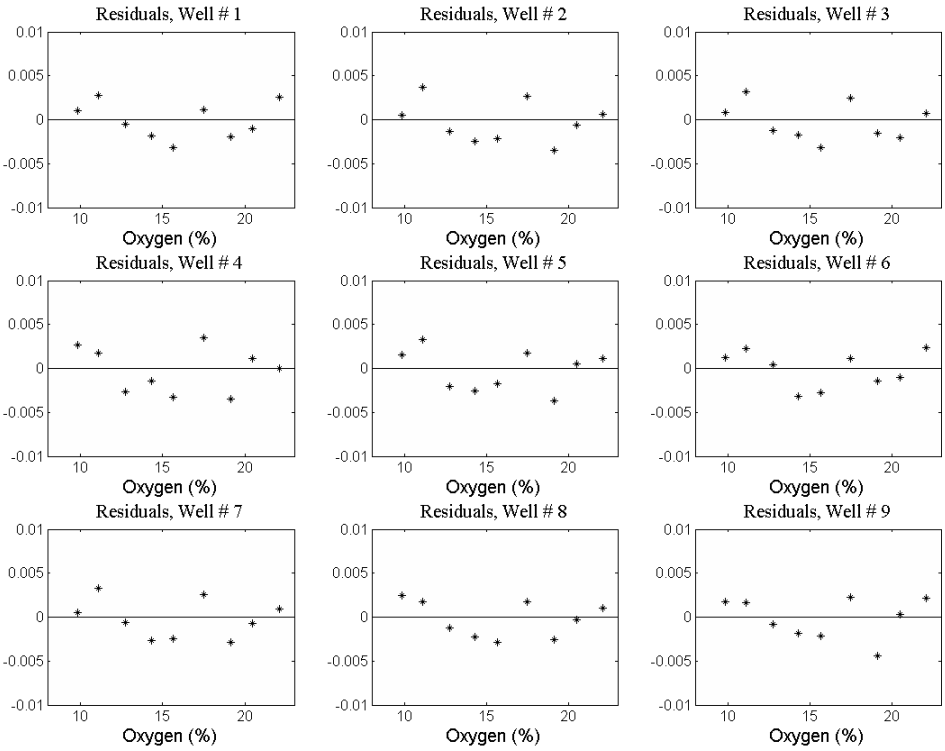

Figure 66: Residuals for the Wetted PtF Senssor

The dynamic range in terms of lifetime over the relevant range (10% to 20% oxygen) was 6.05738 ± 0.00034 μs, which was an improvement over the IB sensor material. The sensitivity parameter for the PtF sensor material was 5.35, substantially better than for the IB sensor material.

The photodegradation data is presented next. Figure 67 shows the trends.

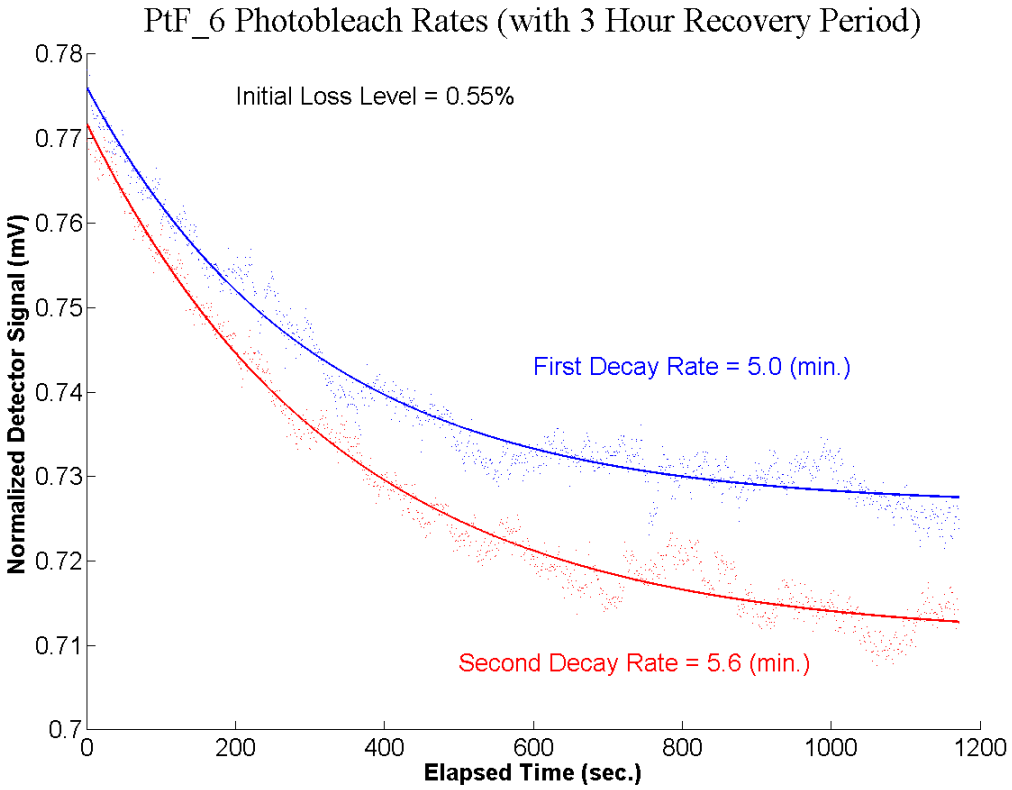

Figure 67: Photodegradation of the PtF Sensor

This material photodegraded a little faster than the IB sensor material, but it nearly returned to its initial value after the three hour rest period. This may indicate that photodegradation is more of a thermal effect, than a damaging effect. The two decay rates were also quite similar.

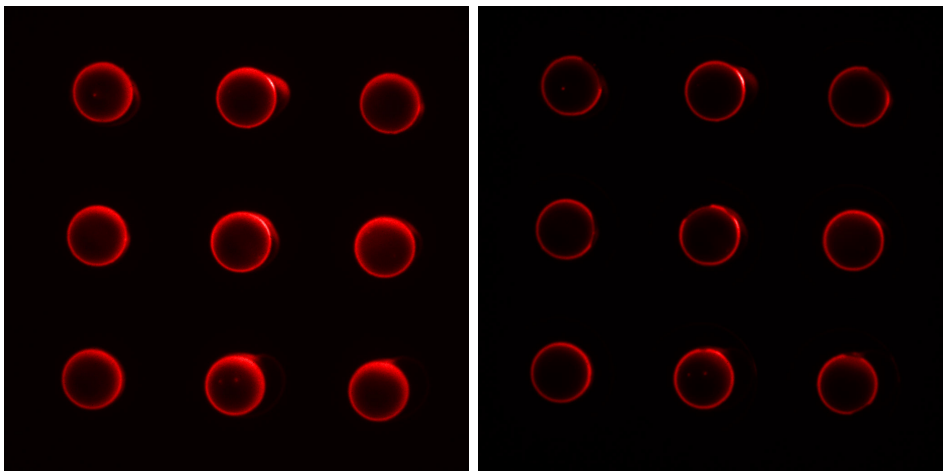

Figure 68: Delamination of the PtF Sensor. The left picture shows an array prior to the delamination test. The right picture shows the same array after 2 minutes of sonication time. Several microwells have begun to show thinning and some delamination of sensor material in small regions.

The delamination test did not go very well for the PtF sensor material. It delaminated very quickly, with a rating of only 2 minutes. Figure 68 shows the result. A thermal cure may help this material adhere to the glass chip. The delamination was not as obvious as with the IB sensor material, but the figure above certainly shows overall thinning and mild loss of material on some of the microwells.

The final characteristic for this sensor was the singlet emission evaluation. The result is shown in Figure 69.

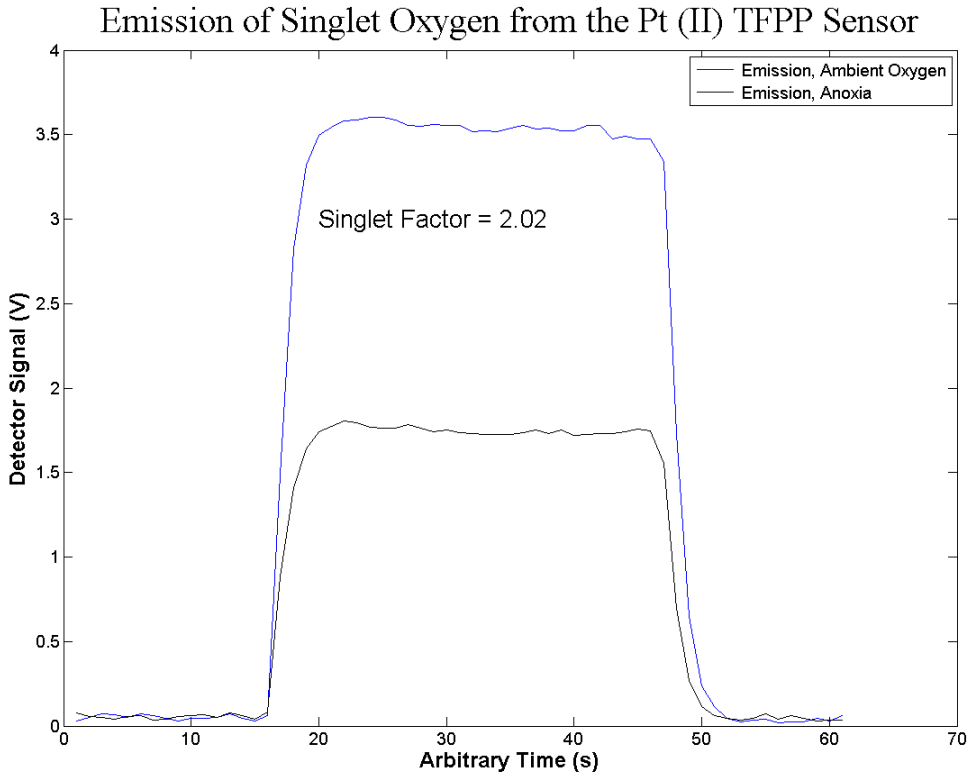

Figure 69: Singlet Factor for the PtF Sensor

The singlet factor was larger than the IB sensor material (see Figure 46). Note that there was also a slight downslope similar to the IB sensor material. This may be indicative of some photodegradation from exposure to excitation light through the 40x objective. It also appears consistent that the rates of photodegradation are similar for both the PtF and IB sensor materials and the appearance of their respective singlet emission plots are also similar.

4.6 Characterization of the MOD Sensor

The Alex Jen Group at the University of Washington also prepared this sensor material. It was prepared by dissolving ~1 mg of the luminophore and ~0.1 g of polystyrene in 10 mL of toluene. The luminophore was presumed to adsorb onto the polymer matrix. The purpose of this sensor was to limit concentration quenching and to decrease photodegradation. The Pt TFPP luminophore was modified to contain bulky groups, while retaining the remaining perfluorinated character of the porphyrin ring substituents. It was thought that any propensity for aggregation or dimerization, might be limited by the addition of bulky groups. The bulky groups may also limit photodegradation attack on the luminophore. The structure is depicted in Figure 70.

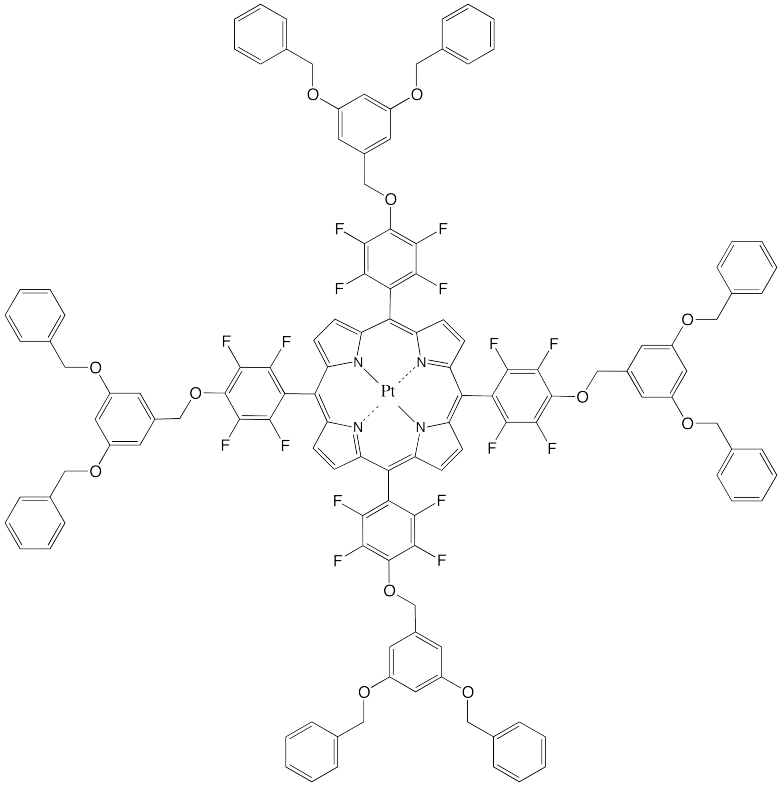

Figure 70: The Modified Pt TFPP Structure. The addition of bulky groups was thought to limit concentration quenching, as it would be more difficult for the luminophore to dimerize. The electronegative oxygen couplings may also limit photodegradation. This sensor will be called the MOD sensor material.

This sensor was also challenging to picoinject. The method used was the TD method with inject pressure 148 kPa for 40 ms and 7 kPa balance pressure. These were the same settings as for the PtF sensor material, though it tended to form better rings than the PtF sensor material. Tip clogs were also frequent, but cleared very readily. A "bulk" chip was also made by simple pipetting of 10 μL of the diluted material onto the flat, backside of a glass chip. No curing process was employed with this sensor material as the researchers that produced it were concerned with thermal degradation. During subsequent use, the sensor ring size was optimized to 57 x 70 pixels, which corresponds to a sensor ring width of approximately 14 μm.

Figure 71 displays the spectra for the MOD sensor material.

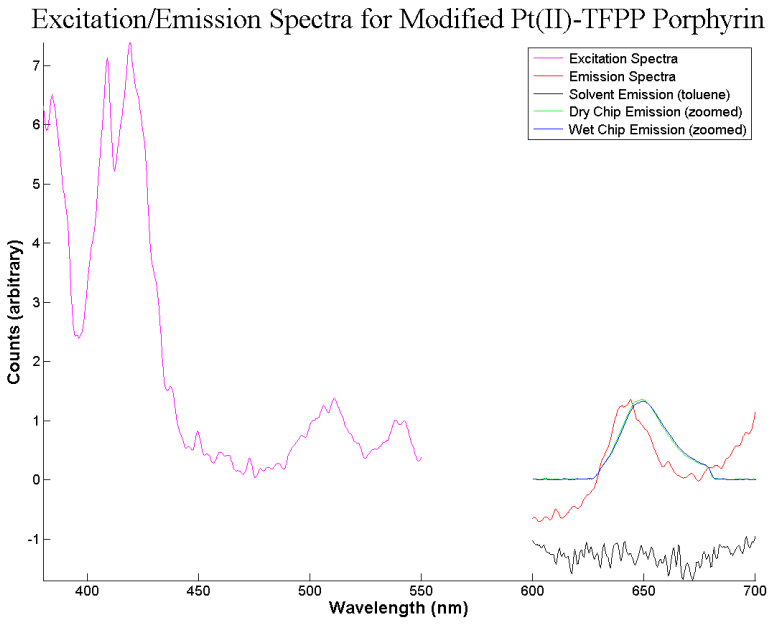

Figure 71: Excitation and Emission Spectra for the MOD Sensor

The excitation spectrum is quite similar to the PtF, with perhaps more distinction in the Soret band. The emission spectra are also very similar to the PtF sensor material. Again,

the bandpass filter is responsible for the unusual shoulder on the emission spectra from the microscope.

A dry run was then conducted for the MOD sensor material. The lifetimes from the three methods are displayed in Figure 72.

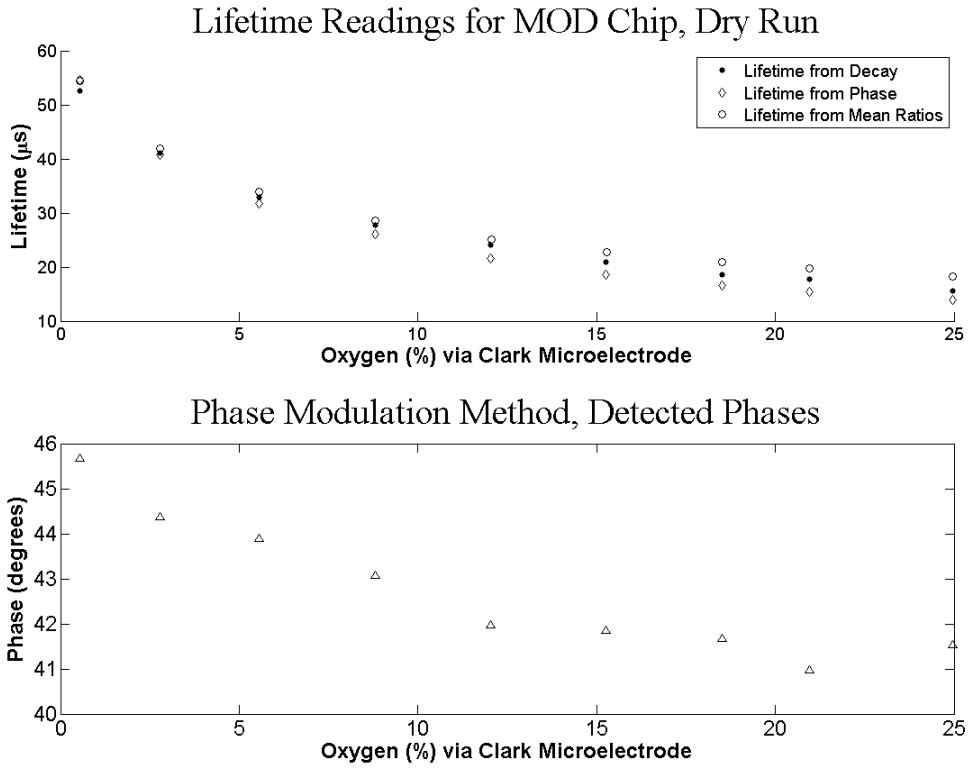

Figure 72: Lifetime Data for the Dry MOD Sensor

The data from all the methods are in a close agreement, with an overall dynamic range around 40 µs, which is improved over the IB sensor material. The phase diagnostic indicates valid phase readings. There is some spread in the data for higher oxygen concentrations. We also see very close agreement between microwells in the ratio data,

Figure 73.

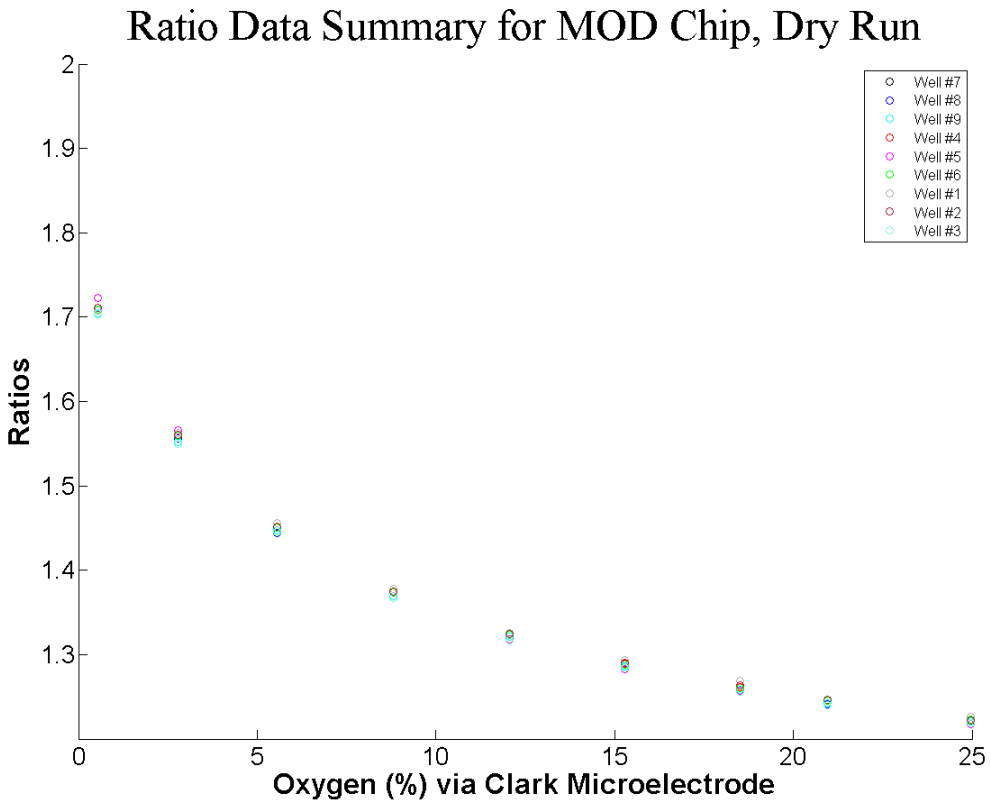

Figure 73: Ratio Data for the Dry MOD Sensor

The SNR for the MOD material was very good and it would be difficult to improve upon the precision in the ratio data. There was some spread at the lowest oxygen

concentration, however. Next, Figure 74

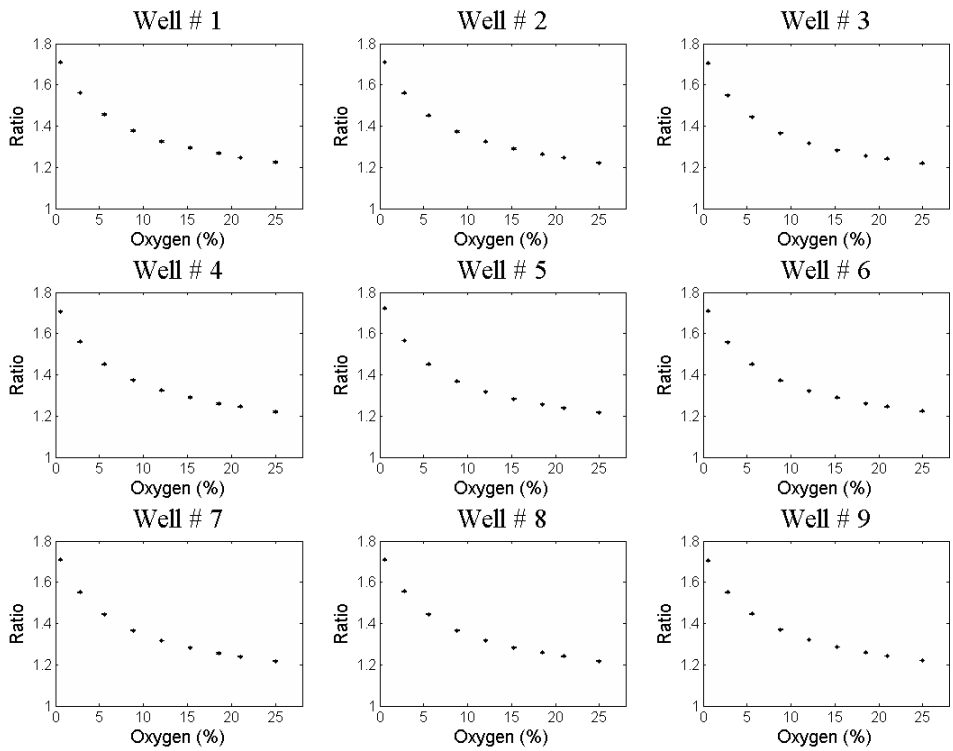

Figure 74: Error Data for the Dry MOD Sensor

shows the error bars for ratio data, which are so small as to be indistinguishable on the plot. Finally, Figure 75

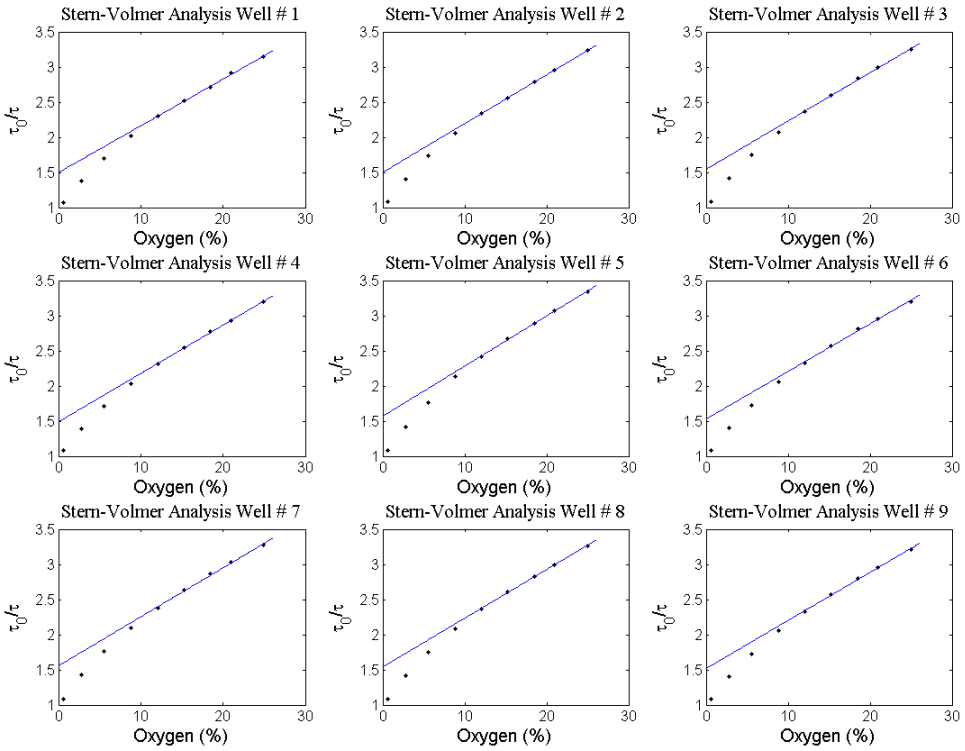

Figure 75: Stern-Volmer Response for the Dry MOD Sensor

shows the Stern-Volmer response for each microwell, which is fairly consistent. The departure from linearity is also quite clear, and in a downward direction.

The hydration effect was not very important for this sensor material. Figure 76 indicates that no more than one hour is ever needed to reach stability, for wet runs.

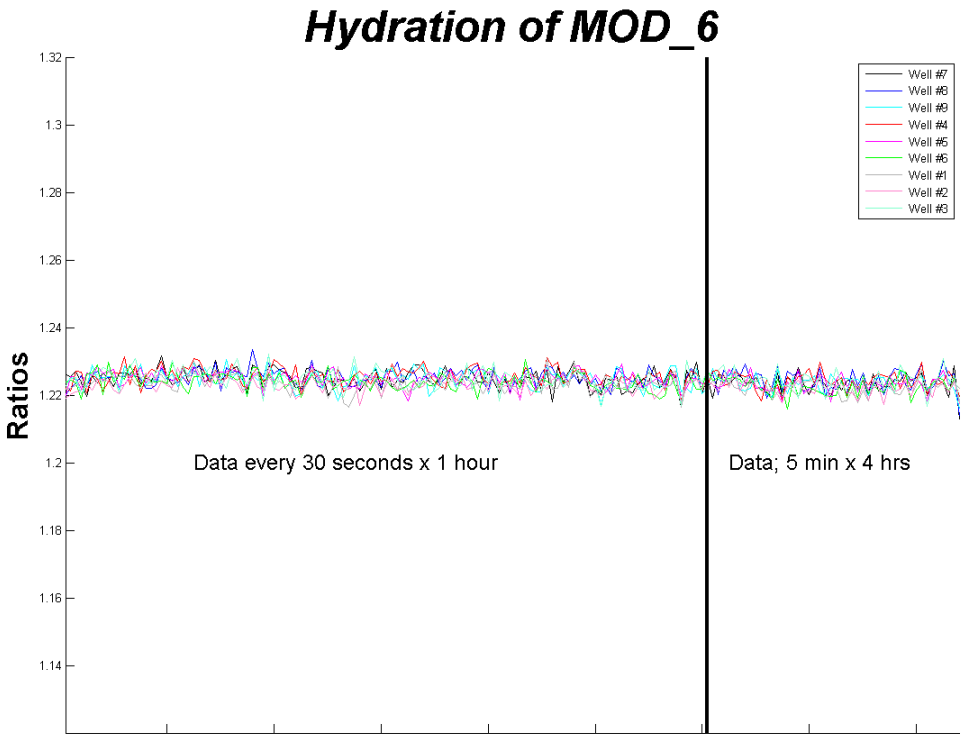

Figure 76: Hydration Effect for the MOD Sensor

There was a slight increase in ratio data that clearly stabilized within an hour. As for the PtF sensor material, this experiment was stopped early due to its obvious stability. Four hours into the run, it was clear that stability had been achieved.

The thickness run with aperturing is provided as Figure 77.

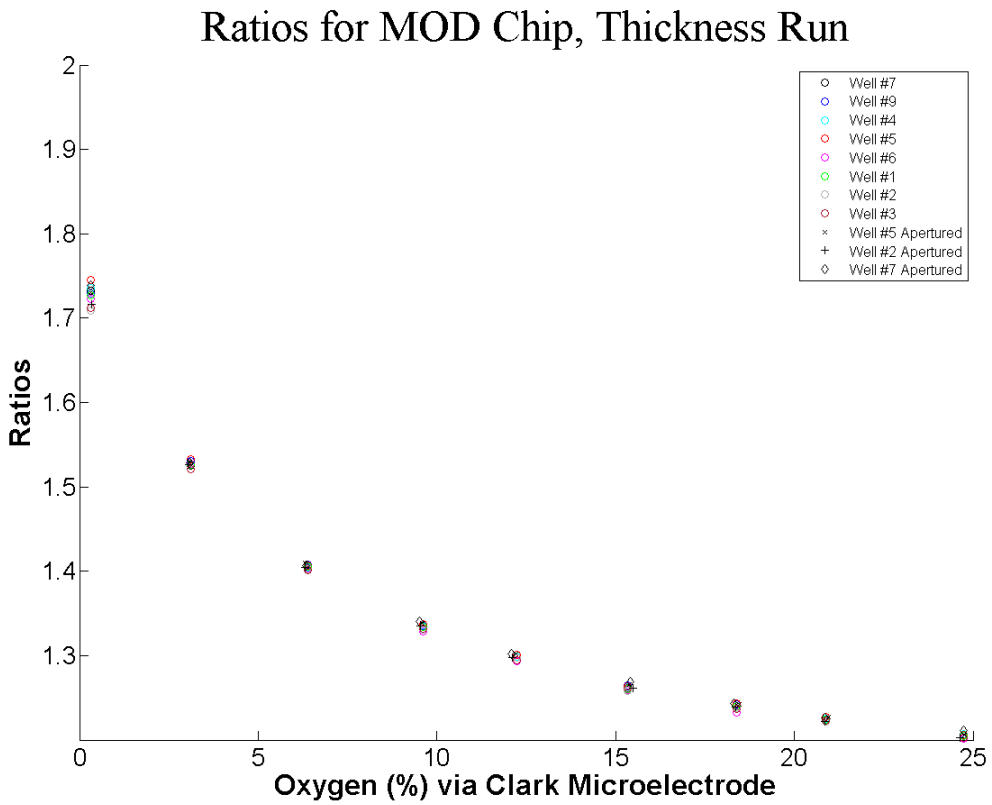

Figure 77: Thickness Data for the Wetted MOD Sensor

For this sensor material, it is very evident that sensor thickness and crosstalk were not an issue of concern, as all nine microwells are tightly clustered for all conditions, except for some spread at the lowest oxygen concentration. It should be noted that the picoinjection process for this sensor material was altered, as compared to the IB sensor material. The first row contained single injections, while the second row contained double injections, and the third row triple injections. The material appeared to deposit in a thicker layer than the IB sensor material and picoinjection was more challenging. It

appeared that any further injections were simply going to create an amorphous blob of sensor material within the microwell, so were not pursued. Note that during this run, microwell #8 was no longer available, suggestive that the delamination results will not be very good.

A wet run was then conducted for the MOD sensor material. The lifetimes from the three methods are displayed in Figure 78.

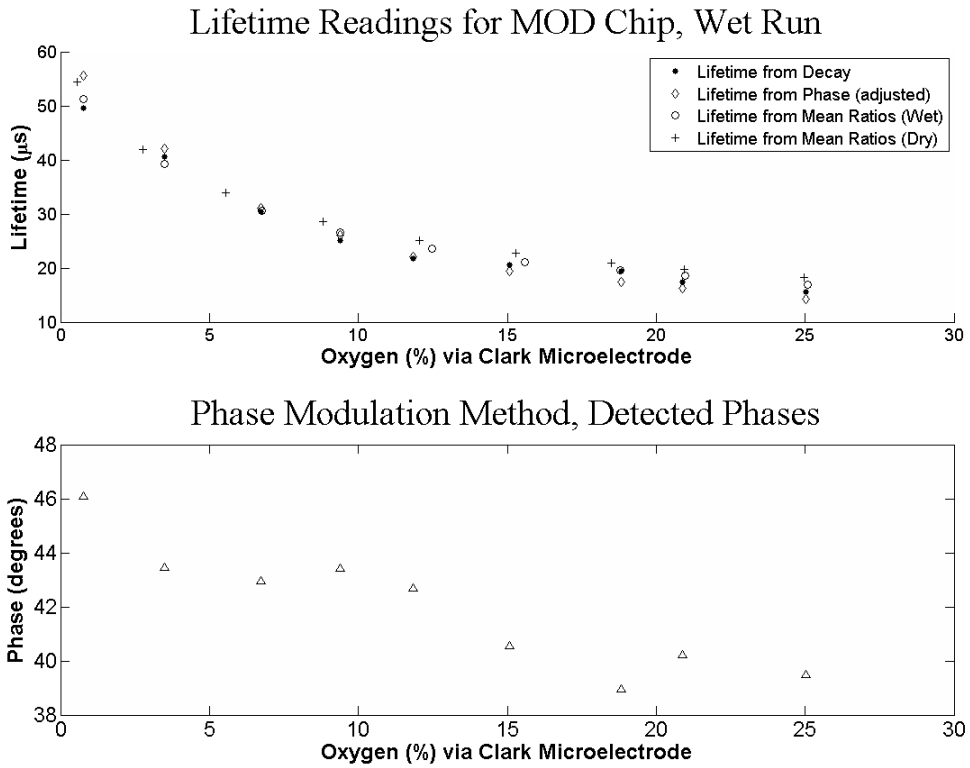

Figure 78: Lifetime Data for the Wetted MOD Sensor

The data from all the methods are in a close agreement, with an overall dynamic range around 40 μs. There was no real discernible difference between lifetimes from the dry run versus the wet run. The phase diagnostic indicates valid phase readings. We also see

very close agreement between microwells in the ratio data, Figure 79.

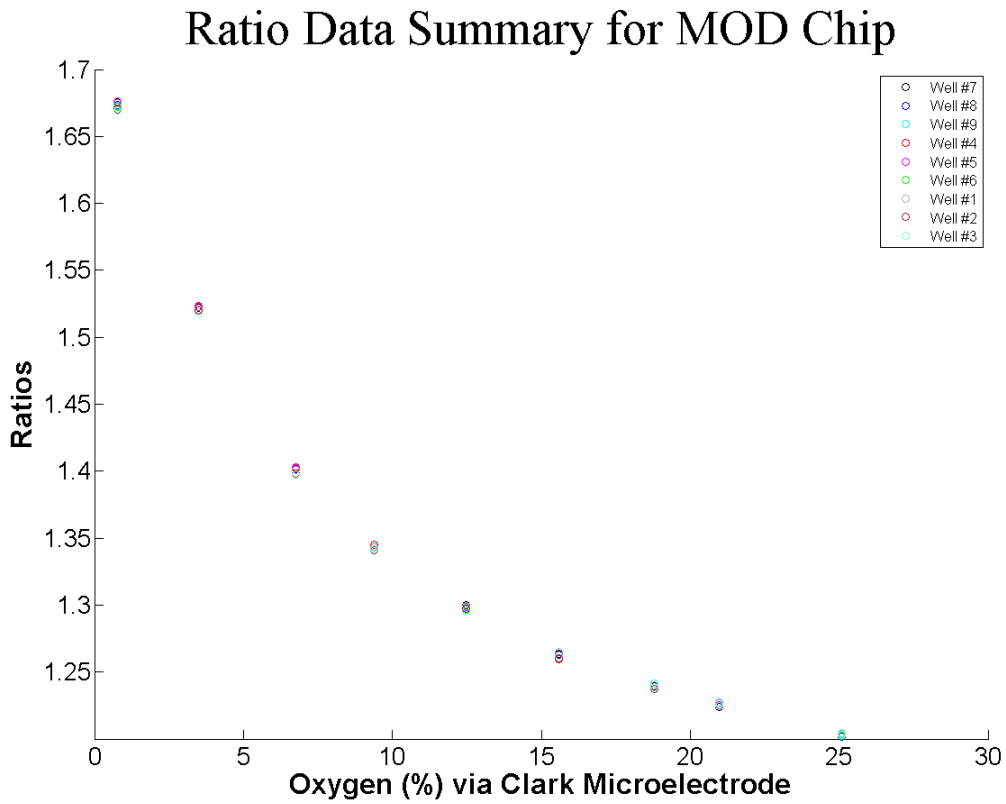

Figure 79: Ratio Data for the Wetted MOD Sensor

The precision in the data continues to be excellent, with a small amount of spread at the lowest oxygen concentration. Next, Figure 80

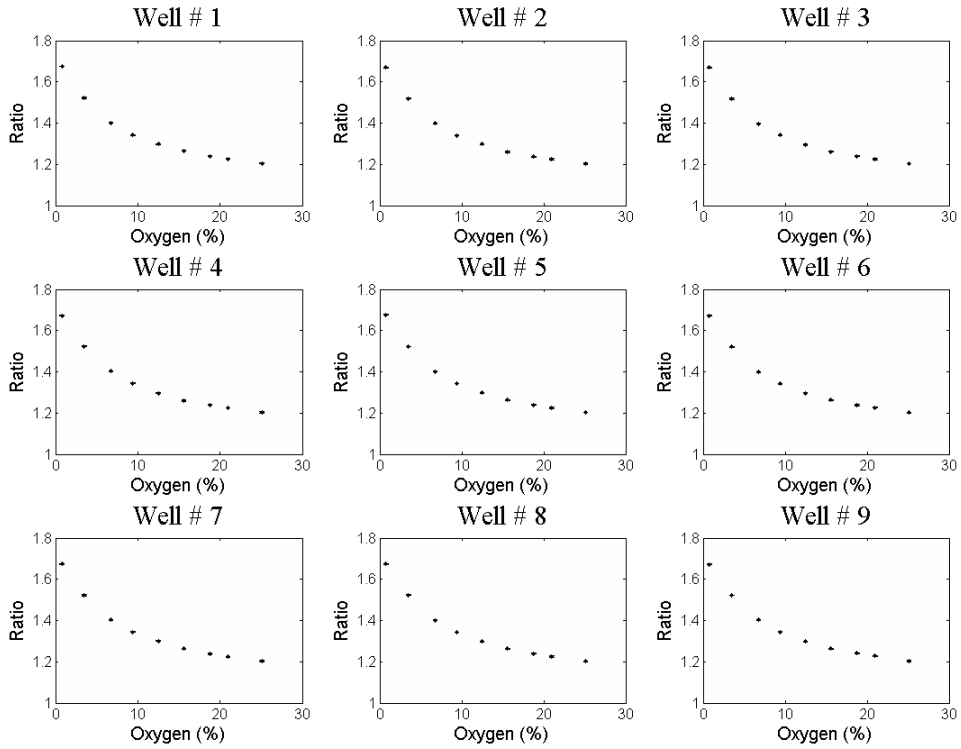

Figure 80: Error Data for the Wetted MOD Sensor

shows the error bars for ratio data, which are so small as to be indistinguishable on the plot. Finally, Figure 81

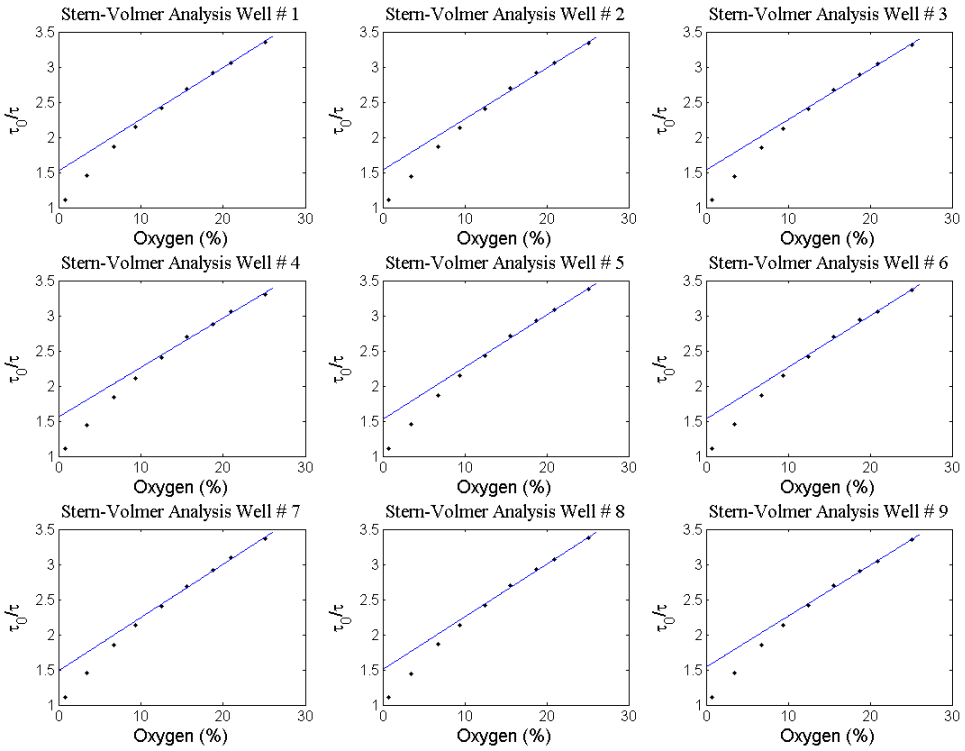

Figure 81: Stern-Volmer Response for the Wetted MOD Sensor

shows the Stern-Volmer response for each microwell, which is fairly consistent. The departure from linearity is also quite clear and in a downward direction. The overall departure from unity was 0.53, which is slightly smaller than for the PtF sensor material.

Next, the dynamic calibration comparative analysis was completed. Figure 82

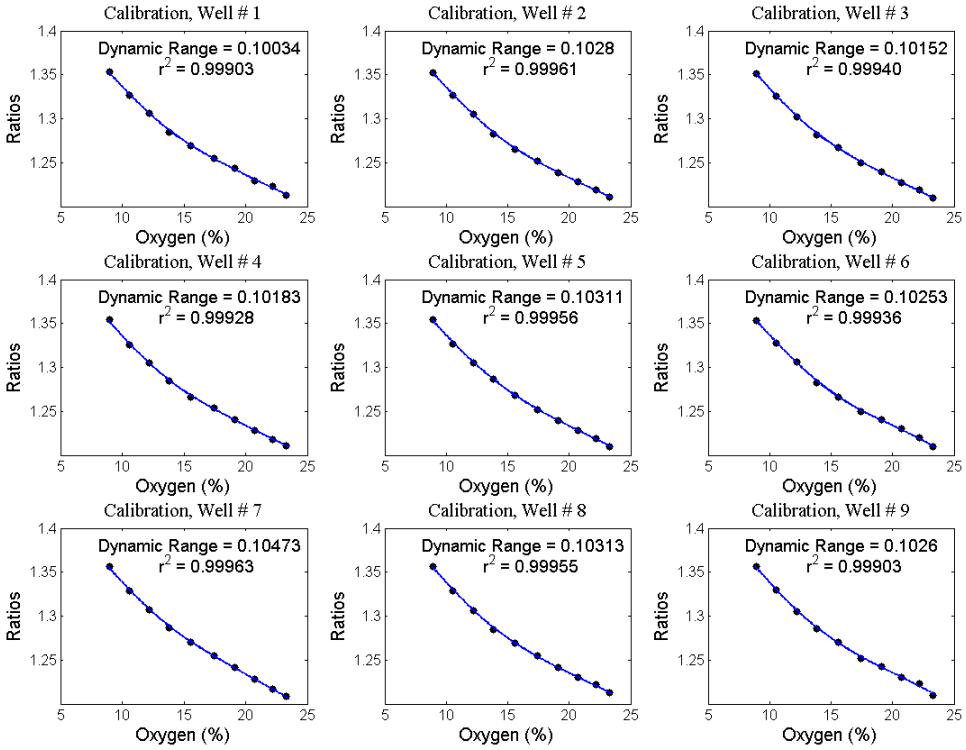

Figure 82: Dynamic Calibration of the Wetted MOD Sensor

indicated the typical nonlinear shape for each microwell. Figure 83 shows random residuals; the smoothing parameter was only 0.05 for this material.

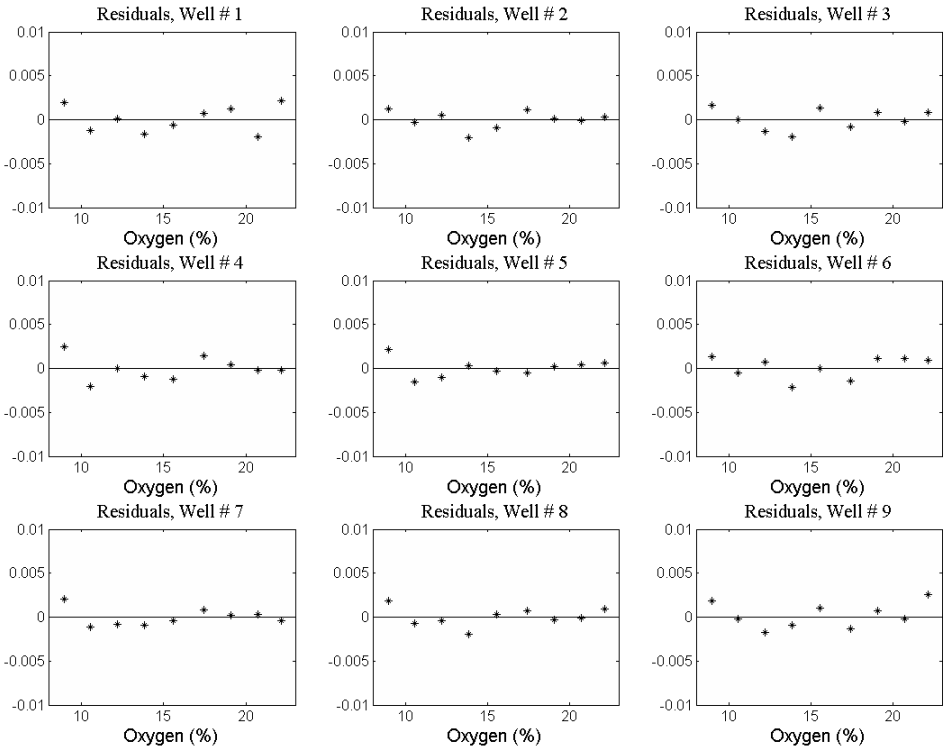

Figure 83: Residuals for the Wetted MOD Senssor

The dynamic range in terms of lifetime over the relevant range (10% to 20% oxygen) was 7.02187 ± 0.00034 μs, which was the best result thus far. The sensitivity parameter was improved, even in comparison to the PtF sensor material. The sensitivity parameter for the MOD sensor material was 7.50.

The photodegradation data is presented next. Figure 84 shows the result.

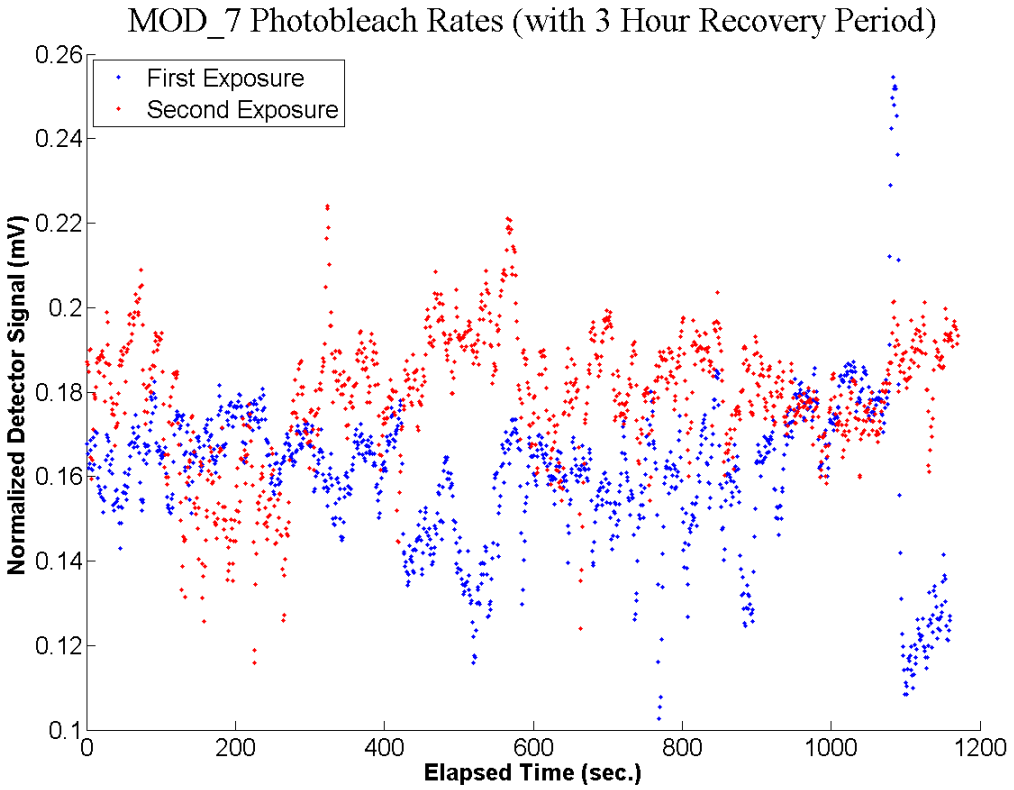

Figure 84: Photodegradation of the MOD Sensor

This material showed no detectable photodegradation within the protocol utilized for the experiment. As stated previously, all sensor materials could be observed to photodegrade via excitation from the 40x objective. However, this experiment was conducted with the 10x objective. The traces simply show some noise and perhaps slight variation in the LED output intensity. This result was very interesting.

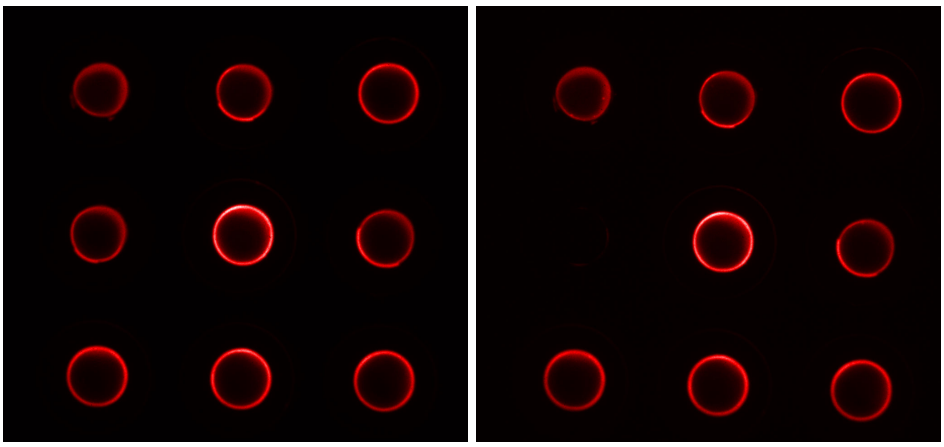

Figure 85: Delamination of the MOD Sensor. The left picture shows an array prior to the delamination test. The right picture shows the same array after 2 minutes of sonication time. The most obvious problem is the total loss of microwell #4.

The delamination test did not go very well for the MOD sensor material. It delaminated very quickly, with a rating of only 2 minutes. Figure 85 shows the result. A thermal cure may help this material adhere to the glass chip. Upon close examination, there was some slight thinning, but the biggest problem was the total loss of microwell #4.

The final characteristic for this sensor was the singlet emission evaluation. The result is shown in Figure 86.

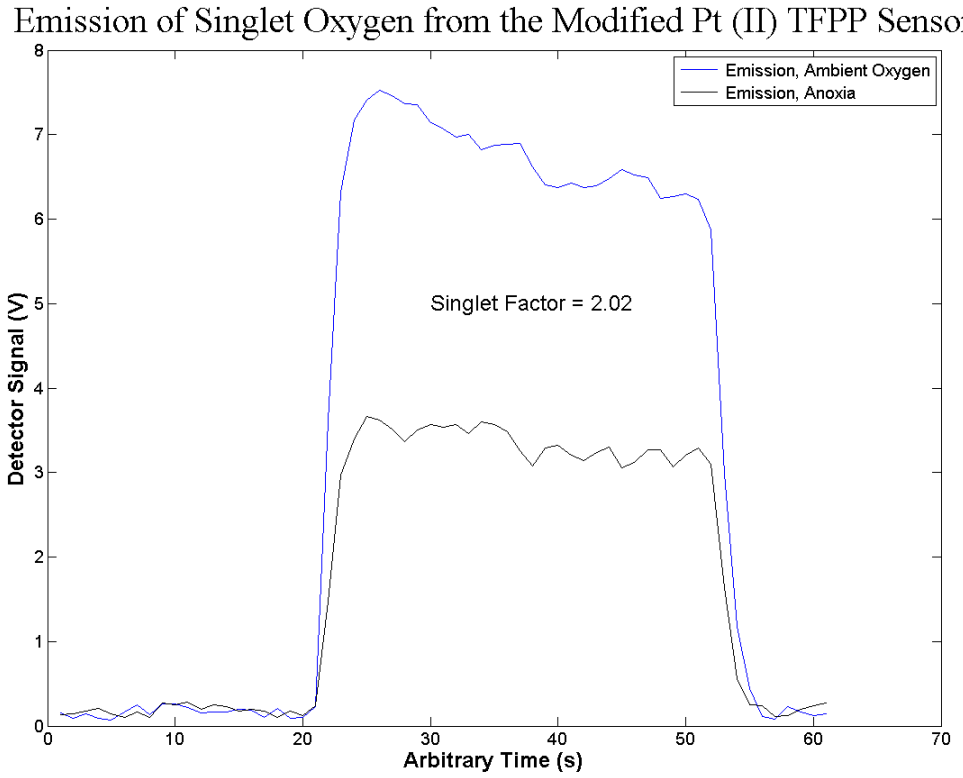

Figure 86: Singlet Factor for the MOD Sensor

The singlet factor was larger than the IB sensor material (see Figure 46), but identical to the PtF sensor material (see Figure 69). There was a substantial downslope to the data at ambient oxygen levels. If that was indicative of photodegradation, that would be interesting, given that the photodegradation experiment did not detect any changes. The difference was the microscope objective, 40x versus 10x. It is possible that the luminophore is resistant to photodegradation, but only up to some threshold value of radiant flux density.

4.7 Characterization of the PSP Sensor

This was pressure-sensitive paint (PSP), another commercially available product. Specifically, fast response paint was used from Innovative Scientific Solutions, Inc. (part number F405, Dayton, OH). The purpose of this sensor was to have another polymer matrix for comparison. There were some thoughts that thin-film sensor materials used in a submerged state would have little difference in their response. That is simply another way of saying that the aqueous environment was more important at limiting the diffusion of oxygen than the polymer matrix would be. The polymer matrix in this material was a fluorinated one, thought to also limit photodegradation. Specifically, it is commonly known as FIB, which is shorthand for Poly(1H,1H-dihydroperfluorobutylmethacrylate-co-1,1,1,3,3,3-hexafluoroisopropylmethacrylate). The luminophore is Pt TFPP, which we are quite familiar with by now (see Figure 47). As a commercial product, the exact formulation was not known, but we would assume that it is something similar to that reported in the literature:[33] 5 mg to luminophore to 1 g polymer to 25 mL of solvent. For this material, the solvent is trifluorotoluene. It is also worth mentioning that biologists did not vet this sensor material; they reported it to be cytotoxic to their cells of interest. It would therefore not be a candidate for a sensor material, but interesting to study, nonetheless.

This sensor was easy to picoinject. The process was not quite as reliable as for the IB sensor material, as there was more of a propensity for spillage on the edge of microwells. The method used was the TTAW, with inject pressure 116 kPa for 20 ms and no balance pressure. Tip clogs were almost unheard of with this sensor material. A "bulk" chip was also made by simple pipetting of 10 μL of the diluted material onto the

flat, backside of a glass chip. The chips were cured for 60 minutes in a 100 °C oven, as per guidelines[34] in the literature. During subsequent use, the sensor ring size was optimized to 55 x 70 pixels, which corresponds to a sensor ring width of approximately 16 μm.

Figure 87 displays the spectra for the PSP sensor material.

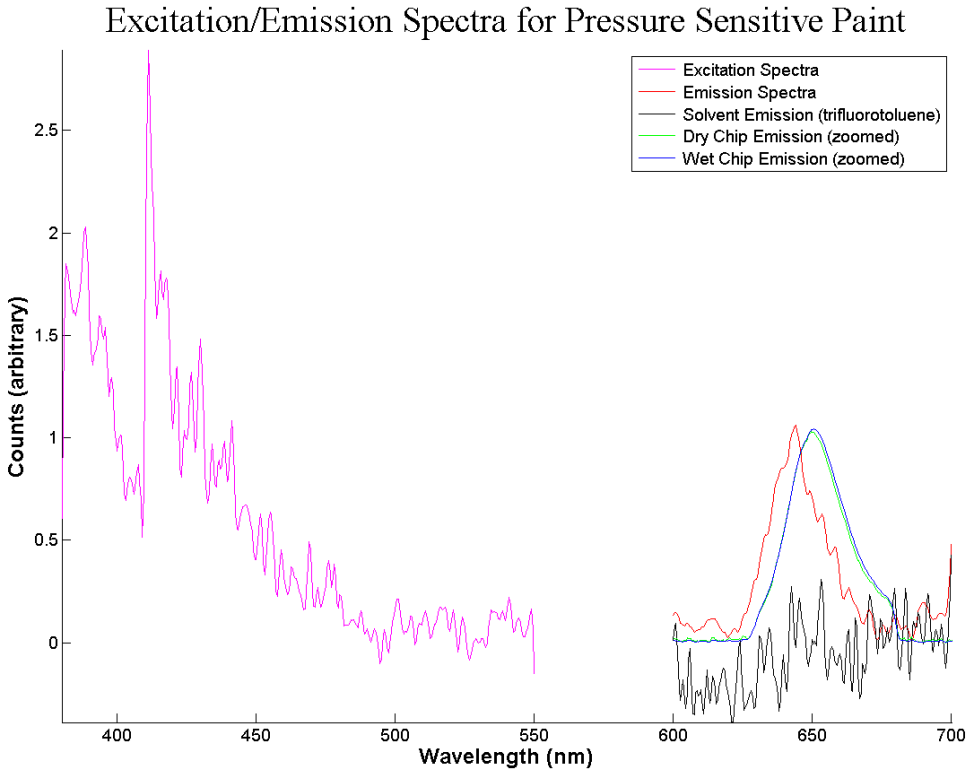

Figure 87: Excitation and Emission Spectra for the PSP Sensor

The excitation spectrum has more structure compared to the other sensor materials. The emission spectra are similar to the MOD sensor material, with perhaps some more blue-shift. The bandpass filter is responsible for the unusual shoulder on the emission spectra from the microscope.

A dry run was then conducted for the PSP sensor material. The lifetimes from the three methods are displayed in Figure 88.

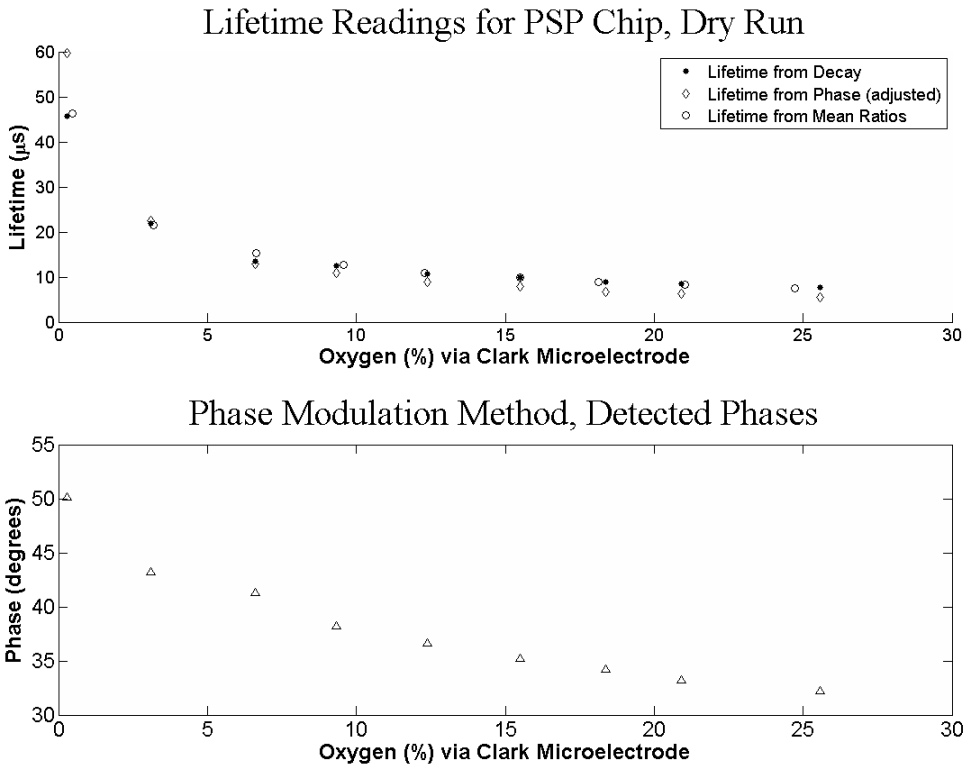

Figure 88: Lifetime Data for the Dry PSP Sensor

The data from all the methods are in a close agreement, with an overall dynamic range around 50 μs, though the spread near 0% oxygen (hypoxia) is much greater than with the other sensors. The phase diagnostic indicates a new behavior, as compared to other sensor materials. At higher oxygen concentrations, the phase angle is lower than ideal (45°), then rises monotonically when moving towards anoxia. There was also another

observed change in the auxiliary diagnostic oscilloscope when the phase angle surpassed 40°. The signal intensity from the lock-in amplifier dropped substantially and such behavior is not physically realizable from the sensors. This would imply an instrumental artifact. In section 3.2, we discussed the frequency limitation of the modulated driver for the LED. These results suggest that the vendor's specifications may be even further off than previously stated. Despite these limitations, the agreement between all methods was quite good, when the adjusted phase value was utilized, with the exception of the hypoxic reading. We also see very close agreement between microwells in the ratio data, Figure 89.

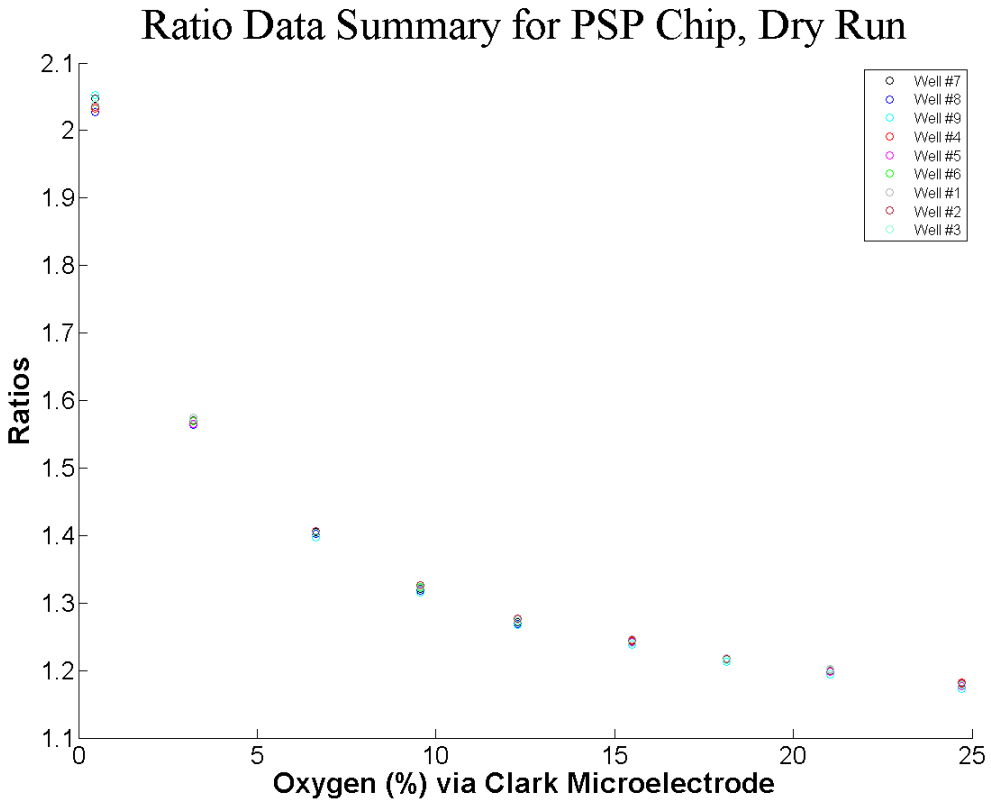

Figure 89: Ratio Data for the Dry PSP Sensor

There was some spread at the lowest oxygen concentration, however. Next, Figure 90

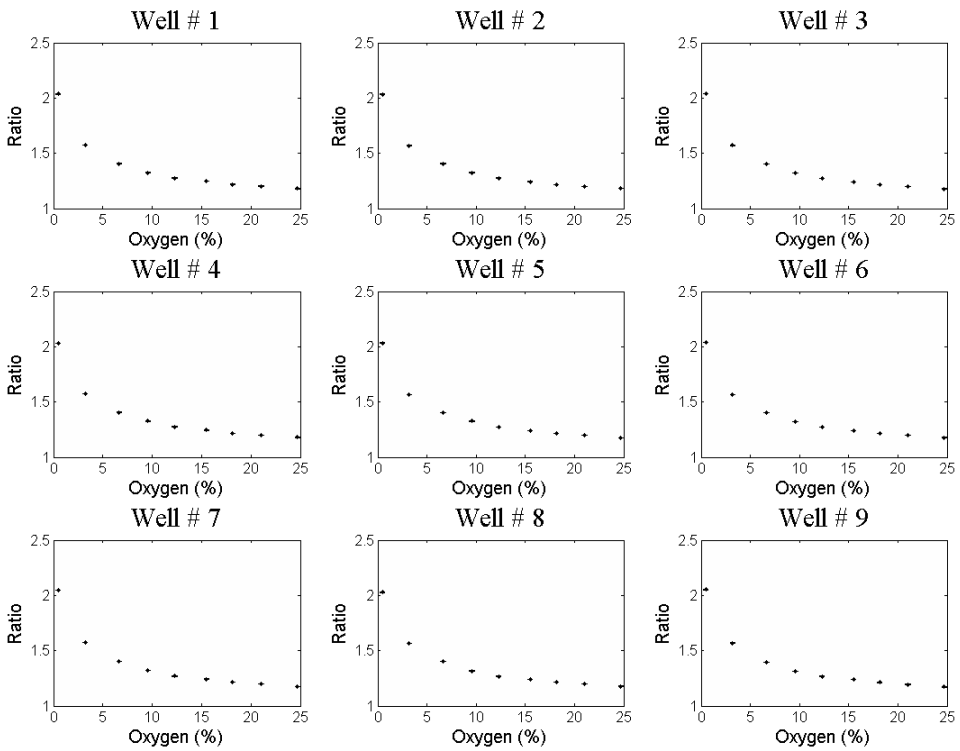

Figure 90: Error Data for the Dry PSP Sensor

shows the error bars for ratio data, which are so small as to be indistinguishable on the plot. Finally, Figure 91

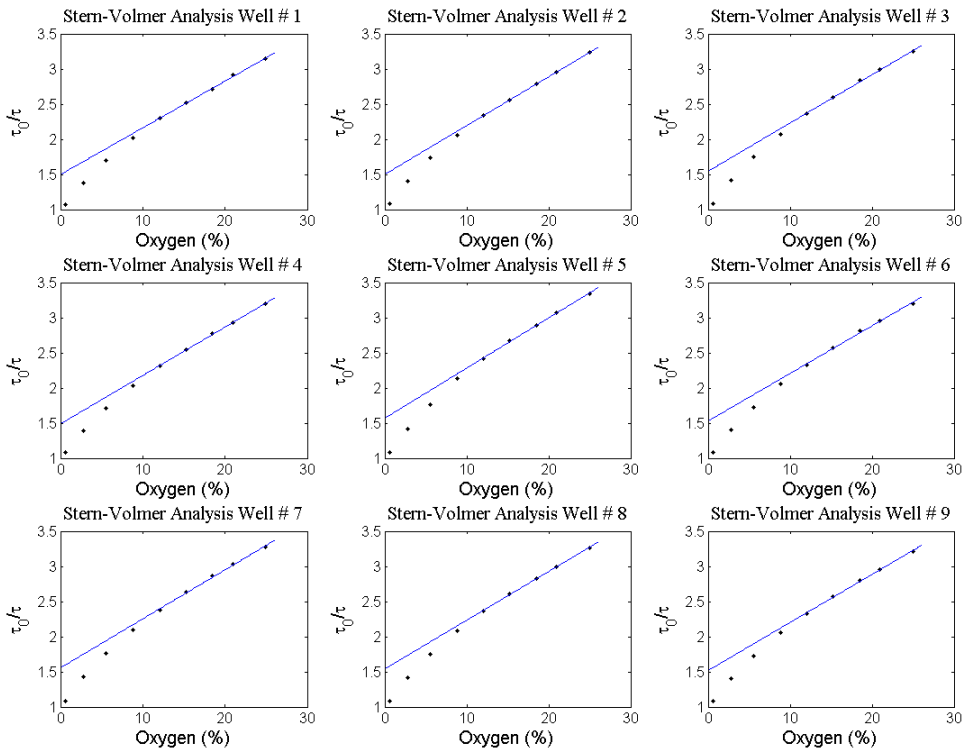

Figure 91: Stern-Volmer Response for the Dry PSP Sensor

shows the Stern-Volmer response for each microwell, which is fairly consistent. The departure from linearity appears to be the most severe of any of the sensor materials. That was not surprising as the lifetime plots and the ratios plots do in fact suggest that the rise in response was quite substantial as low oxygen concentrations were achieved, while the response near ambient conditions appeared quite flat.

The hydration effect yielded unusual results for this sensor material. Figure 92 indicates that there is no obvious hydration effect. The unusual spikes were attributed to early delamination of sensor material that caused debris to float across the field of view. The sensor material was observed early on to lose some bits of material and to present an

increasingly cracked appearance. This may explain the tendency for the traces to begin to separate at later times. It would make sense that a substantial change to surface area could result in a substantial change in diffusion response and thus sensor response. Even if acceptable to biologists, this sensor material would appear to be very unreliable, but further characterization tests were carried out anyway.

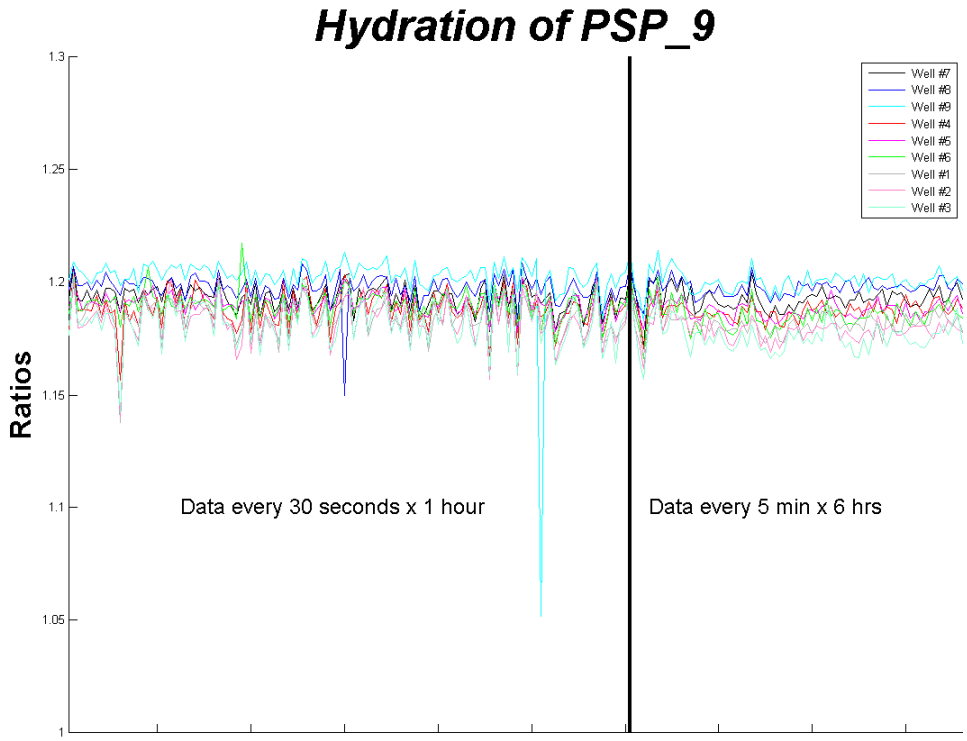

Figure 92: Hydration Effect for the PSP Sensor

The thickness run with aperturing is provided as Figure 93.

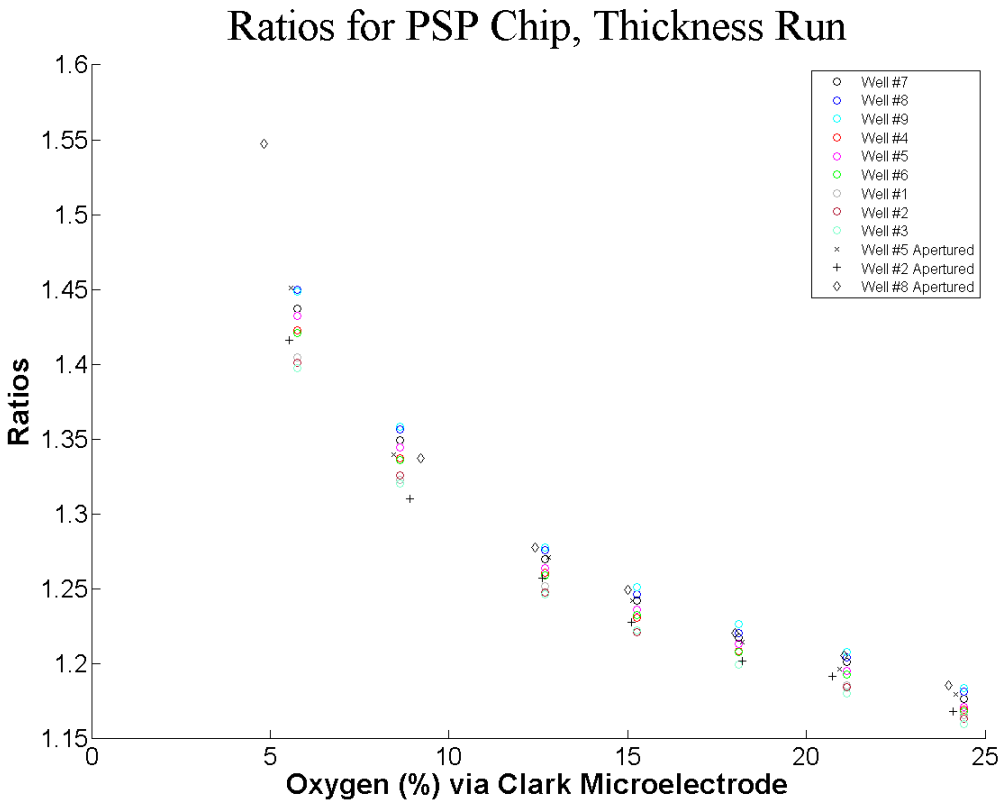

Figure 93: Thickness Data for the Wetted PSP Sensor

For this sensor material, a new behavior was observed. During the hydration test, loss of sensor and sensor "cracking" were noted. During this test, cracking may have worsened and sensor material appeared to slowly migrate away from the rings and toward the center of the microwells. Both of those phenomena caused a lot of tedious manual work to be performed for implementation of the ring finding algorithm. Figure 93 does show quite a bit of spread in the ratiometric data, but it is surprising how robust the data was in the face of such physical changes. Figure 93 would also indicate that there is little concern for crosstalk, though microwell #8 appears to be an exception at the most hypoxic condition. In light of these challenges, it was decided to not pursue the wet run or the dynamic calibration for this sensor material. There was no need for the

delamination test, as the rating would already be classified as zero. Finally, Figure 94 presents pictures that demonstrate the cracking and migration phenomena.

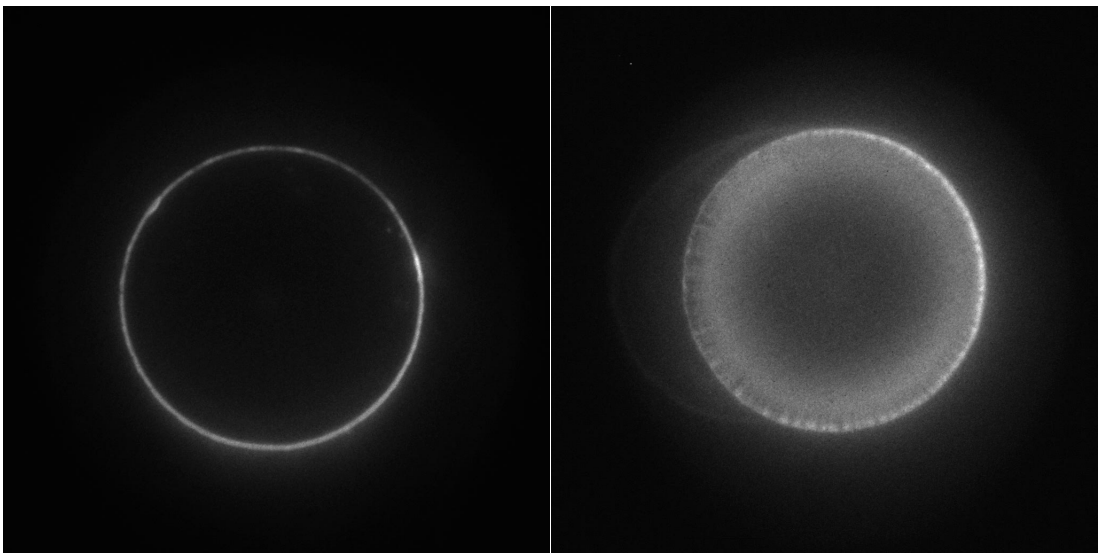

Figure 94: Sensor Cracking and Migration Phenomena. The picture on the left is IB sensor material; the picture on the right is PSP sensor material. Both pictures were obtained with the 40x objective. Note that the IB sensor material makes a nice smooth ring that is fairly uniform in appearance. The PSP material has a "cracked" appearance that worsened with increasing hydration. Increasing amounts of hydration time also resulted in sensor material migrating towards the center of the microwell. The ring structure became less and less distinct as experiments continued, causing difficulties with ring finding algorithms.

The photodegradation analysis of this sensor material was attempted, but failed. This experiment was the final experiment conducted in this study. Unfortunately, the APD detector had begun to exhibit erratic behavior the day following a campus wide power outage, which may have sent electrical surges to the instrument set-up. Given the unstable nature of the PSP sensor material in water, it was not worth the effort to try another detector, such as a photomultiplier tube, or the camera.

The final characteristic for this sensor was the singlet emission evaluation. The result is shown in Figure 95.

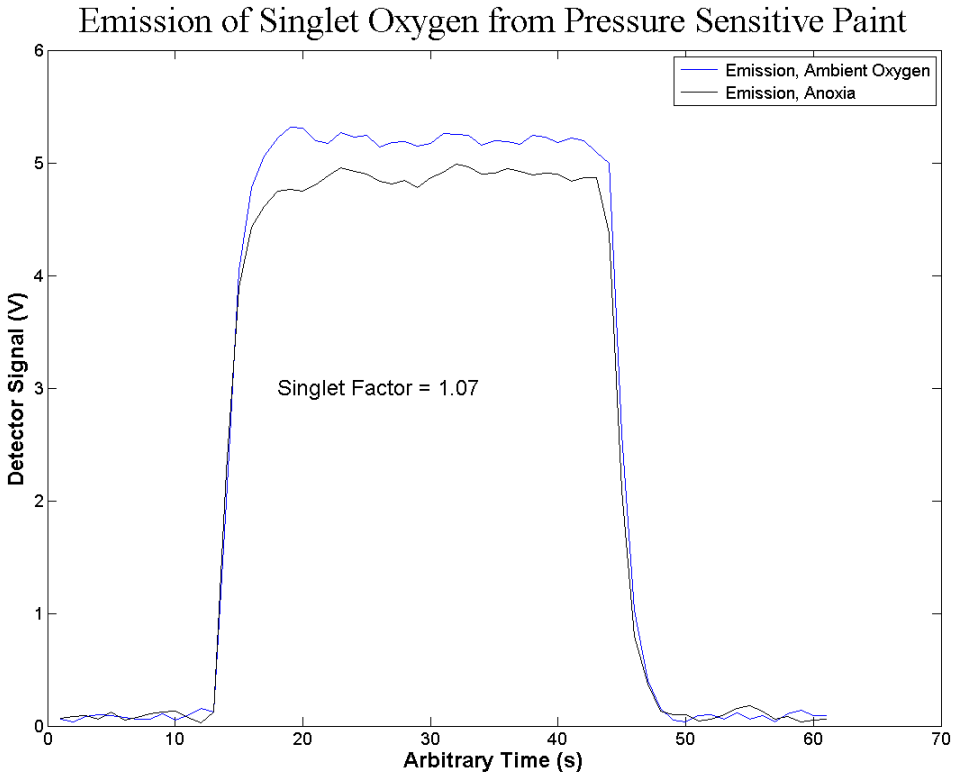

Figure 95: Singlet Factor for the PSP Sensor

The singlet factor was smaller than most of the sensors. The traces are also quite flat. The low value here and the flat traces may indicate that this sensor material is quite resistant to photodegradation, as well as have the potential for reduced induction effect.

4.8 Summary of Characterization Results

A long series of plots and data was presented in this chapter, so it may be worthwhile to summarize the important results. One topic that has not been discussed in very much detail is SNR. While this was a challenge that could not be overcome for all sensor materials in direct decay measurements that analyzed the exponential decay itself,

the LPL model provided a means in which all sensors could be measured. However, the more interesting focus would be on the image data. The general approach to camera operation was semi-quantitative, but shall now be quantified.

The approach was to examine an image at the beginning of a new experiment and randomly click on background areas to assess the background level. At that point, the images were not background corrected, so the "background" would be representative of random noise and any stray background light. The LED brightness setting, number of pulses to collect for IOC mode, and the camera gain were then adjusted such that dimly responding areas of sensor material were ~3-4 times the background level. Then the camera was switched to background corrected image types and data was collected. We can determine the signal-to-background ratio for these images. This was measured for all images collected during the ambient oxygen concentration for the wet run, where possible. The ANH and PSP sensors utilized the dry run, since no wet run was performed. The ring finding algorithm was utilized to locate the sensors and then the average intensity per pixel was determined for the part of the image with sensor, and the part of the image without sensor. Those ratios were then averaged for that data set. Note, that only the early bin was analyzed as the later bin would simply have an increased SNR and presumably, a concomitantly improved signal-to-background. To keep variables to a minimum, all sensor materials utilized in this study employed 750 pulses at 1500 Hz in IOC mode, the LED brightness was only changed if necessary, and then the camera gain was adjusted to reach the desired SNR described above. One additional point should be emphasized. The reader may contemplate that a starting point of 3-4 times background may not be optimal for the camera, which had dynamic range of 2^{16}. However, recall that

these sensors operate in a "reverse" mode from what many are accustomed too. The sensor lifetime increases with decreasing oxygen concentration, but the intensity also increases with decreasing oxygen concentration. The experience of many trials indicated that that was a suitable starting point for ambient oxygen concentration levels, so as to not saturate the CCD at anoxia. The results are included below in Table 4.

Table 4: Signal-to-Background Ratio Results

Sensor	*SBR*	*LED Brightness*	*Camera Gain*	*Amplification*
FB	6.25	100%	150	5465
IB	21.80	100%	120	2783
ANH	1.73	200%	200	16,833
PtF	17.64	100%	0	1
MOD	17.16	100%	0	1
PSP	16.94	100%	75	1011

In Table 4, SBR indicates the signal-to-background ratio as described above. The camera gain setting is not a very meaningful number. While the vendor did not provide a conversion formula, they did provide specification charts, which show the improved electron counts from the intensifier's photocathode for a variety of gain settings. The data was found to fit an exponential function very nicely, in order to develop the following relation:

$$A = 187e^{0.0225G} \tag{4-3}$$

In equation 4-3, A represents the photocathode amplification factor, while G represents the camera gain setting. In light of the procedure described above, it should not be too surprising now that SBR values are mostly similar for the sensors that worked well; the camera gain is more indicative of performance from the perspective of SNR.

From Table 4, we now have a much better sense at how difficult the ANH sensor material was to analyze. The FB sensor material probably could have used more gain, but it served its purpose as a negative control adequately. The most interesting response

was the PtF and MOD sensor materials; these represent quite a substantial improvement in SNR over the commercial IB sensor material. It should also be noted that the MOD sensor material nearly saturated the CCD under hypoxic conditions, hinting at a better dynamic range than the PtF sensor material. The PSP sensor material was an incremental improvement over the IB sensor material.

Some of the effects observed in this study were common to all sensors. Namely, there was not really a substantial difference in response based upon sensor thickness nor was there any obvious crosstalk issues between the microwells. The hydration effect was also of not much concern, given that preparations for an experimental run would utilize a sufficient wait time for the sensors of interest (at 37 °C). However, recall that the ANH sensor material and the PSP sensor material did not respond well to submersion and are not at all adequate for these types of experiments. Other parameters of interest would be photodegradation and the induction effect. Those results are summarized in Table 5.

Table 5: Summary of Degradation Effects

Sensor	*%Loss*	*First decay (min.)*	*Second decay (min.)*	*Singlet Factor*	*Delam. time (min.)*
IB	8.80	9.4	6.6	1.30	62
ANH	-----	----	----	1.07	0
PtF	0.55	5.0	5.6	2.02	2
MOD	0	ND	ND	2.02	2
PSP	-----	----	----	1.07	0

Note that in Table 5, dashes mean the parameter could not be assessed and ND indicates, "not detected." This data shows two important features; the MOD sensor material did not have any detectable photodegradation within the protocol and that IB sensor material is the only one that had acceptable adhesion properties. The singlet factor may indicate that the induction effect may be worse in the PtF and MOD sensor materials, though as discussed previously, this test should be viewed with great skepticism.

At this point, the introductory comment that the IB sensor material was the best performer should be clear. It achieved that ranking because the optical performance was acceptable, the picoinjection behavior was the most reliable, and it was the only material with sufficient adherent properties to be useful. The introductory comments also indicated another sensor material provided the best analyte signal. Table 6 displays a summary of the parameters to reach that conclusion.

Table 6: Summary of Optical Performance

Sensor	*Δt (μs)*	*Dynamic Range (μs)*	*Sensitivity Parameter*	*Stern-Volmer Deviation*
IB	50	4.68	1.75	0.41
ANH	25	-----	-----	-----
PtF	100	6.057	5.35	0.56
MOD	100	7.022	7.50	0.53
PSP	50	-----	-----	-----

In Table 6, the dashes indicate a parameter that was not assessed. The Δt values were provided just for reader interest. The dynamic range listed in Table 6 is for the 10-20% oxygen concentration values, since that was the interest of keen interest to biological researchers. The best optical performance and thus the sensor material that should provide the best analytical signal, would have the highest dynamic range and the greatest sensitivity parameter. It is clear that the MOD sensor material meets the criteria. The Stern-Volmer deviation may predict that calibration stability may be achieved with the lowest value, but a more robust assessment would be needed to really answer that question. Given that the MOD sensor material had superior performance and the Stern-Volmer deviation value is only slightly worse than the IB sensor material, it was chosen for further calibration study.

4.9 A Comparative Calibration

The MOD sensor material was subjected to further calibration analysis. One drawback to employing the LPL method was that long pulses potentially increase photodegradation and make the induction effect worse. The pulse width for the ORLD method was typically 5 μs, while the typical pulse width for the LPL method for the MOD sensor material was 205 μs (~ 40x increase). However, the MOD sensor material was analyzed with a camera gain setting of zero. Dragavon[1] reported the optimal gain setting was 150 and blanks testing during the course of this study would suggest that a gain setting anywhere between 100 and 200 produced the most repeatable data. Instrumental parameters were varied with the camera gain set to 150 for the MOD sensor material, in order to explore reduction of exposure to the excitation light.

It was found that images could still be obtained with the LED brightness setting decreased by a factor of 100 (to 1%). However, those images tended to have less well-defined edges, creating challenges for the ring finding algorithm. It was decided to produce an experiment that was more challenging and perhaps more similar to biological experiments. This was accomplished by maintaining the camera gain setting at 150 and returning the LED brightness setting to 100%, but decreasing the number of pulses by 60% to 300. That should be expected to add more variability to the data, while still decreasing photodegradation and decreasing the induction effect. Ideally, one should really study the induction effect and how it responds to pulse width, LED output, and total exposure time.

With these modified settings, the goal was to evaluate calibration performance of polynomial fitted data versus a Stern-Volmer model. A typical set of calibration points

was measured, and then a set of random oxygen concentrations within the range of biological interest was measured. Then performance of the model with the random points was assessed. Only the static calibration method was evaluated through this process. Originally, the dynamic calibration method appeared to be very attractive as a time saving method. However, throughout this study, it was found that the settings that produced acceptable data involved collection of data with at least 5 minutes of pause between data points. The reduction in experimental time was minimal compared to static calibration, but the analysis steps were more time consuming. It was concluded that there was little benefit to dynamic calibration. The remaining question truly was then which model to utilize. One merely needs a smoothly monotonic response for a reliable analytical signal, so a polynomial fit should suffice. However, the Stern-Volmer model is most often reported in the literature.[31,33,47-51] The disadvantage to the Stern-Volmer model is that τ_0 is needed, and it was quite time consuming to obtain a good reading under anoxic conditions.

Some static calibration runs were conducted for the MOD sensor material. Figure 96 shows a summary of ratiometric data for one run.

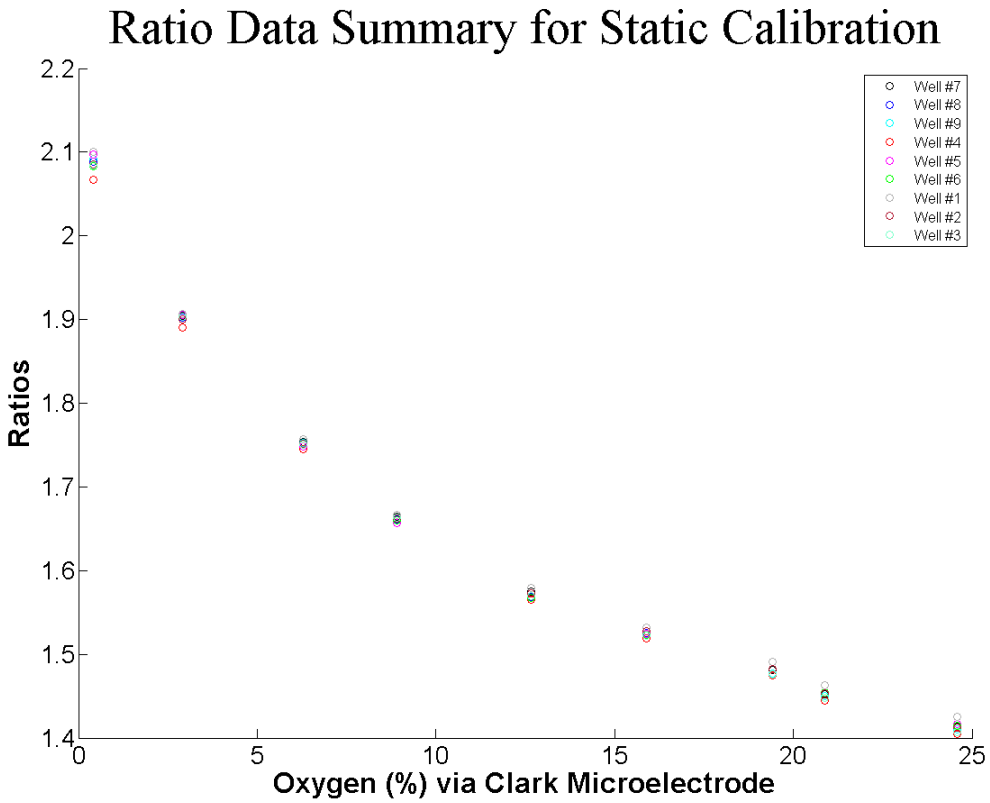

Figure 96: Ratio Summary for Comparative Calibration

The intention was to degrade the data a small amount to more closely resemble real-world data; the slight scatter in the ratios would appear to indicate that the goal was achieved to some extent. Next, the data was fitted to a second-order polynomial

(quadratic fit) and a Stern-Volmer linearization model; Figures 97 and 98.

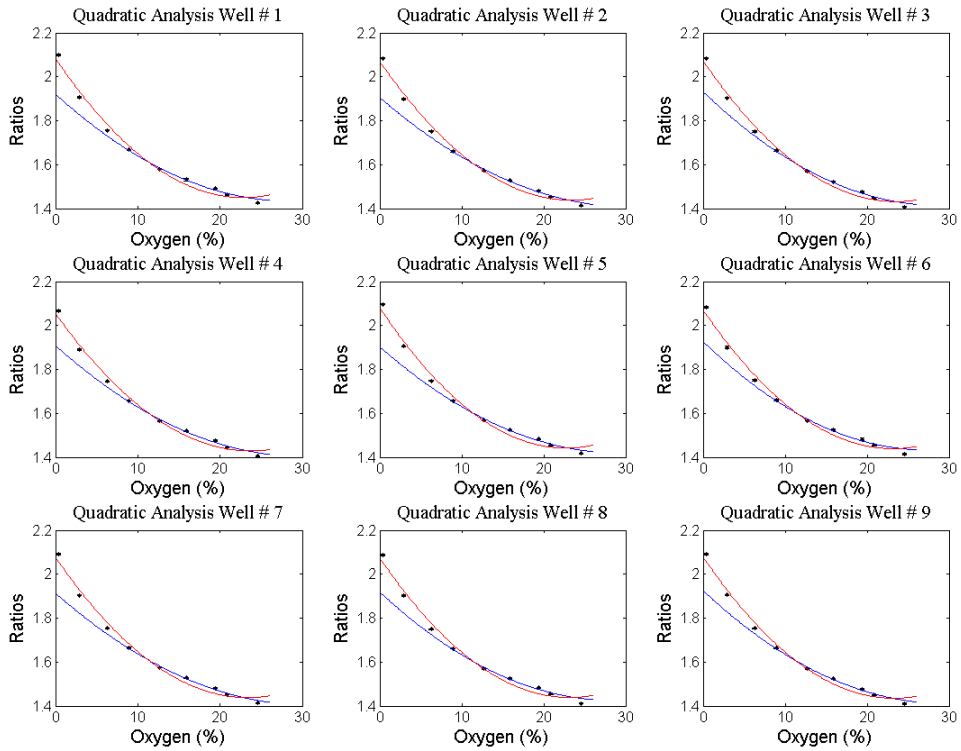

Figure 97: Quadratic Fits for Comparative Calibration

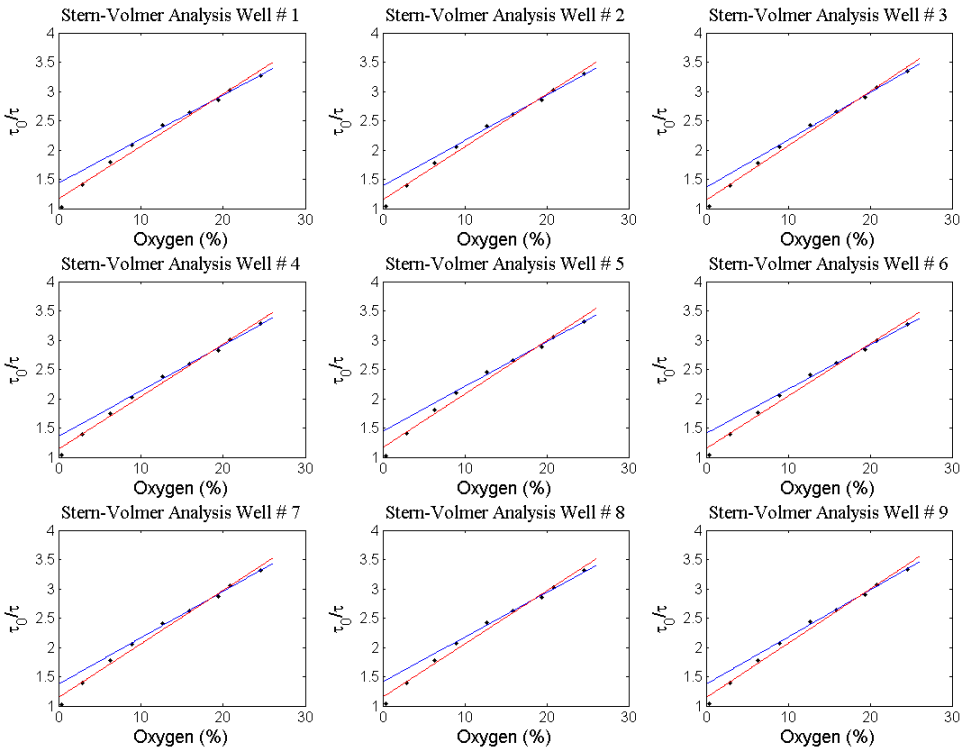

Figure 98: Stern-Volmer Fits for Comparative Calibration

Both Figures 97 and 98 contain red and blue lines, which simply represent a "full" calibration and a "partial" calibration, respectively. That decision was largely driven by the interest in a general approach to calibration (i.e. a need only for a smoothly monotonic response to changes in oxygen concentration). The full calibration is a fit to the data over the entire range measured, while the partial calibration is a fit to only the five last points, which is close to the biological range of interest, 10% to 20% oxygen concentration. It is worth mentioning that the piecewise polynomial method was not employed here. While that was a useful tool for sensor material comparisons, in the realm of calibration, it is less useful because there is no way to invert a piecewise polynomial. To obtain a predicted value from a measured response, one would have to construct an entirely new piecewise polynomial with reversal of stimulus and response

roles, which is not of interest. The polynomial fit was second-order as the fit was sufficient for the data, not to mention any higher orders resulted in loss of monotonicity, as one might expect by the sharp turn in the red lines at higher oxygen concentrations. For the Stern-Volmer fits, it is hard to judge by appearance which model may be best.

An assessment of the fits may also be done more quantitatively. A model utility F-test[81] was performed on the four fits. That test followed equation 4-4,

$$F = \frac{r^2/_k}{(1-r^2)(n-k-1)} \tag{4-4}$$

where r^2 represents the coefficient of determination for the fit, k the degrees of freedom of the model, and n the number of data points. The F statistic was compared to a standard table and it was found that only the partial quadratic fit passed the test ($p < 0.05$). This may not be too surprising as the full quadratic fit does not qualitatively appear to be a good fit and the Stern-Volmer model has been repeatedly shown in this study and in the literature to deviate from ideality. This result would be more important if we were attempting to come up with a physical model for the system, but in this section, we are only interested in calibration performance.

With the models constructed, the next step was to employ each model for each microwell, and to assess the behavior against the randomized points. The randomized points were selected by a random number generator that would generate a real number between 10 and 20, to represent the biological range of interest for oxygen concentrations. For the data discussed here, the random values were 10.2%, 11.6%,

14.9%, 18.1%, and 20.8%. The polynomial fitted data is shown in Figures 99 and 100.

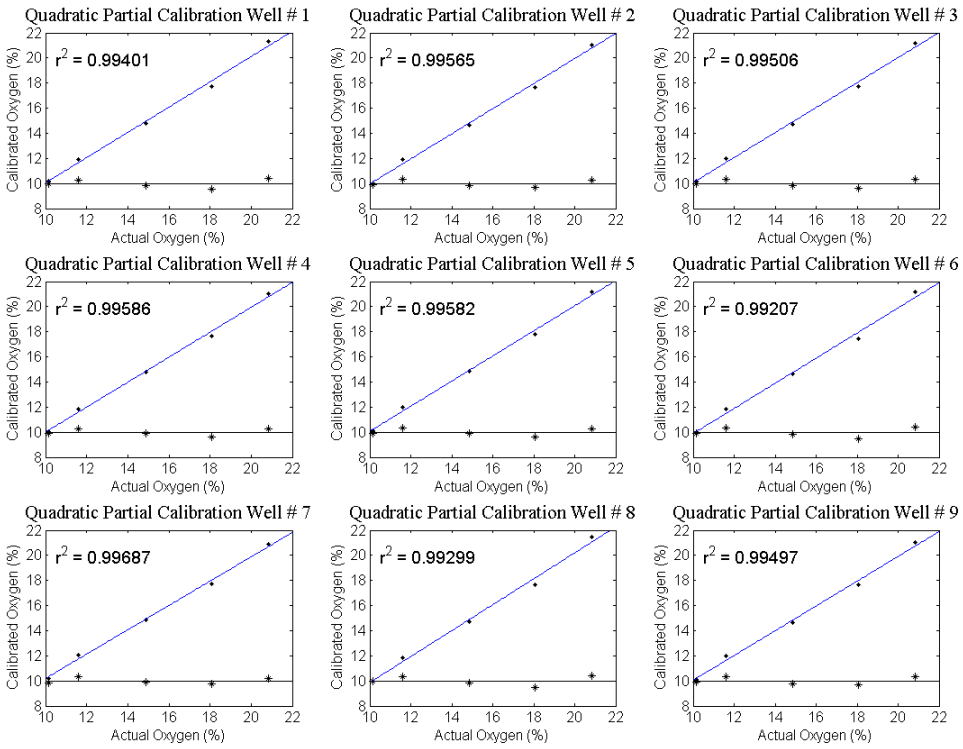

Figure 99: Partial Quadratic Response for Comparative Calibration

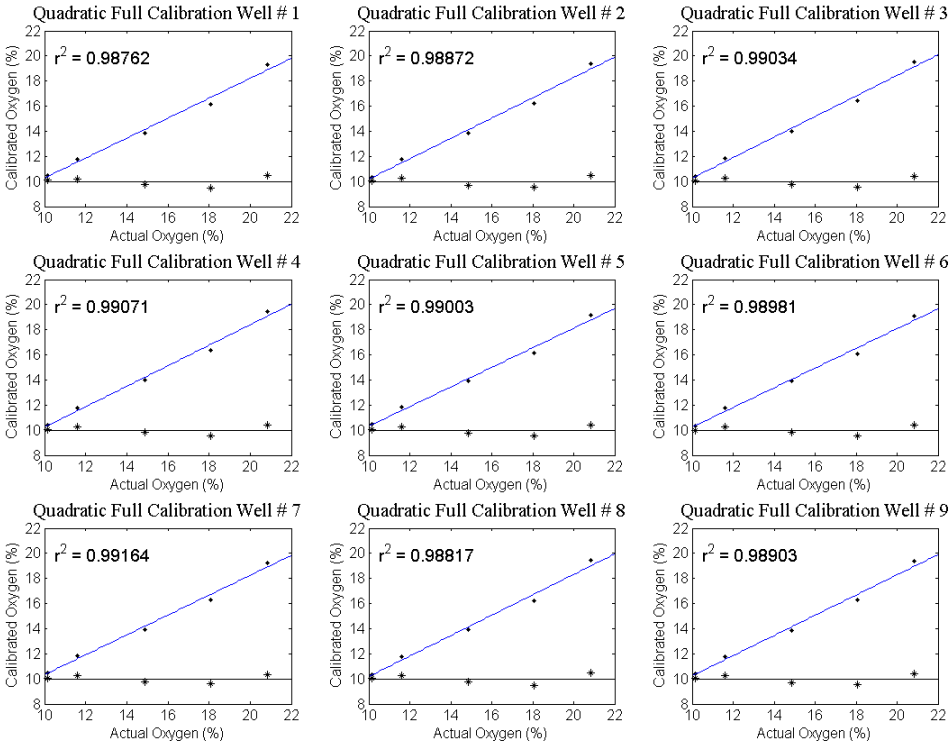

Figure 100: Full Quadratic Response for Comparative Calibration

Note that while the partial and full calibrations refer to how the model was constructed, the comparative calibration response to the randomized values was only analyzed within the range of biological interest, 10% to 20% oxygen concentration. The plots in Figures 99 and 100 may look odd at first glance. That is because the data is displayed, as well as residuals. The residuals were artificially increased by 10, in order to view them clearly on the plot. The black dots represent the measured data points, while the asterisks represent the residual value at that point, from the linear fit. The blue lines represent the fitted data, which was a classic least squares linear fit in every case. This analysis does not particularly reveal much information. All the residuals appear randomized, which is appropriate; all the coefficients of determination were similar and of acceptable value,

though by no means outstanding; and all the qualitative appearances of the blue lines look appropriate to the data.

Next, Figures 101 and 102 display a similar result for the Stern-Volmer analysis.

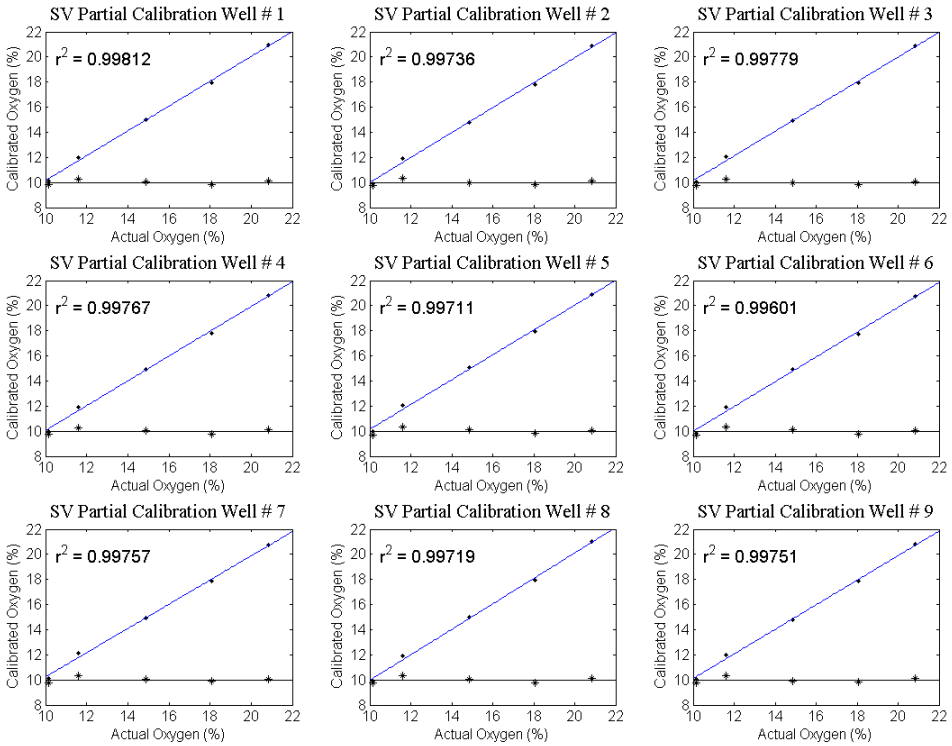

Figure 101: Partial Stern-Volmer Response for Comparative Calibration

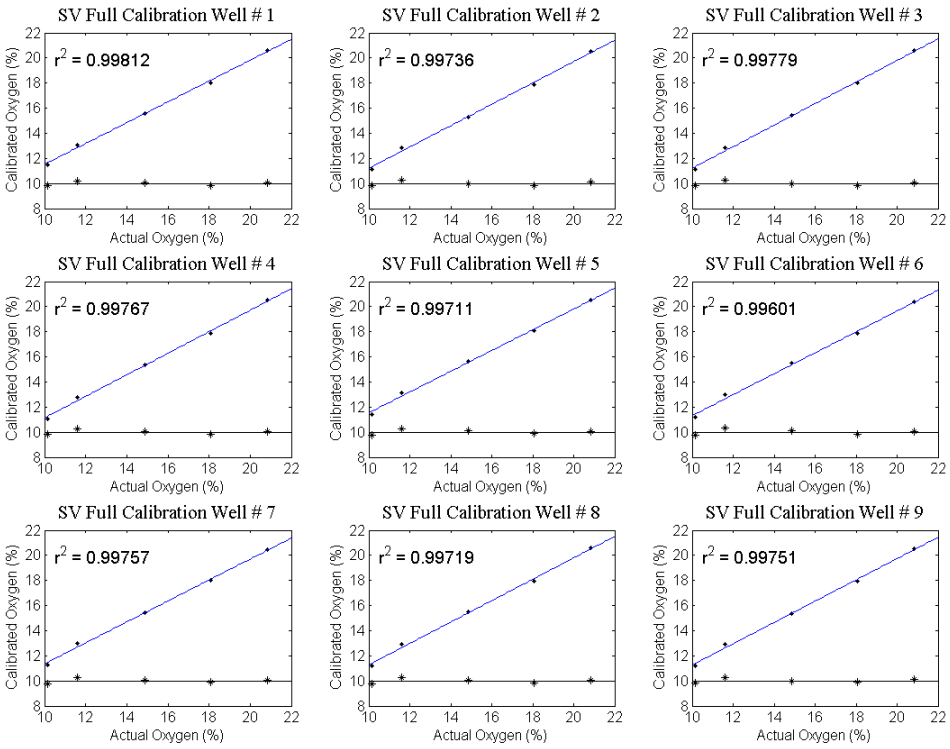

Figure 102: Full Stern-Volmer Response for Comparative Calibration

The data also shows a similar response as the quadratic response. The residual plots are randomized, the coefficients of determination are quite similar, and the fitted data qualitatively looks fine. How then to decide which method is superior?

We can return to Figures 97 and 98 and state subjectively that all fits show potential for a useful analysis, except for the quadratic fit to the full set of data. It was quite convincing that a full quadratic fit always had difficulty, within the range of biological interest. The sharp turn at higher oxygen concentrations was causing too much deviation to be a good model. From Figures 99-102, there was no clear choice, but another statistic to examine would be the root-mean-square error (rmse) from the classic least squares fit. That statistic could be viewed as an average of all the standard

deviations from the presumed normal distribution, from the fitting process, about each measured point. Table 7 summarizes the results.

Table 7: Summary of Comparative Calibration RMSE

Response Model	*rmse Method 1*	*rmse Method 2*
Partial Stern-Volmer	0.258	0.231
Full Stern-Volmer	0.220	0.187
Partial Quadratic	0.366	0.192
Full Quadratic	0.420	-------

In Table 7, method 1 pertains to the current discussion; method 2 will be discussed shortly. The full quadratic response was not analyzed as the previous data showed it not to be a viable model. With the rmse statistic, the best response was when the statistic is minimized (i.e. errors are minimized). Clearly that occurred for the full Stern-Volmer response. That was not expected as it was contemplated that a polynomial fit would suffice. Given this result, a few conclusions may be drawn. Calibration performance in general does not vary a lot, but there was an advantage to the full Stern-Volmer response, when viewed from the perspective of minimal rmse. One could contemplate that calibrations desired over a narrow range would perform adequately from a quadratic fit, but only over the range measured. For larger ranges, or for the minimal rmse over any range, one should perform the full Stern-Volmer linearization. Recall that the disadvantage to that is the need for a good τ_0 measurement, which can be time consuming.

Method 2 in Table 7 was another run that was investigated. The plotted results look quite similar to the last few Figures and again, the rmse statistic was the tool that revealed the subtle difference between response models. Again, the full Stern-Volmer response had the best result. The reader is directed to recall some of the lifetime plots,

such as Figure 78. When many lifetime plots were examined, it would appear that it was often the case for lifetime data from ratiometric methods to display a “sweet” spot. In other words, a narrow range would have excellent overlap between the three methods, but then would deviate slightly in going in either direction. One might contemplate that that was an indication of an optimal bin size for the LPL method. The data for method 2 in Table 7 was collected by varying the bin size. Shorter lifetimes utilized a narrower bin, while longer lifetimes utilized a wider bin; the range varied from 45-90 μs. The improved results would indicate that dynamically adjusting bin size may minimize errors even further.

The method 1 data could also be analyzed one step further. A prediction model could be constructed from the calibration model, as an additional assessment of performance. That is depicted in Figure 103.

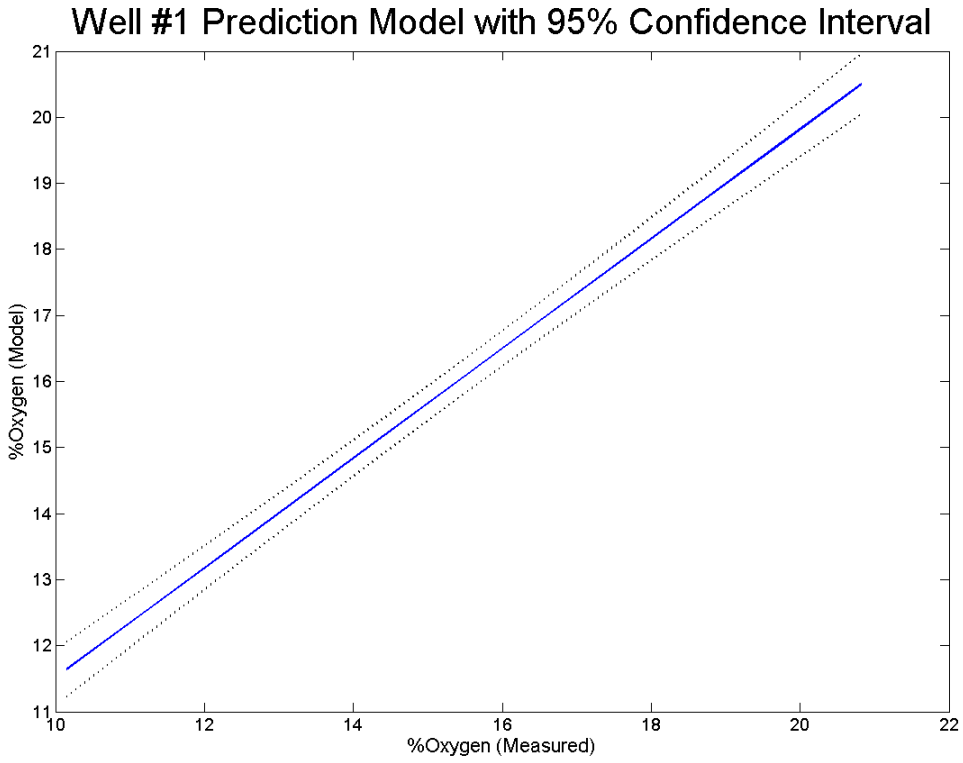

Figure 103: Prediction Model for the MOD Sensor

The prediction model simply means that the model fit is displayed (blue line) along with the 95% confidence interval (dashed line). The confidence interval was constructed based upon the entire data set for the method 1 data, utilizing the full Stern-Volmer response model. In other words, any hypothesis testing for a response within the range of measured data, will fall between the dashed lines at the 95% confidence level. The tightness of the plot is an indication that the calibration methodology was robust.

Some final comments on analytical performance may also be made at this time, given the comparative calibration performance. Generally for any given sensor, there is

interest in its robustness, dynamic range, selectivity, and sensitivity. The sensor materials evaluated in this study do suffer from robustness challenges. Most were unable to retain adhesion to the microwells when submerged in water at 37 °C. The IB sensor material was the exception, but even that material had been observed on many occasions to exhibit delamination problems during actual biological experiments. On the other hand, the analytical performance was quite robust, as performance under various calibration models resulted in only subtle changes, with the exception of the full quadratic response model, which is not recommended for use. Caution should be exercised when utilizing these sensor materials. The experiments in this study were isothermal; response changes to temperature can be quite profound if not accounted for when not under isothermal conditions.

The dynamic range for these sensor materials was just adequate for the biological region of interest. Interest in oxygen concentrations less than 10% will only improve sensor performance. The data would also suggest that the luminophore response may not be adequate for oxygen concentrations exceeding ambient levels (20.95%). The MOD sensor material had the best dynamic range and is worthy of further development.

The sensitivity of the MOD sensor material may also be examined. One can talk of sensitivity in terms of detection limits or the slope of calibration curves. For these optical sensors, detection limits do not have much meaning (also see Section 5.7). Sensitivity only increases rapidly as the sensor approaches its natural, or anoxic, lifetime value. The response is also nonlinear, so sensitivity will always vary with analyte concentration. However, we can look at the full Stern-Volmer response model and obtain some level of a sensitivity response. One can utilize the model to obtain predicted values

in lifetime over the range of biological interest, and then treat that value as a quasi-linear slope. In doing that for the data associated with Figure 103, we obtain a value of ~5 μs/%O_2. A similar procedure could be carried out for the partial quadratic response model, however, there seems to be a loss in meaning by that method, as the result would be expressed in terms of a dimensionless ratio. With the LPL method providing a lifetime measurement for any of the operational sensors (IB, PtF, MOD) to a resolution of at least 0.01 μs or better, the stated sensitivity is adequate for any oxygen concentration measurements of biological interest.

Chapter Five: Concluding Remarks

5.1 Summary

In this study, thin film luminescent sensors were developed along with new methodology to measure dissolved oxygen in highly restricted volumes. The initial goal was to improve experimental repeatability, in order to allow other researchers at the MLSC to conduct research into the mechanisms of esophageal adenocarcinomas related to Barrett's Esophagus. The initial goal was achieved by developing the picoinjection method of sensor deposition into an arrangement of 3x3 arrays of microwells in fused silica glass. The improved sensor deposition then motivated improvements into image processing algorithms, in order to improve image spatial resolution of image data, by a factor of 100x. Data collection methods were also improved to take advantage of the full potential of a scientific grade intensified CCD camera. The resulting improvements in experimental repeatability were very significant.

The next phase of this study was to develop sensors with an improved response over a commercially available material (IB). The PSP material was also commercially available, but failed toxicity screenings. It was analyzed as a matrix comparison test, but the sensor material failed to perform adequately under submerged conditions. A custom bead material was also evaluated (ANH), but that material failed to retain any adhesion very quickly during the hydration evaluation. The IB, PtF, and MOD sensor materials were thus of primary focus for the second phase of this study. All three materials performed adequately for the task at hand, but the MOD material exhibited the best

optical performance. However, the MOD and PtF sensor materials both lost adhesion very quickly when subjected to the delamination test.

The IB sensor material showed an adequate optical response and had the best picoinjection performance. Given that it was the only sensor material with enough adhesion property to be useful, it was selected as the overall best sensor. It is very possible that the methodology utilized to make the IB sensor material could be employed quite readily with the MOD sensor material to make a superior bead type product. It was contemplated that a carboxylate modied polystyrene bead matrix would retain the superior adhesion and picoinjection properties, while having little affect on the optical performance, resulting in an improved sensor material.

During this study, a surprising source of autofluorescence was noted, but the investigations into this problem resulted in discovery of LPL, a new method for lifetime assessment. The ORLD method was also utilized in this study. The ORLD method has the advantage of collecting data after the excitation pulse, eliminating any source of stray light. The LPL method does not have that advantage, since data is collected during the excitation pulse. Results must be meticulously scrutinized for stray light effects. Once stray light is minimized, then the LPL method was found to offer a substantially improved SNR advantage over the ORLD method.

5.2 Automating Sensor Deposition

The picoinjection method for sensor deposition worked very well, especially for the IB sensor material, but there were some challenges. The method is rather tedious. However, it would be amenable to automation. The custom made capillary tips that were

utilized were held over the microwells at approximately a 45° angle. That was done only because it was the only method that would work with the micromanipulator stage that was used. Perhaps an automated xy-translation stage could be utilized with a separate mechanical device to hold the capillary tip, which would then have automated z-axis control. Production of the fused silica microwells utilized in this study produced glass chips that were quite uniform. A uniform microwell appearance would be likely adaptable to easy image recognition algorithms that would place the capillary tip in the correct spot. Any delays that were needed for the injection could also be readily programmed into control software. Additionally, it is contemplated that moving the tip from 45° to 90° would offer additional advantages. During the picoinjection process, one of the most common problems was for sensor solution to slowly crawl up the side of the polyimide coating. A 90° mount should help to reduce or eliminate this problem.

The other common problem was capillary tips clogging. It was believed that solvent evaporation at the tip would create a "skin" over the hole, causing the clog. If the local environment were air-saturated with solvent, then the problem should diminish. There was some evidence to support this belief. For the last two glass chips that were made, a modification was tried. A lab tissue was soaked in the same solvent that was utilized for the sensor material, and then placed immediately adjacent to the picoinjection tip. That was tried for the MOD sensor material and the PSP sensor material. In both cases, tip clogs were dramatically reduced or eliminated. Additionally, inject pressures were reduced. One could contemplate building a chamber around the picoinjection chamber and maintaining an environment that was air-saturated with the appropriate solvent. The problem with that approach would be complexity of such an apparatus and

safety concerns. For aqueous based sensor materials, safety concerns would be minimized. Sensor materials dispersed in organic solvent would potentially create fire, health, or explosion hazards. The excellent response to the tissue test may suggest that a simpler approach would be to have a dish mounted under the injection area to contain solvent. Evaporation could be utilized to maintain the desired atmosphere over a much smaller area. Local ventilation in the injection area to exhaust vapors would minimize health and safety risks.

5.3 Improving Dissolution of Test Gasses

It was mentioned earlier that the volume of the chip holder is approximately 20 million times larger than a microwell. One of the frustrating parts of this study was waiting for equilibration of test gasses. Results were improved and wait times were decreased when the chip holder was modified to enable gas sparging, as well as gas purging. The complexity of multiple tubes connecting near the imaging area was also a challenge. One alternative approach could be to move the gas exchange outside of the sample area. Water or other test solutions could instead be pumped through a much smaller chip holder area. The pumped fluids would travel through an external chamber that could be rapidly purged to the desired gas concentration. Inside the external chamber, highly permeable thin tubing would be exposed to the test gas. In this manner, a large surface area of fluid would be exposed to a large reservoir of test gas, enabling more rapid exchange.

The plumbing would certainly be more complex and a pump would be needed. The advantages would seem to make the idea worthwhile for any pursuits of a next

generation test station. One problem with the current generation sparging system was the introduction of bubbles into the image. The interference from bubbles was surprisingly minimal, when the sparging tube was positioned correctly. Movement of the sparging tube would introduce variation into image data. The external purge system would eliminate that problem. The current chip holder utilized cartridge heaters to heat the aluminum block around the test area. With the proper control system, this worked well with rapid (~5 minute) warm-up times and was stable to ~ 0.1 °C. With a fluid pump, the fluid could be heated directly. This may or may not provide a minor advantage.

Another advantage related to heating, would be control of evaporative losses. Long experimental runs would potentially lose water, resulting in chaotic data, as bubbling became more intense from the loss of water. A smaller chamber could be more readily sealed and fluid levels could be monitored and controlled externally. With a more tightly sealed chamber and external fluid control, evaporative losses would no longer be an issue.

Two disadvantages should be evaluated, however, for a pumped system. The Clark microelectrode was always utilized in a static operational mode. If fluids moved rapidly enough, it may have to be switched to a dynamic operation mode. That adds complexity to the data collection and analysis, but is certainly a well-proven method.[59] The second disadvantage could be delamination of sensor material. It is possible the moving fluids will more readily cause the sensor material to lose adhesion and delaminate.

5.4 Excitation Source Improvements

The LEDs utilized for this study were high-powered excitation sources. The high-power was needed to illuminate the sensor rings adequately. Much of the power was lost in the system. The optical path of an epifluorescence microscope contains several glass optical components, the dichroic mirror must turn the light, there are aperture losses, and finally the narrow band filter utilized to reduce the autofluorescence problem allowed only a fraction of the output light to be transmitted into the microscope. A lowerpowered LED could be utilized if many of those losses could be eliminated.

One option would be to mount an LED on the plunger (see Figure 4). One could replace the steel rod by a magnifying rod to couple the light directly to the correct region. That would also eliminate the need for the dichroic mirror and stray excitation light would likely be minimal. A low-power LED may reduce photodegradation issues and may reduce the induction effect.

Lloyd Burgess, a researcher with the MLSC, constructed a prototype device. Its performance appeared quite promising. Unfortunately, it was accidentally destroyed before any data could be collected and materials to build a new one were not available.

5.5 Data Processing Improvement for Sensor Locations

The processing of image data potentially has room for improvement. That step is a relatively slow step, compared to other analysis steps. While the magnitude for processing is only a few seconds per data point, one could imagine that that would be undesirable in a high throughput system. Alternatives were not examined, as there was sufficient variation in the picoinjection process. However, if the improvements suggested

in section 5.2 were successful and produced highly uniform rings, the ring finding step could be altered. An image processing algorithm that is highly efficient at finding well-defined edge-like features is skeletonization.[78] That algorithm is efficient for geometric patterns and essentially traces out the shape, with a width of one pixel. Highly uniform sensor rings would be very amenable to such a process. If skeletonization were successful, then one would merely perform a pixel dilation to expand the "skeleton" to the proper size for the sensor ring. It is predicted that such an algorithm would be very efficient and rapid.

5.6 Further Explorations of Long-Pulsed Luminescence

A couple of points are worth mentioning in regards to the LPL method. For the purposes of this study, the method worked extremely well. However, all the luminophores utilized in this study operate via phosphorescence. Fluorescence is a more common phenomenon and is a short-lived event, relative to phosphorescence. The convenience of ignoring edge effects in the excitation pulse would be lost. The convolution model would no longer be so simple. However, it may not be that complex. Equation 2-28 suggested that if the LPL method were further refined to account for multiple exponentials, the convolution result is also the sum of exponentials.

The much shorter pulses that would be utilized for fluorescence show significant turn-on and turn-off effects. Those effects for LEDs and laser diodes are related to device capacitance, which is itself an exponential decay or rise. Rather than the detected signal being the convolution of a rectangular pulse with an exponential decay, the excitation pulse could be modeled as the sum of appropriate exponential rise and decays

and a rectangular pulse, which would then be convoluted with the exponential decay of the luminophore. Assuming that an excitation pulse were successfully modeled as a simple sum of exponentials and a rectangular pulse and thus separable for integration, then the remaining question would be, what then is the convolution of two exponentials? If one carries out the integrations, the result is simply a sum of exponentials. Thus for a fluorescent luminophore, the convolutions may be reduced to a sum of various exponentials. Then the challenges would how to best detect and analyze them ratiometrically.

A final problem must always be contemplated in regards to the LPL method. In this study, the importance of minimizing stray excitation light was emphasized and that would always be true. Another source of photons must also be considered. For the luminophores utilized in this study, there were no known complications from either fluorescence or delayed fluorescence. That will not necessarily be the case for all luminophores. A particular luminophore must be studied and its photophysical processes understood in order to choose the proper detection and analysis methods. The presence of delayed fluorescence (for fluorophores) or any type of fluorescence (for phosphors) could render the LPL method useless for analysis. It is possible in some cases to remove such signals via optical filters, but if not, then alternatives would have to be explored.

5.7 Comments on Statistical Analysis

The author realizes that the statistical analysis in this study was not too rigorous. The author has sufficient knowledge to realize that, but not sufficient knowledge to properly explore more advanced analyses. It may be useful to conduct analysis of

variance (ANOVA) type of work on the ratio data. That may or may not glean useful information as to variation between the microwells. It may also be interesting to have a better understanding on the limit of detection in terms of oxygen concentration. As discussed earlier, sensitivity was estimated in terms of a lifetime change per change in oxygen concentration (in %). However, this study revealed the sensors are capable of exquisite repeatability. The independent variable in many of the plots was oxygen concentration. For the simple analyses conducted in this study, oxygen concentration was therefore presumed to be independent and with zero variation. However, the mass flow controllers and the Clark microelectrode did not have zero variation, but more on the order of 10^{-4} in oxygen concentration. Therefore, it would be difficult to determine a detection limit in light of such variation.

The assumption of zero variation in oxygen concentration was also important for regression analysis. Regression analysis should really be performed more generally, where that assumption is not necessary. The lack of a proper physical model was also not satisfactory. The Stern-Volmer model is often utilized as "close enough." In this study, we also explored a simple polynomial fit to ratiometric data. One other possibility that may be explored with more advanced statistical knowledge, would be to apply simple physical principles to the ratiometric data. In other words, perhaps a rational model could be constructed, where the numerator and denominator terms are both composed of exponential terms, which is after all, how the ratiometric data is produced.

REFERENCES

1. J.M. Dragavon, *Development of a Cellular Isolation System for Real-Time Single Cell Oxygen Consumption Monitoring*, University of Washington doctoral dissertation, **2006**.

2. J. Dragavon, T. Molter, C. Young, T. Strovas, S. McQuaide, M. Hall, M. Zhang, B. Cookson, A. Jen, M. Lidstrom, D. Meldrum, L. Burgess, A cellular isolation system for real-time single-cell oxygen consumption monitoring, *Journal Royal Society Interface*, **5** (Supp 2), (2008), S151-9.

3. http://www.lifeonachip.org/

4. M.E. Lidstrom & D.R. Meldrum, Life-on-a-chip, *Nature Reviews Microbiology*, **1**, (2003), 158-64.

5. S.B. Umar & D.E. Fleischer, Esophageal cancer: epidemiology, pathogenesis and prevention, *Nature Clinical Practice Gastroenterology & Hepatology*, **5**, (2008), 517-26.

6. S.J. Spechler, R.C. Fitzgerald, G.A. Prasad, K.K. Wang, History, Molecular Mechanisms, and Endoscopic Treatment of Barrett's Esophagus, *Gastroenterology*, **138**, (2010), 854-69.

7. N.R. Barrett, The lower esophagus lined by columnar epithelium, *Surgery*, **41**, (1957), 881-94.

8. H. Pohl, H.G. Welch, The Role of Overdiagnosis and Reclassification in the Marked Increase of Esophageal Adenocarcinoma Incidence, *Journal of the National Cancer Institute*, **97**, (2005), 142-6.

9. J. Zeng, J. Wang, W. Gao, A. Mohammadreza, L. Kelbauskas, W. Zhang, R.H. Johnson, D.R. Meldrum, Quantitative single-cell gene expression measurements of multiple genes in response to hypoxia treatment, *Annals of Bioanalytical Chemistry*, **401**, (2011), 3-13.

10. C.C. Maley, P.C. Galipeau, J.C. Finley, V.J. Wongsurawat, X. Li, C.A. Sanchez, T.G. Paulson, P.L. Blount, R. Risques, P.S. Rabinovitch, and B.J. Reid, Genetic clonal diversity predicts progression to esophageal adenocarcinoma, *Nature Genetics*, **38**, (2006), 468-73.

11. O. Warburg, On the Origin of Cancer Cells, *Science*, **123**, (1956), 309-14.

12. J.A. Bertout, S.A. Patel, M. Celeste Simon, The impact of O_2 availability on human cancer, *Nature Reviews Cancer*, **8**, (2008), 967-75.

13. M. López-Lázaro, Why Do Tumors Metastasize?, *Cancer Biology & Therapy*, **6**, (2007), 141-4.

14. R.A. Gatenby and R.J. Gillies, A microenvironmental model of carcinogenesis, *Nature Reviews Cancer*, **8**, (2008), 56-61.

15. R.G. Bristow and R.P. Hill, Hypoxia, DNA repair and genetic instability, *Nature Reviews Cancer*, **8**, (2008), 180-92.

16. G.M. Edelman and J.A. Galley, Degeneracy and complexity in biological systems, *Proceedings of the National Academy of Sciences*, **98**, (2001), 13763-68.

17. Unpublished MLSC data collected by T.W. Molter and S.M. McQuaide, 2007.

18. P.R. Allison and A.S. Johnstone, The oesophagus lined with gastric mucous membrane, *Thorax*, **8**, (1953), 87-101.

19. R.E. Sampliner, Updated guidelines for the diagnosis, surveillance, and therapy of Barrett's Esophagus, *The American Journal of Gastroenterology*, **97**, (2002), 1888-95.

20. H. Hampel, N.S. Abraham, and H.B. El-Serag, Meta-Analysis: Obesity and the risk for gastroesophageal reflux disease and its complications, *Annals of Internal Medicine*, **143**, (2005), 199-211.

21. Z.R. Edelstein, D.C. Farrow, M.P. Bronner, S.N. Rosen, and T.L. Vaughan, Central adiposity and risk of Barrett's Esophagus, *Gastroenterology*, **133**, (2007), 403-11.

22. T.L. Vaughan, A.R. Kristal, P.L. Blount, D.S. Levine, P.C. Galipeau, L.J. Prevo, C.A. Sanchez, P.S. Rabinovitch, and B.J. Reid, Nonsteroidal anti-inflammatory drug use, body mass index, and anthropometry in relation to genetic and flow cytometric abnormalities in Barrett's Esophagus, *Cancer Epidemiology, Biomarkers & Prevention*, **11**, (2002), 745-52.

23. T.L. Vaughan, S. Davis, A. Kristal, and D.B. Thomas, Obesity, alcohol, and tobacco as risk factors for cancers of the esophagus and gastric cardia: adenocarcinoma versus squamous cell carcinoma, *Cancer Epidemiology, Biomarkers & Prevention*, **4**, (1995), 85-92.

24. B.J. Reid, X. Li, P.C. Galipeau, and T.L. Vaughan, Barrett's oesophagus and oesophageal adenocarcinoma: time for a new synthesis, *Nature Reviews Cancer*, **10**, (2010), 87-101.

25. K.K. Wang and R.E. Sampliner, Updated guidelines 2008 for the diagnosis, surveillance and therapy of Barrett's Esophagus, *American Journal of Gastroenterology*, **103**, (2008), 788-97.

26. A. Marusyk, V. Almendro and K. Polyak, Intra-tumor heterogeneity: a looking glass for cancer? *Nature Reviews Cancer*, **12**, (2012), 323-34.

27. J.D. Winefordner, S.G. Schulman and T.C. O'Haver, *Luminescence Spectrometry in Analytical Chemistry*, Wiley-Interscience, New York, 1972.

28. D. Dolphin (ed.), *The Porphyrins, V. III*, Academic Press, New York, 1978.

29. S.D. Eben and H. Kasai, Characterization of platinum porphyrins and its interaction with oxygen by density functional theory, *e-Journal of Surface Science and Nanotechnology*, **3**, (2005), 473-75.

30. J. Kavandi, J. Callis, M. Gouterman, G. Khalil, D. Wright, E. Green, D. Burns, B. McLachlan, Luminescent barometry in wind tunnels, *Review of Scientific Instruments*, **61**, (1990), 3340-47.

31. M. Gouterman, Oxygen quenching of luminescence of pressure sensitive paint for wind tunnel research, *Journal of Chemical Education*, **74**, (1997), 697-702.

32. K.S. Schanze, B.F. Carroll, S. Korotkevitch, M.J. Morris, Temperature dependence of pressure sensitive paints, *AIAA Journal*, **35**, (1997), 306-10.

33. E. Puklin, B. Carlson, S. Gouin, C. Costin, E. Green, S. Ponomarev, H. Tanji, M. Gouterman, Ideality of pressure-sensitive paint. I. Platinum tetra(pentafluorophenyl)porphine in fluoroacrylic polymer, *Journal of Applied Polymer Science*, **77**, (2000), 2795-2804.

34. S. Gouin and M. Gouterman, Ideality of pressure-sensitive paint. II. Effect of annealing on the temperature dependence of the luminescence, *Journal of Applied Polymer Science*, **77**, (2000), 2805-14.

35. S. Gouin and M. Gouterman, Ideality of pressure-sensitive paint. III. Effect of the base-coat permeability on the luminescence behavior of the sensing layer, *Journal of Applied Polymer Science*, **77**, (2000), 2815-23.

36. S. Gouin and M. Gouterman, Ideality of pressure-sensitive paint. IV. Improvement of luminescence behavior by addition of pigment, *Journal of Applied Polymer Science*, **77**, (2000), 2824-31.

37. G. Khalil, C. Costin, J. Crafton, G. Jones, S. Grenoble, M. Gouterman, J.B. Callis, L.R. Dalton, Dual-luminophor pressure-sensitive paint I. Ratio of reference to sensor giving a small temperature dependency, *Sensors and Actuators B*, **97**, (2004), 13-21.

38. B. Zelelow, G. Khalil, G. Phelan, B. Carlson, M. Gouterman, J.B. Callis, L.R. Dalton, Dual-luminophor pressure-sensitive paint II. Lifetime based measurement of pressure and temperature, *Sensors and Actuators B*, **96**, (2003), 304-14.

39. S. Grenoble, M. Gouterman, G. Khalil, J. Callis, L. Dalton, Pressure-sensitive paint (PSP): concentration quenching of platinum and magnesium porphyrin dyes in polymeric films, *Journal of Luminescence*, **113**, (2005), 33-44.

40. S. Hyuk Im, G.E. Khalil, J. Callis, B. Hyun Ahn, M. Gouterman, Y. Xia, Synthesis of polystyrene beads loaded with dual luminophors for self-referenced oxygen sensing, *Talanta*, **67**, (2005), 492-7.

41. F. Kimura, G. Khalil, N. Zettsu, Y. Xia, J. Callis, M.Gouterman, L. Dalton, D. Dabiri, M. Rodriguez, Dual luminophore polystyrene microspheres for pressure-sensitive luminescent imaging, *Measurement Science and Technology*, **17**, (2006), 1254-60.

42. F. Kimura, M. Rodriguez, J. McCann, B. Carlson, D Dabiri, G. Khalil, J. Callis, Y. Xia, M. Gouterman, Development and characterization of fast responding pressure sensitive microspheres, Review of Scientific Instruments, 79, (2008), 074102-1-074102-8.

43. G. Teyssedre, D. Mary, C. Laurent, Analysis of the luminescence decay following excitation of polyethylene naphthalate films by an electric field, *Journal of Physics D: Applied Physics*, **31**, (1998), 267-75.

44. S. Pan and L.J. Rothberg, Enhancement of platinum octaethyl porphyrin phosphorescence near nanotextured silver surfaces, *Journal of the American Chemical Society*, **127**, (2004), 6087-94.

45. M. Previte, K. Aslan, Y. Zhang, C.D. Geddes, Metal-enhanced surface plasmon-coupled phosphorescence, *Journal of Physical Chemistry C*, **111**, (2007), 6051-9.

46. B. Minaev, Theoretical study of the external heavy atom effect on phosphorescence of free-base porphin molecule, *Spectrochimica Acta Part A*, **60**, (2004), 3213-24.

47. G. Khalil, A. Chang, M. Gouterman, J.B. Callis, L.R. Dalton, Oxygen pressure measurement using singlet oxygen emission, *Review of Scientific Instruments*, **76**, (2005), 054101-1 to 054101-8.

48. E.R. Carraway, J.N. Demas, B.A. DeGraff, Luminescence quenching mechanism for microheterogeneous systems, *Analytical Chemistry*, **63**, (1991), 332-36.

49. E.R. Carraway, J.N. Demas, B.A. DeGraff, J.R. Bacon, Photophysics and photochemistry of oxygen sensors based on luminescent transition-metal complexes, *Analytical Chemistry*, **63**, (1991), 337-42.

50. J.N. Demas, B.A. DeGraff, W. Xu, Modeling of luminescence quenching-based sensors: Comparison of multisite and nonlinear gas solubility models, *Analytical Chemistry*, **67**, (1995), 1377-80.

51. D. Badocco, A. Mondin, A. Fusar, G. Favaro, P. Pastore, Influence of the real background signal on the linearity of the Stern-Volmer calibration for the determination of molecular oxygen with optical sensors, *Journal of Physical Chemistry C*, **113**, (2009), 15742-50.

52. A. Mills, Controlling the sensitivity of optical oxygen sensors, *Sensors and Actuators B*, **51**, (1998), 60-8.

53. T.W. Molter, S.C. McQuaide, M.T. Suchorolski, T.J. Strovas, L.W. Burgess, D.R. Meldrum, M.E. Lidstrom, A microwell array device capable of measuring single-cell oxygen consumption rates, *Sensors and Actuators B*, **135**, (2009), 678-86.

54. Personal conversations with MLSC Research Scientist, Micheal Konopka.

55. B.B. Benson and K. Krause, Jr., The concentration and isotopic fractionation of gases dissolved in freshwater in equilibrium with the atmosphere. 1. Oxygen, *Limnology and Oceanography*, **25**, (1980), 662-71.

56. B.B. Benson and K. Krause, Jr., The concentration and isotopic fractionation of oxygen dissolved in freshwater and seawater in equilibrium with the atmosphere, *Limnology and Oceanography*, **29**, (1984), 620-32.

57. T.R. Rettich, R. Battino, E. Wilhelm, Solubility of gases in liquids. 22. High-precision determination of Henry's law constants of oxygen in liquid water from T = 274 K to T = 328 K, *Journal of Chemical Thermodynamics*, **32**, (2000), 1145-56.

58. D. Tromans, Temperature and pressure dependent solubility of oxygen in water: a thermodynamic analysis, *Hydrometallurgy*, **48**, (1998), 327-42.

59. M.L. Hitchman, *Measurement of Dissolved Oxygen*, John Wiley & Sons, NY, 1978.

60. D. Tromans, Modeling oxygen solubility in water and electrolyte solutions, *Industrial & Engineering Chemistry Research*, **39**, (2000), 805-12.

61. H.N. Rasmussen and U.F. Rasmussen, Oxygen solubilities of media used in electrochemical respiration measurements, *Analytical Biochemistry*, **319**, (2003), 105-13.

62. Personal conversation with Michael Hagen, Microelectrodes, Inc.

63. T.W. Molter, M.R. Holl, J.M. Dragavon, S.C. McQuaide, J.B. Anderson, A.C. Young, L.W. Burgess, M.E. Lidstrom, D.R. Meldrum, A new approach for measuring single-cell oxygen consumption rates, *IEEE Transactions on Automation Science and Engineering*, **5**, (2008), 32-42.

64. R.D. Shonat and A.C. Knight, Oxygen tension imaging in the mouse retina, *Annals of Biomedical Engineering*, **31**, (2003), 1084-96.

65. E. Gratton, D.M. Jameson, Multifrequency phase and modulation fluorometry, *Annual Reviews in Biophysics and Bioengineering*, **13**, (1984), 105-24.

66. W. Trettnak, C. Kolle, F. Reininger, C. Dolezal, P. O'Leary, Miniaturized luminescence lifetime-based oxygen sensor instrumentation utilizing a phase modulation technique, *Sensors and Actuators B*, **35-36**, (1996), 506-12.

67. S.A. Vinogradov, M.A. Fernandez-Searra, B.W. Dugan, D.F. Wilson, Frequency domain instrument for measuring phosphorescence lifetime distributions in heterogeneous samples, *Review of Scientific Instruments*, **72**, (2001), 3396-3406.

68. M. Valledor, J.C. Campo, I. Sánchez-Barragán, J.M. Costa-Fernández, J.C. Alvarez, A. Sanz-Medel, Determination of phosphorescence lifetimes in the presence of high background signals using phase-shift measurements, *Sensors and Actuators B*, **113**, (2006), 249-58.

69. T.J. Strovas, S.C. McQuaide, J.B. Anderson, V. Nandakumar, M.G. Kalyuzhnaya, L.W. Burgess, M.R. Holl, D.R. Meldrum, M.E. Lidstrom, Direct measurement of oxygen consumption rates from attached and unattached cells in a reversibly sealed, diffusionally isolated sample chamber, *Advances in Bioscience and Biotechnology*, **1**, (2010), 398-408.

70. J.R. Etzkorn, W. Wu, Z. Tian, P. Kim, S. Jang, D.R. Meldrum, A. Jen, B.A. Parviz, Using micro-patterned sensors and cell self-assembly for measuring the oxygen consumption rate of single cells, *Journal of Micromechanics and Microengineering*, **20**, (2010), 1-11.

71. S.P. Chan, Z.J. Fuller, J.N. Demas, B.A. DeGraff, Optimized gating scheme for rapid lifetime determinations of single-exponential luminescence lifetimes, *Analytical Chemistry*, **73**, (2001), 4486-90.

72. C. Moore, S.P, Chan, J.N. Demas, B.A. DeGraff, Comparison of methods for rapid evaluation of lifetimes of exponential decays, *Applied Spectroscopy*, **58**, (2004), 603-7.

73. S.P. Chan, Z.J. Fuller, J.N. Demas, F. Ding, B.A. DeGraff, Optimized gating scheme for rapid lifetime determinations of single-exponential luminescence lifetimes, *Applied Spectroscopy*, **55**, (2001), 1245-50.

74. K.K. Sharman, A. Periasamy, H. Ashworth, J.N. Demas, N.H. Snow, Error analysis of the rapid lifetime determination method for double-exponential decays and new windowing schemes, *Analytical Chemistry*, **71**, (1999), 947-52.

75. S. McGuire, C. Fisher, M. Holl, D. Meldrum, A novel pressure-driven piezodispenser for nanoliter volumes, *Review of Scientific Instruments*, **79**, (2008), 086111-1 to 086111-3.

76. X. Shen, C. Ho, T. Wong, Minimal size of coffee ring structure, *Journal of Physical Chemistry B*, **114**, (2010), 5269-74.

77. T.C. Hales, Historical overview of the Kepler conjecture, *Discrete & Computational Geometry*, **36**, (2006), 5-20.

78. J.C. Russ, *The Image Processing Handbook, 6th ed*., CRC Press, Boca Raton, 2011.

79. S.A. Moore, S.M. Frazier, M.S. Sibbald, B.A. DeGraff, J.N. Demas, On the causes of altered photophysics of luminescent metal complexes embedded in polymer hosts, *Langmuir*, **27**, (2011), 9567-75.

80. H.H. Ku, Notes on the use of propagation of error formulas, *Journal of Research of the National Bureau of Standards C. Engineering and Instrumentation*, **70C**, (1966), 263-73.

81. J.L. Devore and N.R. Farnum, *Applied Statistics for Engineers and Scientists*, Duxbury Press, Pacific Grove, CA, 1999.

APPENDIX A

Procedures for Picoinjection and Tip Production

Operating the Model PLI-100 Picoinjector

1). Turn on the power and make sure that the regulator outlet pressure is set to 90 p.s.i.g. Dry nitrogen was utilized for all injections in this study.

2). Place a glass chip on the micromanipulator platen and obtain a nicely focused image on the camera system.

3). Flush the capillary tube 2-3 times by filling and then pressing the clear button. Use the same solvent that the sensor material is dispersed into. It is strongly recommended that the optional foot pedals for the fill button and the inject button be utilized, if not already attached. This will free the hands for operation of the micromanipulator stage.

4). Verify the inject time, P_{inject}, and $P_{balance}$ are set to desired levels*.

5). Fill the capillary tube (typically filling until the inner-lok glass capillary tube was 50% filled, was deemed to be "full") with sensor material. Immediately move the tube to the first microwell as fast as possible and begin to dispense. Dispense in accord with the TTAW method* or the TD method*.

6). A properly filled capillary tube was typically just enough material to inject all 81 microwells; refill as you go if necessary.

7). In the case of clogs, immediately try flushing the tip in sensor solution. If that fails, attempt to flush with pure solvent. If that fails, attempt a forced flush by moving the tip to an inner-lok glass capillary union attached to a syringe and press on the syringe very firmly (use deionized water in the syringe). If that fails, attempt to sonicate the tip in deionized water and/or methanol. If that fails, make a new tip.

8). Upon completion of a glass chip, clean the tip; do not refill and attempt more glass chips without cleaning first. To clean the tip, flush with the same solvent that the sensor material is dispersed into, and then flush 4x with deionized water.

*Notes: If the injection time and pressure settings are not known, they must be learned. An effective method for this was determined heuristically. First set P_{inject} to a low pressure (100 kPa). Then keep stepping up the inject time until an acceptable volume is achieved. Next, start at a high pressure for P_{inject} and see

how low the inject time can be set. Then try various intermediate settings of inject time and pressure until a satisfactory volume is dispensed. The balance pressure will only need to be set if you can see the drop come out of the capillary, but it repeatedly will not dispense. It was found that this was usually necessary for organic solvents, but never for aqueous suspensions. A typical value for $P_{balance}$ was 6-7 kPa. Be forewarned that this learning step is lengthy and fraught with a frustrating amount of tip clogs. The two methods for dispensing also need to be explained. The TTAW method was typical for aqueous suspensions and means "to touch and wait." The operator should touch the tip to the bottom of the microwell, dispense, lift up immediately, and then wait until the sensor material dries before dispensing again. The TD method means "to drop." The operator should place the tip just above the bottom of the microwell, dispense, and then move immediately to the next microwell without waiting. It takes quite a bit of practice to learn the ideal height for dispensing, but the results are worth it.

Making the tips from polyimide coated glass (fused silica) capillary tubing

1). Cut a piece of tubing from the roll 3-5 cm in length, using a proper capillary tubing cutting tool.

2). Inspect both ends of the cut piece to verify that the ends are cleanly cut and free of debris.

3). Mount the tube in the chuck attached to the motor (see Figure 17). Turn on the motor at the lowest speed.

4). Lower the tip onto the rotating fiber polishing pad (see Figure 17) at an angle of roughly 45° and polish for ~ 2 minutes. The tubing material is flexible and will need to be bent a little to get a nice polish. Use a coarse polishing pad (30 μm grit) that is held to the polishing wheel by water adhesion.

5). Repeat Step 4 with a fine polishing pad (3 μm grit).

6). Inspect the ends for debris. It is recommended that a clear tube be verified by flushing with a syringe filled with deionized water (see Step 7 above).

APPENDIX B

Procedure for Photodegradation Assessment

1). Choose an array that had minimal or no light exposure to this point in the study; typically array #7 was reserved for this purpose.

2). Allow the glass chip to equilibrate in deionized water at 37 °C, with ambient air sparging. Refer to the hydration effect studies for guidelines on how long the equilibration period may be.

3). Set instrumental parameters and microscope focus with as little exposure as possible to the excitation source. Use the 10x objective.

4). Collect overall signal intensity from the APD on the eCorder instrument, at a rate of 1 Hz, with 10 Hz low-pass filtering and line filtering turned on.

5). Set the LED to 50% Brightness and operate continuously for 20 minutes.

6). After 20 minutes, allow the sensor material to rest for 3 hours; maintain the same air sparging and temperature settings.

7). Set the LED to 50% Brightness and operate continuously for 20 minutes.

8). Analyze the intensity data. Save the intensity data after any obvious induction period ends (typically ~ 30 seconds), then normalize the remaining data to maximum intensity and fit to a single exponential decay + baseline.

9). Report the lifetimes for each exposure period and the percent drop in intensity between the two runs for time zero of the saved data.

APPENDIX C

Procedure for Delamination Assessment

1). Place the glass chip into a crystallizing dish with 5-10 mL of media. In this study, the only media utilized was keratinocyte serum free media, Invitrogen (Eugene, OR).

2). Sonicate for 2 minutes, then inspect the arrays for damage on the microscope.

3). If damage or delamination is not evident, repeat sonication for 5 minutes, then inspect for damage.

4). If damage or delamination is not evident, repeat sonication for 10 minutes, then inspect for damage.

5). If damage or delamination is not evident, repeat sonication for 15 minutes, then inspect for damage.

6). If damage or delamination is not evident, repeat sonication in intervals of 30 minutes, with microscopic examination, until damage or delamination is evident.

7). Report the delamination time as the sum total of minutes of sonication time.

APPENDIX D

Procedure for Assessment of Singlet Oxygen Emission

1). Place a glass chip coated with cured sensor material in the chip holder; this experiment is done dry. Focus to the brightest spot with the 40x objective.

2). Utilize the eCorder to monitor the lock-in signal (10 V scale) and the temperature, pressure, and oxygen concentrations. Scan at 1 Hz with line filter and a 10 Hz low-pass filter. Repeat the experiment if there are any large fluctuations in temperature or pressure during the trial.

3). Expose to air purge until a stable signal is achieved on the Clark microelectrode. Set instrumental parameters to produce a signal from the femtowatt receiver with good SNR on a 10 V scale. Keep exposure to excitation light as minimal as possible.

4). Expose the sensor continuously to modulated light for 30 seconds. Verify a valid lock-in signal on the auxiliary oscilloscope.

5). Switch the purge to 500 sccm nitrogen; wait for a stable anoxic condition on the Clark microelectrode.

6). Expose the sensor continuously to modulated light for 30 seconds. Verify a valid lock-in signal on the auxiliary oscilloscope.

7). Analyze collected data to report a “singlet factor.” This is simply the ratio of mean signal intensity at ambient oxygen to mean signal intensity at anoxia.

VITA

Noel Fitzgerald was born in Yonkers, New York, in the midst of a snowstorm, which was perhaps a metaphor for the long and sometimes chaotic educational path to come. Most of his childhood was spent in Wixom, MI, which provided a wide variety of life experiences, including the beginning of a strong interest in volunteer firefighting. High school was followed by a brief stint at Michigan Technological University. MTU was not a good fit for Noel and years later, he returned to school at Green River College, after exploring firefighting opportunities in Colorado. The pleasant campus of Green River College prepared him for further studies at the University of Washington, where he completed B.S. degrees in Chemistry and Applied & Computational Mathematical Sciences (ACMS). Experience was gained as a Research Scientist working for Enertechnix, Inc. on projects that included acoustic pyrometry for clean coal technology, and assistance in developing an aerodynamic lens, for particle sampling. With completion of this project, he hopes to pursue research interests oriented around instrument and method development. He also continues his volunteer firefighting interest by serving as a Captain with East Pierce Fire & Rescue.